Fakultät für Maschinenwesen

Effect of Strain Rate on the Tensile, Compressive, and Shear Response of Carbon-Fiber-Reinforced Thermoplastic Composites

Marina Plöckl

Vollständiger Abdruck der von der Fakultät für Maschinenwesen der Technischen Universität München zur Erlangung des akademischen Grades eines

Doktor-Ingenieurs

genehmigten Dissertation.

Vorsitzender:

Prof. Dr.-Ing. Dirk Weuster-Botz

Prüfer der Dissertation:

1. Prof. Dr.-Ing. Klaus Drechsler

2. Assoc. Prof. Dr. Albert Turon Travesa (University of Girona)

Die Dissertation wurde am 25.06.2018 bei der Technischen Universität München eingereicht und durch die Fakultät für Maschinenwesen am 30.01.2019 angenommen.

Technische Universität München
Fakultät für Maschinenwesen
Lehrstuhl für Carbon Composites
Boltzmannstraße 15
D-85748 Garching bei München

Tel.: + 49 (0) 89 / 289 - 15092
Fax: + 49 (0) 89 / 289 - 15097
Email: info@lcc.mw.tum.de
Web: www.lcc.mw.tum.de

Acknowledgement

In conclusion, I would like to thank all those who contributed to the success of this work. My special thanks goes to:

- Prof. Dr.-Ing. Klaus Drechsler for giving me the opportunity to conduct scientific research within the field of high-strain-rate material characterization at his Chair of Carbon Composites at the Technical University of Munich, for the inspiring discussions and his encouraging support throughout my thesis.
- Assoc. Prof. Dr. Albert Turon Travesa from the University of Girona for acting as second referee.
- Dr. Hannes Körber, group leader of "Material Behavior and Testing", for his excellent supervision in all questions and belongings and for the correction of this thesis and the published Composite Structures journal paper.
- Dr. mont. Elisabeth Ladstätter for her support and advice in the project MAI Plast.
- Prof. Dr. rer. nat. Klaus-Dieter Liss from the University of Wollongong in Australia for his mentorship and discussions about material characterization by using spectroscopy.
- The German Federal Ministry of Education and Research for providing funding within the project MAI Plast.
- The research institute Fraunhofer-ICT for extruding polyamide sheets for the specimens.
- The research institute Fraunhofer-IGCV for borrowing the Photron high-speed camera model SA-Z for the dynamic longitudinal compression tests.
- My colleague Peter Kuhn for prove reading of the thesis and his help and advice during the setup of the dynamic experiments at the split-Hopkinson pressure and tension bar system and the data analysis.
- My colleagues Ulrich Mandel and Robin Taubert for supporting the approach of computing the strain rate in a kink-band.
- Luciano Avila Gray, Veronika Bühler, and all other members of the "Material Behavior and Testing" group for their pleasant assistance during specimen preparation and technical guidance for undertaking the experiments in the laboratory.

- Uli Ebner and the staff from the workshop of the Institute of Medical and Polymer Engineering at the Technical University of Munich for manufacturing experimental equipment for the mechanical tests.
- My colleagues Kalle Kind and Jan Krollmann and all other colleagues of the Chair of Carbon Composites which are not already mentioned in personal for the opportunity to work together and the great time.
- Friederike Gnädigner and all my friends for their encouragement.
- And last but not least my parents Vitus and Elfriede and my sister Teresa for the great support and encouragement in all belongings during my conferral of a doctorate.

Abstract

Carbon-fiber-reinforced composite materials are highly attractive for lightweight structural applications in automotive and aerospace industry due to their outstanding specific strength and stiffness. The composite material's constituents have very different physical and chemical properties but in combination, a material arises that has an overall better performance compared to the individual constituents. The drawback is that this combination of different material classes limits the predictability of the material failure under loading and finally results in high safety margins for the allowable design limits of structural parts. The strain-rate sensitivity is one material property of fiber-reinforced composites being focused on, because many primary structural applications involve exposure to impact and crash loads. This thesis presents an experimental study of the effect of strain rate on the compressive properties of neat resin and on the matrix dominated tensile, compressive, and shear properties of a carbon-fiber-reinforced thermoplastic composite. A simple approach was applied to predict the loading rate effect on the elastic properties of the neat matrix polymer. Experiments were performed by using a dynamic mechanical analysis at different frequencies to measure the strain-rate-dependent elastic properties of the polymer followed by an analytical approach to predict the elastic behavior at higher strain rates that are not measurable via dynamic mechanical analysis. The results show that at a strain rate of around $200\,\mathrm{s}^{-1}$ the elastic behavior of the matrix polymer as well as the compression, tension, and shear strength of the composite material increases significantly. For measuring the stress-strain behavior of the neat matrix polymer and the composite material from low to high strain rates, tests at quasi-static strain rate were performed by using a universal testing machine while for the dynamic tests at high strain rates a split-Hopkinson bar system was used. Due to the fact that national or international standards for dynamic measurements are not present, a new test method had to be developed to measure the strain-rate effect on the longitudinal compressive properties of the unidirectional carbon-fiber-reinforced composite. The main objective for this compression test was to achieve valid material failure in the free gauge section of the specimen. By using specifically designed specimens and a procedure based on classic laminate theory, static and dynamic longitudinal compressive strength values of the investigated unidirectional composite material were obtained. In general, it can be stated that irrespective of the load case, namely compression, tension, and shear a bilinear behavior of the matrix dominated strength values in relation to the strain rate, with a sharp increase in gradient at around $200\,\mathrm{s}^{-1}$, was found.

Kurzfassung

Kohlefaserverstärkte Verbundwerkstoffe sind aufgrund ihrer hervorragenden spezifischen Festigkeits- und Steifigkeitseigenschaften für Leichtbauanwendungen in der Automobil- und Luftfahrtindustrie sehr attraktiv. Die Bestandteile des Verbundwerkstoffes haben sehr unterschiedliche physikalische und chemische Eigenschaften, aber in Kombination entsteht ein Werkstoff, der im Vergleich zu den einzelnen Bestandteilen insgesamt bessere Eigenschaften aufweist. Der Nachteil ist, dass diese Kombination verschiedener Materialklassen die Vorhersagbarkeit des Materialversagens unter Belastung einschränkt und schließlich zu hohen Sicherheitsfaktoren für die zulässigen Auslegungsgrenzen von Strukturbauteilen führt. Die Dehnratenabhängigkeit ist eine der Materialeigenschaften auf der ein besonderer Fokus liegt, da viele primäre Strukturanwendungen mit Impact- und Crash-Belastungen verbunden sind. Diese Arbeit stellt eine experimentelle Studie vor über den Einfluss der Dehnrate auf die Druckeigenschaften von Reinharz und auf die matrixdominierten Zug-, Druck-, und Schubeigenschaften eines kohlefaserverstärkten thermoplastischen Verbundwerkstoffes. Ein einfacher Ansatz wurde angewandt, um den Dehnrateneffekt auf die elastischen Eigenschaften des reinen Matrixpolymers vorherzusagen. Dazu wurden Experimente mit Hilfe der dynamischen mechanischen Analyse bei verschiedenen Frequenzen durchgeführt, gefolgt von einem analytischen Ansatz zur Vorhersage des elastischen Verhaltens bei höheren Dehnraten, die mittels einer dynamischen mechanischen Analyse nicht messbar sind. Die Ergebnisse zeigen, dass bei einer Dehrate um $200\,\mathrm{s}^{-1}$ das elastische Verhalten des Matrixpolymers sowie die Druck-, Zug- und Schubfestigkeit des Verbundwerkstoffes deutlich zunimmt. Zur Messung des Spannungs-Dehnungsverhaltens des reinen Matrixpolymers und des Verbundwerkstoffes wurden Versuche bei quasi-statischer Dehnrate mit einer Universalprüfmaschine durchgeführt, während für die dynamischen Tests bei hohen Dehnraten ein split-Hopkinson Bar System verwendet wurde. Da es keine nationalen oder internationalen Normen für dynamische Messungen gibt, musste eine neue Prüfmethode entwickelt werden, um den Dehnrateneffekt auf die Längsdruckeigenschaften des unidirektionalen kohlefaserverstärkten Verbundwerkstoffes messen zu können. Das Hauptziel dieses Druckversuches war es, gültiges Materialversagen in der freien Messlänge des Prüfkörper zu erreichen. Durch die Verwendung speziell entwickelter Prüfkörper und einer Methode, die auf der klassischen Laminattheorie basiert, konnten statische und dynamische Längsdruckfestigkeitswerte ermittelt werden. Generell kann festgestellt werden, dass unabhängig vom Lastfall, nämlich Druck, Zug und Schub, ein bilineares Verhalten der matrixdominierten Festigkeitswerte in Bezug auf die Dehnrate, mit einem starken Anstieg des Gradienten bei etwa $200\,\mathrm{s}^{-1}$, gefunden wurde.

Contents

Contents xiii

Nomenclature xv

List of Figures xxi

List of Tables xxix

1 Introduction 1

1.1 Motivation 1
1.2 Objectives of the Thesis 2
1.3 Thesis Outline 3

2 Literature Review 5

2.1 Physical Description of the Strain-Rate Effect in Polymers 5
  2.1.1 Viscoelasticity of Polymers 5
  2.1.2 Root Cause of Strain Rate Dependency in Polymers 12
2.2 Strain Rate's Effect on Compressive, Tensile, and Shear Properties . 15
  2.2.1 Neat Polyamide-6 16
  2.2.2 Fiber-Reinforced Polyamide-6 Composites 18

3 Experimental Methods 21

3.1 Split-Hopkinson Pressure Bar Method 24
  3.1.1 Classic SHPB Setup 25
  3.1.2 Operating Principle of an SHPB 26
  3.1.3 Theory of Elastic Waves 27
  3.1.4 SHPB Analysis 31
  3.1.5 Pulse Shaping 36
3.2 Split-Hopkinson Tension Bar Method 38
  3.2.1 General SHTB Setup 38
  3.2.2 Operating Principle of an SHTB 39
3.3 Digital Image Correlation 41
  3.3.1 Basic Principles and Concepts 43
  3.3.2 Shape Function and Displacement Mapping Function 45
3.4 Dynamic Mechanical Analysis 46
  3.4.1 DMA Theory 46
  3.4.2 Viscoelastic Material Transitions in Polyamide-6 49

4 Strain Rate Dependency of the Neat Polyamide-6 51

4.1 Dynamic Mechanical Analysis 51
  4.1.1 Material 52
  4.1.2 Test Procedure 52
  4.1.3 Experimental Results 53
  4.1.4 Data Analysis 54
  4.1.5 Discussion 57
4.2 Compressive Properties of the Neat Polyamide-6 58
  4.2.1 Material and Test Specimens 58
  4.2.2 Quasi-Static Experimental Setup 59
  4.2.3 Dynamic Experimental Setup 60
  4.2.4 Results of Quasi-Static Experimental Tests 63
  4.2.5 Results of Dynamic Experimental Tests 64

5 Transverse Compression and Tension Properties of UD Laminate 73

5.1 Transverse Compression 73
  5.1.1 Material and Test Specimens 73
  5.1.2 Quasi-Static Experimental Setup 75
  5.1.3 Dynamic Experimental Setup 76
  5.1.4 Results of Quasi-Static Experimental Tests 79
  5.1.5 Results of Dynamic Experimental Tests 83
5.2 Transverse Tension 93
  5.2.1 Material and Test Specimens 93
  5.2.2 Quasi-Static Experimental Setup 94
  5.2.3 Dynamic Experimental Setup 96
  5.2.4 Results of Quasi-Static Experimental Tests 98
  5.2.5 Results of Dynamic Experimental Tests 101

6 In-plane Shear Response by Tensile Test of ±45 ° Laminate 107

6.1 Material and Experimental Procedure 107
  6.1.1 Material and Test Specimens 107
  6.1.2 Quasi-Static Experimental Setup 108
  6.1.3 Dynamic Experimental Setup 109
6.2 Results and Discussion 111
  6.2.1 Quasi-Static Experimental Results 111
  6.2.2 Dynamic Experimental Results 114

7 Longitudinal Compression Properties of UD Laminate 119

7.1 Experimental Procedure for UD Composites with Low Fiber Volume Content 119
  7.1.1 Material and Specimen 120

7.1.2 Quasi-Static and Dynamic Experimental Setup 121
7.1.3 Results and Discussion 125
7.2 Development of a Dynamic Test Methodology for UD Composites with High Fiber Volume Content 133
7.2.1 Material and Specimen 135
7.2.2 Quasi-static Test Setup 137
7.2.3 Dynamic Test Setup 137
7.2.4 Experimental Results 140
7.2.5 Discussion of Experimentally and Analytically Derived Material Properties 145
7.3 Strain Rate in Kink-Bands 151

8 Conclusions 163
8.1 Simplified Approach for Prediction of Strain Rate's Effect on Mechanical Response of Polymers 164
8.2 Developed Experimental Methodology for Dynamic Longitudinal Compression Tests 165
8.3 Correlation between Strain-Rate-Dependent Mechanical Properties . 167
8.3.1 Neat and Carbon-Fiber-Reinforced Polyamide-6 167
8.3.2 Carbon-Epoxy Prepreg IM7/8552 170

9 Outlook 173

Bibliography 175

Nomenclature

Abbreviations

2D	Two-dimensional
ASTM	American Society for Testing and Materials
BA	Bars-apart
BF	Back-out factor
BT	Bars-together
CC	Cross-correlation criterion
CCD	Charge-coupled device
CF	Carbon fiber
CFRP	Carbon-fiber-reinforced plastic
CLC	Combined-loading-compression
CV	Coefficient of variance
DIC	Digital image correlation
DIN	Deutsches Institut für Normung
DMA	Dynamic mechanical analysis
DSR	Decompose/shift/reconstruct method
EN	Europäische Norm
GF	Glass fiber
GOM	Gesellschaft für Optische Messtechnik mbH
HBM	Hottinger Baldwin Messtechnik GmbH
HR	High rate
ICT	Fraunhofer-Institut für Chemische Technologie
IGCV	Fraunhofer-Einrichtung für Gießerei-, Composite- und Verarbeitungstechnik
IR	Intermediate strain rate
ISO	Internationale Organisation für Normung
LED	Light-emitting diode
LHS	Left hand side
NMR	Nuclear magnetic resonance
PA	Polyamide
PC	Polycarbonate
PMMA	Poly(methyl methacrylate)
PS	Pulse shaper

QI	Quasi-isotropic
QS	Quasi-static
RHS	Right hand side
SHPB	Split-Hopkinson pressure bar
SHPBA	Split-Hopkinson pressure bar analysis
SHTB	Split-Hopkinson tension bar
SSD	Sum of squared differences criterion
STDV	Standard deviation
TC	Tungsten-carbide
TP	Thermoplast
UD	Unidirectional

Greek

α	Angle between cameras
γ_{12}	Shear strain
γ_{m}	Fiber rotation
Δl_{SG1}	Distance between strain gauge 1 on incident-bar and incident-bar/specimen interface
Δl_{SG2}	Distance between strain gauge 2 on transmission-bar and transmission-bar/specimen interface
δ	Phase lag
ϵ	Strain
$\dot{\epsilon}$	Strain rate
ϵ_0	Strain amplitude
ϵ_1	Strain of strain gauge number 1
ϵ_2	Strain of strain gauge number 2
$\epsilon_{\mathrm{C}}^{\mathrm{u}}$	Ultimate compressive failure strain
$\epsilon_{\mathrm{C}}^{\mathrm{y}}$	Compressive yield strain
ϵ_{d}	Strain of the damper
$\dot{\epsilon}_{\mathrm{d}}$	Strain rate of the damper
ϵ_{I}	Incident wave
$\epsilon_{\mathrm{I}}^{\mathrm{max}}$	Incident pulse amplitude
ϵ_{R}	Reflected wave
ϵ_{S}	Specimen strain
ϵ_{s}	Strain of the spring
$\dot{\epsilon}_{\mathrm{S}}$	Specimen strain rate

$\dot{\epsilon}_\mathrm{s}$	Strain rate of the spring
ϵ_T	Transmitted wave
ϵ_T	Total strain of spring and damper
$\dot{\epsilon}_\mathrm{T}$	Total strain rate of spring and damper
$\epsilon_\mathrm{T}^\mathrm{u}$	Ultimate tensile failure strain
ϵ_x	Strain in x-direction
ϵ_y	Strain in y-direction
η	Viscosity
η_0	Zero-order shape function
η_1	First-order shape function
η_2	Second-order shape function
θ_c	Misalignment angle
θ_i	Initial misalignment angle
ν_{12}	Major Poisson's ratio
ν_{21}	Minor Poisson's ratio
ξ_0	Zero-order shape function
ξ_1	First-order shape function
ξ_2	Second-order shape function
ρ	Density
ρ_A	Density of material A
ρ_B	Density of material B
σ	Stress
σ_a	Stress in a-direction
$\sigma_{\mathrm{a}^\mathrm{m}}$	Stress in a-direction in the misalignment frame
σ_b	Stress in b-direction
$\sigma_{\mathrm{b}^\mathrm{m}}$	Stress in b-direction in the misalignment frame
σ_d	Stress on the damper
σ_I	Stress of incident wave
$\sigma_{\mathrm{multi-direct.}}$	Compressive stress of a multi-directional laminate
σ_R	Stress of reflected wave
σ_S	Specimen stress
σ_s	Stress on the spring
σ_T	Stress of transmitted wave
σ_x^0	Longitudinal compressive stress of a UD ply
τ	Relaxation time
τ_{12}	Shear strength
τ_ab	Shear stress
$\tau_{\mathrm{a}^\mathrm{m}\mathrm{b}^\mathrm{m}}$	Shear stress in the misalignment frame

$\tau_{12\mathrm{M}}^{\mathrm{hr}}$	Dynamic shear strength
$\tau_{12\mathrm{M}}^{\mathrm{qs}}$	Quasi-static shear strength
ω	Oscillation frequency

Latin

A	Cross-sectional area
A	Ramberg-Osgood fitting parameter
a	Acceleration
A_{b}	Bar cross-sectional area
A_{ij}	The ij element in the ABD-matrix of the classic laminate theory
A_{s}	Specimen cross-sectional area
A_{s0}	Initial specimen cross-sectional area
B_y	Percent bending
C	Velocity
C	Wave velocity in bar material
C_{A}	Wave velocity in bar material A
C_{B}	Wave velocity in bar material B
c_{b}	Wave velocity of bar material
d_{b}	Diameter of the bar
E	Young's modulus
E'	Storage modulus
E''	Loss modulus
E^*	Complex modulus
E_1	Young's modulus in longitudinal direction
E_2	Young's modulus in transverse direction
E_{b}	Young's modulus of bar material
F	Force
F_1	Force at incident-bar/specimen interface
F_2	Force at specimen/transmission-bar interface
G	Shear modulus
G_{12}	Ramberg-Osgood fitting parameter
G_{ab}	Shear modulus
G_{12}^{hr}	Dynamic shear modulus
G_{12}^{qs}	Quasi-static shear modulus
h	Specimen thickness
J	Reciprocal of the modulus

l_b	Length of the bar
l_g	Specimen gauge length
l_striker	Striker-bar length
l_S	Specimen length
M	Number of pixels
m	Mass
n	Ramberg-Osgood fitting parameter
$\dot{p}$	Momentum
Q_ij	The ij element in the plane stress reduced stiffness matrix for a unidirectional lamina
$\tan\delta$	Loss tangent
T	Pulse duration
t	Time
T_α	α-transition temperature
T_β	β-transition temperature
t_{ϵ_I}	Arrival time of incident wave at specimen
t_{ϵ_R}	Time of reflected wave
t_{ϵ_T}	Time of transmitted wave
t_SG1	Time at strain gauge 1 on incident-bar
t_t	Tansit time
u	Displacement along bar axis
u_0	Initial displacement
$\dot{u}_1$	Particle velocity at incident-bar/specimen interface
$\dot{u}_2$	Particle velocity at specimen/transmission-bar interface
u_I	Displacement along bar axis due to incident wave
U_p	Particle velocity
U_pI	Particle velocity of incident wave
U_pR	Particle velocity of reflected wave
U_pT	Particle velocity of transmitted wave
u_R	Displacement along bar axis due to reflected wave
u_T	Displacement along bar axis due to transmitted wave
V_0	Striker-bar impact velocity
w	Specimen width
X_c	Ultimate failure strength in compression
$X_\mathrm{C}^\mathrm{y,hr}$	Dynamic compressive yield strength
$X_\mathrm{C}^\mathrm{y,ir}$	Intermediate rate compressive yield strength
$X_\mathrm{C}^\mathrm{y,qs}$	Quasi-static compressive yield strength
X_C^hr	Dynamic longitudinal compressive strength

$X_{\mathrm{C}}^{\mathrm{qs}}$	Quasi-static longitudinal compressive strength
x	Position
$Y_{\mathrm{C}}^{\mathrm{hr}}$	Dynamic transverse compressive strength
$Y_{\mathrm{C}}^{\mathrm{ir}}$	Intermediate rate transverse compressive strength
$Y_{\mathrm{C}}^{\mathrm{qs}}$	Quasi-static transverse compressive strength
$Y_{\mathrm{T}}^{\mathrm{hr}}$	Dynamic transverse tensile strength
$Y_{\mathrm{T}}^{\mathrm{qs}}$	Quasi-static transverse tensile strength

List of Figures

2-1 The Maxwell element with a serial connection of a spring and a damper (left) and the creep and creep recovery behavior of the Maxwell element (right) after [17]. 8

2-2 Stress relaxation of the Maxwell model after [18]. 9

2-3 The Voigt element with a parallel connection of a spring and a damper (left) and the creep and creep recovery behavior of the Voigt element (right) after [17]. 10

2-4 Storage modulus and tanδ for polycarbonate (PC) at frequencies of 1, 10, and 100 Hz, over temperatures from -100 to 180 °C in a single cantilever configuration. The strain amplitude was 0.030 ± 0.001 and the equivalent strain rates are therefore $(6 \pm 0.2) \cdot 10^{-4}\,\mathrm{s}^{-1}$, $6 \cdot 10^{-3}\,\mathrm{s}^{-1}$, and $6 \cdot 10^{-2}\,\mathrm{s}^{-1}$ [20]. 14

2-5 Specimens of polycarbonate (PC) tested over a range of strain rate and temperature. a) Plot of maximum stress against strain rate at 21 °C, showing two distinct regions in the data. b) Plot of maximum stress against temperature at $5500 \pm 500\,\mathrm{s}^{-1}$. c) Comparison of the variation of peak stress with temperature, and the variation of peak stress with strain rate mapped onto temperature [20]. 15

2-6 Compressive stress-strain curves for dry nylon 6 at six different strain rates (left) and plot of the maximum stress as a function of strain rate for dry nylon 6 (right) [19]. 16

2-7 The first yield stress as a function of (left) draw temperature at different nominal strain rates and (right) log of strain rate, lg(ϵ'), at different draw temperatures [35]. 17

2-8 Comparison between tension (left) and compression (right) test data for different strain rates with proposed model of Pouriayevali et al. [33]. 17

2-9 Effect of strain rate on the stress-strain curves of short E-glass-fiber-reinforced polyamide-6 in the extrusion direction (left) and normal to the extrusion direction (right) [38]. 19

2-10 Stress strain relations of carbon-fiber-reinforced polyamide composites obtained at low and high strain rates (left) [41]. Dependency of the tensile strengths of polyamide composites on the strain rate (right) [41]. 19

3-1 Strain rate regimes and associated instruments and experimental conditions [37]. 22

3-2 Schematic drawing of a servohydraulic testing machine of type Instron VHS 25/25-20 [43]. 22

3-3 Schematic drawing of a drop tower with a specimen clamping device [44]. 23
3-4 Split-Hopkinson pressure bar setup. 26
3-5 Longitudinal wave inciding on boundary between two media A and B in normal trajectory: (a) prior to encounter with boundary; (b) forces exerted on boundary (equilibrium condition); (c) particle velocities (continuity). Direction of arrows for reflected wave for case impedance A > impedance B [64]. 29
3-6 Time shifts of incident-, and transmission-bar strain signals for the SHPB Analysis. 33
3-7 Schematic drawing of the particle displacement directions (u_1, u_2) and bar strain wave directions in the incident-, and transmission-bar (ϵ_I, ϵ_R, ϵ_T) after [61]. 36
3-8 Schematic illustration of the influence of incident pulse shaping on the stress-strain response of a ceramic specimen. (a) Rectangular-shaped pulse on a ductile specimen. (b) Rectangular pulse on a ceramic specimen. (c) Ramp-shaped pulse on a ceramic specimen according to [69]. 37
3-9 Comparison of (a) rectangular-shaped pulse with (b) ramp-shaped pulse obtained from the same length striker-bar [69]. 37
3-10 Split-Hopkinson tension bar setup. 40
3-11 SHTB (left) with a sliding carriage connected to pulling rods that guides the striker-bar (right). 40
3-12 Sketch of an image acquisition system for 3D digital image correlation (DIC) measurement. 44
3-13 Schematic illustration of a reference square subset before deformation and after deformation [80]. 44
3-14 Sketch of tension clamps in a typical DMA setup for tensile tests. . 47
3-15 Schematic drawing of storage modulus, E', loss modulus, E'', and loss tangent, tanδ, as a function of the logarithmic frequency for a typical polymer in the vicinity of the glass transition after [92]. . . . 48
3-16 Sketch of the chemical structure of polyamide-6 with long-chain segmental motion (α) and local motion within the amide group (β). 50
3-17 Loss tangent as a function of temperature for different polyamides (nylons) [93]. The peaks from high to low temperatures indicate the α, β and γ-transition temperatures. 50

4-1 Storage modulus (left) and loss tangent (right) as a function of temperature for specimen number 1. 54

4-2 Storage modulus (left) and loss tangent (right) as a function of temperature for specimen number 2. 54
4-3 Decomposition of the α- and β-component of the experimental storage modulus curve (specimen 2) at $1.66 \cdot 10^{-3}\,\mathrm{s}^{-1}$. 56
4-4 Application of the decompose/shift/reconstruct (DSR) method developed by [28] on the measured storage modulus of polyamide-6. The dashed line indicates the room temperature at 20 °C. 56
4-5 Prediction of the storage modulus of PA 6 at room temperature with the decompose/shift/reconstruct (DSR) method developed by [28] as a function of strain rate. 57
4-6 Quasi-static compression test setup with tungsten-carbide (TC) inserts. 60
4-7 Incident- and transmission-bar strain signals of the bars-together tests with the used SHPB configuration for HR1 (left) and HR2 (right). 62
4-8 Quasi-static compressive stress-strain curves from reference tests (left) and enlarged view (right). The yield strength is marked with a symbol for each curve. 63
4-9 Intermediate strain rate test results. 64
4-10 Bar strain wave groups from HR1 (left) and HR2 (right) tests with shaped incident waves for a representative specimen, respectively. . 66
4-11 Dynamic stress equilibrium check and corresponding strain rate for a representative specimen tested at HR1 (left) and HR2 (right). . . 67
4-12 Uniform development of specimen strain along axial direction for a representative specimen tested at HR1 (left) and HR2 (right). . . . 67
4-13 Comparison of the quasi-static compressive stress-strain curves from reference tests with dynamic tests at HR1 (left) and HR2 (right). . 68
4-14 In-plane strain fields in loading direction of compression specimens at HR2 a)-d), HR1 e)-h), and quasi-static loading i)-l). 68
4-15 Comparison of the quasi-static, intermediate, and high strain rate compressive test results. 70
4-16 Comparison of experimental results with literature results regarding the strain rate's effect on the compressive properties of polyamide-6. 71

5-1 Incident- and transmission-bar strain signals of the bars-together tests with the used SHPB configuration for HR1, HR2, and HR3. . 78
5-2 Quasi-static transverse compressive stress-strain curves from reference tests. 79
5-3 Fracture under uniaxial compressive stress σ_2^c [119]. 80
5-4 Quasi-static transverse compressive stress-strain curves from static ASTM tests. 81

5-5 Comparison of the quasi-static longitudinal compressive stress-strain curves from reference and ASTM tests. 82
5-6 Quasi-static specimen failure mode of ASTM tests. 82
5-7 Transverse compressive stress-strain curves from intermediate strain rate tests. 83
5-8 Bar strain wave groups from HR1 (top left), HR2 (top right), and HR3 (bottom) tests with trapezoidal shaped incident waves for a representative specimen, respectively. 85
5-9 Dynamic stress equilibrium check and corresponding strain rate for a representative specimen tested at HR1 (top left), HR2 (top right), and HR3 (bottom). 86
5-10 Uniform development of specimen strain along axial direction for a representative specimen tested at HR2 (left) and HR3 (right). . . . 87
5-11 Dynamic (HR1) transverse compressive stress-strain response of all tested specimens. 88
5-12 Dynamic (HR2) transverse compressive stress-strain response of all tested specimens. 89
5-13 Dynamic (HR3) transverse compressive stress-strain response of all tested specimens. 90
5-14 In-plane strain fields in loading direction of transverse compression specimens at HR3 a)-d), HR2 e)-h), HR1 i)-l), and quasi-static loading m)-q). 91
5-15 Comparison of the quasi-static transverse compression stress-strain curves from reference and dynamic tests. 92
5-16 Specimen geometry (nominal thickness 2 mm) for quasi-static and dynamic tests with threaded endcaps. 94
5-17 Quasi-static tensile test setup. 95
5-18 Dynamic transverse tension specimen in an SHTB setup. 97
5-19 Incident- and transmission-bar strain signals of the bars-together test with the used SHPB configuration. 97
5-20 Quasi-static transverse tension stress-strain curves from reference tests. 98
5-21 Quasi-static specimen failure mode of reference tests. 98
5-22 Quasi-static transverse tension stress-strain curves from static DIN tests. 99
5-23 Quasi-static specimen failure mode of DIN tests. 100
5-24 Comparison of the quasi-static longitudinal tension stress-strain curves from reference and DIN tests. 101
5-25 Bar strain wave groups from dynamic tests with triangular shaped incident waves for a representative specimen. 101

5-26 Dynamic stress equilibrium check and corresponding strain rate for a representative specimen. 102
5-27 Uniform development of specimen strain along axial direction for a representative specimen. 103
5-28 Dynamic transverse tension stress-strain response of all tested specimens. 103
5-29 Dynamic specimen failure mode. 104
5-30 In-plane strain fields in loading direction of transverse tension specimens at HR a)-c) and quasi-static loading d)-f). 105

6-1 Incident- and transmission-bar strain signals of the bars-together tests with the used SHPB configuration. 110
6-2 Quasi-static in-plane shear stress-strain curves from reference tests. 111
6-3 Quasi-static in-plane shear stress-strain curves from static DIN tests (left) and Load-displacement curves from static DIN tests (right). . 112
6-4 Quasi-static specimen failure mode of DIN tests. 113
6-5 Comparison of the quasi-static in-plane shear stress-strain curves from reference and DIN tests. 114
6-6 Bar strain wave groups from dynamic tests with trapezoidal shaped incident waves for a representative specimen. 115
6-7 Dynamic stress equilibrium check and corresponding strain rate for a representative specimen tested at high strain rate. 115
6-8 Uniform development of specimen strain along axial direction for a representative specimen tested at high strain rate. 116
6-9 Dynamic in-plane shear stress-strain response of all tested specimens. 117

7-1 Top view a) and side view b) of end-loaded compression specimen geometry for quasi-static and high strain rate measurements. 121
7-2 Quasi-static compression test setup with tungsten-carbide inserts. . 122
7-3 Split-Hopkinson pressure bar test setup with modified Dynamic Compression Fixture (DCF). 123
7-4 Incident- and transmission-bar strain signals of the bars-together test with the used SHPB configuration. 124
7-5 Modified Dynamic Compression Fixture used in the SHPB setup. . 124
7-6 Quasi-static longitudinal compressive stress-strain curves from reference tests. 125
7-7 Tested quasi-static reference specimens. Arrow indicates position of compressive failure mode (kink band). 126
7-8 Quasi-static longitudinal compressive stress-strain curves from static ASTM tests. 127
7-9 Quasi-static specimen failure mode of ASTM tests. 127

7-10 Comparison of the quasi-static longitudinal compressive stress-strain curves from reference and ASTM tests. 128

7-11 Incident- and transmission-bar signals of the specimen HR-1 a) and SHPB Analysis results of the specimen HR-1 for the shifted bar strain waves b), the loads acting on the specimen c), the specimen strain behavior d), the specimen strain rate e) over time, and the stress-strain response f). 130

7-12 Dynamic longitudinal compressive stress-strain response of all tested specimens. 131

7-13 Dynamic specimen failure mode. 132

7-14 High-speed camera images and stress-time response of the dynamic compression specimen HR-1 at t_0 a), $t_0 + 183\,\mu s$ b), $t_0 + 188\,\mu s$ c), and $t_0 + 199\,\mu s$ d). 132

7-15 Comparison of the quasi-static longitudinal compressive stress-strain curves from reference and dynamic tests. 133

7-16 Compression device for quasi-static and dynamic measurements. . . 136

7-17 Compression device developed in a universal testing machine for quasi-static tests (left) and in a split-Hopkinson pressure bar for dynamic tests (right). 138

7-18 Incident- and transmission-bar strain signals of the bars-together test with the SHPB configuration used. 139

7-19 Representative incident- and transmission-bar strain signals of a UD IM7/8552 specimen. 140

7-20 Equilibrium check of forces acting on opposite sides of a representative specimen of UD IM7/8552 (top left), QI IM7/8552 (top right), and UD carbon-fiber-reinforced polyamide-6 (bottom). 141

7-21 Quasi-static and dynamic longitudinal compressive stress-strain curves for UD IM7/8552 (top left), QI IM7/8552 (top right), and UD carbon-fiber-reinforced polyamide-6 (bottom). 142

7-22 Failure initiation and propagation during a dynamic experiment on a UD IM7/8552 specimen (a), QI IM7/8552 specimen (b), and UD carbon-fiber-reinforced polyamide-6 specimen (c). 144

7-23 Bending behavior as a function of longitudinal strain for all quasi-static UD IM7/8552 (top left), QI IM7/8552 (top right), and UD carbon-fiber-reinforced polyamide-6 (bottom) specimens. 146

7-24 Bending behavior as a function of longitudinal strain for all dynamic UD IM7/8552 (top left), QI IM7/8552 (top right), and UD carbon-fiber-reinforced polyamide-6 (bottom) specimens. 147

7-25 Strain rate and stress as a function of time of a representative QI IM7/8552 specimen. Dashed vertical lines indicate time interval in which the mean strain rate is calculated. 147
7-26 Comparison of the predicted IM7/8552 longitudinal compressive strength by measurement of a quasi-isotropic laminate and the longitudinal compressive strength by measurement of a unidirectional laminate for two different strain rates. 150
7-27 Normalized strength as a function of the axial strain rate for transversal and longitudinal compression. 151
7-28 (a) Kinking band; (b) fiber misalignment frame [130]. 153
7-29 In-plane shear curve from dynamic experiment and Ramberg-Osgood fit curve. 153
7-30 Iterative process to find tangential point for example $\theta_\mathrm{i} = 2°$ (left) and $\theta_\mathrm{i} = 1.16°$ (right) (Equation 7-23). 154
7-31 Scheme for the determination and verification of the initial misalignment angle, θ_i. 155
7-32 In-plane shear curve from dynamic experiment and Ramberg-Osgood fit curve. 156
7-33 Iterative process to find tangential point for 1.16° (dynamic fitting parameters). 156
7-34 Left and right hand side of Equation 7-27 for a material with a nonlinear shear behavior and failure by matrix cracking (left), and failure by instability (right) [136]. 157
7-35 Example for solving the Equation 7-28. The stress values for different instants of time are listed in Table 7-6. 159
7-36 Normalized strength as a function of the strain rate for transversal and longitudinal compression. The strain rate is shown in axial loading direction and in the failure plane of the kink-band. 161

8-1 Normalized strength values from experiment as a function of strain rate for different load cases and trend line. 169
8-2 Normalized 0° compression strength determined from IM7/8552 UD and QI laminate compared with normalized tension and compression strength results of published data from Koerber et al. [14], Koerber and Camanho [15], Kuhn et al. [126], and Cui et al. [137]. 171

List of Tables

3-1 Experimental methods for high strain material characterization [37]. 21

4-1 Calculated strain rate for 1 Hz, 10 Hz, and 100 Hz. 53
4-2 α- and β-temperature at different frequencies. Delta 1 determines the temperature difference from 1 Hz to 10 Hz and delta 2 from 10 Hz to 100 Hz. 55
4-3 Shift factor for transitions. 55
4-4 SHPB setup for compression tests of the neat polyamide-6. 61
4-5 Parameters for post processing with the software GOM ARAMIS-4M. 62
4-6 Quasi-static compression reference test results. 63
4-7 Intermediate rate compression test results. 64
4-8 Dynamic (HR1) compression test results. 69
4-9 Dynamic (HR2) compression test results. 69

5-1 SHPB setup for transverse compression tests. 77
5-2 Parameters for post processing with the software GOM ARAMIS-4M. 79
5-3 Quasi-static transverse compression reference test results. 80
5-4 Quasi-static transverse compression ASTM test results. 81
5-5 Intermediate rate transverse compression test results. 84
5-6 Dynamic (HR1) transverse compression test results. 88
5-7 Dynamic (HR2) transverse compression test results. 89
5-8 Dynamic (HR3) transverse compression test results. 90
5-9 Quasi-static transverse tension reference test results. 99
5-10 Quasi-static transverse tension DIN-test results. 100
5-11 Dynamic transverse tension test results. 104

6-1 Quasi-static in-plane shear reference test results. 112
6-2 Quasi-static in-plane shear DIN test results. 113
6-3 Dynamic in-plane shear test results. 116

7-1 Quasi-static reference test results. 126
7-2 Quasi-static longitudinal compression ASTM test results. 128
7-3 Dynamic longitudinal compression test results. 131
7-4 Quasi-static and dynamic longitudinal compression test results. . . 143
7-5 IM7/8552 material properties used to compute the static and dynamic back-out factor, BF. 149
7-6 Stress and corresponding time values of a typical dynamic longitudinal compression test and shear strain calculated with Equation 7-28 (intersection and tangential points in Figure 7-35). 159

7-7 Strain rate in axial direction and in the failure plane of the kink-band for the quasi-static and dynamic tests. 160

1 Introduction

Life in the present time and economy is affected by a steady increase in mobility. Large distances must be overcome within a short time period. Hardly nothing characterizes life in a globalized society as much as mobility. This has great effect on the word-wide volume of traffic. An increasing number of traffic participates makes it necessary to be prepared by passive safety precautions for possible collisions. Thus crash structures are required when people and objects need to be protected from high kinetic energy. In case of an accident this structures are the first parts of the vehicle which should absorb almost all impact energy. Besides automotive and aerospace structural applications also safety structures for railed vehicles, buses, and marine applications are used. In civil engineering the earthquake protection of buildings, road transport infrastructure, e.g. bridges, ropeways, and elevators are of great importance. In addition, objects like transport containers, packaging, or helmets for the direct protection of persons are safety-related. The future design of such applications in aerospace, automotive, marine, and civil engineering have to take safety precautions as a basic design guide.

1.1 Motivation

In the history of automotive and especially aviation industry, lightweight constructions always played an important role. Nowadays a key requirement for new vehicle and aircrafts beside safety precautions is the reduction of weight for improving energy efficiency or increasing larger carrying capacity for a better competitiveness. The contribution of carbon-fiber-reinforced plastic (CFRP) composite materials with extraordinary strength to weight and stiffness to weight ratios optimizes the mechanical performance of structures due to predictable load limits. The usage of thermoplastic matrix systems with carbon or glass fibers particularly for high volume automotive applications offers not only the possibility to make manufacturing processes more cost effective, but also can improve the mechanical properties of structural parts during a crash or impact. Due to the more ductile matrix, the impact resistance is higher compared to thermoset based matrix systems [1].

It is generally known that the mechanical properties of various materials and particularly of polymer materials are strain rate sensitive [2]. That means, the mechanical behavior of the material under static loading is different compared to the behavior under short-term loading. Thus, for the design of load carrying structures, e.g. bumpers in the car body, which have to withstand dynamic loading, strain-rate-dependent material data and knowledge about the failure behavior is necessary. Therefore the investigation of the carbon-fiber-reinforced composite materials concerning the inter- and intralaminar properties significantly contribute to the construction of structures which absorb a high amount of energy in the case of crash or impact.

In the recent decades large experimental effort in the field of metallic materials was conducted to investigate the stain-rate-dependent material behavior [3–7]. Likewise with the application of composite materials in aerospace structures the development of experimental characterization methods for high strain rate data was mainly driven by the usage of fiber-reinforced thermoset composite materials [8–16]. Nevertheless, the damage initiation and failure propagation within thermoset resin system is not completely understood. In recent years, the proportion of parts and components made of fiber-reinforced plastics in the automotive industry continuously rose. In contrast to the aerospace industry reinforced thermoplastic matrix systems are used to a greater extent due to advantages in processing, damage tolerance, and recyclability. The design of composite structures for modern vehicle and aircrafts with corresponding safety precautions has to take into account high strain rate loading conditions. Besides, finite-element simulations of impact and crash scenarios are often used to ensure reliable reproduction of the mechanical response. These models become more accurate and may be improved, if more knowledge about the dynamic material behavior is available. The study of fiber-reinforced composite materials in terms of the strain rate sensitivity is therefore subject of this research.

1.2 Objectives of the Thesis

Based on the previous motivation the question arises: How does the loading velocity affect the mechanical properties of unidirectional fiber-reinforced thermoplastic composites when the material is subjected to tensile, compression, and shear loads? To give a well-grounded answer to this question several major objectives were set:

- In the framework of previous studies a simple experimental approach should be found and if necessary modified to predict the strain-rate-dependent material properties of a neat polymer material up to strain rates of several hundred per second without conducting challenging and time consuming quasi-static (QS) and dynamic measurements.
- It should be demonstrated that a simple rectangular end-loaded compression specimen geometry can be used to analyze the strain rate sensitivity of neat thermoplastic polymer by means of the split-Hopkinson pressure bar (SHPB) method. The background of this objective is, that reported studies

use cylindrical shaped neat resin (mainly thermoset polymers) specimens for dynamic tests.

- A characterization of the strain-rate-dependent transverse compression and tension properties of a unidirectional carbon-fiber-reinforced thermoplastic composite will be conducted. These parameters are strongly influenced by the matrix of the composite material.
- The in-plane shear tensile test of ±45 ° laminates should be applied for dynamically testing the shear properties of carbon-fiber-reinforced thermoplastic composites with a split-Hopkinson tension bar (SHTB) setup. This mechanical property of the composite material is influenced by the matrix and therefore a relevant parameter to be analyzed to get a comprehensive description of the material behavior.
- A experimental methodology for the dynamic characterization of the longitudinal compressive properties of unidirectional fiber-reinforced composites with a split-Hopkinson pressure bar system should be developed. Previous studies have shown that especially failure occurs frequently at the specimen loading-surfaces and not in the free gauge section. Thus an under predicted strength on the specimen is measured due to an invalid failure mode. Therefore a key requirement is to develop an experimental methodology which prevents a premature material failure. Additionally the dynamic experimental setup should be designed in such a way that the failure mode can be recorded via high-speed photography.
- A comparison should be drawn to show the major correlations between the strain-rate-dependent properties of the thermoplastic matrix material without fibers and the fiber-reinforced composite material of the same thermoplastic polymer. Is it possible to predict the strain-rate effect of the composite material on the basis of few relatively simple measurements?
- The thesis should clarify if there is a general relationship between strain-rate-dependent tensile, compressive, and shear properties of the investigated fiber-reinforced thermoplastic composite.

1.3 Thesis Outline

Chapter 1 gives an introduction to the necessity of high strain rate material characterization for the design of composite parts for aerospace and automotive applications. Furthermore, the central research question is formulated that motivates a study within the frame work of a thesis project. Several objectives are drafted based on the motivation and an outline of the whole thesis document is given.

Chapter 2 gives a general description of the physical mechanism that causes the strain-rate effect in polymers. Moreover, the current state of research with focus on the investigations of the strain rate sensitivity on compressive, tensile, and shear properties of neat thermoplastic polyamide-6 and fiber-reinforced thermoplastic polyamide-6 is presented.

In Chapter 3 the experimental methods for the material characterization are introduced. Particular attention is paid to the split-Hopkinson pressure and the split-Hopkinson tension bar method. A brief description of digital image correlation and the dynamic mechanical analysis is given.

Chapter 4 deals with the investigation of the strain rate sensitivity of a neat polyamide polymer. The analytically derived results from dynamic mechanical analysis data and experimental results gained from quasi-static compressive and dynamic compressive experiments are discussed and compared with results documented in literature.

In Chapter 5 the focus lies on the transverse compression and tension properties of the unidirectional laminate of carbon-fiber-reinforced polyamide-6 under quasi-static and high strain rate loading. The strain rate's effect on these two basic material parameters will be shown.

In Chapter 6 the experimental results of the in-plane shear response by tensile tests of $\pm 45\,^\circ$ laminate of the investigated composite material at different strain rates are obtained and discussed.

Chapter 7 focuses on the development of a dynamic methodology for a split-Hopkinson pressure bar system to investigate the strain-rate-dependent longitudinal compression properties of unidirectional carbon-fiber-reinforced composites. A numerical approach is given to calculate the strain rate in a kink-band which occurs during longitudinal compression of a specimen.

Chapter 8 summarizes and evaluates the experimental results obtained within this study. General conclusions are drawn which show the overall relationship of the strain rate's effect on the material properties at different load cases.

In Chapter 9 an outlook is given about further research concerning high strain material characterization of composite materials.

2 Literature Review

This chapter starts with a general description of the physical mechanism that cause the strain rate dependency of polymers. In the second part of this chapter the current state of research concerning high strain rate material characterization is described. The focus thereby lies on the literature review of the strain rate dependency on compressive, tensile, and shear properties of the neat polyamide-6 and the fiber-reinforced polyamide-6 composite material, because these materials are subject of this study.

2.1 Physical Description of the Strain-Rate Effect in Polymers

The mechanical behavior of polymers depends on the microstructure or morphology which in turn is strongly influenced by many structural and environmental factors. The time and temperature dependency of polymers is more pronounced compared to metals and ceramics. This can be attributed to the viscoelastic nature of the polymers which will be discussed in section 2.1.1 of this chapter. The mechanical response of polymers differs due to temperature and stress levels and may result in linear elastic material behavior, plastic deformation, yielding of the material or cold drawing effects. Some amorphous polymers with glass transition temperature below room temperature may exhibit nonlinear but recoverable deformation or even viscous flow material behavior. In general various structural and environmental factors such as molecular weight, cross-linking, crystallinity, copolymerization, plasticizers, polarity, pressure, and as already mentioned temperature affect the mechanical properties. In addition, polymers are sensitive to the rate of loading. An increase of the strain rate often results in a decrease of the ductility of the polymer. In contrast, the modulus and the yield or tensile strength increase with increasing loading rate [17]. In section 2.1.2 the reasons for this effect are described and discussed.

2.1.1 Viscoelasticity of Polymers

The transition of an amorphous polymer from a solid state into a low viscosity melt does not happen instantaneously but over a broad temperature region where the material behaves elastically and the form stability is kept. If the amorphous polymer is heated above the glass transition temperature rotations of molecular chain segments around single bonds in the main polymer chain are possible. Due to this flexibility in the molecular chain a deformation of the tangled polymer can occur without breaking bonds. If the polymer chain length is longer than a distinct critical length the locking of the molecular chains counteracts the deformation of the specimen. At temperatures far above the glass transition temperature the locking of the polymer chains dissolves very quickly and no elastic behavior of the material can be seen. In this case the polymer melt behaves like a "normal" liquid with a low viscosity. In contrast, at temperatures around the glass transition temperature a deformation of the polymer material leads to an energetic unfavorable conformation of the molecular chains where elastic energy can be stored in the material. Hence, depending on the time period of loading the polymer shows a different behavior. If the time of loading is very short, in comparison to the relaxation time of the polymer, the molecular chains receive their original energetically favorable state of conformation. Thus the deformation of the specimen is completely reversible. On the other hand, at prolonged loading the polymer chains can reorientate themselves relative to each other because the external force hinders the chains to reach their original tangled conformation [18].

The deformation behavior of an ideal material can be described in the first instance by simple models. Hooke's law for the linear elasticity in the solid state and Newtonian's law of linear viscosity in the liquid state. The Hooke's law is defined by the following equation with the parameter stress, σ, the Young's modulus, E, and the elastic strain, ϵ:

$$\sigma = E \cdot \epsilon. \tag{2-1}$$

The viscose fluid determined by Newton depends on the viscosity, η, and the strain rate, $\dot{\epsilon} = \frac{d\epsilon}{dt}$:

$$\sigma = \eta \dot{\epsilon}. \tag{2-2}$$

In a viscose fluid the stress response is proportional to the strain rate but independent of the strain. Both laws can be illustrated with mechanical elements like a damper (Newton) or a spring (Hooke). The spring saves elastic energy and releases it. Thus the applied stress, σ, is proportional to the strain, ϵ. The analogous model of the damper is described via a plate that performs work in a liquid with the viscosity, η. In this model the energy dissipates and thus the applied stress is independent of the strain [18].

The mechanical behavior of many real materials can be approximated by these idealized models. However, for polymers these models are not sufficient to describe the mechanical response. Their solid state deformation behavior is time-dependent and nonlinear. These polymers combine the characteristics of both elastic and viscous materials and thus are denoted as viscoelastic materials [17].

Applying stress on a perfectly elastic material an instantaneous and corresponding strain response can be observed. In the same way, when the load is removed the strain instantaneously returns to zero. The material responds instantaneously to the applied stress. Thus, the material is independent of the deformation rate. The energy does not dissipate as either heat or sound. The spring as a mechanical element, shows always a proportional stress to strain behavior when neglecting inertial effects. For a perfectly elastic material the mechanical response is described by Hooke's law.

In contrast, the deformation behavior of viscoelastic materials under stress is time dependent. By applying a certain load which is held constant an increase in strain with time can be seen. This is attributed to creep in the polymer. Considering a constant deformation of the viscoelastic material the induced stress will relax with time. As already mentioned mechanical elements such as springs or dampers are introduced to describe the material behavior of polymers. But the viscoelastic material behavior cannot be described accurately with neither a spring nor a damper. It has been demonstrated that a combination of both elements is more appropriate. But even then only a qualitative description can be drawn that provides a valuable visual aid but no further details due to restrictions of the model [17].

Maxwell Model

The simplest model, which combines a spring and a damper in a series, is referred to as the Maxwell element. In Figure 2-1 the Maxwell model [17] is shown. The applied load to the system is carried by the Maxwell elements in the same way. The stresses on the spring, σ_{s}, and on the damper, σ_{d}, are equal:

$$\sigma = \sigma_{\mathrm{s}} = \sigma_{\mathrm{d}}. \tag{2-3}$$

Concerning the overall strain, ϵ_{T}, and strain rate, $\dot{\epsilon}_{\mathrm{T}}$, the summation of the elemental strain and strain rates, respectively, can be defined as:

$$\epsilon_{\mathrm{T}} = \epsilon_{\mathrm{s}} + \epsilon_{\mathrm{d}} \tag{2-4}$$

and

$$\dot{\epsilon}_{\mathrm{T}} = \dot{\epsilon}_{\mathrm{s}} + \dot{\epsilon}_{\mathrm{d}}. \tag{2-5}$$

The substitution of Equation 2-1 and 2-2 in 2-4 yields the rheological equation of the Maxwell model:

$$\dot{\epsilon}_{\mathrm{T}} = \frac{1}{E}\dot{\sigma} + \frac{1}{\eta}\sigma. \tag{2-6}$$

As it can be seen from the above equation the Maxwell model is a combination of the response of an ideally elastic material and a material behavior of pure viscous flow [17]. In the case of creep, an instantaneous constant stress, σ_0, is applied on the material while $\frac{d\sigma}{dt} = 0$ this leads to:

$$\dot{\epsilon}_{\mathrm{T}} = \frac{1}{\eta}\sigma_0. \tag{2-7}$$

Differentiating this equation after time and considering the initial strain as $\frac{\sigma_0}{E}$ yields:

$$\epsilon(t) = \sigma_0 \left(\frac{1}{E} + \frac{t}{\eta} \right). \tag{2-8}$$

The polymer experiences creep recovery when the applied stress is removed [17]. In Figure 2-1 the creep and the creep recovery curves of the Maxwell element are plotted. At the beginning it can be seen that the applied constant stress causes an instantaneous deformation by the amount of $\frac{\sigma_0}{E}$ and with increasing time the damper follows by relieving the stress as long as the stress is maintained. When the stress is removed from the system the strain response follows instantaneously while the damper retains a permanent set [17].

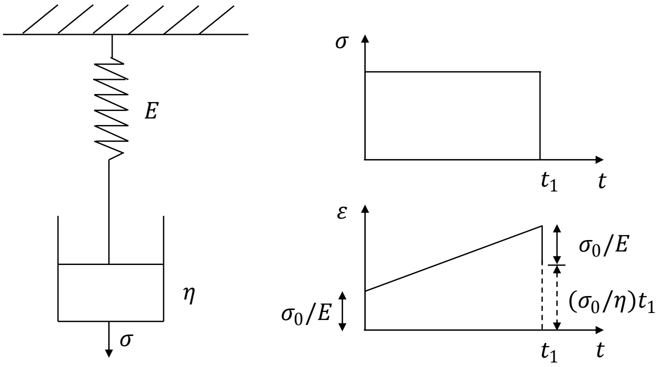

Fig. 2-1 The Maxwell element with a serial connection of a spring and a damper (left) and the creep and creep recovery behavior of the Maxwell element (right) after [17].

In the case of a relaxation experiment where an instantaneous strain is applied on the specimen, only the spring of the Maxwell model initially responds while the damper relaxes with time and thus the stress decreases with increasing time [17]. As a consequence of a constant strain and thus $\dot{\epsilon}_{\mathrm{T}} = 0$ the rheological equation of the Maxwell model can be simplified to:

$$\frac{1}{E}\dot{\sigma} + \frac{1}{\eta}\sigma = 0. \tag{2-9}$$

Solving this first-order differential equation with the boundary condition of $\sigma = E\epsilon_0$ and $t = 0$ yields:

$$\sigma = \sigma_0 \, e^{-\frac{E}{\eta} t}. \tag{2-10}$$

This equation describes the stress response of the Maxwell model that decreases exponentially with time. In general this model illustrates the stress relaxation of a viscoelastic system that is deformed by a distinct amount and held at this displacement. An instantaneous displacement only affects the spring in the first moment due to the inertness of the damper. When applying a load over a long time period the damper is deformed irreversible while the spring contracts. Hence, the stress decreases exponentially with time until zero [18].

In conclusion, this simple model describes the mechanical response of a viscoelastic polymer under a constant strain. The polymer chains have enough time to move relative to each other during the time of constant strain to reach an energetic favorable conformation. The quotient of viscosity and the Young's modulus is defined as the relaxation time:

$$\tau = \frac{\eta}{E}. \tag{2-11}$$

The Maxwell model describes the time dependent stress relaxation at constant strain (Figure 2-2). In contrast to an actually observable behavior of a viscoelastic materials system the model does not predict the elastic behavior for a long time period nor the dependency of the strain with time because a constant strain in time is assumed for this model.

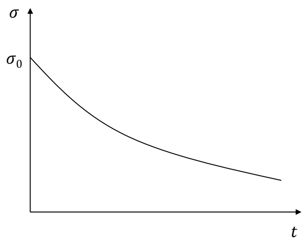

Fig. 2-2 Stress relaxation of the Maxwell model after [18].

Voigt-Kelvin Model

The previous described model does not fulfill all requirements to describe the material behavior of a polymer under loading. A further logical step is, to consider a parallel arrangement of the spring and the damper. This model is commonly known as Voigt-Kelvin model (Figure 2-3). The connection of the spring and the damper is parallel and thus the strain in each element is the same. The summation of the stresses in the spring and the damper gives the total stress on the system [17]:

$$\sigma_{\mathrm{T}} = \sigma_{\mathrm{s}} + \sigma_{\mathrm{d}}. \tag{2-12}$$

By substituting the stresses with the known parameters, Equations 2-1 and 2-2, the rheological equation yields:

$$\sigma_{\mathrm{T}} = E\epsilon + \eta\frac{d\epsilon}{dt}. \tag{2-13}$$

In the case of a creep experiment the applied stress is constant and thus:

$$\sigma_0 = E\epsilon + \eta\frac{d\epsilon}{dt}. \tag{2-14}$$

This equation is a linear differential equation which has the following solution in case of the integrating between $\epsilon(0) = 0$ and $\epsilon(t) = \epsilon(\tau)$:

$$\epsilon(t) = \frac{\sigma_0}{E}(1 - e^{-Et/\eta}), \tag{2-15}$$

$$\epsilon(t) = \frac{\sigma_0}{E}(1 - e^{-t/\tau}), \tag{2-16}$$

or

$$J(t) = \frac{\epsilon(t)}{\sigma_0} = J(1 - e^{-t/\tau}) \tag{2-17}$$

with the reciprocal of the modulus $J = 1/E$. In Figure 2-3 the creep and creep recovery curves of the parallel arrangement of the spring and damper are illustrated.

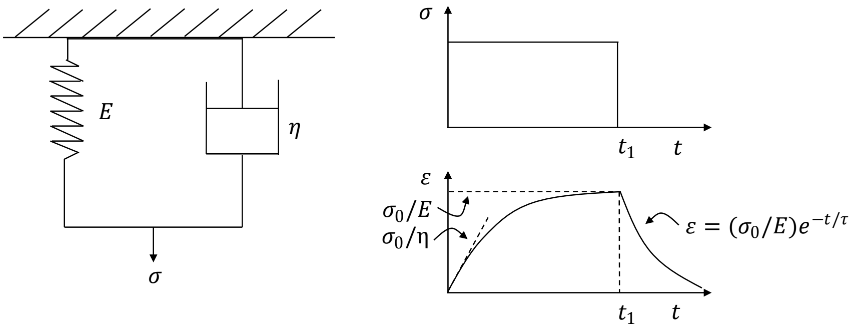

Fig. 2-3 The Voigt element with a parallel connection of a spring and a damper (left) and the creep and creep recovery behavior of the Voigt element (right) after [17].

Assuming that in a creep experiment a sudden constant stress is applied to the Voigt element, then the spring would be the only part of the system which offers the initial resistance to the deformation. But this instantaneous elongation of the spring is constrained by the elongation behavior of the damper. As mentioned before the strain of the spring and damper are equal in the Voigt element. This implies that the initial total stress of the system is introduced by the damper. During the creep experiment a constant force is applied. The damper slowly starts to transfer the applied load to the spring. Thus the stress in the damper decreases and hence the strain rate decreases which behaves proportional to the magnitude of the stress in the damper. After a sufficient time equilibrium strain can be reached where the strain rate is zero. At this point the resistance of the damper is zero while the entire stress on the Voigt element is supported by the spring element (σ_0/E). When the load is removed in this stadium of equilibrium, the strain decays exponentially. It can be concluded that the response of the Voigt model shows that the strain does not follow the stress continuously, i.e. the element approaches the strain not instantaneously but gradually. The Voigt element exhibits retarded elasticity in creep recovery. In contrast the Maxwell element retracts instantaneously but not completely [17].

Considering a stress relaxation experiment where the strain is constant, the rheological equation of the Voigt element is reduced to:

$$\sigma(t) = E\epsilon. \tag{2-18}$$

This is obviously Hooke's law. This leads to the conclusion that the Voigt model cannot describe the mechanical behavior of a polymer during a stress relaxation experiment. When an instantaneous strain would be applied to the Voigt element an infinite resistance of the damper would be induced. As a consequence an infinite stress would be needed to overcome the resistance [17]. But this is not realistic.

The Maxwell model nor the Voigt model is suited to accurately predict the stress-strain behavior of a polymeric material. Thus various combinations of these two models were developed to have more precise models which simulate a more realistic material behavior. The simplest combination of the Maxwell and Voigt model is a series arrangement. This element is known as the four-parameter model. By using this model a crude prediction of the phenomena generally known from viscoelastic polymers can be simulated. This phenomena are: instantaneous elastic strain, retarded elastic strain, viscous flow, instantaneous elastic recovery, retarded elastic recovery and plastic deformation [17]. This model can describe a variety of molecular mechanism which are responsible for the viscoelastic behavior of linear amorphous polymers under creep conditions. The Maxwell element spring is the first element in the chain of the series arrangement and describes the instantaneous elastic deformation behavior. On the molecular level of polymers primary valence bonds in molecular chains have equilibrium bond angles and lengths. The deformation of the equilibrium state is resisted and additionally accompanied by an instantaneous elastic deformation. On the other hand the Voigt element describes the recoverable retarded elastic deformation of a viscoelastic polymer. In general the process of coiling and uncoiling of molecular chains does only occurs with hindrances because a cooperative motion of thousands of chain segments has to take place and thus only happens in a retarded manner. Besides, the damper of the Maxwell element in the four-parameter model describes the irrecoverable viscous flow of the polymer. On the microscopic level this process can be associated to the slippage of molecular chains or chain segments past one another [17].

Also this model does not completely describe the material behavior of a polymer and more complex models have been proposed to simulate the viscoelastic behavior of polymers under loading more realisticly. More detail information is given in [17] for example.

2.1.2 Root Cause of Strain Rate Dependency in Polymers

Polymers are very sensitive to the deformation rate. In general, polymers show an increase of the yield strength with increasing strain rate accompanied with a decrease in ductility. A similar response can be seen by reducing the temperature. In literature this is discussed as the time-temperature superposition principle. The decreasing of the temperature is equivalent to the increasing of the strain rate.

At low temperatures or at high strain rates the molecular movement of the polymer chains are restricted and consequently the overall material behavior shows a rigid and brittle response. With increasing temperatures the rotations and translational displacements of side groups or small molecular groups or repeat units in the main polymer chain are possible. At the glass transition temperature the mobility of the molecular chains over the whole length is no longer restricted and the solid polymer becomes softer and softer until it melts. DMA experiments show that with high strain rates the secondary and primary transition temperatures are shifted to higher temperatures, that means that the polymer chains are stiffer and distinct degrees of freedom for the molecular motion are blocked. Thus the macroscopic polymer behaves stiffer and the material strength increases.

Many authors examined the influence of temperature and strain rate on the material behavior of polymers. Walley and Field [19] performed tests at room temperature over strain rates ranging from $10^{-2}\,\mathrm{s}^{-1}$ to $10^{4}\,\mathrm{s}^{-1}$. They used suitable lubrication and specimen sizes to avoid friction and inertia effects on the results. Due to the results of yield stress as a function of logarithmic strain rate, which were measured for various polymers in this work [19], they concluded that the different materials can be categorized into three different group [19, 20]:

- Polymers with a linear relationship of yield stress and strain rate with no change at higher strain rates.
- Polymers with a bilinear behavior with a sharp increase in gradient at a strain rate of $10^3\,\mathrm{s}^{-1}$.
- Polymers with a decrease in maximum stress at a strain rate of $10^3\,\mathrm{s}^{-1}$ possibly followed by an increase.

The root cause of the bilinear behavior of polymers is attributed to the different molecular relaxation processes of the polymer chains in the material [20–29]. Through nuclear magnetic resonance (NMR) experiments, dynamic mechanical analysis (DMA), and creep experiments these specific intramolecular motions of a polymer chain can be observed. In amorphous polymers the cooperative segmental motion of repeating units along the chain backbone is determined as the primary or α-relaxation process. These motions can be conformational changes of the main chain bonds, for instance the change between the stable conformation states "trans", "+ gauche", and " - gauche". This process is observed in all polymers and takes place at the glass transition temperature region. Besides this segmental motion of the main polymer chain secondary relaxation processes denoted as β-, γ-, and δ-relaxations exist. The secondary processes are related to localized motions of side groups for instance rotational movements. In subsection 3.4.2 a detailed description of the different relaxation processes occurring in polyamide-6 is given. The α-relaxation plays a major role in the overall mechanical polymer behavior at high temperatures or rather low strain rates. On the other hand the secondary β-relaxation comes into account at low temperatures or high strain rates, respectively.

In the work of Siviour et al. [20] the correlation of the molecular relaxation processes and the strain rate and temperature dependent material behavior is explained (Figure 2-4). The authors [20] investigated the bilinear behavior of the amorphous thermoplastic polymer polycarbonate (PC). They conducted compression tests by using a mechanical testing machine and a split-Hopkinson pressure bar system and compared the results with dynamic mechanical analysis tests. The results of the DMA tests, the storage modulus and damping, $\tan\delta$, at different frequencies or strain rates respectively are shown in Figure 2-4. The glass transition temperature is associated with a drop in modulus at approximately 150 °C. The decrease of the storage modulus at around $-30\,^{\circ}\mathrm{C}$ indicated the β-transition region. With increasing strain rate the β-transition temperature region shifts to higher temperatures.

In Figure 2-5 the results of the mechanical tests at different strain rates and temperatures are shown for the polycarbonate material. Siviour et al. developed a mapping approach which is described in detail in [20]. The result of the one variable parameter mapping is shown in Figure 2-5.

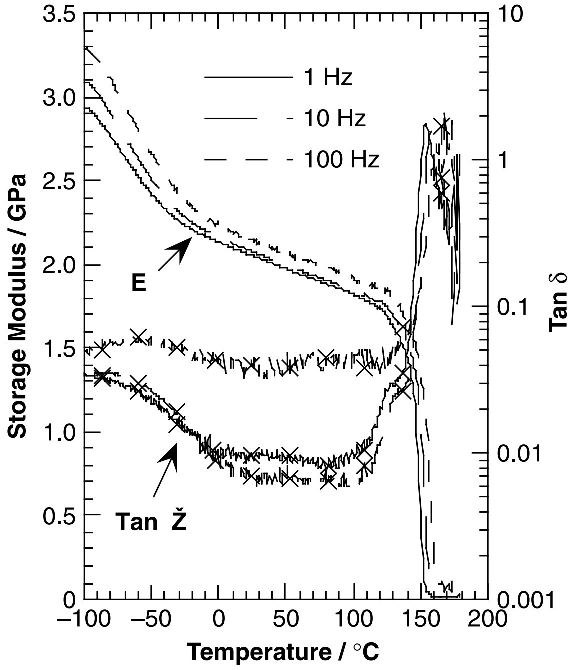

Fig. 2-4 Storage modulus and tanδ for polycarbonate (PC) at frequencies of 1, 10, and 100 Hz, over temperatures from -100 to 180 °C in a single cantilever configuration. The strain amplitude was 0.030 ± 0.001 and the equivalent strain rates are therefore $(6 \pm 0.2) \cdot 10^{-4}\,\mathrm{s}^{-1}$, $6 \cdot 10^{-3}\,\mathrm{s}^{-1}$, and $6 \cdot 10^{-2}\,\mathrm{s}^{-1}$ [20].

This diagram illustrates that the peak stress as function of strain rate shows the same bilinear curve trend as the peak stress as function of temperature. Thus the authors [20] concluded that at high deformation rates the increased strain rate sensitivity of the peak stress is a material property. They suppose that the movement of the β-transition region towards room temperature at this high strain rates causes an increased strain rate dependence of the strength. For other polymer materials a similar correlation between strain rate and temperature was found [20–29]. The shift of the primary and secondary transition temperatures to higher temperatures at high strain rates leads to a higher material strength.

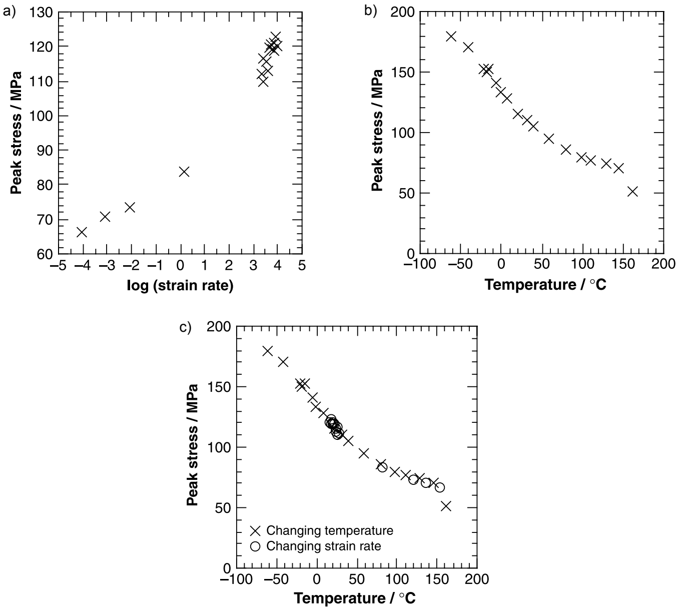

Fig. 2-5 Specimens of polycarbonate (PC) tested over a range of strain rate and temperature. a) Plot of maximum stress against strain rate at 21 °C, showing two distinct regions in the data. b) Plot of maximum stress against temperature at $5500 \pm 500\,\mathrm{s}^{-1}$. c) Comparison of the variation of peak stress with temperature, and the variation of peak stress with strain rate mapped onto temperature [20].

2.2 Strain Rate's Effect on Compressive, Tensile, and Shear Properties

Carbon-fiber-reinforced thermoplastic matrix composites are becoming increasingly attractive for automotive structural applications due to advantages in processing, damage tolerance, and recyclability compared to conventional composites with thermoset resin systems. The design of composite parts for modern vehicles with corresponding safety precautions has to take into account high strain rate loading conditions especially for primary structures. In addition, finite-element simulations of impact and crash scenarios require dynamic material data to ensure a reliable prediction of the mechanical response. Especially the compressive, tensile, and shear material properties are important parameters for the design and simulation approach. In this study the focus of the material characterization is on the unidirectional carbon-fiber-reinforced polyamide-6 (PA 6) composite material. In the following a literature survey is given for the characterization of the strain rate dependency of the neat polymer polyamide-6 and the carbon-fiber-reinforced polyamide-6 composite material under different loading conditions.

2.2.1 Neat Polyamide-6

The semi-crystalline thermoplastic polymer PA 6 is one of the most commonly used polymers and currently receives much attention as a matrix material for future automotive composite structures. Common material properties of polyamide-6 under quasi-static conditions are well documented [30–32]. Walley and Field [19] studied the strain rate sensitivity of the uniaxial compressive stress-strain response of moist and dry polyamide-6 using a direct impact Hopkinson bar (Figure 2-6). The compression specimens, right circular cylinders, were tested at six different strain rates from $2 \cdot 10^{-2}\,\mathrm{s}^{-1}$ to $2.03 \cdot 10^{4}\,\mathrm{s}^{-1}$. Each curve in the left diagram in Figure 2-6 represents the average of four experiments. It is obvious that the stress-strain curves do not start in the origin. Walley and Field [19] gave three reasons for these experimental errors. During loading with low to medium velocities the lubricant layer adjusts to the applied stresses. This "bedding down" process causes a raising force without deforming the specimen at the same time. The second pronounced reason is that dispersion effects influence the stress pulse in the transmission-bar before reaching the strain gauge position. Additionally the authors 2-6) quote that mould shrinkage and defects caused by the punching out process during the production, leads to specimens with none perfectly right circular cylinders. Thus multiple stress states can appear during loading. Due to these reasons the compressive Young's modulus of PA 6 was not deduced from the experimental results [19]. In Figure 2-6 the maximum stress is plotted as a function of strain rate.

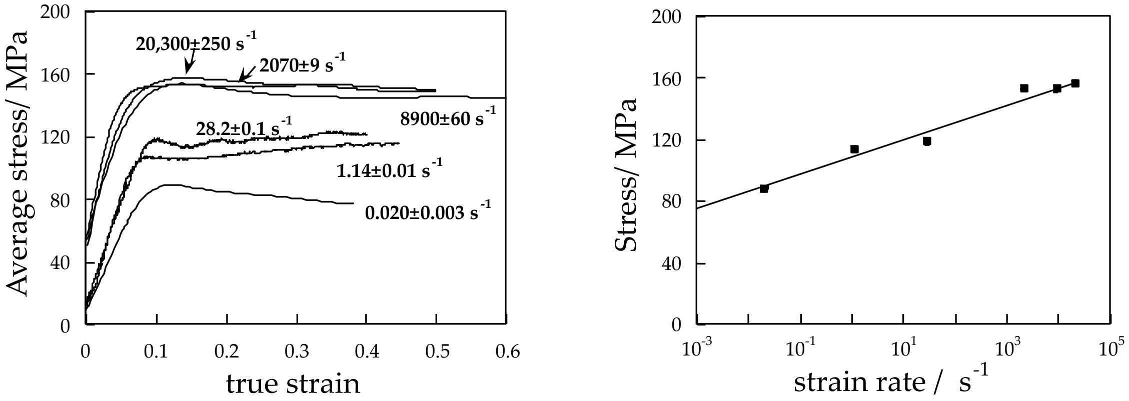

Fig. 2-6 Compressive stress-strain curves for dry nylon 6 at six different strain rates (left) and plot of the maximum stress as a function of strain rate for dry nylon 6 (right) [19].

Similar results for the compressive [33] and tensile [33–36] behavior of the pure polymer under dynamic loading were observed. In 2007 the influence of temperature, tensile specimen geometry, and strain rate on the failure behavior of polyamide-6 was investigated by Shan et al. [35]. All tension tests were carried out on a Instron universal testing machine. The strain rate regime ($0.33 \cdot 10^{-3}\,\mathrm{s}^{-1}$ to $1.67 \cdot 10^{-2}\,\mathrm{s}^{-1}$)

lies according to the definition of Nemat-Nasser [37] (see also Figure 3-1) within the quasi-static region. In Figure 2-7 the yield strength is plotted as a function of temperature for different loading velocities. Between the temperature range of 15 °C to 35 °C the tensile strength increases with loading rate, whereas above this temperature range almost no strain-rate effect is observable. The diagram on the right hand side in Figure 2-7 shows the yield strength behavior over the logarithmic strain rate for different draw temperatures. The tensile tests at lower temperatures indicate that with increasing strain rate the yield strength increases linearly.

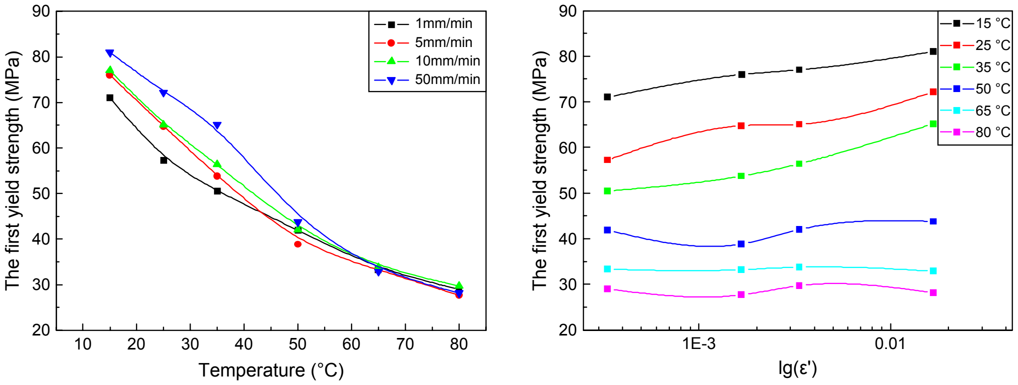

Fig. 2-7 The first yield stress as a function of (left) draw temperature at different nominal strain rates and (right) log of strain rate, lg(ϵ'), at different draw temperatures [35].

Pouriayevali et al. [33] performed compression and tension tests from quasi-static to high strain rates at room temperature to validated their developed constitutive model. The dynamic experiments were carried out on compressive and tensile split-Hopkinson bar devices. A broad strain rate region ($0.5 \cdot 10^{-3}\,\mathrm{s}^{-1}$ to $3.2 \cdot 10^{3}\,\mathrm{s}^{-1}$) is covered. The experimental results of the stress-strain response for compression and tension are shown in Figure 2-8.

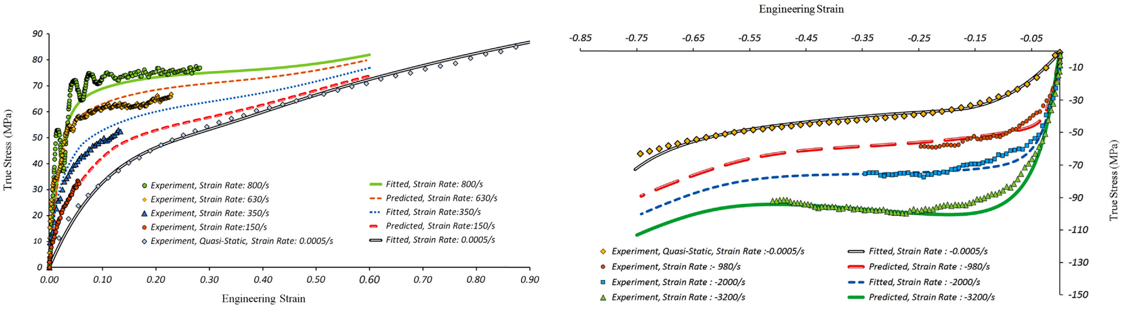

Fig. 2-8 Comparison between tension (left) and compression (right) test data for different strain rates with proposed model of Pouriayevali et al. [33].

Additionally, the fitted and predicted curves with the proposed model of Pouriayevali et al. [33] are included. Both material properties show a significantly rate-sensitivity.

The tensile stress-strain curves oscillate at high strain rates. Moreover, no distinct yield behavior of the polymer is visible at strain rates below $3.50 \cdot 10^2\,\mathrm{s}^{-1}$. A slight increase of the Young's modulus might be visible. In comparison to the tensile properties the compressive stress-strain behavior (Figure 2-8) indicates yielding of the thermoplastic polymer. A broad stress plateau is formed at each tested strain rate. A sharp increase of the Young's modulus from quasi-static strain rate to $9.8 \cdot 10^2\,\mathrm{s}^{-1}$ can be determined.

2.2.2 Fiber-Reinforced Polyamide-6 Composites

The quasi-static mechanical properties of short glass-fiber-reinforced polyamide-6 are well documented [30–32]. The tensile strength of short and long glass-fiber-reinforced polyamide-6 was found to increase with strain rate [34, 36, 38–40]. Wang et al. [38] investigated the effects of temperature and strain rate on the tensile behavior of short E-glass-fiber-reinforced polyamide-6 composite sheet to establish a constitutive model. The temperature region lies around the glass transition temperature (50 °C) from 21.5 °C to 100 °C. The considered strain rate regime was in a small range from $8.3 \cdot 10^{-4}\,\mathrm{s}^{-1}$ to $8.3 \cdot 10^{-2}\,\mathrm{s}^{-1}$. The extruded composite sheets contain 33 % fibers by weight. Figure 2-9 shows the stress-strain curves in the extrusion direction and normal to the extrusion direction for three different strain rates at 21.5 °C. As supposed, the influence of the fiber direction on the material properties is significant, due to the extrusion direction of the polymer during manufacturing. The overall stress level increases with increasing strain rate. However only a small influence on the failure strain was observed. Based on the experimental data of the tests under temperature (not shown here) the authors concluded a decrease of the elastic modulus and the tensile strength of the composite with increasing temperature. In addition, they measured a change in the strain rate sensitivity and the temperature sensitivity between 21.5 °C and 50 °C which they refer to the glass transition of the polyamide-6. Finally they stated a lower strain rate and temperature sensitivity of the fiber-reinforced composite in the extrusion direction than normal to the extrusion direction.

To the knowledge of the author of this thesis only few attempts were carried out to characterize the dynamic stress-strain response of endless-carbon-fiber reinforced polyamide-6 composites with continuous fibers. Todo et al. [41] investigated the material properties of two material systems; woven carbon-fiber-reinforced (CF) polyamide-6 (PA-6) and a woven carbon-fiber-reinforced modified polyamide-6 (mPA-6) composite. Additionally the same material configuration with woven glass-fiber-reinforced (GF) PA-6 and mPA-6 were characterized. Using a servohydraulic testing machine, measurements in the strain rate regime from $1.1 \cdot 10^{-2}\,\mathrm{s}^{-1}$ up

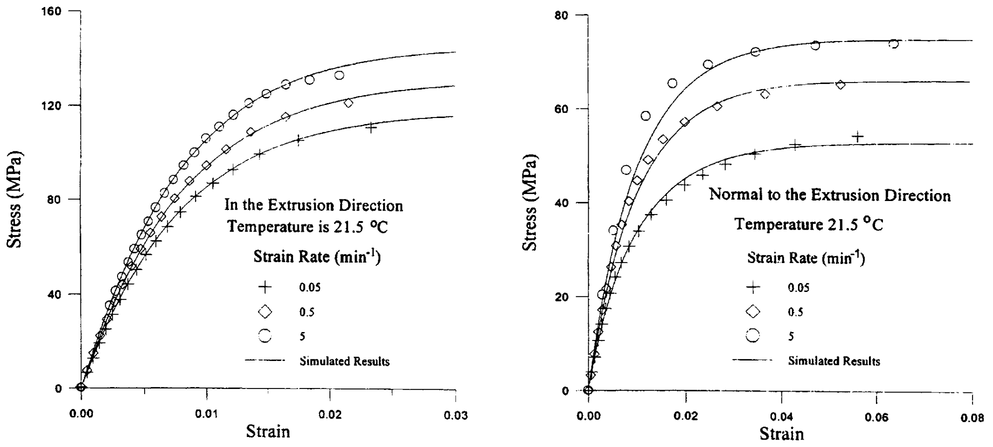

Fig. 2-9 Effect of strain rate on the stress-strain curves of short E-glass-fiber-reinforced polyamide-6 in the extrusion direction (left) and normal to the extrusion direction (right) [38].

to $2.4 \cdot 10^1\,\mathrm{s}^{-1}$ were carried out. The test results of the stress-strain response of the carbon-fiber-reinforced composite are shown in Figure 2-10. The authors [41] suggested a linear relationship between the tensile strength behavior of the composite and the logarithmic strain rate. Furthermore an increase of the failure strain and the absorbed energy with increasing strain rate was found.

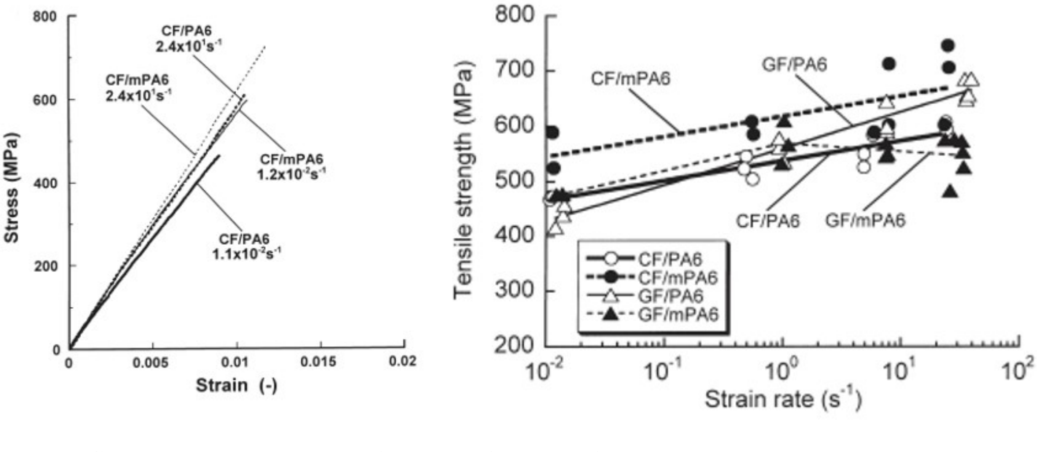

Fig. 2-10 Stress strain relations of carbon-fiber-reinforced polyamide composites obtained at low and high strain rates (left) [41]. Dependency of the tensile strengths of polyamide composites on the strain rate (right) [41].

A recent study of Jendli et al. [42] shows the characterization of twill woven carbon-fiber-reinforced polyamide-66 under 0 °, 90 °, and ±45 ° tensile loading from quasi-static ($1 \cdot 10^{-2}\,\mathrm{s}^{-1}$) to high strain rates ($300\,\mathrm{s}^{-1}$). The tests were carried out with a servohydraulic tensile testing machine. The authors [42] observed positive strain rate effects on the tensile strength for all loading directions.

In general, the comparison of high strain rate experimental results is difficult. This can be attributed to the fact that there are no established testing standards. For such measurements a variety of testing methods and specimen geometries exist. Furthermore only few studies were carried out at very high strain rate in the regime from approximately $1 \cdot 10^2\,\mathrm{s}^{-1}$ to $2 \cdot 10^3\,\mathrm{s}^{-1}$.

In the above mentioned studies the focus is on the characterization of the strain-rate effect of the pure thermoplastic polymer, glass-fiber-reinforced or woven carbon-fiber-reinforced PA 6. Despite the previous efforts, the effects of the strain rate sensitivity of unidirectional carbon-fiber-reinforced polyamide composites are still not completely understood. But for the design of composite parts exact strain-rate-dependent material data for unidirectional layups are of great relevance. Particularly the basic in-plane properties of a unidirectional lamina such as the transverse and longitudinal tensile and compression strength and elastic modulus are necessary. The present study contributes to the description of the strain rate dependency of a unidirectional (UD) carbon-fiber-reinforced PA 6 polymer. The composite material is loaded under compression, tension, and shear using an electro-mechanical testing machine for the quasi-static tests and a split-Hopkinson bar for the dynamic tests. The matrix material, the neat PA 6 polymer, is investigated using dynamical mechanical analysis . In addition, the polymer is tested under compression at different strain rates. For the quasi-static compression tests an electro-mechanical testing machine and for the dynamic compression tests a split-Hopkinson pressure bar is used. For all loading conditions of the carbon-fiber-reinforced PA 6 polymer quasi-static reference tests are carried out by means of a universal testing machine according to the respective test standard, to obtain a characterization of the material with established testing methods.

3 Experimental Methods

For the experimental investigation of the strain rate sensitivity of materials, different test methods are available. Table 3-1 shows an overview of test methods for quasi-static and dynamic mechanical tests. A typical quasi-static measurement is carried out at around $10^{-4}\,\mathrm{s}^{-1}$ (Figure 3-1). Conventional universal testing machines can reach strain rates up to around $0.1\,\mathrm{s}^{-1}$. For higher strain rates other experimental testing machines are necessary (Table 3-1). At these high loading velocities additional physical effects occur for instance inertia effects or thermal effects (Figure 3-1).

Tab. 3-1 Experimental methods for high strain material characterization [37].

Applicable Strain Rate (s^{-1})	**Testing Technique**
Compression Tests	
< 0.1	Conventional load frames
$0.1 - 100$	Special servohydraulic frames
$0.1 - 500$	Cam plastometer and drop test
$200 - 10^4$	Hopkinson (Kolsky) bar in compression
$10^3 - 10^5$	Taylor impact test
Tension Tests	
< 0.1	Conventional load frames
$0.1 - 100$	Special servohydraulic frames
$100 - 10^3$	Hopkinson (Kolsky) bar in tension
10^4	Expanding ring
$> 10^5$	Flyer plate
Shear and Multiaxial Tests	
< 0.1	Conventional shear tests
$0.1 - 100$	Special servohydraulic frames
$10 - 10^3$	Torsional impact
$100 - 10^4$	Hopkinson (Kolsky) bar in torsion
$10^3 - 10^4$	Double-notch shear and punch
$10^4 - 10^7$	Pressure-shear plate impact

The most commonly used testing machines for tension tests at around $0.1\,\mathrm{s}^{-1}$ up to around $100\,\mathrm{s}^{-1}$ (Figure 3-1) are special servohydraulic testing machines (Figure 3-2). These machines are characterized by the fact that the load on the specimen, as opposed to quasi-static tensile tests, are not carried out according to the principle of power coupling, but to the principle of energy transfer. The kinetic energy is abruptly introduced as deformation work in the specimens. The specimen is fixed with an accelerated clamping (Figure 3-2). A cylinder piston, which surrounds the

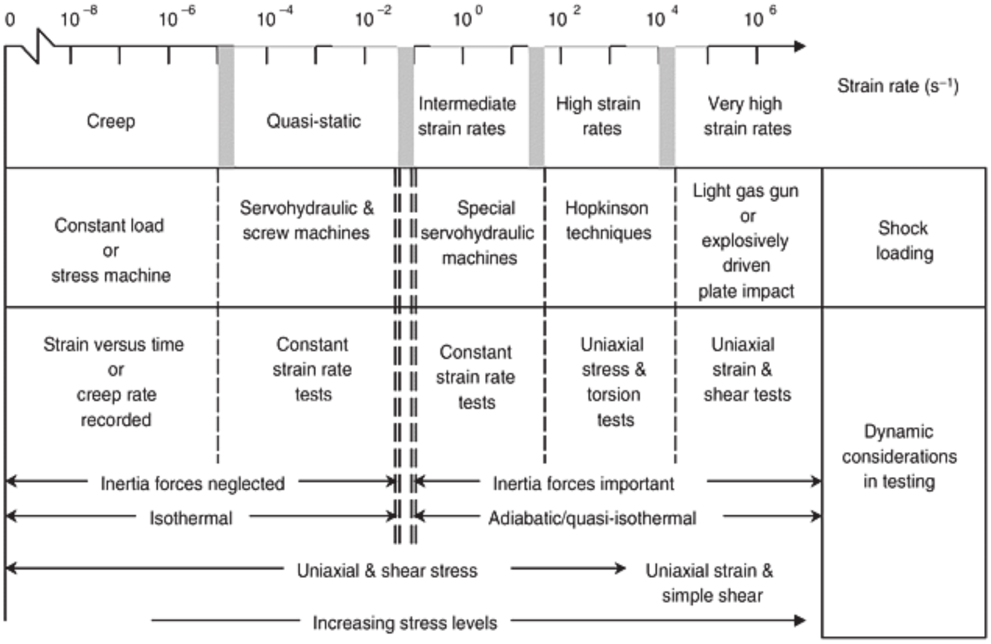
0
10⁻⁸
10⁻⁶
10⁻⁴
10⁻²
10⁰
10²
10⁴
10⁶
Strain rate (s⁻¹)
Creep
Quasi-static
Intermediate strain rates
High strain rates
Very high strain rates
Constant load or stress machine
Servohydraulic & screw machines
Special servohydraulic machines
Hopkinson techniques
Light gas gun or explosively driven plate impact
Shock loading
Strain versus time or creep rate recorded
Constant strain rate tests
Constant strain rate tests
Uniaxial stress & torsion tests
Uniaxial strain & shear tests
Dynamic considerations in testing
Inertia forces neglected
Inertia forces important
Isothermal
Adiabatic/quasi-isothermal
Uniaxial & shear stress
Uniaxial strain & simple shear
Increasing stress levels

Fig. 3-1 Strain rate regimes and associated instruments and experimental conditions [37].

end of the clamping is brought up to a constant displacement rate within a start-up length. At the end of the start-up length the cylinder piston drags the bolt under force-fit with it and thus the specimen. The energy of the system is released rapidly into the specimen. Special servohydraulic testing machines can reach loading rates of approximately 20 m/s. A drawback of this method is, that heavy masses (clamping system, bolt, etc.) must be set in motion. Therefore the measured stress-strain curves might be influenced by arising inerta effects.

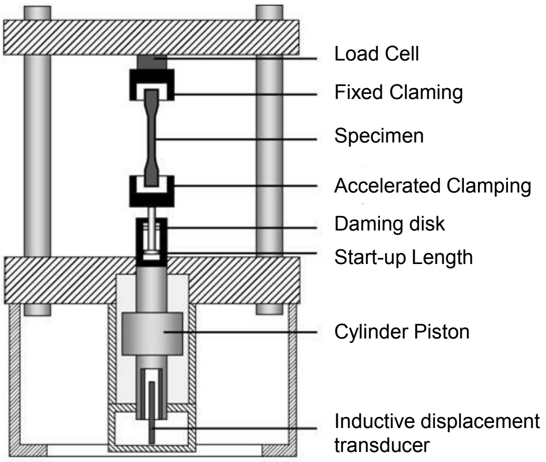
Load Cell
Fixed Claming
Specimen
Accelerated Clamping
Daming disk
Start-up Length
Cylinder Piston
Inductive displacement transducer

Fig. 3-2 Schematic drawing of a servohydraulic testing machine of type Instron VHS 25/25-20 [43].

Another method often used to carry out dynamic tests at high strain rates are drop towers (Figure 3-3). Thereby, falling weights are used to introduce compression loads into a specimen. This test method allows to apply strain rates from around $0.1\,\mathrm{s}^{-1}$ to $500\,\mathrm{s}^{-1}$ (Table 3-1) [37]. Drop towers are mainly used for compression tests to measure compressive strength, Yield's Modulus, and the stress-strain behavior of a material. By using particular fixtures the load can also be introduced into the specimen as a tensile force. Furthermore, drop towers offer the possibility to evaluate the crash-worthiness of components. A test setup consists of the drop tower itself with a massive foundation, a weight with buffer, a clamping device for the specimen, and rubber sheets to slow down the falling weight. Figure 3-3 shows one example how to set up a drop tower experiment. This testing method has some non negligible drawbacks, which have to be taken into account. The loading rate depends, among other things, on the available energy of the falling weight, the impact velocity, the specimen itself and the test system compliances. Thus the inertia loading of the system is the limiting factor of the reachable strain rates [37].

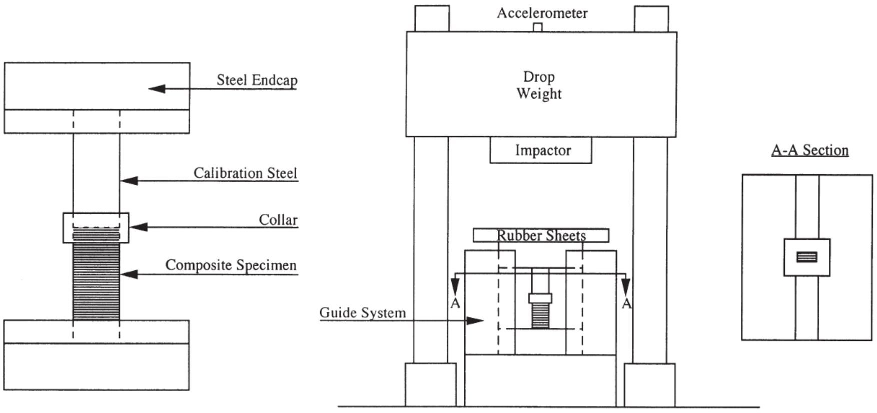

Fig. 3-3 Schematic drawing of a drop tower with a specimen clamping device [44].

In this study the split-Hopkinson bar method is used for the high strain rate experiments. This method is based on the work of John Hopkinson and his son Bertram Hopkinson [3–6] in 1901. By using this setup high strain rates from around $100\,\mathrm{s}^{-1}$ up to around $10000\,\mathrm{s}^{-1}$ (see Figure 3-1), can be reached. Davies [45] was the first who critically scrutinized in a paper the work of John and Bertram Hopkinson. By using a plate capacitor and an oscilloscope, Davies [45] recorded for the first time the propagation of the elastic compression waves in the bars. One year later, in 1949, Kolsky [46] modified the classic Hopkinson bar setup. Instead of one elastic bar, Kolsky used two elastic bars and established with this setup the so called split-Hopkinson pressure bar method. This measurement technique is also known as Kolsky-bar method [46]. Besides, Kolsky evolves the classic SHPB analysis method, which is used to calculate the stress-strain behavior of the tested material, by means of the recorded strain signals in the bars.

A further step in the development of the Hopkinson bar method was the construction and design of a tension bar system. Harding et al. [47] and Lindholm and Yeakley [48] were the first ones who build up a setup for tension tests. The challenging part of dynamic tensile tests is to generate a tensile stress pulse in the incident-bar. Commonly a loading bar with a striker tube around it is used. The striker tube is accelerated and hits an impact flange at the end of the loading bar. There the desired tensile strain wave is generated [49–58]. In 2012 Gerlach et al. [59] presented a new design of a split-Hopkinson tensile bar. This setup uses a U-shaped striker-bar as projectile that allows the support of the loading bar along the entire length. This support together with the guiding mechanism employed for the U-shaped striker-bar and impact flange prevent significant bending. Gerlach et al. [59] assume that this is the reason why the generated pulse with the new Hopkinson bar design has less oscillations in the stress-time curve compared to the pulse generated with the striker tube design. Moreover the design offers the possibility to easily adapt different pulse shaping methodologies.

In general, the development of the split-Hopkinson bar method offers the possibility to measure the material behavior under different loading conditions at higher strain rates than with a conventional testing machine. Unlike special servohydraulic testing machines or dropt towers no large masses must be accelerated. The influence of inertia effects on the measured stress-strain curve is therefore reduced. By shaping the incident pulse to a certain manner the loading of the specimen can be controlled in such a way that this happens at constant strain rate. Thus, it was decided to use a split-Hopkinson pressure bar and a split-Hopkinson tension bar within this study.

3.1 Split-Hopkinson Pressure Bar Method

In the research field of high strain rate material characterization the classic experimental technique is the split-Hopkinson pressure bar method. By means of these techniques the mechanical properties of various materials (composites, metals, ceramics, polymers etc.) can be determined. Although the terms split-Hopkinson pressure bar is often used interchangeable with the term Kolsky bar, the SHPB only implies the performance of compression tests and the term Kolsky bar may include all compression, tension, and torsion experiments [60].

3.1.1 Classic SHPB Setup

A detailed review of SHPB testing is summarized by Davies [45] and Kolsky [46] and further descriptions are given by Gray III [61]. A critical review of these three classic papers [45, 46, 61] with a general guideline for Hopkinson bar testing and data-processing are described in the work of Gama et al. [62]. The schematic drawing of a classic split-Hopkinson pressure bar setup is shown in Figure 3-4. The setup is made up of the following components:

- Three cylindrical bars (e.g. steel, titanium, aluminum, magnesium or polymeric materials), often but not mandatory of the same material and diameter, denoted by striker-, incident-, and transmission-bar. The bars must be machined with high precision to a symmetrical shape with orthogonal and, if procurable, hardened ends. Only then a good contact between striker- and incident-bar, incident-bar and specimen and between specimen and transmission-bar can be guaranteed. To record interference-free signals of the bar strain, the lengths of the incident- and transmission-bar must be chosen sufficiently long, with respect to the striker-bar.
- Bearing and alignment fixtures for the incident- and transmission-bar. A concentric and frictionless arrangement of the bearings of the bars is necessary for interference free propagation of the elastic wave.
- Gas gun with adjustable pressure valve to fire the striker-bar against the incident-bar.
- Linear strain gauges mounted on the incident- and transmission-bar, connected with a Wheatstone bridge arrangement, to measure the bar strains. The position of the strain gauges must be chosen in such a way that the generated elastic wave is measured without interference with the reflected wave at the free end of the incident- and transmission-bar, respectively.
- Light barrier in the vicinity of the incident-bar end to measure the striker-bar velocity right before the impact.
- Specimen clamped between the incident- and transmission-bar.
- High-speed amplifier system to amplify the measured bar strain signals.
- Oscilloscope to record the amplified bar strain signals and the striker-bar impact velocity.
- Computer for further data reduction of the recorded signals.

Additional components or measurement techniques which are sometimes used in combination with an SHPB are:

- High-speed camera to record images of the deformation and failure behavior of the specimen during loading and to provide images for the digital image correlation. The latter is used to calculate the strain field on the specimen surface. This optical strain measurement technique is chosen in this study (Figure 3-4), which is discussed in section 3.3.
- High-speed thermographic camera to measure the temperature distribution on the specimen.
- Temperature chamber around the specimen to measure the influence of the temperature on the mechanical behavior of the material.
- Acoustic emission sensors to identify different failure mechanism in the specimen.

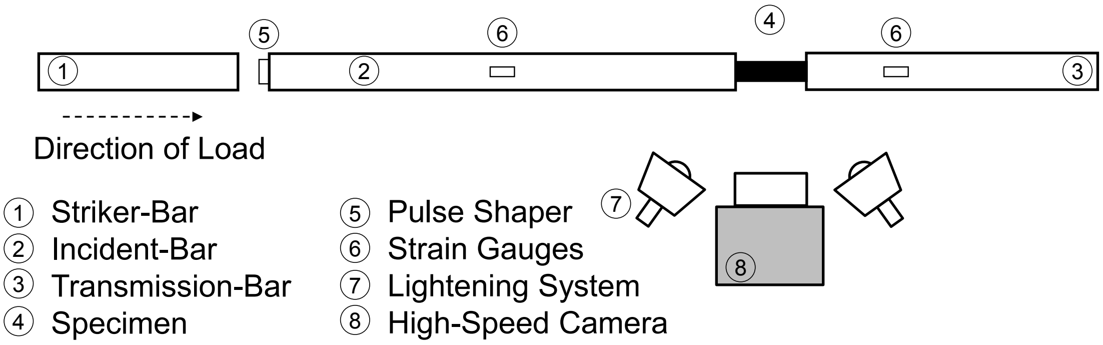

Fig. 3-4 Split-Hopkinson pressure bar setup.

3.1.2 Operating Principle of an SHPB

The operating principle of an SHPB can be subdivided into four steps; the creation of the incident wave (ϵ_{I}), the creation of the reflected wave (ϵ_{R}), the stress wave reverberation in the specimen and the creation of the transmitted wave (ϵ_{T}) [63].

By means of the gas gun the striker-bar is fired with a velocity V_0 onto the incident-bar. As a result of the impact, a longitudinal elastic compressive strain wave is generated in the incident-bar. The wave propagates along the incident-bar towards the incident-bar/specimen interface. The strain gauge on the incident-bar measures the almost rectangular strain pulse which is referred to as incident wave ϵ_{I}. The geometric length of the pulse is twice the striker-bar length l_{striker}, i.e. the striker-bar length must be chosen appropriate to generate a pulse which is sufficiently long to load the specimen to failure. The pulse duration T can then be calculated as the ratio of the pulse length and the elastic wave velocity of the bar material c_{b}:

$$T = \frac{2l_{\mathrm{striker}}}{c_{\mathrm{b}}}. \tag{3-1}$$

The generated pulse has an amplitude of:

$$\epsilon_{\mathrm{I}}^{\max} = \frac{V_0}{2c_{\mathrm{b}}}. \tag{3-2}$$

When the pulse reaches the incident-bar/specimen interface, the wave is reflected because of the change of the mechanical impedance. This reflected wave ϵ_{R} is a longitudinal elastic tensile wave and travels back to the free end of the incident-bar. The strain gauge on the incident-bar measures this strain wave as a change in the voltage signal with inverted sign.

The incident wave is not completely reflected but also partly propagates through the interface of the incident-bar/specimen surface into the specimen. Within the specimen reverberations of the wave occur.

A portion of the wave travels through the specimen/transmission-bar interface into the transmission-bar. This waves is referred to as transmitted wave ϵ_{T} and can be measured with the strain gauge on the transmission-bar. The difference in the above described impedance of the incident-bar/specimen and specimen/transmission-bar interfaces lead to a relative motion of the two interfaces. Thus the specimen is deformed until ultimate failure.

These three bar strain signals ϵ_{I}, ϵ_{R} and ϵ_{T} are then used for the SHPB Analysis, described in section 3.1.4. Previously, the physical description of the reflection, refraction and interaction of an elastic wave in a cylindrical bar is discussed in the next section.

3.1.3 Theory of Elastic Waves

Dynamic Wave Propagation of Deformation

Applying an external force to a body causes internal stresses and strains. However, these stresses are not distributed instantaneously from the region of force application to the whole body [64]. Considering individual atoms, the deformation is transferred from one to another atom at a certain velocity. The transfer of the assigned force in the material can be regarded as a sequence of impacts between adjacent atoms. The momentum is partially transmitted from one atom to all neighboring atoms. This transfer takes place with a velocity which is influenced by the mass of the atoms, the distance between the atoms and the forces of attraction and repulsion between the atoms. In addition one has to consider that the individual atoms oscillate continuously about their equilibrium position. A detailed description of the wave propagation in a body can be given by the concept of lattice dynamics [65–68].

There the lattice vibrations are described in a way related to the wave-particle duality of quantum mechanics, the so called phonons.

Wave Propagation in a Cylindrical Bar

The velocity of a wave propagating in a bar generated by the impact of a striker-bar on the incident-bar can be calculated if one hires the following considerations [64]. The front of the wave is at time t at the position u away from free end of the incident-bar. Assuming that no strains and inertia effects occur in the transverse direction to the bar, Newton's second law can be applied to a infinitesimally small section of the cylinder with length δx and cross-section A:

$$F = ma, \tag{3-3}$$

$$-A\sigma + A(\sigma + \frac{\partial \sigma}{\partial x}\delta x) = A\rho\delta x\frac{\partial^2 u}{\partial t^2}, \tag{3-4}$$

$$\frac{\partial \sigma}{\partial x} = \rho\frac{\partial^2 u}{\partial t^2}. \tag{3-5}$$

The compressive forces acting on both sides of this cylinder section are calculated with the cross-section area and the stress σ. The mass m is calculated via the density ρ of the bar material and the volume of the considered cylinder section. Assuming that the bar material is elastic, Hooke's law holds:

$$\sigma = E\epsilon \tag{3-6}$$

with strain ϵ, defined as $\partial u/\partial x$ and Young's modulus E. Thus, the differential equation for the 1D wave is defined as:

$$\frac{\partial^2 u}{\partial t^2} = \frac{E}{\rho}\frac{\partial^2 u}{\partial x^2}. \tag{3-7}$$

The solution of this second-order hyperbolic differential equation to a restricted case is the general harmonic wave equation:

$$u = u_0 \sin\left(2\pi f\left(t - \frac{x}{c_\mathrm{b}}\right)\right). \tag{3-8}$$

where c_b is the velocity of the wave in the bar. The dual derivation with respect to u and t gives:

$$\frac{\partial u}{\partial x} = -u_0\left(\frac{2\pi f}{c_\mathrm{b}}\right)\cos\left(2\pi f\left(t - \frac{x}{c_\mathrm{b}}\right)\right), \tag{3-9}$$

$$\frac{\partial^2 u}{\partial x^2} = -u_0\left(\frac{4\pi^2 f^2}{c_\mathrm{b}^2}\right)\sin\left(2\pi f\left(t - \frac{x}{c_\mathrm{b}}\right)\right), \tag{3-10}$$

$$\frac{\partial^2 u}{\partial t^2} = -u_0 4\pi^2 f^2 \sin\left(2\pi f\left(t - \frac{x}{c_\mathrm{b}}\right)\right). \tag{3-11}$$

Substituting Equations 3-10 and 3-11 into Equation 3-7 and solving for c_b yields:

$$c_\mathrm{b} = \sqrt{\frac{E}{\rho}}. \tag{3-12}$$

With this equation the propagation velocity of a wave in a bar material can be calculated.

Wave Reflection and Transmission

The effects of reflection and transmission of a wave occurs at the boundary of two mediums. There the wave encounters a change of acoustic impedance. The acoustic impedance is defined as the product of the density ρ and the wave velocity c_b (Equation 3-12). Figure 3-5 shows a sketch of a longitudinal wave propagating in a bar with cross-section A from media A with a wave velocity C_A into media B with C_B. The particle velocity is denoted as U_p with different indices for the incident, transmitted or reflected waves respectively. The same holds for the stresses σ.

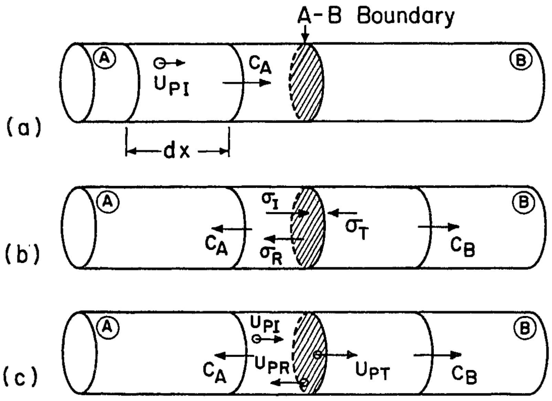

Fig. 3-5 Longitudinal wave inciding on boundary between two media A and B in normal trajectory: (a) prior to encounter with boundary; (b) forces exerted on boundary (equilibrium condition); (c) particle velocities (continuity). Direction of arrows for reflected wave for case impedance A > impedance B [64].

When considering a segment of length dx (Figure 3-5 (a)) and the conservation of momentum relationship states, the uniaxial stress σ acting on the particles can be calculated:

$$F = \dot{p} = \frac{dp}{dt} \Rightarrow Fdt = d(mU_\mathrm{p}) \Rightarrow \sigma A dt = \rho A dx U_\mathrm{p}, \tag{3-13}$$

$$\sigma = \rho \frac{dx}{dt} U_\mathrm{p} = \rho C U_\mathrm{p}. \tag{3-14}$$

Figure 3-5 (b) shows the stresses exerted on the boundary. In this ideal case the equilibrium conditions:

$$\sigma_\mathrm{I} + \sigma_\mathrm{R} = \sigma_\mathrm{T} \tag{3-15}$$

and

$$U_\mathrm{pI} + U_\mathrm{pR} = U_\mathrm{pT} \tag{3-16}$$

hold. Taking into account that the particle velocity of the reflected wave is caused by a negative stress and under consideration of Equation 3-14 the following equation is obtained:

$$\frac{\sigma_\mathrm{I}}{\rho_\mathrm{A} C_\mathrm{A}} - \frac{\sigma_\mathrm{R}}{\rho_\mathrm{A} C_\mathrm{A}} = \frac{\sigma_\mathrm{T}}{\rho_\mathrm{B} C_\mathrm{B}}. \tag{3-17}$$

The stress-ratios $\sigma_\mathrm{T}/\sigma_\mathrm{I}$ and $\sigma_\mathrm{R}/\sigma_\mathrm{I}$ can then be calculated with Equation 3-15 and 3-17:

$$\frac{\sigma_\mathrm{T}}{\sigma_\mathrm{I}} = \frac{2\rho_\mathrm{B} C_\mathrm{B}}{\rho_\mathrm{B} C_\mathrm{B} + \rho_\mathrm{A} C_\mathrm{A}}, \tag{3-18}$$

$$\frac{\sigma_\mathrm{R}}{\sigma_\mathrm{I}} = \frac{\rho_\mathrm{B} C_\mathrm{B} - \rho_\mathrm{A} C_\mathrm{A}}{\rho_\mathrm{B} C_\mathrm{B} + \rho_\mathrm{A} C_\mathrm{A}}. \tag{3-19}$$

As in the beginning of this subsection already introduced, the product ρC referred to as acoustic impedance, influences the amplitude of transmitted and reflected pulses. In the case of the impedance of media B is in excess of the impedance of media A (Figure 3-5), a wave with the same sign as the incident wave is reflected. In the opposite case the sign of the reflected wave is inverted.

In reality the cylindrical bars are not infinite, but have a free end surface or end with a rigid boundary. These two limiting conditions influence the behavior of the wave propagation. In the case of a free surface ($\rho_\mathrm{B} C_\mathrm{B} = 0$) Equations 3-18 and 3-19 yield:

$$\frac{\sigma_\mathrm{T}}{\sigma_\mathrm{I}} = 0 \tag{3-20}$$

and

$$\frac{\sigma_\mathrm{R}}{\sigma_\mathrm{I}} = -1. \tag{3-21}$$

At the boundary the incident wave is totally reflected and thus no transmitted wave is generated. The result of Equation 3-21 shows that a compressive incident wave is transferred into a tensile wave and vice versa.

In the case of a rigid boundary condition ($E_\mathrm{B} = \infty \rightarrow C_\mathrm{B} = \infty$) at the bar end the two stress ratios reach:

$$\frac{\sigma_\mathrm{T}}{\sigma_\mathrm{I}} = \frac{2}{1 + \frac{\rho_\mathrm{A} C_\mathrm{A}}{\rho_\mathrm{B} C_\mathrm{B}}} \approx 2 \tag{3-22}$$

and

$$\frac{\sigma_{\mathrm{R}}}{\sigma_{\mathrm{I}}} = \frac{1 - \frac{\rho_{\mathrm{A}} C_{\mathrm{A}}}{\rho_{\mathrm{B}} C_{\mathrm{B}}}}{1 + \frac{\rho_{\mathrm{A}} C_{\mathrm{A}}}{\rho_{\mathrm{B}} C_{\mathrm{B}}}} \approx 1. \tag{3-23}$$

At a rigid boundary the incident wave is also totally reflected (Equation 3-22). There is no change of the stress direction of the reflected wave (Equation 3-23), i.e. a compressive incident wave is reconverted into a compressive wave at the boundary. In general one can state, if the particle velocity and the wave velocity are identical in direction and sense, the stress is compressive [64]. If the two velocities have opposite senses the stress of the wave is of tensile behavior. Considering a cylindrical specimen, for instance made of metal or ceramic, sandwiched between a steel cylindrical incident- and transmission-bar. The cross-sectional area A_1 of the incident-bar (ρ_1, C_1) and the cross-sectional area A_2 of the cylindrical specimen (ρ_2, C_2) differ from each other. Thus a geometric impedance change has to be taken into account. The stress ratios are then calculated according to the following equations:

$$\frac{\sigma_{\mathrm{T}}}{\sigma_{\mathrm{I}}} = \frac{2 A_1 \rho_2 C_2}{A_1 \rho_1 C_1 + A_2 \rho_2 C_2} \tag{3-24}$$

and

$$\frac{\sigma_{\mathrm{R}}}{\sigma_{\mathrm{I}}} = \frac{A_2 \rho_2 C_2 - A_1 \rho_1 C_1}{A_1 \rho_1 C_1 + A_2 \rho_2 C_2}. \tag{3-25}$$

It has to be denoted that the above stress ratio equations only hold for materials which are deformed elastically. There the wave passes from one elastic into another elastic material. In a real SHPB experiment the specimen material typically deforms plastically. In that case, the determination of the stress ratios may be analyzed with a finite element (FE) simulation.

3.1.4 SHPB Analysis

Assumptions and Conditions for valid SHPB experiment

The stress-strain behavior of a material measured with an SHPB can be calculated with the SHPB Analysis (SHPBA) which is presented in the following subsection. The SHPB Analysis goes hand in hand with assumptions and conditions that need to be satisfied [62]:

- The bars of the SHPB setup satisfy the following conditions to ensure a one-dimensional propagation of the waves:
    - The material of the striker-, incident-, and transmission-bar is homogeneous and isotropic.

  - The incident- and transmission-bar are uniform in cross-section along the length and the center axis is perfectly straight.
  - The bar material is under a linear-elastic stress state during loading with an incident-pulse.
  - The distribution of the axial strain in the bar maintains uniform over the entire cross section. Thus the measured strain on the outer bar surface is equal with the strain in the bar. Therefore the length to diameter ratio of the bars should be $l_\mathrm{b}/d_\mathrm{b} > 20$ [45].
  - The striker-, incident-, and transmission-bar are dispersion free. In reality this assumption is not valid for a finite diameter bar. But if the transit time ($t_\mathrm{t} = d_\mathrm{B}/c_\mathrm{b}$) of the incident-pulse across the bar diameter is only 1/10 of the total pulse duration the dispersion effects are reduced. This means, the incident-pulse does not significantly change its shape after passing the incident-bar strain gauge where the strain wave is measured. The same holds for the reflected and transmitted waves. The pulses remain unchanged after being generated at the bar/specimen interface.

- The interfaces of the incident-bar/specimen and the specimen/transmission-bar remain plane throughout the experiment. Thus, the acoustic impedance of the specimen should be lower than the acoustic impedance of the bar material. The geometry of the specimen should not overhang the bar diameter.
- Stress equilibrium is reached within the specimen after an initial "ringing-up" period. The pulse shaping technique can positively influence the stress equilibrium for instance by reducing the initial "ringing-up" period (section 3.1.5).
- The specimen material is not compressible.
- Friction and inertia effects in the specimen occur only to a minimum. To satisfy this condition lubricants such as molybdenum disulfide (MoS_2) between the specimen end-surfaces and the bars are applied.

Time-Shifting of bar strain signals

The SHPB Analysis uses the recorded bar strain signals for the calculation of the stress-strain behavior of the specimen. The strain gauge on the incident-bar measures the wave signal before it reaches the specimen and measures the reflected wave. On the other hand the strain gauge on the transmission-bar measures the wave after passing through the specimen. Thus the signals are recorded before and after they have reached or passed the specimen. However the elastic wave acts on the specimen at a particular time. Due to this fact, the bar strain signals are shifted to this time at which they occur at the specimen. Figure 3-6 shows an example of the bar strain signal time shifting.

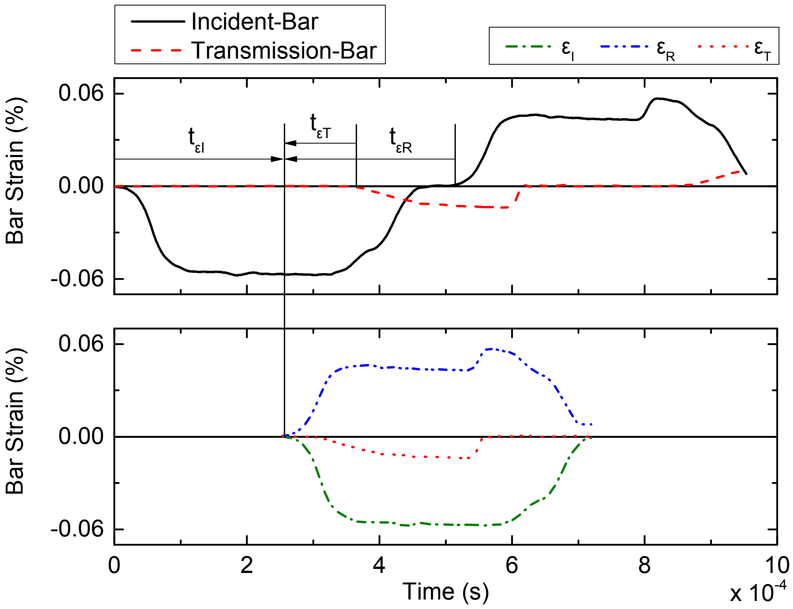

Fig. 3-6 Time shifts of incident-, and transmission-bar strain signals for the SHPB Analysis.

The incident-bar strain signal is shifted forward to the time t_{ϵ_I} at which it arrives at the specimen:

$$t_{\epsilon_\mathrm{I}} = t_\mathrm{SG1} + \frac{\Delta l_\mathrm{SG1}}{c_\mathrm{b}}. \tag{3-26}$$

The variable t_SG1 determines the timescale at the strain gauge 1 (SG1) on the incident-bar, Δl_SG1 the distance between the strain gauge 1 and the incident-bar/specimen interface and c_b is the wave velocity of the bar material. The time of the reflected bar strain signal, t_{ϵ_R}, must be shifted backward with the same time step:

$$t_{\epsilon_\mathrm{R}} = t_\mathrm{SG1} - \frac{\Delta l_\mathrm{SG1}}{c_\mathrm{b}}. \tag{3-27}$$

Similarly to the reflected wave the transmitted bar strain signal must be shifted back in time, because the strain gauge 2 (SG2) is positioned at a distance, Δl_SG2, away from the specimen:

$$t_{\epsilon_\mathrm{T}} = t_\mathrm{SG2} - \frac{\Delta l_\mathrm{SG2}}{c_\mathrm{b}}. \tag{3-28}$$

The bar strain signals at the strain gauges 1 and 2 are recorded at the same time, i.e. $t_\mathrm{SG1} = t_\mathrm{SG2}$.

One-dimensional stress wave SHPB Analysis

The fundamental assumptions presented in the first section of 3.1.4 are the basis of the one-dimensional wave equation. This 1D stress wave propagation theory is the starting point of the SHPB Analysis:

$$\frac{\partial^2 u}{\partial x^2} = \frac{1}{c_\mathrm{b}^2}\frac{\partial^2 u}{\partial t^2}. \tag{3-29}$$

By using the D'Alembert's method, this second-order hyperbolic differential equation can be solved with three arbitrary functions f, g and h [62] for the incident-bar:

$$u = f(x - c_\mathrm{b}t) + g(x + c_\mathrm{b}t) = u_\mathrm{I} + u_\mathrm{R} \tag{3-30}$$

and for the transmission-bar:

$$u = h(x - c_\mathrm{b}t) = u_\mathrm{T}. \tag{3-31}$$

The one-dimensional strain is defined by:

$$\epsilon = \frac{\partial u}{\partial x}. \tag{3-32}$$

Thus the differentiation of the Equations 3-30 and 3-31 with respect to the position, x, yields:

$$\epsilon = f' + g' = \epsilon_\mathrm{I} + \epsilon_\mathrm{R} \tag{3-33}$$

and

$$\epsilon = h' = \epsilon_\mathrm{T}. \tag{3-34}$$

Figure 3-7 shows the bar strain wave directions in the incident-, and transmission-bar (ϵ_I, ϵ_R, ϵ_T) and particle displacement directions (u_1, u_2). To calculate the particle velocities, $\dot{u}_1$, and $\dot{u}_2$ at the interfaces the Equations 3-30 and 3-31 are differentiated with respect to time, t:

$$\dot{u}_1 = c_\mathrm{b}(-f' + g') = c_\mathrm{b}(-\epsilon_\mathrm{I} + \epsilon_\mathrm{R}) \tag{3-35}$$

and

$$\dot{u}_2 = -c_\mathrm{b}h' = -c_\mathrm{b}\epsilon_\mathrm{T}. \tag{3-36}$$

The ratio of the particle velocity difference at the interfaces of the incident-, and transmission-bar and the specimen length, l_S, defines the specimen strain rate, $\dot{\epsilon}_\mathrm{S}$, when the specimen cross-section stays constant:

$$\dot{\epsilon}_\mathrm{S} = \frac{\dot{u}_1 - \dot{u}_2}{l_\mathrm{S}}. \tag{3-37}$$

The substitution of Equations 3-35 and 3-36 in Equation 3-37 gives:

$$\dot{\epsilon_{\mathrm{S}}} = \frac{c_{\mathrm{b}}}{l_{\mathrm{S}}}(-\epsilon_{\mathrm{I}} + \epsilon_{\mathrm{R}} + \epsilon_{\mathrm{T}}). \tag{3-38}$$

The strain rate is referred to as "nominal" or "true" depending on whether the initial specimen length, l_{S0}, or the true value, $l_{\mathrm{S}}(t)$, is applied in Equation 3-38. The specimen strain, ϵ_{S}, can then be calculated by integrating Equation 3-38 with respect to time. This yields:

$$\epsilon_{\mathrm{S}} = \frac{c_{\mathrm{b}}}{l_{\mathrm{S}}}\int(-\epsilon_{\mathrm{I}} + \epsilon_{\mathrm{R}} + \epsilon_{\mathrm{T}})dt. \tag{3-39}$$

The forces, F_1 and F_2, which act on the incident-bar/specimen interface and the specimen/transmission-bar interface, assuming that the bars are made of the same material, are defined by:

$$F_1 = A_{\mathrm{b}}E_{\mathrm{b}}(\epsilon_{\mathrm{I}} + \epsilon_{\mathrm{R}}) \tag{3-40}$$

and

$$F_2 = A_{\mathrm{b}}E_{\mathrm{b}}\epsilon_{\mathrm{T}} \tag{3-41}$$

with the cross-sectional area, A_{b}, of the bar and the Young's modulus, E_{b}, of the bar material. Dynamic equilibrium is reached when both forces are equal, then the following equation holds:

$$\epsilon_{\mathrm{T}} = \epsilon_{\mathrm{I}} + \epsilon_{\mathrm{R}}. \tag{3-42}$$

This condition of force equilibrium then simplifies the specimen strain rate (Equation 3-38):

$$\dot{\epsilon_{\mathrm{S}}} = 2\frac{c_{\mathrm{b}}}{l_{\mathrm{S}}}\epsilon_{\mathrm{R}}. \tag{3-43}$$

The "nominal" and "true" specimen stress, σ_{S}, can then be calculated by the ratio of the force and the initial cross-section, A_{s0} or true cross-section, $A_{\mathrm{s}}(t)$. Using the Equation 3-41 results in:

$$\sigma_{\mathrm{S}} = \frac{F_2}{A_{\mathrm{s}}} = \frac{A_{\mathrm{b}}E_{\mathrm{b}}\epsilon_{\mathrm{T}}}{A_{\mathrm{s}}}. \tag{3-44}$$

This equation is so called "1-wave analysis" or "back-stress" of the bar signal, because it represents the condition at the specimen/transmission-bar interface. The specimen stress can also be obtained via the "2-wave analysis" ("front stress") with:

$$\sigma_{\mathrm{S}} = \frac{F_1}{A_{\mathrm{s}}} = \frac{A_{\mathrm{b}}E_{\mathrm{b}}(\epsilon_{\mathrm{I}} + \epsilon_{\mathrm{R}})}{A_{\mathrm{s}}}. \tag{3-45}$$

Considering the average force acting on the specimen implies the use of all three bar strain signals. The specimen stress is then calculated via the "3-wave analysis":

$$\sigma_\mathrm{S} = \frac{F_1 + F_2}{2A_\mathrm{s}} = \frac{A_\mathrm{b}E_\mathrm{b}(\epsilon_\mathrm{I} + \epsilon_\mathrm{R} + \epsilon_\mathrm{T})}{2A_\mathrm{s}}. \tag{3-46}$$

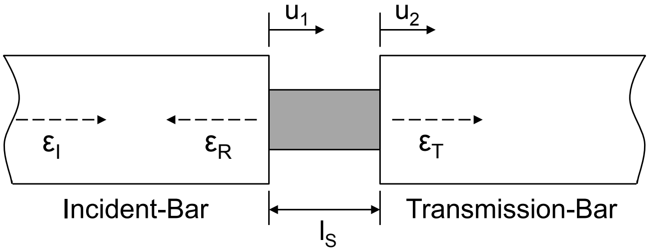

Fig. 3-7 Schematic drawing of the particle displacement directions (u_1, u_2) and bar strain wave directions in the incident-, and transmission-bar (ϵ_I, ϵ_R, ϵ_T) after [61].

3.1.5 Pulse Shaping

Each material tested with a classic split-Hopkinson pressure bar system requires a distinct rise time, defined as the time required for reverberations in the specimen to achieve a uniaxial stress state [62]. The aim is to reach a constant strain rate and thus dynamic equilibrium within an appropriate time duration. For metallic specimens a near rectangular pulse is ideal because metals deform under large plastic strains and the pulse imposes a uniform strain rate during loading (Figure 3-8 (a)). By contrast, ceramics have small failure strains and in this case a near rectangular pulse is not recommended. The abrupt increase of the incident pulse stress level may cause a non uniform strain rate because of the different curves of the stress-strain material response and the imposed loading rate [69] (as seen in Figure 3-8 (b)). Thus an incident pulse with a modified shape according to the material response is more suitable. An example of a triangular shaped pulse is shown in Figure 3-8 (c) which schematically illustrates a recommended pulse for ceramic materials. For composite materials a suitable incident pulse has to be used where the slope of the shaped pulse and the stress-strain response of the tested material match as good as possible. This guarantees a constant strain rate throughout the specimen deformation.

In addition, a near rectangular pulse generated by a direct impact of the striker on the incident-bar typically contains high frequency oscillations, the so called Pochhammer modes, which increases dispersion effects. Therefore suitable ramp shaped incident pulses are commonly used [62]. In 1980 Franz et al. [70] and Follansee [71] reported that a slowly rising incident pulse is preferred to minimize

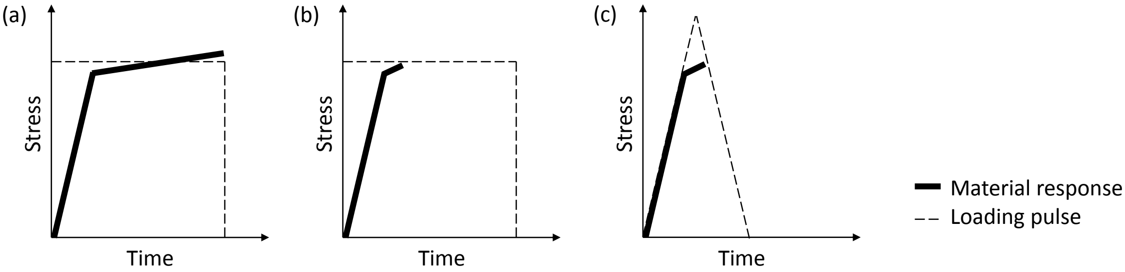

Fig. 3-8 Schematic illustration of the influence of incident pulse shaping on the stress-strain response of a ceramic specimen. (a) Rectangular-shaped pulse on a ductile specimen. (b) Rectangular pulse on a ceramic specimen. (c) Ramp-shaped pulse on a ceramic specimen according to [69].

the effects of dispersion and reach dynamic equilibrium in a metal specimen. They used a tip material in the form of a disk made of paper, aluminum, brass or stainless steel. During the impact of the striker-bar on the disk the compressives forces are gradually introduced into the incident-bar [72]. An increase of the deformation of the disk, also denoted as pulse shaper, increases the load carrying capacity and thus influences the shape of the pulse. These deformations are in the form of strain hardening of the pulse shaper material and increasing the cross-sectional area of the pulse shaper [72]. An example of different shaped pulses is shown in Figure 3-9 where different thin ductile metallic pulse shapers are used.

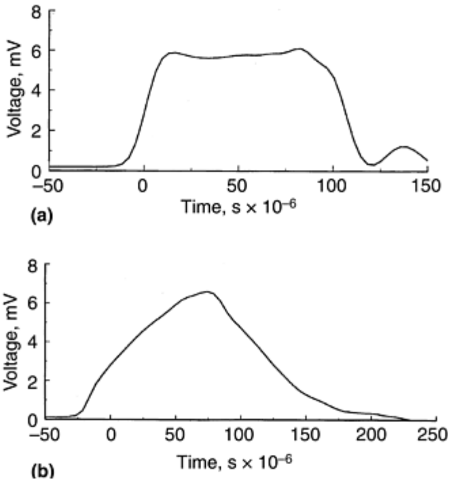

Fig. 3-9 Comparison of (a) rectangular-shaped pulse with (b) ramp-shaped pulse obtained from the same length striker-bar [69].

More details concerning different pulse shaper materials and methods are given in [37, 61, 73, 74]. Nowadays, copper pulse shaper with different diameter and thicknesses are often used. Nemat-Nasser et al. [74] proposed a pulse shaping analysis method that predicts the incident strain pulse, because it is normally not possible without adapting preliminary experiments to choose the right pulse shaper dimensions. Other pulse shaper models followed, for example from Frew et al. [72].

Finally it has to be noted that the pulse shaping technique reduces the achievable strain rate in the specimen, if the near rectangular pulse is shaped to a ramp or even to a triangular pulse where the maximum amplitude of the pulse might be reduced. But nevertheless, according to Gama et al. [62] every SHPB test should be carried out with pulse shaper regardless of stress-strain behavior of the tested material.

3.2 Split-Hopkinson Tension Bar Method

For the high strain rate tensile testing with the split-Hopkinson tension bar method, different designs and methods are available. Detailed descriptions are provided in [47–59]. In this study the design developed by Gerlach et al. [59] with a U-shaped striker is used due to the following reasons compared to an SHTB with striker tube:

- A rectangular stress pulse without significant stress peaks and oscillations can be generated.
- Stress pulses of long duration are achieved.
- The loading-bar and consequently the specimen itself does not move prior to impact with the striker. No constraints concerning the longitudinal movement are applied.
- Different forms of pulse shaping techniques can be applied.
- The design allows a speedy modification of different striker-bar lengths.
- The reloading mechanism is efficient and reliable.

3.2.1 General SHTB Setup

A schematic drawing and pictures of the split-Hopkinson tension bar setup used in this study are shown in Figure 3-10 and Figure 3-11. The design of the setup bases upon a concept proposed by Gerlach et al [59]. The setup is made up of the following components:

- Three cylindrical bars of the same material (e.g. titanium) denoted by loading-bar, incident-bar, and transmission-bar. The loading-bar and incident-bar are connected via a coupling. A symmetrical shape of the bars is required.
- A striker with a U-shaped cross-section for instance made of titanium. The striker-bar is supported by bearings in such a way that it may not affect the loading-bar. Thus the entire loading bar can be supported and does not bend.

The brass railings at the circumference of the striker allows a free sliding along the total length.

- An impact flange at the free end of the loading-bar.
- A sliding carriage connected to pulling rods guides the striker-bar (Figure 3-11).
- Two pistons, each in one pressure chamber, pull the pulling rods (Figure 3-11). The latter in turn accelerates the U-shaped striker towards the impact flange via the sliding carriage. After a distinct distance the piston is decelerated and the sliding carriage loses contact with the striker. The striker keeps on moving until it hits the impact flange and generates the input stress pulse.
- Alignment fixtures and bearings for the three bars. For an interference free propagation of the elastic wave, a concentric and frictionless arrangement of the bearings on the bars is needed.
- Linear strain gauges bonded to the incident- and transmission-bar to measure the bar strain. The positions of the strain gauges are chosen in such a way that a uniform strain-state is measured.
- Light barrier in the vicinity of the impact flange to measure the striker velocity right before the impact.
- Specimen glued into slotted endcaps. The threaded endcaps are then screwed into the incident-, and transmission-bar.
- High-speed amplifier system to amplify the measured bar strain signals.
- Oscilloscope to record the amplified bar strain signals and the striker-bar impact velocity.
- Computer for further data reduction of the recorded signals.

An additional measurement technique which is used in combination with an SHTB is a high-speed camera to record images of the deformation and failure behavior of the specimen during loading and to provide images for the digital image correlation (Figure 3-10) (section 3.3). The latter is used to calculate the strain field on the specimen surface and is used in this study.

3.2.2 Operating Principle of an SHTB

The operating principle of an SHTB is similar to that of an SHPB. The four steps are: the generation of the incident wave (ϵ_I) with a tensile behavior, the creation

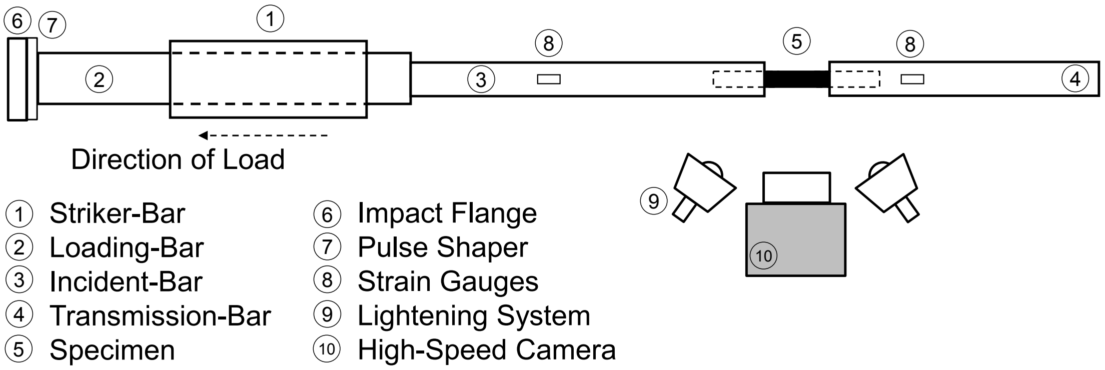
⑥ ⑦
①
②
③
⑧
⑤
⑧
④
Direction of Load
⑨
⑩
① Striker-Bar
② Loading-Bar
③ Incident-Bar
④ Transmission-Bar
⑤ Specimen
⑥ Impact Flange
⑦ Pulse Shaper
⑧ Strain Gauges
⑨ Lightening System
⑩ High-Speed Camera

Fig. 3-10 Split-Hopkinson tension bar setup.

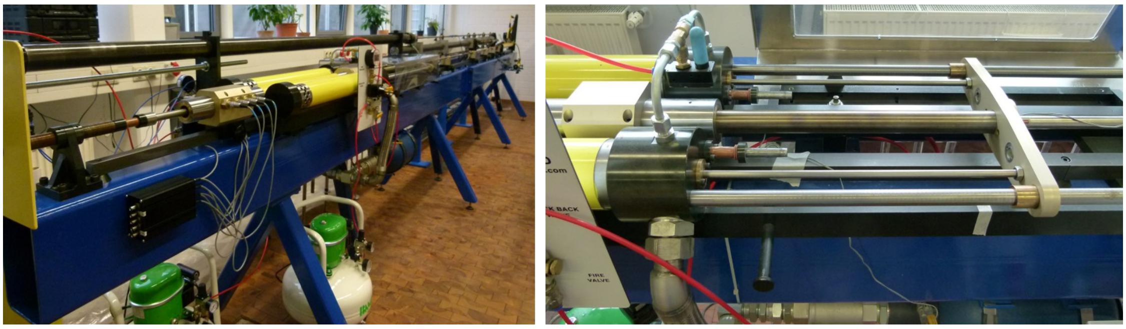

Fig. 3-11 SHTB (left) with a sliding carriage connected to pulling rods that guides the striker-bar (right).

of the reflected wave (ϵ_{R}) at the incident-bar/specimen interface, the stress wave reverberation in the specimen and the creation of the transmitted wave (ϵ_{T}).

By means of two gas guns a anchor is is fired which pushes the U-shaped striker until the striker bar releases itself from the anchor and hits the impact flange at the free end of the loading-bar with a velocity V_0. As a result of the impact, a longitudinal elastic tensile wave is generated. The wave travels along the loading-bar through a joint into the incident-bar and there toward the incident-bar/specimen interface. In this case of an SHTB the interface is strictly the transition of the incident-bar and the endcap of the specimen. Later it is shown which consequences this fact has on the calculation of the stress-strain behavior. The rectangular strain pulse, which is referred to as incident wave, ϵ_{I}, is measured with a Wheatstone bridge arrangement with a strain gauge on the incident-bar. The geometric length of the pulse is twice the striker length, l_{striker}. That means, the striker length must be long enough to generate a stress pulse which loads the specimen to failure. With the Equation 3-1 already introduced for the compression system the pulse duration, T, can be calculated.

When the wave reaches the incident-bar/specimen interface, the pulse is reflected because of the change in acoustic impedance caused by two different materials. The reflected wave, ϵ_{R}, is a longitudinal elastic compression wave and propagates back to the loading-bar. This wave is also measured with the strain gauge on the incident-bar in combination with a Wheatstone bridge arrangement. At the oscilloscope this signal shows an inverted sign of the voltage unit.

The pulse is not only partitioned into the reflected wave but also propagates through the interface of the incident-bar/specimen surface into the specimen. The wave within the specimen reverberates and a portion of the wave also propagates through the specimen/transmission-bar surface into the transmission-bar. This pulse is referred to as transmitted wave, ϵ_{T}, and can be measured with the strain gauge on the transmission-bar. The difference in the above described impedance of the incident-bar/specimen and specimen/transmission-bar interfaces causes a relative motion of the two interfaces. Due to this relative motion of the interfaces the specimen is deformed until ultimate failure.

Another limitation that comes along with a split-Hopkinson tensile bar system is the incorrect result of the specimen strain calculation via the SHPB Analysis method. One has to consider that deformations do no only occur in the specimen but also take place in the threads of the bar, in the endcaps, in the adhesive and in the interface between the adhesive and the specimen. Therefore the real specimen strain has to be measured directly on the specimen surface.

3.3 Digital Image Correlation

The measurement of surface deformations due to mechanical or thermal loading is a common method to characterize materials and structural parts. The most widely used method is the strain gauge technique. The sensor consists of a metallic foil pattern which is surrounded by a flexible polymer film and adhesively attached to the surface of an object. As the object deforms the metallic foil deforms and causes a change in the electrical resistance. By means of a Wheatstone bridge the resistance change can be measured and is then related to the strain including the gauge factor. It has to be noted that this technique measures the strain only pointwise and typically to a maximum strain of 5 %. Additional corrections may be considered concerning the transverse sensitivity of the foil and non-linearity errors.

Besides the strain gauge technique various full-field contactless optical strain measurement methods exist. On the one hand interferometric techniques such as holography interferometry [75], speckle interferometry [76] and moiré interferometry [77] have been developed and on the other hand non-interferometric methods for example the grid method [78, 79] and digital image correlation (DIC) [80].

Interferometric techniques need a coherent light source, e.g. laser equipment, and a vibration isolated optical platform. The deformation of the specimen are determined by recording the phase difference of the scattered light wave from the surface of the specimen in the undeformed and deformed state. The results of an interferometric measurement are commonly in the form of fringe patterns. By means of phase analysis techniques and fringe processing the measurement data has to be post processed to finally get the result.

Non-interferometric methods have typically less stringent requirements for the experimental conditions. For example for DIC the changes in gray intensity of the object surface are compared to determine the deformation behavior. In this study for the majority of the quasi-static and dynamic experiments the digital image correlation method was used to measure the two-dimensional (2D) strain field of the specimen surface. Therefore one camera or two cameras in stereo position were used, while for the latter setup the displacement towards and away from the camera can be additionally measured.

This non-interferometric optical metrology is increasingly used in experimental mechanics of solid materials and testing of structural components. The full displacement and strain field of the surface can be calculated by comparing the digital images of the specimen surface before and after deformation. For the calculation digital principally image processing and numerical computing is required. During the infancy of digital image processing and numerical computing, researchers of the University of South Carolina in the 1980s [81–86] were the first ones who developed the DIC metrology. The following advantages show, why DIC is a metrology increasingly used for the strain measurement at small coupons up to large scale structures in the field of research and in industry:

- Size of measuring object can vary from microscopic (e.g. scanning electron microscopy specimens) to large scale (e.g. auto body, airplane wings, wind turbines).
- Range of strain measurement from 0.01 % to several 100 %.
- Simple and fast specimen preparation with black-on-white speckle pattern.
- Strain field in in-plane and out-of-plane direction can be measured.
- Fast specimen replacement possible.
- Manageable experimental setup and environment. For the illumination of the specimen surface no laser equipment is required; standard white light source is suitable.
- Measuring technique is contact-less; specimen surface is not destroyed or influenced.

- Data corrections are unnecessary because the true strain of the specimen surface is measured.
- Determination of the full displacement and strain field instead of pointwise data.
- DIC results can be used for the verification of finite element simulation models.
- Besides the strain field calculation the digital images provide information about deformation and failure mechanism.
- Different types of digital cameras, which are suitable for the respective tests, can be used. For instance, measurements from static to high-speed loading rates are possible.

3.3.1 Basic Principles and Concepts

In Figure 3-12 a schematic drawing of a typical experimental setup using an optical imaging device for the 3D DIC is shown. The specimen surface must have a random gray speckle pattern. The speckle pattern can be the specimen surface texture or a spray painting. The layer of painting should not be too thick, because it is the carrier of the deformation information on the surface and has to deform together with the specimen surface. The size of the speckles depends on the camera resolution, measuring specimen size and required strain field resolution. The CCD-cameras are placed in a stereo view position, i.e. the optical axes build an angle, α. The focal point of the optical axis lies on the specimen surface. As a rule of thumb one pixel displacement per shutter speed is required. In the vicinity of the cameras a lightening system illuminates the speckle pattern to obtain a suitable gray-scale distribution. The cameras are connected with a computer for data processing. With a user defined frame rate, digital images of the specimen surface before and after deformation are recorded and then analyzed with a DIC software. First of all the basic principles and concepts involved in 2D DIC are introduced. Later this concept is transferred to calculate the 3D strain field measured with two cameras in stereo position.

As a first step of the DIC the surrounding of the area of interest on the image has to be masked. The remaining area is then the measuring field which is divided into evenly spaced pixel subsets (facets). The size of these facets is defined and depends on the camera resolution and strain field. Optionally the facets can have an overlap (facet step) in horizontal and vertical direction by a defined value of pixels. Each facet generates one measurement point for the displacement field in the center of the subset. The single facets are then tracked from one to the next image. The tracking only works if each facet is unique. Due to this reason subsets of pixels

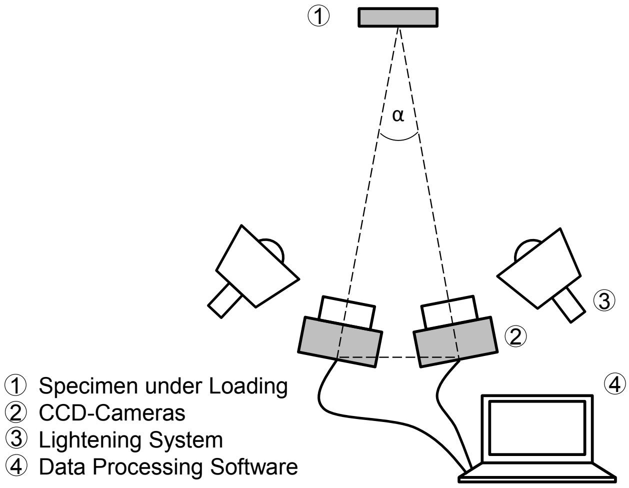
①
α
③
②
④
① Specimen under Loading
② CCD-Cameras
③ Lightening System
④ Data Processing Software

Fig. 3-12 Sketch of an image acquisition system for 3D digital image correlation (DIC) measurement.

are used which contain a gray scale distribution and therefore are distinguishable. In general square facets of $(2M+1)$x$(2M+1)$ pixels, while M is an integer, are used for the DIC. If strains of several 100 % are expected the facet size should be of rectangular shape.

In order to compute the displacements of a point, P, a square reference facet from the reference image centered at point $P(x_0, y_0)$ is chosen (Figure 3-13).

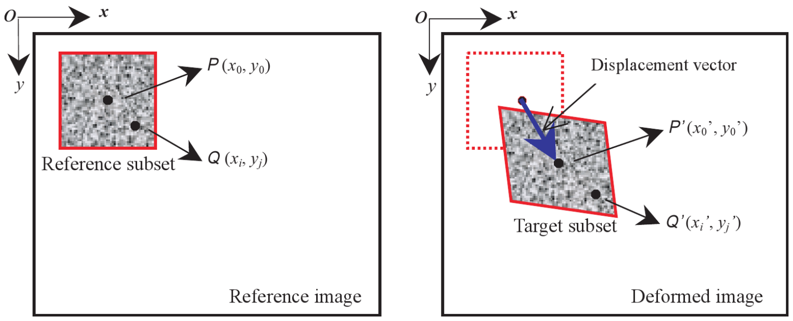
o
x
y
$P\ (x_0, y_0)$
$Q\ (x_i, y_j)$
Reference subset
Reference image
o
x
y
Displacement vector
$P'(x_0', y_0')$
$Q'(x_i', y_j')$
Target subset
Deformed image

Fig. 3-13 Schematic illustration of a reference square subset before deformation and after deformation [80].

Furthermore a correlation criterion must be defined to figure out the degree of matching between the reference subset and the deformed subset. For instance the cross-correlation (CC) criterion or the sum-squared difference (SSD) correlation criterion can be used [80]. The position of the deformed subset is then determined by searching the extremum of the correlation coefficient. In Figure 3-13 the in-plane displacement vector is drawn from the point P to the center of the deformed facet (point P'). In literature different definitions of correlation criteria can be found. In general two groups the CC criteria and the SSD correlation criteria [87, 88] exist. In the topical review of Pan et al. [80] these criteria are summarized and listed.

3.3.2 Shape Function and Displacement Mapping Function

During deformation the shape of the reference facet changes. It is assumed on the basis of deformation continuity of a deformed solid object, that the pixels in the vicinity of point P in the reference facet stay the same in the deformed facet [80]. As illustraded in Figure 3-13 a arbitrary point, $Q(x_i{,}y_j)$, in the neighboring of the center $P(x_0{,}y_0)$ of the reference facet can be tracked to point $Q'(x'_i{,}y'_j)$ in the deformed facet. For the tracking of point Q a shape function or displacement mapping function can be used [89, 90]:

$$x'_i = x_i + \xi(x_i{,}y_j) \tag{3-47}$$

and

$$y'_j = y_j + \eta(x_i{,}y_j) \tag{3-48}$$

where

$$i{,}j = -M : M. \tag{3-49}$$

The simplest case is when the displacements of each point from the reference facet to the deformed subset are the same. This case can be related to the rigid body translation and can is described with the zero-order shape function:

$$\xi_0(x_i{,}y_j) = u \tag{3-50}$$

and

$$\eta_0(x_i{,}y_j) = v. \tag{3-51}$$

The most common case depicts the change of the facet shape. Using the first-order function involves translation, rotation, shear, normal strain and their combinations of the facet:

$$\xi_1(x_i{,}y_j) = u + u_\mathrm{x}\Delta x + u_\mathrm{y}\Delta y \tag{3-52}$$

and

$$\eta_1(x_i{,}y_j) = v + v_\mathrm{x}\Delta x + v_\mathrm{y}\Delta y. \tag{3-53}$$

If more complex deformations of the facet occur, then the second-order shape functions proposed by Lu et al. [90] should be used:

$$\xi_2(x_i{,}y_j) = u + u_\mathrm{x}\Delta x + u_\mathrm{y}\Delta y + \frac{1}{2}u_\mathrm{xx}\Delta x^2 + \frac{1}{2}u_\mathrm{yy}\Delta y^2 + u_\mathrm{xy}\Delta x\Delta y \tag{3-54}$$

and

$$\eta_2(x_i{,}y_j) = v + v_\mathrm{x}\Delta x + v_\mathrm{y}\Delta y + \frac{1}{2}v_\mathrm{xx}\Delta x^2 + \frac{1}{2}v_\mathrm{yy}\Delta y^2 + v_\mathrm{xy}\Delta x\Delta y. \tag{3-55}$$

The variables $\Delta x = x_i - x_0$, $\Delta y = y_i - y_0$, u, and v in the above equations are the x- and y-directional displacement components of the reference facet center $P(x_0,y_0)$. The first-order displacement gradients of the reference facet are referred to as u_x, u_y, v_x, and v_y. The second-order displacement gradients are denoted as u_xx, u_xy, u_yy, v_xx, v_xy, and v_yy.

After computing the displacement field, the strain field can be determined via a subset of points in the displacement field which is referred to as computation size. The area of 3 x 3 subsets in the displacement field is the smallest to be calculated. Thus a very local strain field can be determined. A summary of the deformation and strain field calculations and detailed descriptions are given by Pan et al. [80].

The discussion so far showed the detailed calculations within a 2D DIC analysis. However, more and more measurements are carried out using an optical image acquisition system consisting of two cameras shown in Figure 3-12. Then the measurement data consists of 3D points of the specimen surface. Therefore an extended definition for the local directions is needed. A comprehensive description about this topic can be found in the review work of Sutton et al. [91].

3.4 Dynamic Mechanical Analysis

In the framework of this thesis the thermoplastic polymer PA 6 as a matrix material of the carbon-fiber-reinforced composite is studied in order to characterize the strain rate dependency. As discussed in chapter 2.1.2 the material transition locations shift with both temperature and strain rate acts as indicator for materials which are strain rate sensitive. The dynamic mechanical analysis (DMA) is a measurement technique which is often used to investigate material transitions in the viscoelastic behavior. Usually the viscoelastic material transitions of polymers are labeled as α, β, γ, δ, etc. The α-transition occurs at the highest temperature, the β-transition at the next lower temperature and so on. The commonly known glass transition temperature T_G is referred to as the α-transition; within a small temperature range the mechanical properties of the polymer significantly change. The material initially behaves glassy and changes its behavior to rubbery like with increasing temperature. The β-transition and all other transitions are so called "secondary" transitions where the material changes its behavior to a lesser extent.

3.4.1 DMA Theory

In principal, DMA instruments are constructed to apply oscillatory load programs in tension/compression, three-point bending or shear (Figure 3-14). The oscillation is controlled either by the displacement, strain or force. The viscoelastic material response, as the name suggests, has two components which behave in different manner compared to the oscillatory loading. One component oscillates in phase with the load program and the other out of phase from the load program. The first one is characteristic for the elastic/solid-like material response. The second one for the viscous/fluid-like material behavior.

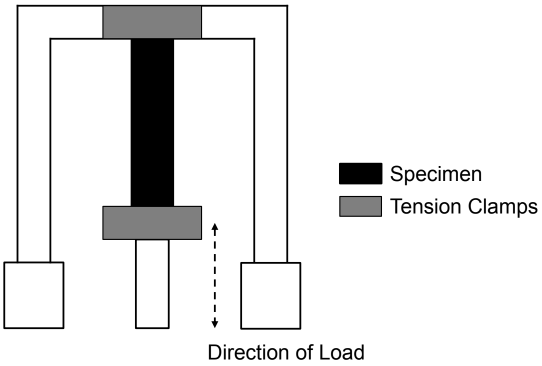

Fig. 3-14 Sketch of tension clamps in a typical DMA setup for tensile tests.

A strain controlled sinusoidal load on the specimen can be mathematically described with the following equation:

$$\epsilon(t) = \epsilon_0 \sin(\omega t). \tag{3-56}$$

Where ϵ_0 is the strain amplitude and ω is the frequency of the oscillation. The stiffness of the viscoelastic material under oscillatory loads can be described by means of the complex modulus, E^*:

$$E^* = E' + \mathrm{i}E'' \tag{3-57}$$

with the absolute value

$$|E^*| = \sqrt{E'^2 + E''^2} = \frac{\sigma_0}{\epsilon_0}. \tag{3-58}$$

The complex modulus consists of two components: the storage modulus E' (the real part) and the loss modulus E'' (the imaginary part):

$$E' = |E^*|\cos\delta \tag{3-59}$$

and

$$E'' = |E^*|\sin\delta. \tag{3-60}$$

The viscoelastic material response in terms of the stress-time behavior can be defined as:

$$\sigma(t) = \sigma_0\sin(\omega t + \delta) = \sigma_0\cos(\delta)\sin(\omega t) + \sigma_0\sin(\delta)\cos(\omega t). \tag{3-61}$$

Where σ_0 is the stress amplitude of the oscillatory response and δ is the phase lag of the viscous response. The Equation 3-61 can be also written as:

$$\sigma(t) = \epsilon_0 E' \sin(\omega t) + \epsilon_0 E'' \cos(\omega t). \tag{3-62}$$

The storage modulus is assigned to the energy stored during viscoelastic deformation. Assuming a uniaxial tension/compression DMA test in sinusoidal mode for a polymer below the glass transition temperature, the storage modulus and the Young's modulus are approximately the same. Due to the sinusoidal loading of the specimen the deformations of the specimens are small and in the region of linear elastic behvior compared to the stress-strain curves of the mechanical tests.

In contrast, the loss modulus describes the dissipated energy during viscoelastic deformation of the specimen. The ratio of the storage and loss modulus is defined as the loss tangent or tanδ:

$$\tan\delta = \frac{E''}{E'}. \tag{3-63}$$

The two viscoelastic quantities, the loss modulus and the loss tangent, show a relative maximum in the vicinity of the transition temperature location. In Figure 3-15 a schematic graph of storage modulus, loss modulus and loss tangent as a function of the logarithmic frequency of a typical polymer at the glass transition is plotted.

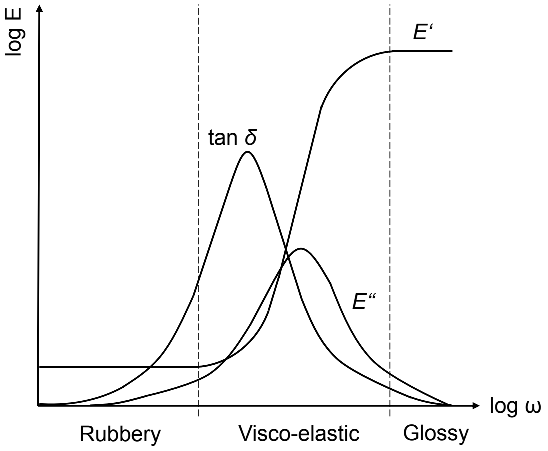

Fig. 3-15 Schematic drawing of storage modulus, E', loss modulus, E'', and loss tangent, tanδ, as a function of the logarithmic frequency for a typical polymer in the vicinity of the glass transition after [92].

For viscoelastic solid that shows no flow the polymer is rubbery-like at low frequencies. The storage modulus is very low and independent of the frequency. The rubber changes its phase to a glassy solid at very high frequencies where the storage modulus is again independent of the frequency. In the phase transition region where the material behaves viscoelastically the storage modulus increases with increasing frequency. The loss modulus is zero at low and high frequencies. In this case the stress and strain are in phase for the rubbery and glassy states. In the viscoelastic region the loss modulus has a maximum value close to the inflection point of the storage modulus. The loss tangent, tanδ, has also a peak in the viscoelastic region but at lower frequencies compared to the loss modulus, since the storage modulus also changes very quickly in this region. These frequency dependent changes in the storage and loss modulus of a viscoelastic material can be exploited to characterize and quantify the strain rate sensitivity of the material and its consequences on the overall mechanical strength. It should be pointed out that in chapter 4.1 of this study a method is described that determines the strain rate dependency of polyamide-6 by using DMA.

3.4.2 Viscoelastic Material Transitions in Polyamide-6

The analysis of the thermoplastic polymer PA 6 with different measurement techniques such as DMA and nuclear magnetic resonance (NMR) spectroscopy shows that three transitions occur in the semi-crystalline polymer [32, 93–95]. These are defined as alpha, beta and gamma transition in order of decreasing temperature. The α-transition correlates with the glass transition temperature and is caused by the motion of long-chain segments in the main polymer chain (Figure 3-16). In the temperature regime between $-60\,^\circ\mathrm{C}$ and $40\,^\circ\mathrm{C}$ the β-transition takes place which is initiated by the local motion within the amide groups of PA 6 (Figure 3-16). The γ-transition between $-120\,^\circ\mathrm{C}$ and $-110\,^\circ\mathrm{C}$ is attributed to the motion of the methylene (CH_2) groups between the amide side groups and the amorphous regions. Kawaguchi [93] dried different polyamides in vacuum over P_2O_6 at room temperature for one month before measuring the storage and loss modulus. Figure 3-17 shows the loss tangent versus temperature of the study [93]. The three transition temperatures are correlated to the peaks in the curves from high to low temperatures. The absolute temperature values are listed in the upper left of the diagram. The α-transition takes places at approximately $85\,^\circ\mathrm{C}$, the β-transition at around $-46\,^\circ\mathrm{C}$ and the γ-transition at around $-120\,^\circ\mathrm{C}$.

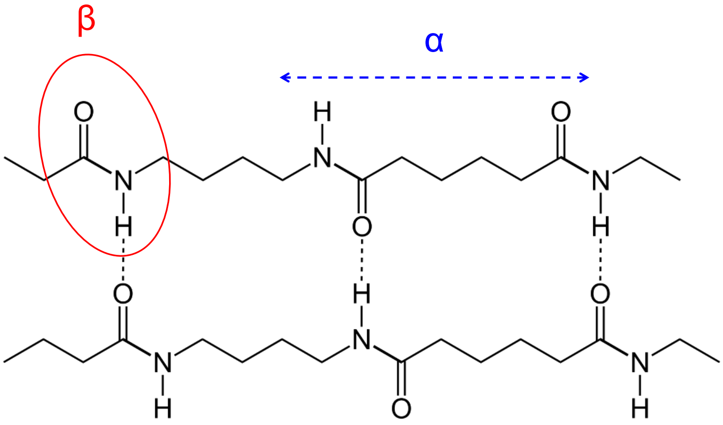

Fig. 3-16 Sketch of the chemical structure of polyamide-6 with long-chain segmental motion (α) and local motion within the amide group (β).

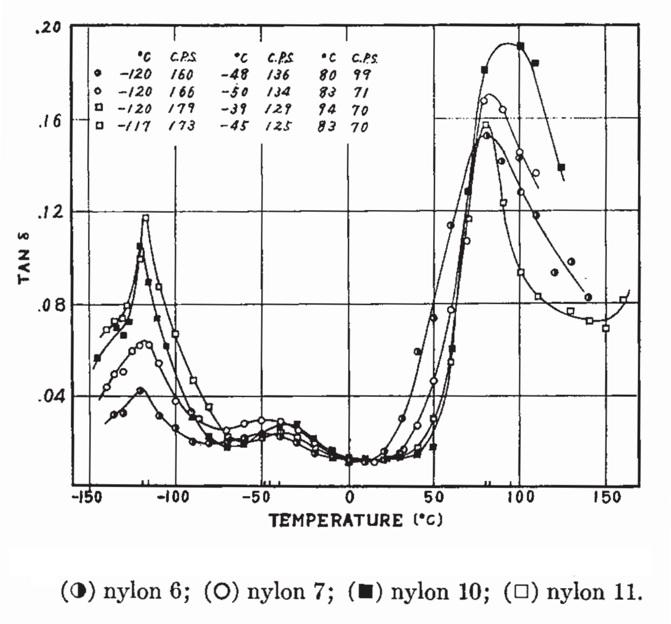

Fig. 3-17 Loss tangent as a function of temperature for different polyamides (nylons) [93]. The peaks from high to low temperatures indicate the α, β and γ-transition temperatures.

4 Strain Rate Dependency of the Neat Polyamide-6

Within this thesis the material characterization is related to the investigation of the strain rate sensitivity of unidirectional (UD) carbon-fiber-reinforced polyamide-6 under various loading conditions. From literature it is known that carbon fibers do not show any strain rate sensitivity [54, 96, 97]. Zhou et al. [96] performed tensile tests with T300 and M40J carbon fiber bundles. The ultimate strength and failure strain of these two materials were shown to be strain rate insensitive. Moreover, the tensile tests of UD laminates in fiber direction carried out by Harding and Welsh [97] and Taniguchi et al. [54] indirectly prove, that carbon fibers show no strain rate sensitivity. On the other hand, the matrix materials of composites regardless of whether thermoset polymers [51, 55, 98–103], elastomeric polymers [104–106] or thermoplastic polymers [19, 20, 28, 29, 33, 35, 51, 107–112] all show strain rate effects. Walley and Field [19] and Pouriayevali et al. [33] studied the compressive stress-strain response of polyamide-6 over a broad strain rate regime, while Shan et al. [35] studied the tensile properties. The objective of this chapter lies therefore on the investigation of the strain rate dependency of the matrix material of the neat polyamide-6. A dynamic mechanical analysis was performed at different frequencies to study the strain rate dependency. The results were used to apply a method developed by Mulliken and Boyce [28] which predicts the elastic modulus at strain rates that cannot be reached with a DMA. In the second part of this chapter the results of the quasi-static compressive and high strain rate compressive measurements are discussed. The measured yield strength is compared with literature results and the results of the dynamic mechanical analysis tests.

4.1 Dynamic Mechanical Analysis

It is well known that the mechanical behavior of polymers is influenced by strain rate and temperature. One common technique to study the strain rate's effect on polymers is the dynamic mechanical analysis. With this method simple measurements concerning the loading rate and temperature dependency can be carried out. Only small and thin test specimens and a DMA instrument are needed for the investigation. The measurement itself is simple compared to mechanical tests under temperature with a universal testing machine or an SHPB where more test equipment, for example a huge thermal chamber, strain gauges or an optical method for strain measurement are needed. Due to this reasons DMA measurements are a good choice for a first analysis of a polymer material. As with any method, this method also has limitations in terms of applicability. Only small displacements can be applied on the specimen and therefore it is not possible to load the specimen until failure. Due to this reason no complete stress-strain curve can be measured. This can only be done by using appropriate testing machines and experimental setups for dynamic tests such as an SHPB.

In the framework of this study a closer look on the work of Mulliken and Boyce [28] was taken. The two authors performed a combined experimental and analytical investigation to study the mechanical behavior of the amorphous polymers polycarbonate (PC) and poly(methyl methacrylate) (PMMA) from low to high strain rates. The aim of their work was to develop a physically based constitutive model to predict the temperature and strain-rate-dependent post-yield and large strain behavior of the thermoplastic polymers. One topic of their experimental study was the development of a method to predict the elastic modulus of PC and PMMA at strain rates which are beyond the potential of a DMA instrument. Within the approach the different changes of the temperature dependent glass transition and secondary β-transition with higher strain rates are considered. The results of the method were verified with SHPB data of dynamic tests at comparable high strain rates.

4.1.1 Material

A semi-crystalline polyamide-6 (Ultramid® B3S, BASF) [113] polymer was studied in the present work. A thermoplastic PA 6 sheet was produced though an extrusion process. All specimens were cut into a rectangular 25 x 3.5 x 2 mm^3 (length x width x thickness) shape. To establish a common basis for mechanical material characterization, all specimens were dried in an oven under vacuum at 80 °C for 72 hours to minimize possible moisture effects arising from the PA 6 polymer's hygroscopic behavior. The dry specimens were stored in a multi-layer polymer-aluminum-film bag until start of the experiment to prevent moisture absorption after drying.

4.1.2 Test Procedure

Two specimens were tested on a TA Instruments DMA Q800 Dynamic Mechanical Analyzer. The specimens were mounted with two tension clamps in the furnace and pre-loaded with 0.01 N (Figure 3-14). A temperature range from -110 °C to $+100$ °C was chosen to cover the temperature locations at which significant material transitions of the polymer are likely to occur. The temperature was controlled with a ramp rate of 2 °C/min and the amplitude of the displacement was set to be 3.5 µm. The specimens were then tested with a frequency sweep of 1 Hz, 10 Hz, and 100 Hz. The temperature dependent storage modulus and loss modulus of PA 6 were measured and the corresponding loss tangent was calculated. The chosen frequencies of the measurement can be converted into strain rates. This calculation principally involves the specimen free gauge length and displacement amplitude and is described in the work of Mulliken and Boyce [28]. The load in the DMA program follows a sinusoidal behavior. It is assumed that the increase in strain over time within one-quarter of a loading cycle is linear. The average strain rate can then be calculated by the ratio of the known displacement amplitude d_0 and the specimen gauge length l_g divided by this time period:

$$\dot{\epsilon} = \frac{\frac{d_0}{l_\mathrm{g}}}{\frac{1}{4}\frac{1}{\omega}} \tag{4-1}$$

The calculated strain rates with a displacement amplitude of 3.5 µm for the three different frequencies are summarized in Table 4-1. The mean specimen gauge length for specimen 1 was 8.43 mm and for specimen 2 was 8.66 mm.

Tab. 4-1 Calculated strain rate for 1 Hz, 10 Hz, and 100 Hz.

	Specimen 1 $\dot{\epsilon}\,(\mathrm{s}^{-1})$	Specimen 2 $\dot{\epsilon}\,(\mathrm{s}^{-1})$
1 Hz	$1.66 \cdot 10^{-3}$	$1.62 \cdot 10^{-3}$
10 Hz	$1.66 \cdot 10^{-2}$	$1.62 \cdot 10^{-2}$
100 Hz	$1.66 \cdot 10^{-1}$	$1.62 \cdot 10^{-1}$

4.1.3 Experimental Results

The results of the dynamic mechanical analysis of specimen 1 and 2 are shown in Figure 4-1 and 4-2, respectively. For each specimen the measured storage modulus and calculated loss tangent are plotted as a function of temperature for the three different frequencies. The drop in the storage modulus curve by three orders of magnitude centered around 70 °C can be clearly recognized. This change in the material behavior is associated with the glass transition (α-transition) of the PA 6. As previously described in section 3.4 the α-transition is attributed to long-chain sectional motion within the main polymer chain at this temperature region. During this transition a macroscopic softening of the material occurs. Besides the glass transition a secondary viscoelastic transition of PA 6 can be identified. The storage modulus curve shows a second drop at a temperature of −75 °C. This transition is labeled as the β-transition and is attributed to the local motion within the amide groups of the thermoplastic polymer (see also section 3.4). As expected the storage modulus curve is shifted to higher temperatures with increasing frequency. Even in this low strain rate regime from approximately $1.6 \cdot 10^{-3}\,\mathrm{s}^{-1}$ to $1.6 \cdot 10^{-1}\,\mathrm{s}^{-1}$ a change of the viscoelastic material behavior with increasing strain rate is observable. The shift of the α-peak and β-peak towards higher temperatures is shown in the graph of the loss tangent versus temperature (Figure 4-1 and 4-2).

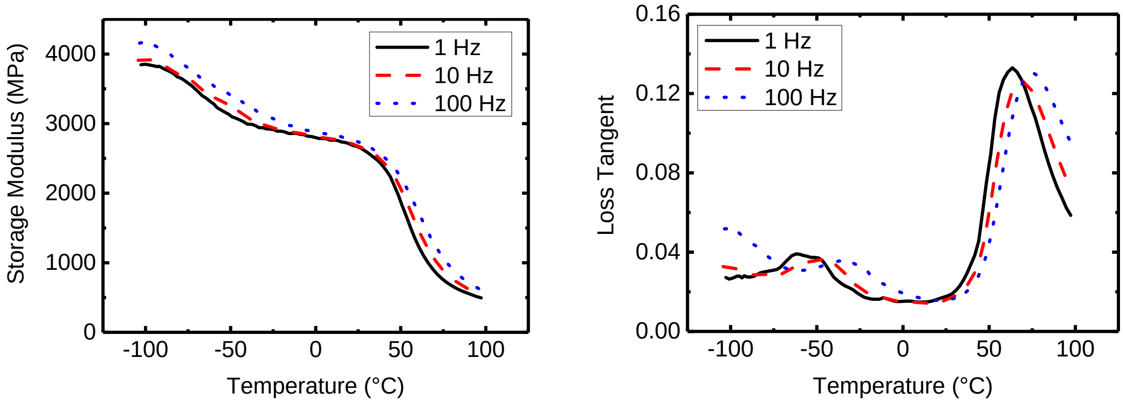

Fig. 4-1 Storage modulus (left) and loss tangent (right) as a function of temperature for specimen number 1.

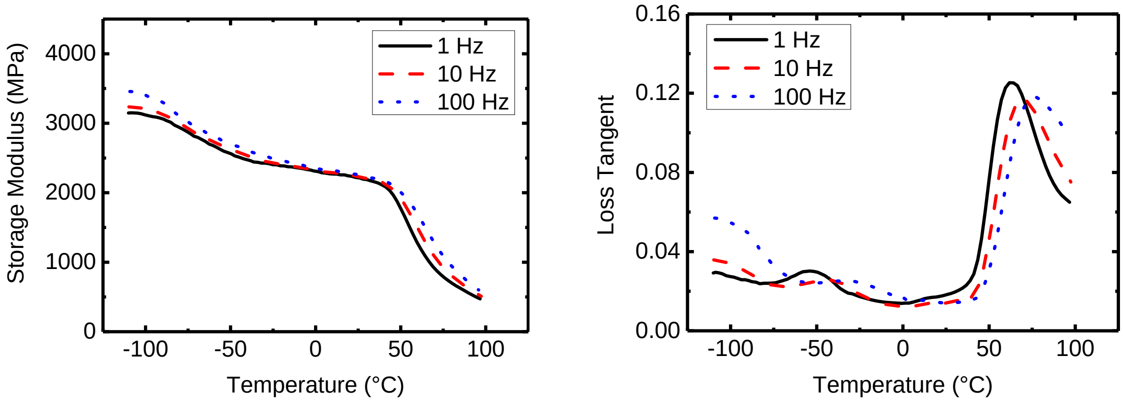

Fig. 4-2 Storage modulus (left) and loss tangent (right) as a function of temperature for specimen number 2.

4.1.4 Data Analysis

The aim of the data analysis is to apply the time-temperature shift established by Mulliken and Boyce [28] for amorphous polymers, to the results of the dynamic mechanical analysis of the semi-crystalline polyamide-6. The method predicts the rate-dependent viscoelastic material behavior at high strain rates around $1000\,\mathrm{s}^{-1}$, or rather high frequencies, which cannot be realized with a DMA test instrument.

In principle, the different rate dependencies of the α- and β-transitions are analyzed and used for a general approach to shift the storage modulus curve to higher temperatures.

As a first step of the approach of Mulliken and Boyce [28] the shift of the α- and β-transitions locations per decade strain rate is quantified. For this purpose the α- and β-peak temperatures are determined via the loss tangent curves for each frequency (Figure 4-1 and 4-2). The transition temperatures measured for each specimen are summarized in Table 4-2. Then the temperature differences from 1 Hz to 10 Hz and from 10 Hz to 100 Hz are calculated which are in the following referred to as delta 1 and delta 2 (Table 4-2). The PA 6 glass transition temperature was found to shift with a factor of (6.93 ± 0.096) °C/decade strain rate (Table 4-3). Mulliken and Boyce [28] have noted for PC and PMMA that the β-transition is more strain rate sensitive. The same observation was made for PA 6 in this study. A shift factor of (11.29 ± 3.04) °C/decade strain rate for the secondary transition of PA 6 was identified (Table 4-3).

Tab. 4-2 α- and β-temperature at different frequencies. Delta 1 determines the temperature difference from 1 Hz to 10 Hz and delta 2 from 10 Hz to 100 Hz.

	Specimen 1		Specimen 2	
	T_β (°C)	T_α (°C)	T_β (°C)	T_α (°C)
1 Hz	-61.96	63.49	-54.04	61.82
10 Hz	-46.12	69.57	-44.36	69.60
100 Hz	-36.08	75.70	-34.77	77.34
Delta 1	15.83	6.087	9.679	7.779
Delta 2	10.05	6.123	9.590	7.744

Tab. 4-3 Shift factor for transitions.

	Shift factor β-transition (°C/decade strain rate)	Shift factor α-transition (°C/decade strain rate)
Mean	11.29	6.93
STDV	3.04	0.96
CV (%)	26.91	13.78

The storage modulus curve at the lowest measured frequency (1 Hz) of specimen 2 is chosen to be used as reference curve for the shift approach. At a temperature of around −25 °C where the storage modulus increases significantly the decomposition of the curve into a α- and β-component is conducted (Figure 4-3). These components were then shifted with the respective factor (Table 4-3) and then summated at every temperature to gain the entire modulus curve at a strain rate one decade higher as the reference curve (black solid line in Figure 4-4). Mulliken and Boyce [28] named this procedure decomposed/shift/reconstruct (DSR) method. Figure 4-4 shows the resulting prediction of the elastic modulus of PA 6 for eight different strain rates ($1 \cdot 10^{-2}\,\mathrm{s}^{-1}$ to $1 \cdot 10^{5}\,\mathrm{s}^{-1}$). The shift factors for the transition regions influence especially the overall shape of the modulus curve due to their different amount of degrees per decade strain rate and do not only shift the curve to higher temperatures.

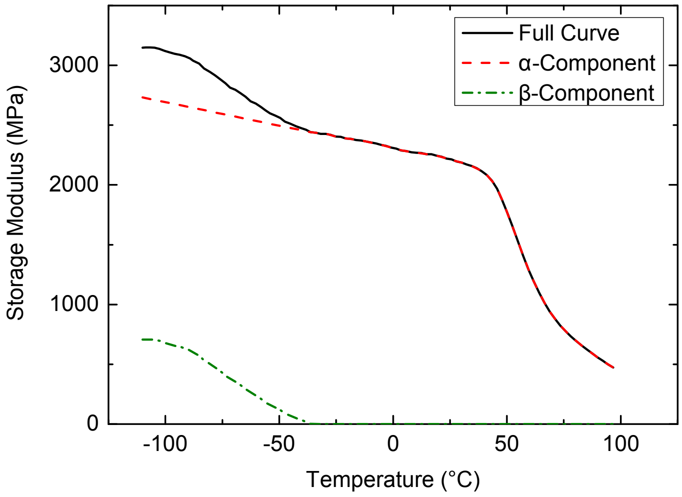

Fig. 4-3 Decomposition of the α- and β-component of the experimental storage modulus curve (specimen 2) at $1.66 \cdot 10^{-3}\,\mathrm{s}^{-1}$.

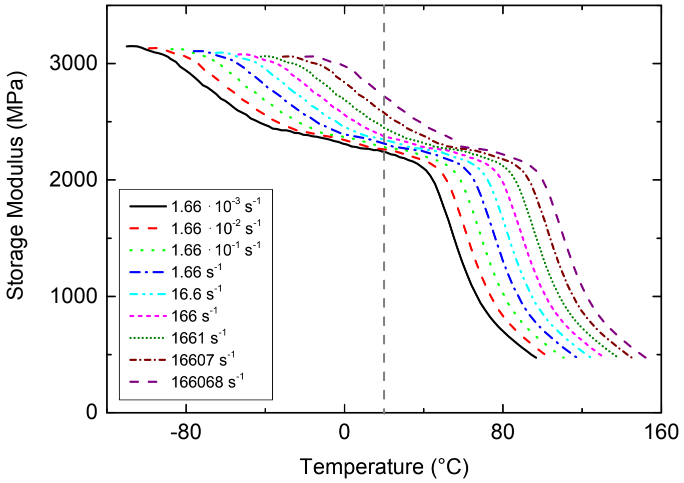

Fig. 4-4 Application of the decompose/shift/reconstruct (DSR) method developed by [28] on the measured storage modulus of polyamide-6. The dashed line indicates the room temperature at 20 °C.

4.1.5 Discussion

The DSR approach [28] could successfully be applied to analyze the DMA results of the semi-crystalline polyamide-6 polymer. The shift of the storage modulus curve towards higher strain rates can now be used to analyze the strain rate sensitivity of the thermoplast especially at room temperature (dashed line in Figure 4-4). In Figure 4-5 the storage modulus at room temperature (20 °C) is plotted as a function of strain rate. Right with the beginning of the curve at quasi-static strain rates around $1 \cdot 10^{-3}\,\mathrm{s}^{-1}$ the storage modulus increases with increasing strain rate. At a strain rate between $1 \cdot 10^{2}\,\mathrm{s}^{-1}$ and $1 \cdot 10^{3}\,\mathrm{s}^{-1}$ a significant increase of the modulus can be found. The characteristic trend of the modulus curve gives an impression of the rate-dependent viscoelastic material behavior over a broad strain rate regime. This results will then be later compared with the results of the dynamic compression tests of PA 6 at high strain rates at the split-Hopkinson pressure bar (see section 4.2.5). The objective of the comparison is, whether the observed distinctive strain rate regime around $200\,\mathrm{s}^{-1}$ where a significant change of the rate-dependent storage modulus occurs is comparable with the behavior of the rate-dependent yield strength of polyamide-6 measured with an SHPB in this strain rate regime.

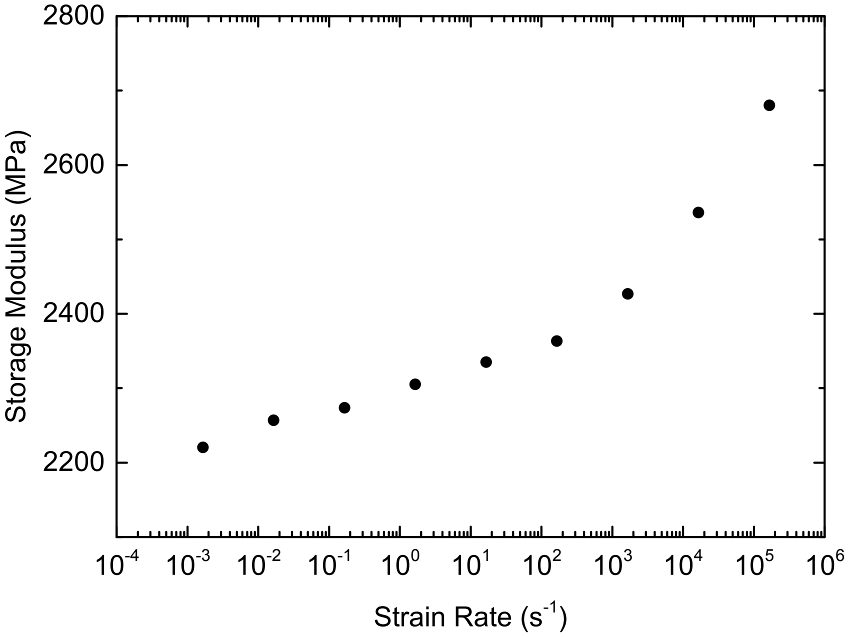

Fig. 4-5 Prediction of the storage modulus of PA 6 at room temperature with the decompose/shift/reconstruct (DSR) method developed by [28] as a function of strain rate.

4.2 Compressive Properties of the Neat Polyamide-6

The strain-rate effect of the compressive properties of polyamide-6 were studied by different authors. Walley and Field [19] used a conventional screw driven mechanical testing machine for quasi-static tests and a hydraulic testing machine for the intermediate strain rate in the range of $1\,\mathrm{s}^{-1}$ to $20\,\mathrm{s}^{-1}$. The high strain rate measurements up to $2 \cdot 10^4\,\mathrm{s}^{-1}$ were obtained in a direct impact Hopkinson bar. The authors Pouriayevali et al. [33] drew up a constitutive description of the rate dependency of the viscoelastic polymer PA 6. To calibrate the model, compression tests at quasi-static strain rate and high strain rates up to $3200\,\mathrm{s}^{-1}$ were carried out. For the measurements a universal testing machine and an SHPB were used. The tested PA 6-specimens from [19] and [33] had a right circular cylindric geometry. Both groups reported an increase of the compressive yield strength at higher strain rates. The strain rate's effect on the Young's modulus was not investigated within the framework of these two studies [19, 33].

In this section the aim is to identify the strain rate dependency on the compressive modulus and on the compressive yield strength of polyamide-6. The quasi-static tests are conducted on an electro-mechanical testing machine. For the high strain rate measurements a split-Hopkinson pressure bar is used. Unlike to the reported measurements [19, 33], a rectangular end-loaded compression specimen geometry was chosen. The results of this investigation concerning the yield strength of the neat polyamide will later be compared with the results of a unidirectional carbon-fiber-reinforced polyamide-6. The manufacturing and subsequently testing of cylinders made of fiber-reinforced composite materials is not widespread. Composite specimens are commonly in a rectangular shape. Therefore the idea was to use the same rectangular geometry for the unreinforced polyamide-6 material, too. The experimental results of the strain rate sensitivity investigation of the compressive properties of PA 6 carried out in this work will then be compared with the literature results.

4.2.1 Material and Test Specimens

The same semi-crystalline polyamide-6 (Ultramid® B3S, BASF) [113] polymer, which was used for the dynamic mechanical analysis, was used for the investigation of the strain-rate dependency in compressive loading. A thermoplastic PA 6 sheet was produced through an extrusion process. The specimens were milled to rectangular end-loaded compression specimens with varying specimen length for the different strain rate regimes. The nominal dimensions for the quasi-static specimens was 10 x 10 x 3.5 mm^3 (length x width x thickness). To measure the compressive strength in the intermediate strain rate regime, the specimen geometry with 10 x 10 x 3.5 mm^3 and the maximum displacement rate of the used universal testing machine was chosen. For the dynamic tests two different nominal specimen lengths, 20 mm and 10 mm, accompanied with the enhancement of the striker velocity were used, to measure the compressive strength at two different high strain rates. The specimen width (10 mm) and thickness (3.5 mm) remain unchanged for the dynamic tests.

A black-on-white speckle pattern for the digital image correlation method was applied on the surface of each specimen using aerosol spray painting. Based on the different image resolutions of the respective cameras the random speckles of the quasi-static specimens were smaller than the speckles of the dynamic specimens.

The specimens were treated with the same drying process described in the subsection 4.1.1 which was used for drying the DMA-specimens. This ensures a common state of the specimens for the mechanical material characterization. Just as the DMA-specimens the dry compression specimens were stored in an aluminum multi-layer film bag until start of the measurement to avoid moisture absorption after drying.

4.2.2 Quasi-Static Experimental Setup

Four quasi-static reference tests were performed using an electro-mechanical testing machine of the type Hegewald & Peschke Inspekt Table 100 with a 100 kN load cell. The tests were carried out with a constant displacement rate of 0.25 mm/min, which corresponds to a quasi-static axial strain rate of approximately $4 \cdot 10^{-4}\,\mathrm{s}^{-1}$, when considering a nominal specimen length of 10 mm. The load was introduced by means of a self-aligning end-loaded compression setup with embedded polished tungsten-carbide (TC) inserts at the loading surfaces (Figure 4-6) [14]. To minimize friction effects at the loading surfaces, a thin layer of molybdenum disulfide (MoS_2) lubricant was applied to the end-surface of the specimen. The GOM ARAMIS-4M DIC system, consisting of two CCD cameras with a resolution of 2352 pixels x 1728 pixels and two lenses of the type Titanar 50 mm, were used to obtain the strain field of the specimen front surface. A measurement volume of 35 mm x 26 mm was defined to cover the whole specimen surface. To ensure a uniform illumination of the specimen surface two LED lamps were used. The acquisition rate of the cameras was set to 2 frames per second (fps) with a shutter speed of 55 ms. For post processing of the recorded images with the ARAMIS software a facet size of 17 pixels x 17 pixels and a facet step of 15 pixels x 15 pixels was used. The computation size for deriving the strain field was set to 3 x 3 facets^2. For the determination of the compressive strain, used in the later shown stress-strain curves, the mean value of a 6 x 6 mm^2 strain field at the center of the specimen surface was calculated. The quasi-static compressive strength is defined as the ratio of the failure load and the specimen cross-section.

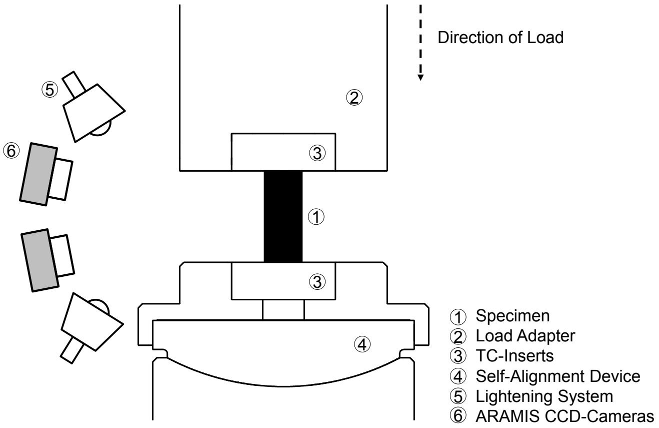

Fig. 4-6 Quasi-static compression test setup with tungsten-carbide (TC) inserts.

4.2.3 Dynamic Experimental Setup

Test Setup for Intermediate Strain Rate Regime

For measuring the compressive strength in an intermediate strain rate (IR) regime, the previous mentioned electro-mechanical testing machine with a 100 kN load cell and the self-aligning end-loaded compression setup (Figure 4-6) was used. Three tests were carried out with a constant displacement rate of 380 mm/min, which corresponds to an axial strain rate of approximately $0.6\,\mathrm{s}^{-1}$, when considering a nominal specimen length of 10 mm. A thin layer of MoS_2-lubricant was applied to the end-surface of the specimen to minimize friction effects at the loading surfaces. To obtain the three-dimensional strain field of the specimen front surface the already mentioned GOM ARAMIS-4M DIC system was used. The two cameras were positioned at a distance of 225 mm away from the specimen surface. Two spotlights of type DEDOLIGHT 400D were used to ensure a uniform illuminated specimen surface. In comparison to the quasi-static tests the acquisition rate of the cameras was raised to 100 fps with a shutter speed of 8.5 ms. The facet size of 17 pixels x 17 pixels and the facet step of 15 pixels x 15 pixels remain unchanged for post processing of the recorded images with the ARAMIS software. Also the computation size for deriving the strain field was set to 3 x 3 facets^2. For the calculation of the specimen strain, the mean value of a 6 x 6 mm^2 strain field at the center of the specimen surface was chosen. The compressive strength is calculated by dividing the failure load by the specimen cross-section.

Test Setup for High Strain Rate Regimes

Dynamic tests at two different strain rates (Table 4-4) were carried out using a split-Hopkinson pressure bar setup (Figure 3-4) consisting of steel striker-, incident-, and transmission-bars with lengths of 0.6 m, 2.6 m, and 1.6 m, respectively. For each strain rate four end-loaded compression specimens were tested. The strain gauges for the detection of the elastic wave are located on the incident-bar at 1.3 m and on the transmission-bar at 0.3 m away from the bar-specimen interfaces and operate with a supply voltage of 7 V. The bar-gauge signals were amplified by using a high-speed transducer amplifier of the type FYLDE FE-H379-TA with a gain setting of 100 and a frequency setting of 300 kHz. The amplified signals and the impact velocity of the striker-bar were each recorded with a TEKTRONIX TDS2004C oscilloscope. To generate an elastic wave with a trapezoidal shape in the incident-bar, a copper pulse shaper was used. The diameter and thickness of the pulse shaper (PS) for the different strain rate regimes are listed in the Table 4-4. In addition, the striker-bar velocity was adjusted to obtain two different high strain rates (Table 4-4). As a result of the nominal specimen geometry and the striker-bar velocity, a strain rate of approximately 233 s^{-1} and 1260 s^{-1} was reached. In the following these two strain rate regimes are denoted as "High-Rate 1(HR1)" and "High-Rate 2 (HR2)".

Tab. 4-4 SHPB setup for compression tests of the neat polyamide-6.

	Strain Rate (s^{-1})	**Striker Length** (mm)	**Bar Ø** (mm)	**PS Ø; Thickness** (mm; mm)	**Striker Velocity** (m/s)	**Frame Rate** (fps)	**Reso-lution** (pixels x pixels)
HR1	233	800	16	5; 0.3	6.21	100000	320 x 192
HR2	1260	400	16	4; 0.8	14.68	262500	128 x 128

To verify the configuration of the split-Hopkinson pressure bar setup for the dynamic tests, bars together (BT) tests, with incident- and transmission-bars directly in contact, were carried out. The striker-bar impacted with a velocity of 6.52 m/s (HR1) and 14.45 m/s (HR2) in combination with the chosen pulse shaper respectively on the incident-bar. Figure 4-7 shows the inverted incident-bar strain signal and the transmission-bar strain signal. The horizontal dashed line indicates the theoretical bar strain amplitude. This amplitude is defined by the relation $\epsilon_{\mathrm{I}}^{\max} = V_0/(2c_{\mathrm{B}})$ with the striker bar impact velocity V_0 and the longitudinal wave speed of $c_{\mathrm{B}} = 5123\,\mathrm{m/s}$ in the bars.

As it can be seen in the left diagram of Figure 4-7 for the BT test at HR1 the theoretical strain amplitude correlates well with the measured incident- and transmission-bar strain signal. The measured bar strain signals show, that the elastic wave travels from the incident- into the transmission-bar without changing the amplitude, duration and shape. Due to the similarity of the two signals at HR1 a correct specimen stress-time response can be expected.

The theoretical strain amplitude for the BT test at HR2 is 4 % lower then the average amplitude of the incident- and transmission-bar strain signal, which might be treated as a small systematic error in the stress-time signal. Also a slight broadening of the transmitted strain wave signal is observed. This indicates that at high strain rates dispersion effects occur. Therefore the equilibrium condition will be proved in a different way (section 4.2.5).

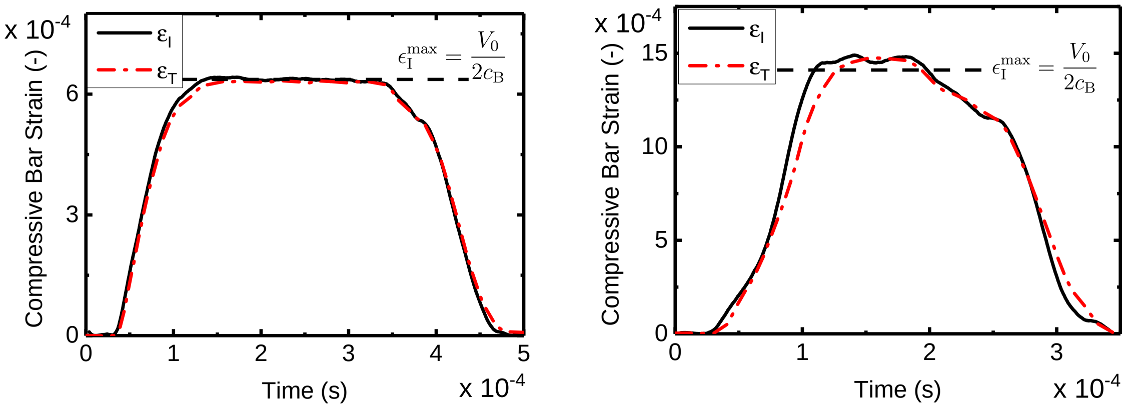

Fig. 4-7 Incident- and transmission-bar strain signals of the bars-together tests with the used SHPB configuration for HR1 (left) and HR2 (right).

A Photron SA5 high-speed camera with a ZEISS Makro-Planar T* 2/100 mm ZF lens was used with different frame rates and resolutions (Table 4-4) during the experiment. The lens aperture was set to f/2.8. Two spotlights of type DEDOLIGHT 400D were used to provide a well illuminated specimen surface. Table 4-5 shows the facet size, facet step and computation size for post processing of the recorded images with the digital image correlation software GOM ARAMIS-4M. For the determination of the axial specimen strain, the mean value of a strain field at the center of the specimen surface was calculated (Table 4-5).

Tab. 4-5 Parameters for post processing with the software GOM ARAMIS-4M.

	HR1	**HR2**
Facet Size (pixels x pixels)	10 x 10	10 x 10
Facet Step (pixels x pixels)	8 x 8	8 x 8
Computation Size (facets^2)	3 x 3	3 x 3
Strain Field (mm x mm)	12 x 6	6 x 6

4.2.4 Results of Quasi-Static Experimental Tests

Four quasi-static reference specimens were loaded with a constant displacement rate. The compressive stress-strain response for all tested specimens is shown as a diagram on the left hand side in Figure 4-8. The results of the reference tests are summarized in Table 4-6. The end point of each curve in Figure 4-8 determines the end of the test. The specimen does not fail during testing but deforms strongly. At round 24 % strain the deformation of the specimen causes a slip out of the specimen between the to compression plates and thus a drop in the stress-strain curve. The right hand side of Figure 4-8 shows an enlarged view from 0 % to 10 % strain.

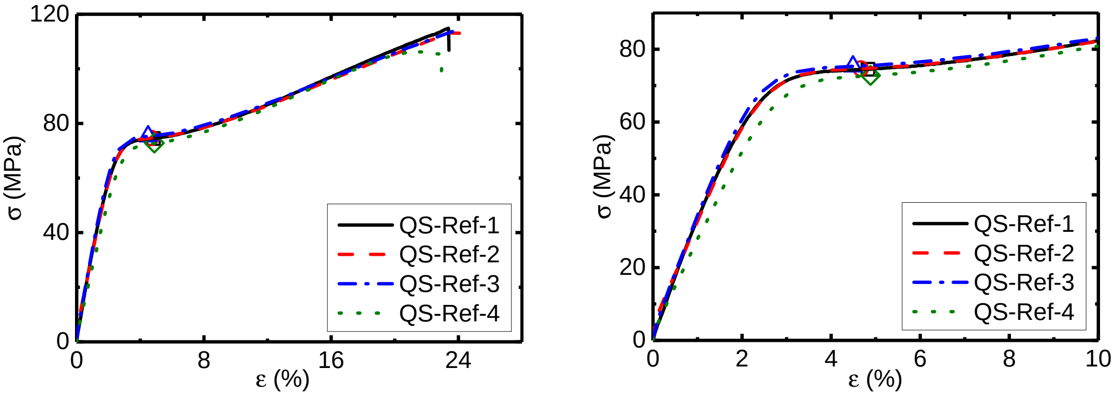

Fig. 4-8 Quasi-static compressive stress-strain curves from reference tests (left) and enlarged view (right). The yield strength is marked with a symbol for each curve.

Tab. 4-6 Quasi-static compression reference test results.

Test	**Yield Strength** $X_C^{y,qs}$ (MPa)	**Yield Strain** ϵ_C^y (%)	**Modulus** E (GPa)
QS-Ref-1	74.49	4.83	3.22
QS-Ref-2	74.67	4.66	2.96
QS-Ref-3	75.30	4.49	3.56
QS-Ref-4	72.80	4.88	2.72
Mean	74.32	4.72	3.12
STDV	1.07	0.18	0.36
CV (%)	1.44	3.76	11.64

The quasi-static compressive yield strength $X_C^{y,qs}$ and yield strain ϵ_C^y are determined where the slope of the curve is almost zero. For each individual curve this is marked with a symbol (Figure 4-8). The strain field shows a homogeneous distribution from the beginning of the test and beyond the yield strength. After the stress plateau is reached the specimen deforms not only in the loading direction but deforms strongly and twists in itself until it slips out between the compression plates. It can be concluded that a valid experimental test is performed until the stress plateau and consequently the yield point of the polymer is reached. The mean quasi-static compressive yield strength of (74.32 ± 1.07) MPa shows a low coefficient of variance with 1.44 %. The Yield's modulus E, evaluated in the strain interval between 0.05 % to 0.25 % by using a linear curve fit was found to be (3.12 ± 0.36) GPa.

4.2.5 Results of Dynamic Experimental Tests

Results of Intermediate Strain Rate Tests

Three specimens were tested in the intermediate strain rate regime. Figure 4-9 shows the compressive stress-strain response for all specimens. The end point of the curves shows the end of the test due to slipping of the specimen out of the compression plates. The specimens deform strongly but do not fail. The yield strength is defined as the maximum stress (Table 4-7).

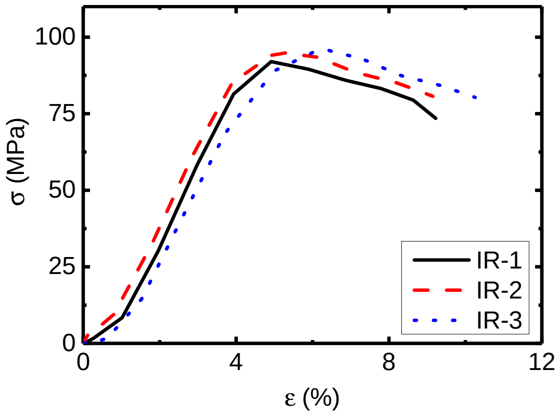

Fig. 4-9 Intermediate strain rate test results.

Tab. 4-7 Intermediate rate compression test results.

Test	**Yield Strength** $X_{\mathrm{C}}^{\mathrm{y,ir}}$ (MPa)	**Yield Strain** $\epsilon_{\mathrm{C}}^{\mathrm{y}}$ (%)
IR-1	92.00	4.92
IR-2	95.23	5.06
IR-3	96.28	6.23
Mean	94.50	5.40
STDV	2.23	0.72
CV (%)	2.36	13.27

A mean compressive yield strength of (94.50 ± 2.23) MPa with a coefficient of variance of 2.36 % was measured. It has to be noted that the measure intermediate yield strength and yield strain are affected by the below mentioned errors. Therefore the material behavior must be analyzed very carefully. The standard setting of the electro-mechanical testing machine has an integration time of 20 ms for recording the load. Thus, each 20 ms a load value is generated that represents the average load value of the last 20 ms. The test duration takes about 220 ms using a displacement rate of 380 mm/min. During the test approximately 12 measuring points of the load are recorded. Thus the recorded force data is somewhat inaccurate. A shorter integration time would have enhanced the accuracy of the load-time response. Due to this reason no elastic modulus was calculated. Even the experiments are not as accurate for several reasons, the measured stress-strain curves represent to some extent the real composite material behavior at intermediate strain rate.

Results of High-Strain-Rate Tests

The dynamic test results were calculated by using the classic SHPB analysis already presented in chapter 3.1.4 which is based on the one-dimensional wave propagation theory [61]. The wave velocity is calculated by using the equation $c_\mathrm{b} = (E_\mathrm{b}/\rho)^{0.5} = 5123\,\mathrm{m/s}$ with $E_\mathrm{b} = 206000\,\mathrm{MPa}$ and $\rho = 7850\,\mathrm{kg/m^3}$ for the steel bars used in the SHPB setup. The specimen strain and the specimen strain rate were directly obtained by contactless optical strain measurement via digital image correlation. In the following the specimen stress σ_S is calculated with the SHPB "1-wave analysis" Equation 3-44. The strain rate $\dot{\epsilon}$ was calculated as the time derivative of the optical measured strain via DIC. Figure 4-10 shows the filtered incident- and transmission-bar signals for the HR1 and HR2 setup. For filtering the signals, a Savitzky-Golay filter was used to eliminate the digitalization noise from the oscilloscope without changing the overall signal shape. Due to the different pulse shaper the incident strain signal shows either a trapezoidal or slight triangular shape of the wave.

To check the dynamic equilibrium in the specimen, the 1-wave and the 2-wave stress-time signals, calculated with Equation 3-44 and 3-45, respectively, are plotted in a diagram (Figure 4-11) for the HR1 and HR2 tests. In addition the strain rate-time signals from the classic SHPB Analysis and from the DIC are shown in the graphs. For the HR1 specimens the comparison of the 1- and 2-wave stresses does not fulfill the dynamic equilibrium condition. The signals underlie dispersion effects which did not appear in the initial bars together test without specimen. Reflections of the elastic wave within the specimen length can cause interference. Presumable the interfaces between the specimen surfaces and the bar ends might be

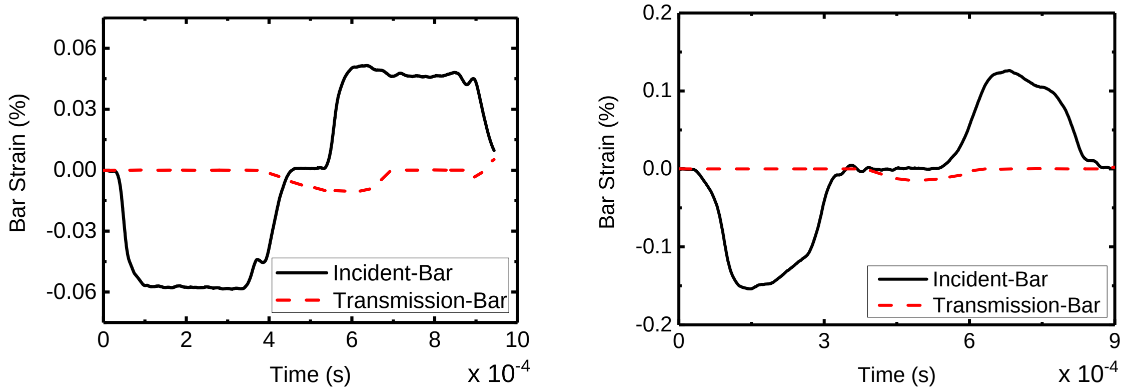

Fig. 4-10 Bar strain wave groups from HR1 (left) and HR2 (right) tests with shaped incident waves for a representative specimen, respectively.

influenced by friction which in turn changes the mechanical impedance. At the HR2 loading rate the dispersion effects are magnified [16] and the 1-wave and 2-wave stress curves deviate (Figure 4-11).

During the time period in which the reflected and transmitted signal is detected at the strain gauges on the bars, the shape of the elastic wave is disturbed by dispersion effects. The specimen may underlie different stress levels and is therefore not in dynamic equilibrium [16]. Thus the calculated stress-time response with the SHPB Analysis must be treated with care. In the work of Koerber et al [16] the same SHPB setup with the travel distances of 2.6 m for the wave in the incident-bar and 0.3 m in the transmission-bar since the signal is detected, were used. The authors argue that the dispersion effects on the transmitted signal are presumable small due to a small travel distance. The calculation of the specimen stress with the transmission wave strain signal (Equation 3-44) is assumed to describe the real stress-state of the specimen more closely. Moreover the authors [16] consider, that even if the transmission signal is not dispersion free the effect on the measured axial stress-strain response is only minor. The 1-wave stress signal was therefore used for all dynamic stress-strain curves.

The strain rate-time response of the HR1 test, calculated via SHPB Analysis and DIC, are shown in Figure 4-11 (left). The curves indicate a constant strain rate shortly after beginning of the experiment. The HR2 experiments also show a constant strain rate right after beginning of the specimen loading (Figure 4-11, right). As a further evidence of the existence of dynamic equilibrium within the specimen during testing, the in-plane axial specimen strain field measured via DIC on the specimen surface was determined. The same representative specimens for which the dynamic stress equilibrium check is shown in Figure 4-11 were adducted to demonstrate the time dependent evolution of the centrally measured axial strain along the specimen length. Figure 4-12 shows this multi-stage-section graphs for the HR1 and HR2 tests, respectively. For each diagram the curve with the highest strain level corresponds to the moment of specimen failure. In general, the axial strain along the specimen length shows a characteristic distribution with time. Thus it is concluded that the specimen was not subjected to different stresses over its length but rather was in an equilibrium state at both strain rate regimes.

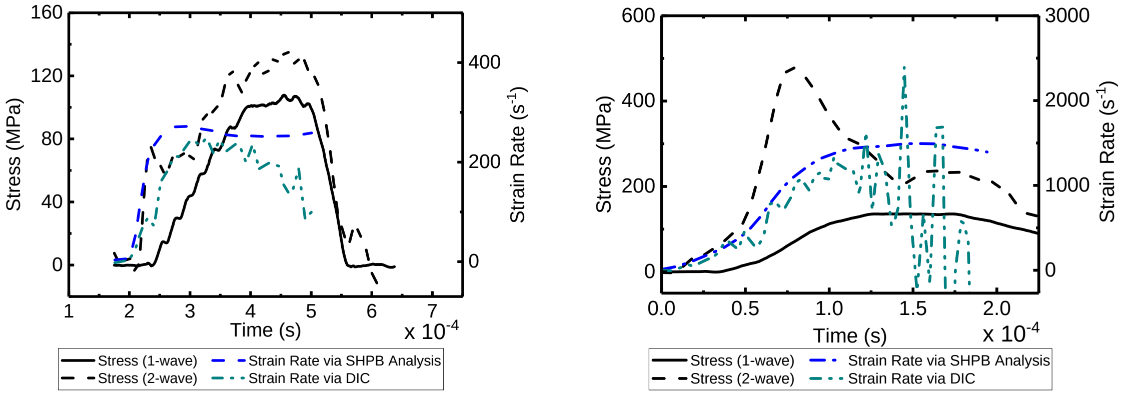

Fig. 4-11 Dynamic stress equilibrium check and corresponding strain rate for a representative specimen tested at HR1 (left) and HR2 (right).

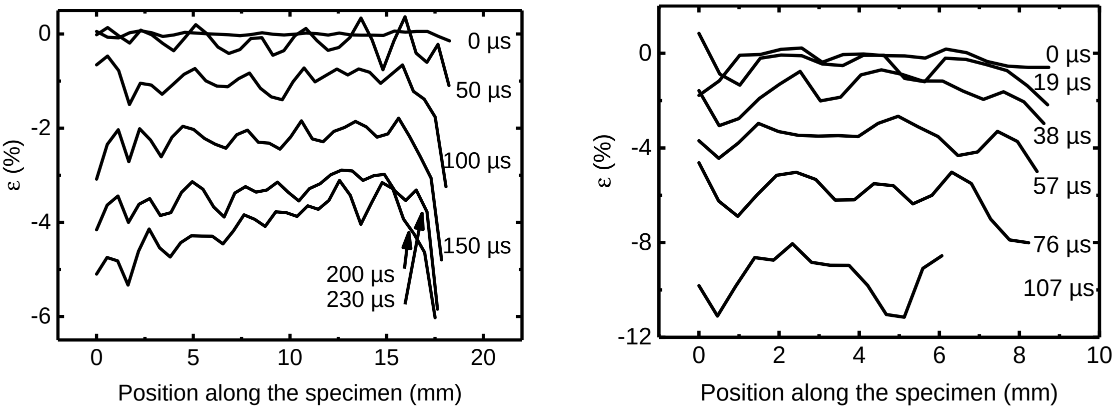

Fig. 4-12 Uniform development of specimen strain along axial direction for a representative specimen tested at HR1 (left) and HR2 (right).

Figure 4-13 shows the compressive stress-strain response for all tested specimens at the HR1 and HR2 strain rate regime. The end point of each curve represents the end of the experimental test while all specimens are strongly deformed. The specimens do not fail in the sense of splitting into several parts but they are deformed plastically. In Figure 4-14 sequences of the deformation behavior of the specimen with superimposed axial strain fields for representative HR2, HR1, and quasi-static compression tests are shown. In the corresponding stress-strain curve the positions of the respective strain state is marked with a symbol and named in alphabetic order.

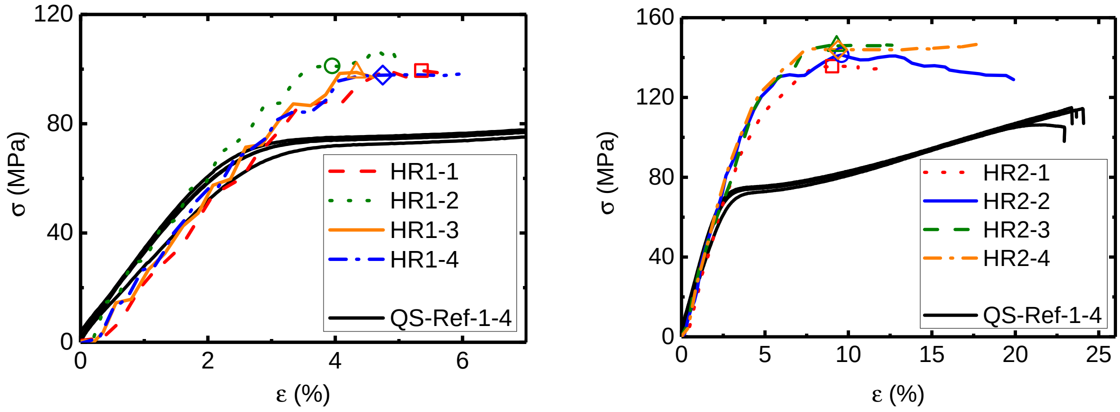

Fig. 4-13 Comparison of the quasi-static compressive stress-strain curves from reference tests with dynamic tests at HR1 (left) and HR2 (right).

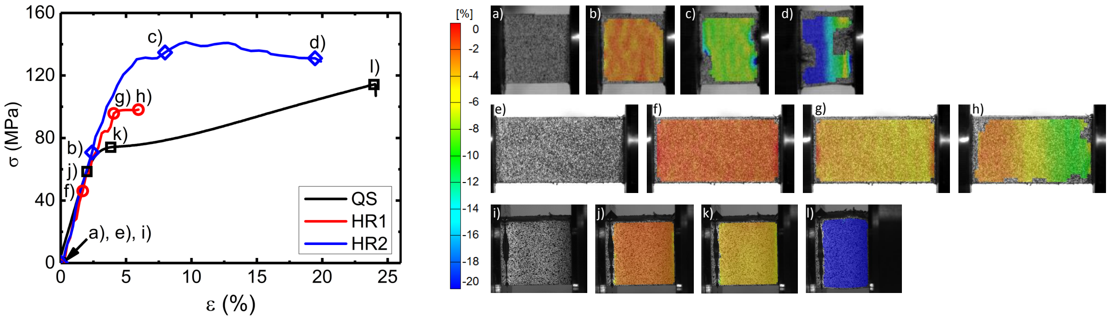

Fig. 4-14 In-plane strain fields in loading direction of compression specimens at HR2 a)-d), HR1 e)-h), and quasi-static loading i)-l).

The deformation sequence of Figure 4-14 a)-d) shows the strain fields at HR2 and the sequence of Figure 4-14 e)-h) shows the strain field distribution at HR1. The distribution of the strain field for both tests is homogeneous until the stress plateau. After reaching the yield point the specimen deforms no longer only in loading direction but also twists itself until it slips out between the bars. The deformation of the HR1-specimens after the stress plateau region causes an instantaneous twist and slip out of the specimen. The HR2-specimen length is shorter and therefore a longer deformation before slip out can occur. In Figure 4-14 i)-l) the sequence of the quasi-static compression experiment is shown. The images shown here are from the left camera of the used ARAMIS system in 3D configuration. The quasi-static strain field in Figure 4-14 i)-l) is homogeneous until the yield point is reached. A strong deformation and compaction of the material can be observed beyond the yield point until the specimen slips out between the compression plates. It is therefore concluded that from the tests at different strain rate levels, valid stress-strain curves for uniaxial compression loading can be obtained up to the stress-plateau.

The dynamic yield strength $X_\mathrm{C}^\mathrm{y,hr}$ and yield strain $\epsilon_\mathrm{C}^\mathrm{y}$ indicate the stress-strain level where the stress does not increase with increasing strain any longer. For each individual curve this is marked with a symbol (Figure 4-13). In Table 4-8 the HR1 experimental results and in Table 4-9 the HR2 experimental results are listed, respectively.

Tab. 4-8 Dynamic (HR1) compression test results.

Test	**Strain Rate**		**Modulus**	**Yield Strength**	**Yield Strain**
	elastic* (s^{-1})	failure** (s^{-1})	E (GPa)	$X_\mathrm{C}^\mathrm{y,hr}$ (MPa)	$\epsilon_\mathrm{C}^\mathrm{y}$ (%)
HR1-1	183.12	227.07	2.55	99.47	5.35
HR1-2	181.78	220.75	3.70	101.18	3.95
HR1-3	201.65	249.35	2.69	98.79	4.34
HR1-4	204.61	233.07	3.30	97.80	4.75
Mean	192.79	232.56	3.06	99.31	4.60
STDV	12.02	12.27	0.54	1.42	0.60
CV (%)	6.23	5.28	17.52	1.43	13.06

* averaged between 0.45 % and 0.65 % strain
** averaged between 0.6 % and failure strain

Tab. 4-9 Dynamic (HR2) compression test results.

Test	**Strain Rate**		**Modulus**	**Yield Strength**	**Yield Strain**
	elastic* (s^{-1})	failure** (s^{-1})	E (GPa)	$X_\mathrm{C}^\mathrm{y,hr}$ (MPa)	$\epsilon_\mathrm{C}^\mathrm{y}$ (%)
HR2-1	278.89	1144.70	3.39	135.66	9.03
HR2-2	390.30	1381.58	2.32	141.31	9.58
HR2-3	348.55	1252.74	3.87	145.81	9.29
HR2-4	342.47	1261.61	4.16	143.93	9.38
Mean	340.06	1260.16	3.43	141.68	9.32
STDV	45.99	96.83	0.81	4.42	0.23
CV (%)	13.52	7.68	23.65	3.12	2.48

* averaged between 0.45 % and 0.65 % strain
** averaged between 5 % and 10 %

A mean compressive yield strength of (99.31 ± 1.42) MPa (HR1) and (141.68 ± 4.42) MPa (HR2) with coefficients of variance of 1.43 % and 3.12 % were measured for the unreinforced polyamide-6. The obtained mean value of the Young's modulus, evaluated in the linear part of the stress-strain curve between 0.45 % and 0.65 % strain, is (3.06 ± 0.54) GPa (HR1) and (3.43 ± 0.81) GPa (HR2).

Comparison

The comparison of the compressive stress-strain curves of the polyamide-6 polymer, loaded at quasi-static, intermediate, and two high strain rates (Figure 4-15), indicates a slight increase of the compressive modulus (10 %) and a significant increase of the compressive yield strength (91 %) from quasi-static to approximately 1260 s^{-1}.

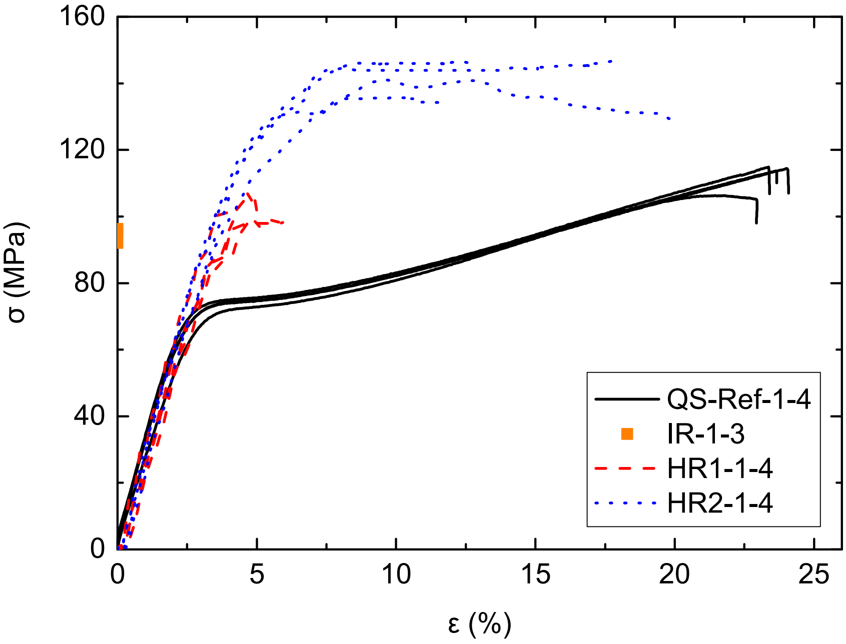

Fig. 4-15 Comparison of the quasi-static, intermediate, and high strain rate compressive test results.

Chou et al. [114] studied the compressive stress-strain response of polyamide 6.6 over a broad strain rate regime. Later Walley and Field [19] and Pouriayevali et al. [33] studied the compressive stress-strain response of polyamide-6 also at low and high strain rates. The normalization of the literature results of the yield strength with respect to the reported quasi-static value enables to visualize possible trends in the strain rate behavior. Figure 4-16 compares the normalized yield strengths from the literature with the normalize yield strengths obtained in this study. It can be noted that the results of the presented work correlate very well with the reported literature results. It is further noted that the rectangular specimen geometry chosen in this study does not seam to have an effect on the determination of the strain rate dependency of the investigated polymer.

Finally the results of the measured yield strength as function of strain rate can be compared with the DMA results shown in Figure 4-5. The DMA measurements show that the storage modulus of 2220 MPa at quasi-static strain rate increases up to 2420 MPa at a strain rate of around 1600 s^{-1}, which is only a minor increase of 10 %. Interestingly, this is approximately what was measured with the SHPB tests. The measured Young's modulus also increases of about 10 % from quasi-static strain rate to around 340 s^{-1}, which is above the strain rate of 200 s^{-1}, where the material behavior changes strongly in the DMA experiment as well as in the SHPB measurement. However, the normalized yield strength increases significantly by 91 % from low to high strain rate. But the two behaviors have in common that at a strain rate of approximately 200 s^{-1} both material parameters, storage modulus and yield strength, significantly increase with each subsequent decade of strain rate.

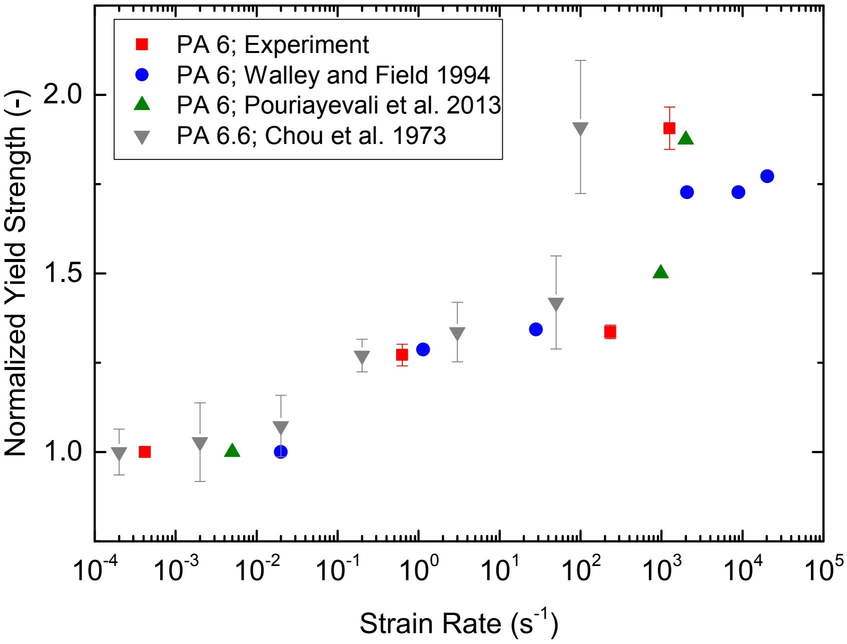

Fig. 4-16 Comparison of experimental results with literature results regarding the strain rate's effect on the compressive properties of polyamide-6.

5 Transverse Compression and Tension Properties of UD Laminate

In this chapter the investigation of the strain-rate-dependent transverse compression (section 5.1) and tension (section 5.2) properties of the unidirectional carbon-fiber-reinforced polyamide-6 composite material are presented. The mechanical properties of the composite material are most effected by the viscoelastic and viscoplastic behavior of the thermoplastic polymer material. On the basis of the knowledge of the strain rate effects on the neat polymer which is described in detail in the previous chapter, the compression and tensile tests are planned and carried out. The results of this characterization contribute to the development of constitutive models and failure criteria for this type of lightweight construction material. For both tests compression and tension quasi-static and dynamic measurements at different high strain rates were performed. The high strain rate transverse compression experiments were carried out with the same SHPB setup used for the characterization of the neat polyamide-6 polymer. For the transverse tension tests at high strain rates a split-Hopkinson tension bar system was used. The operating principle of this characterization method is already given in section 3.2.

5.1 Transverse Compression

5.1.1 Material and Test Specimens

The specimens were prepared from Celstran® CFR-TP PA6 CF60-01, a 60 % carbon fiber by weight polyamide-6 unidirectional reinforced thermoplastic composite tape [115]. According to the material data sheet [115] a fiber volume content of 48 % is then obtained. In the present study the fiber volume content of the manufactured laminate was determined to be 49 %, using the test standard ASTM D3171, Method II, Procedure B (digestion of the matrix by a mixture of sulfuric acid and hydrogen peroxide) [116] . This material system is used in industrial, automotive, and sporting goods applications and is commonly processed with automated fiber placement technologies. A unidirectional plate with 16-plies was manufactured for the specimens which were tested according to ASTM D6641 and a unidirectional plate with 28-plies was manufactured for the quasi-static and dynamic specimens. The laminates were made of single tape stripes laid parallel and brick-like above each other such that the abutting edges of the stripes are at different locations in the individual layers. For a better handling of the stack the frame was welded at few points with an ultra-sonic welding apparatus (ProteUS, EM-Systeme GmbH) with a sonotrode frequency of 30 kHz. Using a RUCKS hot press and a compression mold the composite plates were consolidated at 260 °C with 0.5 MPa pressure for 15 minutes.

In the presented study, a rectangular end-loaded compression specimen geometry with varying specimen length for the different strain rate regimes was used. The nominal dimensions for the quasi-static specimens was 20 x 10 x 3.5 mm^3 (length x width x thickness). To measure the transverse compressive strength in the intermediate strain rate regime, the specimen length was reduced to 10 x 10 x 3.5 mm^3 and the maximum displacement rate of the used universal testing machine was chosen. For the dynamic tests the nominal specimen length was reduced from 20 mm to 10 mm and 5 mm accompanied with the enhancement of the striker velocity to obtain significantly higher strain rates. The specimen width (10 mm) and thickness (3.5 mm) remain unchanged for the dynamic tests. Woldesenbet and Vinson [117] studied the effect of the specimen geometry on the results of high strain rate compression tests for unidirectional composite materials. On the one hand the authors altered the length-to-diameter ratios of cylindrical specimens and on the other hand they compared the test results of cylindrical specimens with the test results of square/rectangular shaped specimens. For either length-to-diameter ratio or specimen shape no statistically significant effects were found. A study of Koerber et al. [16] had proven, that it is eligible to use planar rectangular specimen with different lengths to obtain different strain rates on the Hopkinson bar apparatus.

The specimens were cut on a water-cooled diamond saw. The loading surfaces were treated with a grinding machine to generate plane and parallel end-faces of good quality. A black-on-white speckle pattern for the digital image correlation method was applied on the surface of each specimen using aerosol spray painting. Based on the different image resolutions of the respective cameras the random speckles of the quasi-static specimens were smaller than the speckles of the dynamic specimens.

An approach was set up to provide on the one hand the strain-rate dependency which is measured with specially designed smaller specimens, as described above, and on the other hand static material data determined via recognized test standards. The results of the ASTM-tests are later compared with the quasi-static reference test results to verify if an influence on the material properties due to the size effect and an influence of different test methodologies can be measured.

Thus quasi-static tests according to ASTM D6641 were carried out. The specimen geometry with nominal dimensions of 137.5 x 12 x 2 mm^3 (length x width x thickness) and a free gauge section of 10 mm was used. For these specimens glass-epoxy composite tabs were bonded to each side using the adhesive Scotch-Weld™ DP 490 from 3M. All specimens were cut on a water-cooled diamond saw. The specimens were equipped with two linear strain gauges of the type TML FLA-3-11-1L in a back-to-back configuration at the free gauge section to measure the strain and possible bending of the specimen.

To establish a common basis for mechanical material characterization, all specimens were dried in a drying oven under vacuum at 80 °C for 72 hours to minimize possible moisture effects arising from the PA 6 polymer's hygroscopic behavior. The dry specimens were stored in a multi-layer polymer-aluminum-film bag until start of the experiment to prevent moisture absorption after drying.

5.1.2 Quasi-Static Experimental Setup

Test Setup for Reference Tests

Four quasi-static reference tests were performed using the same electro-mechanical testing machine like for the previous experiments (type Hegewald & Peschke Inspekt Table 100) with a 100 kN load cell. The tests were carried out with a constant displacement rate of 0.5 mm/min, which corresponds to a quasi-static axial strain rate of approximately $4 \cdot 10^{-4}\,\mathrm{s}^{-1}$, when considering a nominal specimen length of 20 mm. The load was introduced by means of the already shown self-aligning end-loaded compression setup with embedded polished tungsten-carbide inserts at the loading surfaces (Figure 4-6). The latter prevent damage on the loading surfaces of the compression fixture due to the high compressive strength of the tested material. To minimize friction effects at the loading surfaces, a thin layer of molybdenum disulfide lubricant was applied to the end-surface of the specimen. The same GOM ARAMIS-4M DIC system used for the previous tests, consisting of two CCD cameras with a resolution of 2352 pixels x 1728 pixels and two lenses of the type Titanar 50 mm, were used to obtain the three-dimensional quasi-static strain field of the specimen front surface. The DIC system was positioned at a distance of 225 mm away from the specimen surface. To ensure a uniform illumination of the specimen surface two LED lamps were used. The acquisition rate of the cameras was set to 2 frames per second (fps) with a shutter speed of 48 ms. For post processing of the recorded images with the ARAMIS software a facet size of 17 pixels x 17 pixels and a facet step of 15 pixels x 15 pixels was used. The computation size for deriving the strain field was set to 3 x 3 facets^2. For the determination of the longitudinal compressive specimen strain, used in the later shown stress-strain curves, the mean value of a 12 x 6 mm^2 strain field at the center of the specimen surface was calculated.

The ratio of the failure load and the specimen cross-section gives the quasi-static transverse compressive strength.

Test Setup According to ASTM D6641

Four quasi-static transverse compression tests according to the standard ASTM D6641 [118] were carried out on the aforementioned electro-mechanical testing machine at a constant displacement rate of 1.3 mm/min. For these tests the combined loading compression (CLC) test fixture defined in [118] was used. The strain gauges were connected to an HBM MX840A amplifier, used for the data acquisition. As defined in the standard, the specimen strain was obtained by calculating the average value from the two strain gauge signals and the quasi-static longitudinal compressive strength was calculated as the ratio of the failure load and the specimen cross-section.

5.1.3 Dynamic Experimental Setup

Test Setup for Intermediate Strain Rate Regime

For measuring the transverse compressive strength in an intermediate strain rate regime the previous mentioned electro-mechanical testing machine with a 100 kN load cell and the self-aligning end-loaded compression setup (Figure 4-6) was used. Four tests were carried out with a constant displacement rate of 380 mm/min, which corresponds to an axial strain rate of approximately $0.6\,\mathrm{s}^{-1}$, when considering a nominal specimen length of 10 mm. A thin layer of molybdenum disulfide lubricant was applied to the end-surface of the specimen to minimize friction effects at the loading surfaces. To obtain the three-dimensional strain field of the specimen front surface the GOM ARAMIS-4M DIC system was positioned at a distance of 225 mm away from the specimen surface. Two spotlights of type DEDOLIGHT 400D were used to ensure a uniform illuminated specimen surface. In comparison to the quasi-static tests the acquisition rate of the cameras was raised to 60 fps with a shutter speed of 3 ms. The facet size of 17 pixels x 17 pixels and the facet step of 15 pixels x 15 pixels remain unchanged for post processing of the recorded images with the ARAMIS software. Also the computation size for deriving the strain field was set to 3 x 3 facets^2. For the calculation of the transverse compressive specimen strain, the mean value of a 6 x 6 mm^2 strain field at the center of the specimen surface was chosen. The quotient of failure load and specimen cross-sectional area yields the transverse compressive strength.

Test Setup for High Strain Rate Regimes

Dynamic tests at three different strain rates (Table 5-1) were carried out using a split-Hopkinson pressure bar setup (Figure 3-4) consisting of steel striker-, incident-, and transmission-bars with lengths of 0.6 m, 2.6 m and 1.6 m, respectively. For each strain rate four end-loaded compression specimens were tested. The position of the strain gauges on the bars is comparable to that of the dynamic setup for the compression tests of PA 6. The bar-gauge signals were amplified by using a high-speed transducer amplifier of the type FYLDE FE-H379-TA with a gain setting of 100 and a frequency setting of 300 kHz. The amplified signals and the impact velocity of the striker-bar were each recorded with a TEKTRONIX TDS2004C oscilloscope. To generate an elastic wave with a trapezoidal shape in the incident-bar, a copper pulse shaper was used. The diameter and thickness of the pulse shaper for the different strain rate regimes are listed in the Table 5-1. In addition, the striker-bar velocity was adjusted to obtain three different high strain rates (Table 5-1). As a result of the nominal specimen geometry and the striker-bar velocity a strain rate of approximately 175 s^{-1} , 936 s^{-1}, and 2253 s^{-1} was reached. In the following these three strain rate regimes are denoted as "High-Rate 1 (HR1)", "High-Rate 2 (HR2)", and "High-Rate 3 (HR3)".

Tab. 5-1 SHPB setup for transverse compression tests.

	Strain Rate (s^{-1})	**Striker Length** (mm)	**Bar Ø** (mm)	**PS Ø; Thickness** (mm; mm)	**Striker Velocity** (m/s)	**Frame Rate** (fps)	**Resolution** (pixels x pixels)
HR1	175	800	16	5; 0.3	5.60	100000	320 x 192
HR2	936	400	16	4; 0.8	14.74	262500	128 x 128
HR3	2253	400	18	4; 0.8	19.02	420000	64 x 96

To verify the configuration for the dynamic tests, a bars together (BT) test, with incident- and transmission-bars directly in contact, was carried out. The striker-bar was impacting with a velocity of 6.77 m/s (without pulse shaper), with 14.45 m/s (with pulse shaper) and with 19.11 m/s (with pulse shaper) on the the incident-bar. Figure 5-1 shows the inverted incident-bar strain signal and the transmission-bar strain signal. The horizontal dashed line indicates the theoretical bar strain amplitude. This amplitude is defined by the relation $\epsilon_{\text{I}}^{\text{max}} = V_0/(2c_{\text{B}})$ with the striker bar impact velocity V_0 and the longitudinal wave speed of $c_{\text{B}} = 5123\,\text{m/s}$ in the bars.

In the upper left diagram in Figure 5-1 the result for the BT test at HR1 is shown. The theoretical strain amplitude is slightly higher than the measured incident- and transmission-bar strain signal. But this difference of 2 % is negligible. The measured bar strain signals show, that the elastic wave travels from the incident- into the transmission-bar without changing the amplitude, duration and shape. Due to the similarity of the two signals at HR1 a correct specimen stress-time response can be expected.

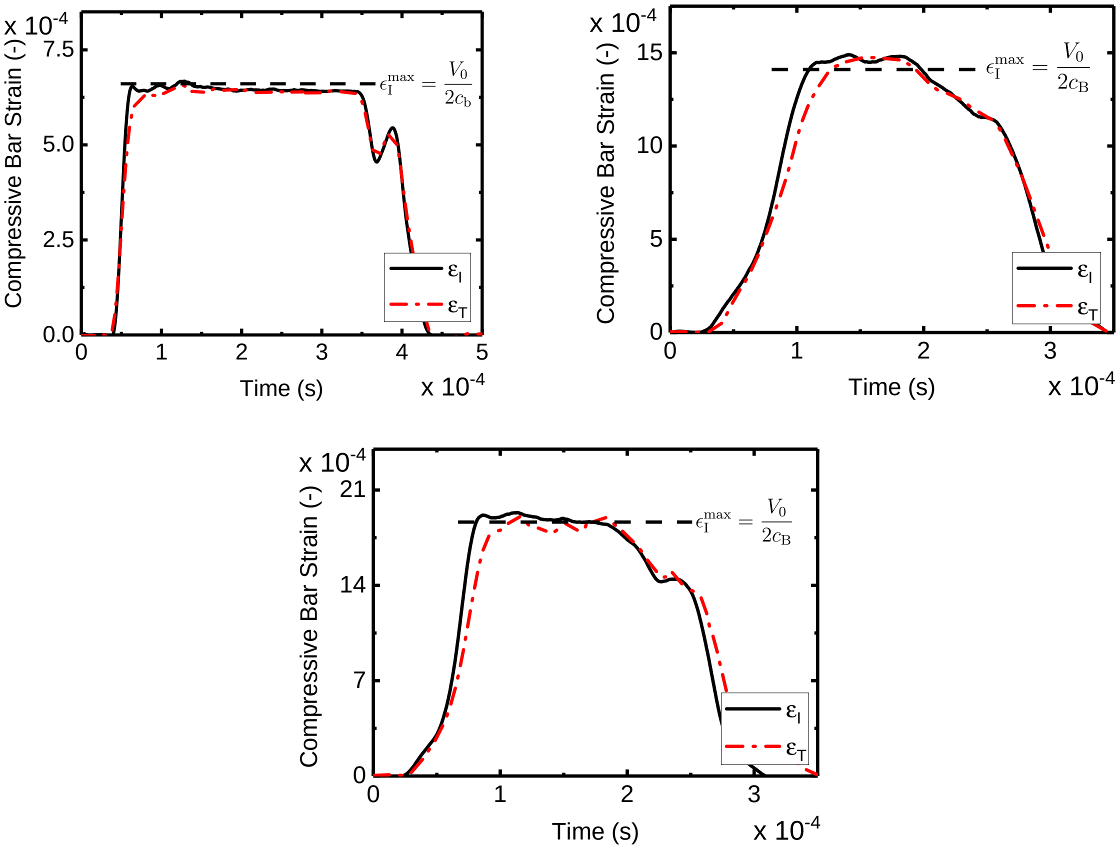

Fig. 5-1 Incident- and transmission-bar strain signals of the bars-together tests with the used SHPB configuration for HR1, HR2, and HR3.

The theoretical strain amplitude for the BT test at HR2 is 4 % lower then the average amplitude of the incident- and transmission-bar strain signal, which might be treated as a small systematic error in the stress-time signal. Also a slight broadening of the strain wave signal in the transmission-bar is observed. This indicates that at high strain rates dispersion effects occur. Therefore the equilibrium condition will be proved in a different way (section 5.1.5). For the BT test at HR3 the theoretical bar strain amplitude correlates well with the measured incident- and transmission-bar strain signal. Due to the similarity of the two signals a correct specimen stress-time response can be expected. A Photron SA5 high-speed camera with a ZEISS Makro-Planar T* 2/100 mm ZF lens was used with different frame rates and resolutions (Table 5-1) during the experiment. The lens aperture was set to f/2.8. Two spotlights of type DEDOLIGHT 400D were used to provide a well illuminated specimen surface.

Table 5-2 shows the facet size, facet step, and computation size for post processing of the recorded images with the digital image correlation software GOM ARAMIS-4M. For the determination of the axial specimen strain, the mean value of a strain field at the center of the specimen surface was calculated (Table 5-2).

Tab. 5-2 Parameters for post processing with the software GOM ARAMIS-4M.

	HR1	**HR2**	**HR3**
Facet Size (pixels x pixels)	10 x 10	10 x 10	10 x 10
Facet Step (pixels x pixels)	8 x 8	8 x 8	8 x 8
Computation Size (facets^2)	3 x 3	3 x 3	3 x 3
Strain Field (mm x mm)	12 x 6	6 x 6	3 x 6

5.1.4 Results of Quasi-Static Experimental Tests

Results of Reference Tests

Quasi-static reference tests with constant displacement rate were carried out for four specimens. The transverse compressive stress-strain response for all specimens is shown in Figure 5-2. The quasi-static compressive strength Y_C^{qs} is determined where the stress reaches a plateau. There the strain ϵ_C^u is identified (Table 5-3).

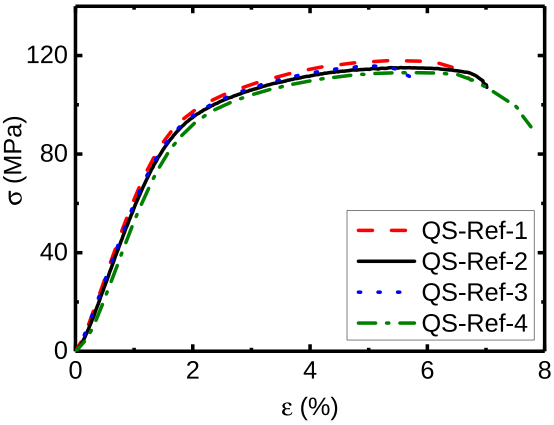

Fig. 5-2 Quasi-static transverse compressive stress-strain curves from reference tests.

When the specimen reaches the stress plateau it shows a localization of the strain field. At higher load levels this local field of high strain increases and finally causes the ultimate failure of the material with an angle of around 58 ° to the action plane of the transverse compressive stress. Due to shear stresses the fracture plane is not equal to the action plane of the loading. A detailed description of this phenomenon

Tab. 5-3 Quasi-static transverse compression reference test results.

Test	Strength $Y_{\mathrm{C}}^{\mathrm{qs}}$ (MPa)	Failure Strain $\epsilon_{\mathrm{C}}^{\mathrm{u}}$ (%)	Modulus E (GPa)
QS-Ref-1	117.99	5.53	6.83
QS-Ref-2	115.13	5.54	6.55
QS-Ref-3	115.84	5.05	6.53
QS-Ref-4	113.12	5.54	6.14
Mean	115.52	5.42	6.51
STDV	2.01	0.24	0.28
CV (%)	1.74	4.52	4.34

can be found in [119], where a fracture plane of 53 ° is considered. The action plane is denoted with σ_2^{c} and $\theta = 0$. There only a pure transverse compression stress is acting $\sigma_n^{\mathrm{c}} = \sigma_2^{\mathrm{c}}$ and no shear stress $\tau_{\mathrm{nt}} = 0$ (Figure 5-3).

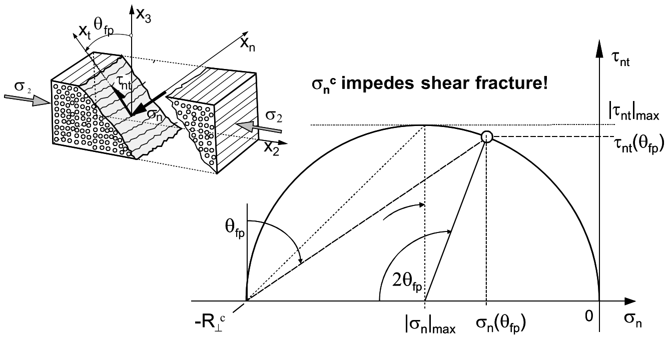

Fig. 5-3 Fracture under uniaxial compressive stress σ_2^{c} [119].

On the action plane no fracture can occur. In contrast, no stresses act in the perpendicular plane $\theta = 90\,°$. All other planes with $0\,° < \theta < 90\,°$ are exposed to stress combinations of a transverse compressive stress $\sigma_n^{\mathrm{c}}(\theta)$ and a transverse shear stress $\tau_{\mathrm{nt}}(\theta)$. The maximum shear stress occurs at an angle of $\theta = 45\,°$ ($\tau_{\mathrm{nt,max}} = \tau_{\mathrm{nt}}(45\,°)$) and has the same value as the transverse compressive stress $\sigma_n^{\mathrm{c}}(45\,°)$. Considering the fracture plane at $53\,° \pm 2$ the shear stress $\tau_{\mathrm{nt}}(53\,°)$ is marginal smaller than the maximum shear stress $\tau_{\mathrm{nt,max}}$. Though, the transverse compressive stress at this angle $\sigma_n^{\mathrm{c}}(53\,°)$ is remarkable smaller compared to the value under 45 °. Consequently, failure occurs at a fracture plane angle of approximately 53 °.

The results of the reference tests are listed in Table 5-3. A mean quasi-static transverse compressive strength of (115.52 ± 2.01) MPa was measured. The Young's modulus determined from 0.4 % and 0.6 % strain was found to be (6.51 ± 0.28) GPa.

Results of ASTM-Tests

Four quasi-static tests according to the test standard ASTM D6641 were carried out by using the corresponding specimen geometry and test fixture. In Figure 5-4 the stress-strain curves for all tested specimens are shown. The end of each curve denotes the failure load and defines the quasi-static transverse compressive strength Y_C^{qs} and the ultimate failure strain ϵ_C^u. Table 5-4 gives an overview of all previous named material properties including the Young's modulus.

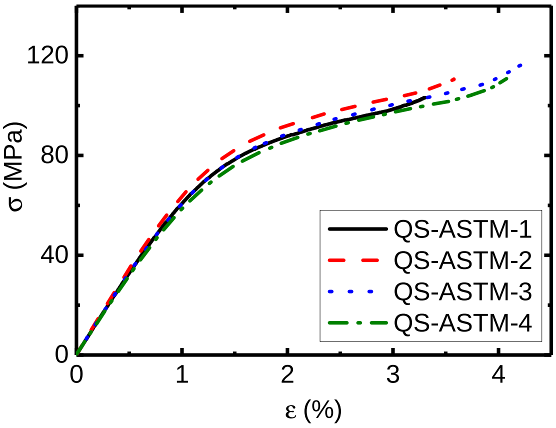

Fig. 5-4 Quasi-static transverse compressive stress-strain curves from static ASTM tests.

Tab. 5-4 Quasi-static transverse compression ASTM test results.

Test	**Strength** Y_C^{qs} (MPa)	**Failure Strain** ϵ_C^u (%)	**Modulus** E (GPa)
QS-ASTM-1	103.17	3.31	6.60
QS-ASTM-2	110.65	3.58	6.95
QS-ASTM-3	116.47	4.23	6.56
QS-ASTM-4	110.78	4.08	6.40
Mean	110.27	3.80	6.63
STDV	5.45	0.43	0.23
CV (%)	4.95	11.30	3.51

The measured strength of (110.27 ± 5.45) MPa is somewhat lower (4.5 %) than the compressive strength measured at the reference tests. Moreover, the ASTM-specimens exhibit a slightly higher coefficient of variance for the strength parameter. Nevertheless the coefficient of variance of both tests, standard and reference, are still below 5 %, which is generally an acceptable value for composite materials. The Young's modulus of (6.63 ± 0.23) GPa is slightly higher than the reference test result. But it has to be mentioned again that the strain of the reference specimens is measured only on one side of the specimen surface and not on both like for the standard specimens where the strain signals are averaged. This might be the reason why the curves of the reference tests are somewhat non-linear in the strain region between 0.1 % and 0.3 %, where the Young's Modulus is determined.

An obvious difference in the failure strain between the two tests was found (Figure 5-5). The reason for this difference might be the limited measurement range of the strain gauges, because the maximum strain at room temperature that can be measured is approximately 5 %. Above this value the strain gauge does not work anymore because it is already broken. All ASTM-specimens show a fracture plane of approximately 52 ° ± 2 ° (Figure 5-6), while they exhibit a percent bending of around ±10 %. The ASTM D6641 standard defines a test as valid when the percent bending value lies in between this range. In conclusion, it can be stated that in comparison with the standard tests the end-loaded specimen test results are a reliable basis for a further analysis of the strain-rate dependency of the material properties.

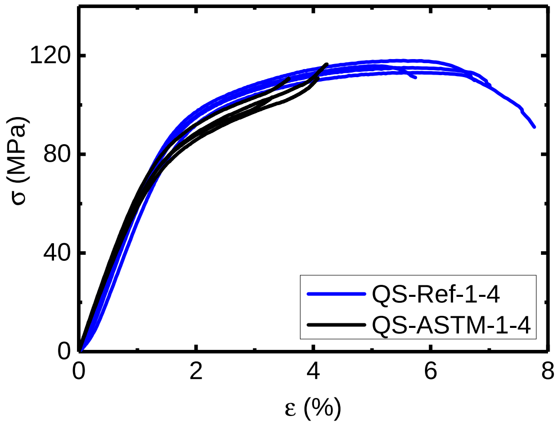

Fig. 5-5 Comparison of the quasi-static longitudinal compressive stress-strain curves from reference and ASTM tests.

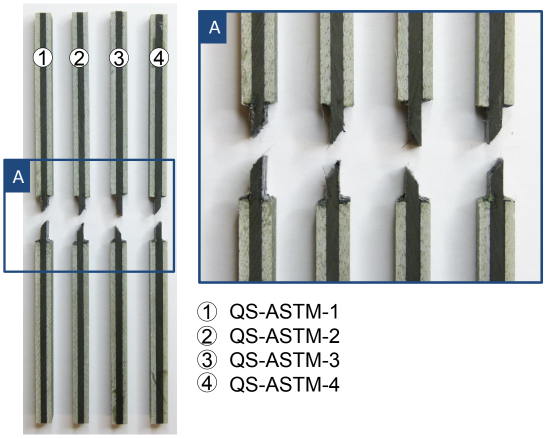

Fig. 5-6 Quasi-static specimen failure mode of ASTM tests.

5.1.5 Results of Dynamic Experimental Tests

Results of Intermediate Strain Rate Tests

In the intermediate strain rate regime four specimens were tested in compression transverse to the fiber direction. The specimens were loaded until ultimate failure of the material. The stress-strain responses are documented in a diagram (Figure 5-7), where the maximum stress is denoted as the material strength (Table 5-5).

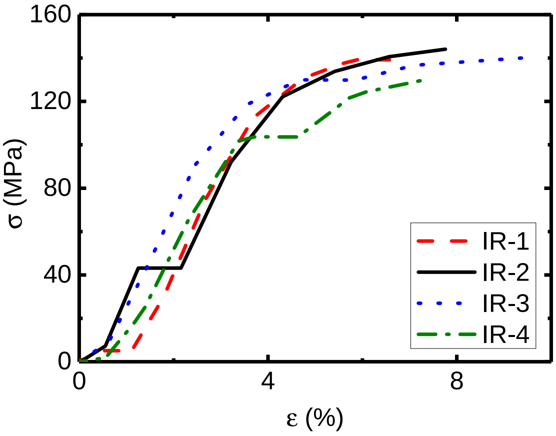

Fig. 5-7 Transverse compressive stress-strain curves from intermediate strain rate tests.

A mean transverse compressive strength of (138.33 ± 5.91) MPa with a coefficient of variance of 4.27 % was determined. At this point it must be noted, that these measured material parameter is afflicted with some measurement errors. Therefore the mechanical material behavior must be analyzed very carefully. Comparable to the compressive intermediate strain rate tests of the neat polyamide-6 (subsection 4.2.5) the standard setting of the integration time of the electro-mechanical testing machine of 20 ms for recording the load is too long. So each 20 ms a load value is generated that represents the average load value of the last 20 ms. This might also be the reason why there are some kind of constant stress plateaus in the curves. Thus, no Young's modulus was computed.

Therefore the recorded force data is somewhat inaccurate. The load-time response would have been more accurate by using a shorter integration time. Nevertheless, due to a pronounced plastic material behavior the maximum strength of the material can be treated as valid. Even the experiments are not as accurate for several reasons, the measured stress-strain curves represent to some extent the real composite material behavior at intermediate strain rate.

Tab. 5-5 Intermediate rate transverse compression test results.

Test	**Strength** $Y_{\mathrm{C}}^{\mathrm{ir}}$ (MPa)	**Failure Strain** $\epsilon_{\mathrm{C}}^{\mathrm{u}}$ (%)
IR-1	139.21	6.58
IR-2	144.06	7.76
IR-3	140.00	9.37
IR-4	130.06	7.34
Mean	138.33	7.76
STDV	5.91	1.18
CV (%)	4.27	15.19

Results of High-Strain-Rate Tests

The dynamic stress response was computed by using the classic SHPB Analysis presented in subsection 3.1.4. In the following the specimen stress was calculated via the "1-wave-analysis" (Equation 3-44). Similarly to the dynamic compression tests of neat polyamide-6 the strain rate $\dot{\epsilon}$ was derived as the time derivative of the optical measured strain via DIC. In Figure 5-8 graphs of the filtered incident- and transmission-bar signals for the HR1, HR2, and HR3 measurement are shown. Again, a Savitzky-Golay filter was applied to eliminate the digitalization noise from the oscilloscope. A change of the overall signal shape was not found after filtering. For the HR1 setup a pulse shaper was used which generates a trapezoidal shaped incident wave. Another pulse shaper with different thickness and diameter was used for the HR2 and HR3 incident pulse (Table 5-1). The trapezoidal shape of the HR3 incident wave and the reflected wave respectively shows a local peak at the end of the wave. This was observed for all three tested specimens. In this strain rate regimen (around $2253\,\mathrm{s}^{-1}$) the velocity of the striker-bar is very high. The experiments are performed at the loading capacities of the total setup. Due to the large bar diameter and high velocity of the striker-bar dispersion effects of the wave may occur. Apart from this, the transmitted wave shows no peculiarities.

The equilibrium condition in the specimen is checked with the 1-wave and 2-wave stress-time signals (Equation 3-44 and 3-45). Figure 5-9 shows the plotted diagrams for the HR1, HR2, and HR3 tests. In each diagram the strain rate-time signals from the classic SHPB Analysis and the strain-rate time signal via DIC are included. For all HR1 specimens the comparison of the 1- and 2-wave stresses does fulfill the dynamic equilibrium condition. The initial offset of the stresses is due to the nonzero bar strain at the beginning of the reflected signal. Taking this into account, the

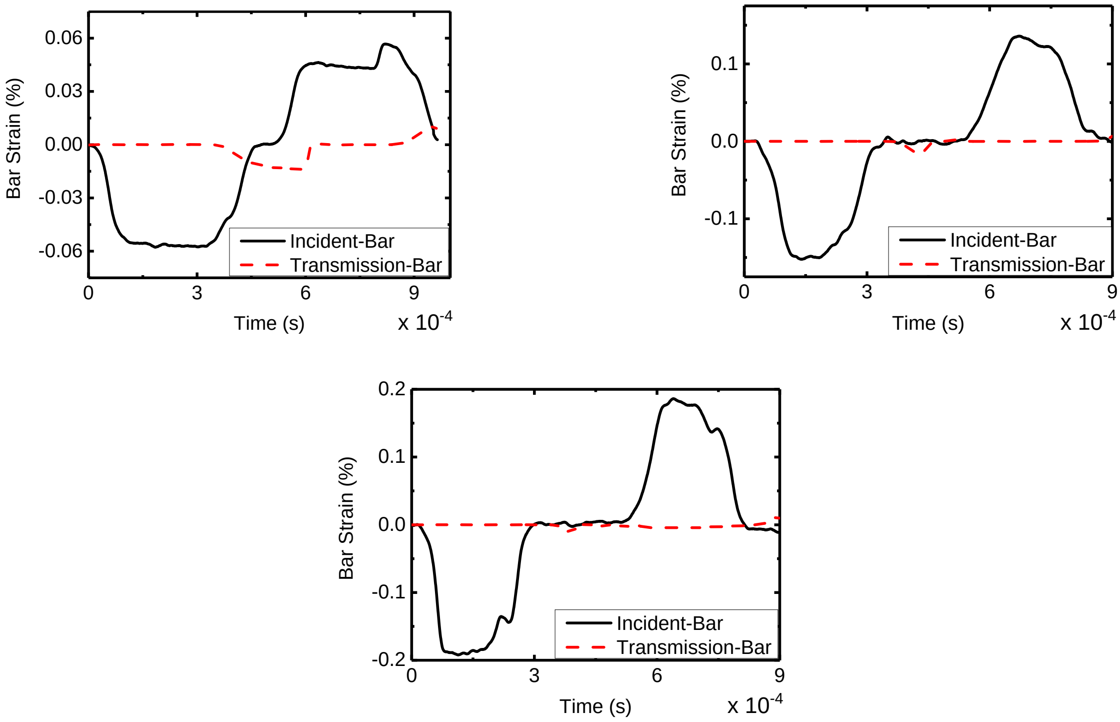

Fig. 5-8 Bar strain wave groups from HR1 (top left), HR2 (top right), and HR3 (bottom) tests with trapezoidal shaped incident waves for a representative specimen, respectively.

stress-time responses are similar and dynamic equilibrium during the experiment can be presumed.

In contrast to the HR1 experiments, the comparison of the 1- and 2-wave stresses for the HR2 tests no longer fulfill the requirements for the dynamic equilibrium condition. Although no dispersion effects were observed in the initial bars together test without specimen the stress signals drift apart. Thus it is assumed that reflections of the elastic wave within the specimen length can cause interference of the pulse. The interfaces between the specimen load surfaces and the bar ends might be influenced by friction. Thus the mechanical impedance of the interfaces changes. The experiments at HR3 show a magnification of the dispersion effects [16] and the 1- and 2-wave signals deviate from each other (Figure 5-9). The shape of the elastic pulse might be disturbed by dispersion effects which occur during the time period in which the reflected and transmitted signal are detected at the strain gauges on the bars. Thus the specimen may underlie different stress levels and therefore no dynamic equilibrium appears [16]. Due to this reason the stress-time response calculated with the SHPB Analysis must be treated with care. As already mentioned in subsection 4.2.5 of the dynamic compression tests of polyamide-6 the dispersion effects on the transmitted signal are presumable small because of a small travel distance of the wave in the transmission-bar. Thus the calculation of the

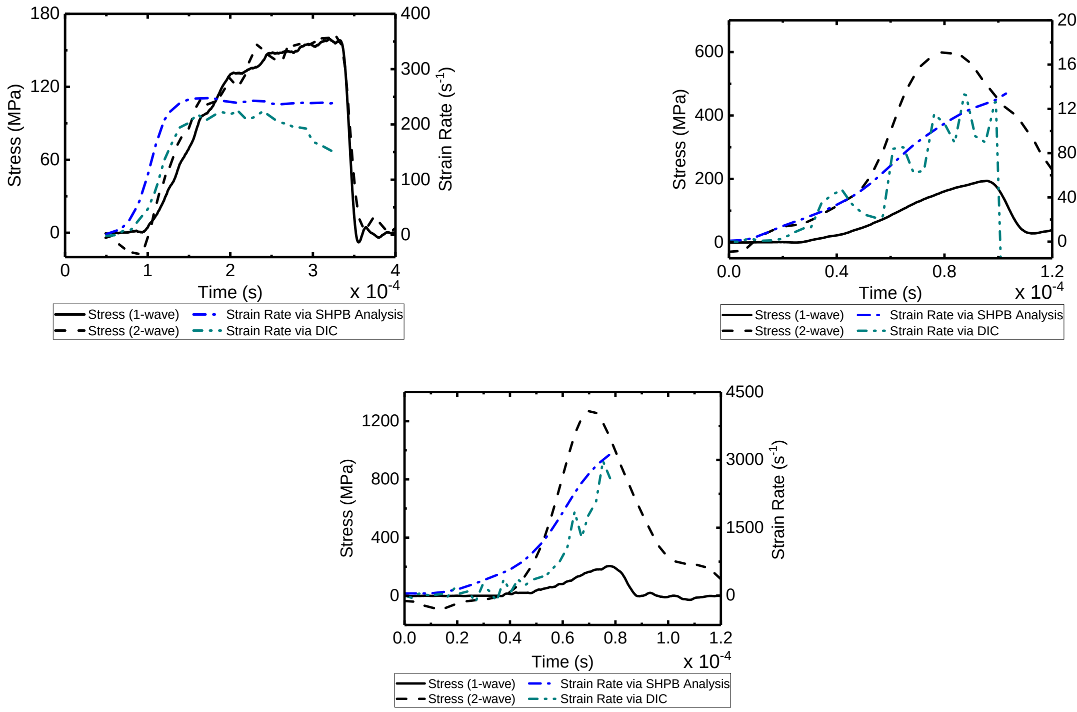

Fig. 5-9 Dynamic stress equilibrium check and corresponding strain rate for a representative specimen tested at HR1 (top left), HR2 (top right), and HR3 (bottom).

specimen stress by using the transmission wave strain signal (Equation 3-44) is assumed to describe the real stress-state of the tested specimen more closely. Even if the transmission signal is not dispersion free, the effect on the measured axial stress-strain response might be only minor [16]. Therefore the 1-wave stress signal was used for the determination of the stress-strain curves for all dynamic specimens.

Besides the stress signals, the strain rate-time responses of the dynamic experiments for each strain rate are shown in the graphs of Figure 5-9. The strain rates were computed once with the SHPB Analysis and once with DIC. The HR1 tests indicate a constant strain rate right after beginning of the experiment. For the strain rate-time curve via DIC of the HR2 tests a noisier signal was found. A constant strain rate is here reached after half of the experiment. The HR3 results show a similar picture. A constant strain rate is hardly found at the end of the experiment.

In addition, the in-plane axial specimen strain field measured via DIC on the specimen surface was determined to demonstrate the existence of dynamic equilibrium during testing for the HR2 and HR3 experiments. The same representative specimens, the results shown in Figure 5-9, were used to demonstrate the time dependent evolution of the centrally measured axial strain along the specimen length. In Figure 5-10 the multi-stage-section graphs for HR2 and HR3 are shown, respectively.

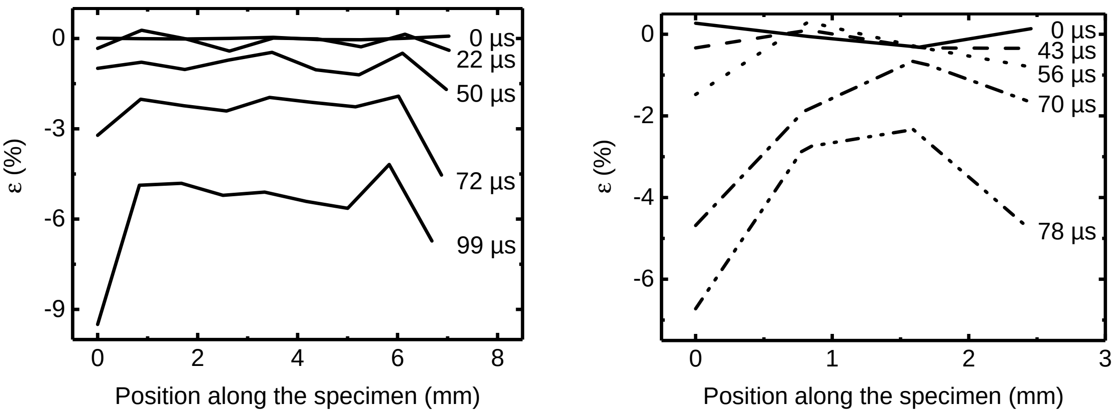

Fig. 5-10 Uniform development of specimen strain along axial direction for a representative specimen tested at HR2 (left) and HR3 (right).

Thereby, the curve with the highest strain level indicates the moment of specimen failure. In the left diagram of Figure 5-10 the characteristic distribution of the axial strain along the specimen length with time is presented. The higher strain levels between position 0 mm to 1 mm and 5.5 mm to 7 mm are caused by the molybdenum disulfide lubricant which is squeezed between the specimen loading surface and the bar ends and interferes with the black-on-white speckle pattern. The same happened to the specimen measured at HR3. Due to the small specimen geometry and low resolution of the high-speed camera only four strain data point along the specimen length are possible for the evaluation. In general, a continuous growth of the strain level with time was observed for the HR2 experiments. Due to these results it is concluded that the specimens were not subjected to different stresses over their lengths but rather in an equilibrium state at both strain rate regimes.

The results of the HR3 show in the first 56 µs nearly no difference in the strain level but an increase with further duration of the experiment. Due to the interference of the lubricant with the speckle pattern and especially the low camera resolution no reliable statement concerning the equilibrium state can be made. The test setup for these high-strain-rate tests must be improved to get better experimental material data.

In Figure 5-11 the transverse compressive stress-strain response for all tested specimens at HR1 is shown. The curves describe the specimen behavior under loading until failure of the material. The transverse compressive strength $Y_{\mathrm{C}}^{\mathrm{hr}}$, the ultimate failure strain $\epsilon_{\mathrm{C}}^{\mathrm{u}}$, and the Young's modulus E were computed and the results listed in Table 5-6. A mean transverse compressive strength of (162.03 ± 5.57) MPa with a coefficient of variance of 3.44 % was measured for the carbon-fiber-reinforced polyamide-6. The obtained mean value of the Young's modulus, evaluated between 0.4 % and 0.6 % strain, is (7.65 ± 0.66) GPa. In addition, a decrease of the non-linearity of the stress-strain curve at high strain rates was measured. A similar stiffness behavior from low to high strain rates for a composite material was already shown in the work of Koerber et al. [14].

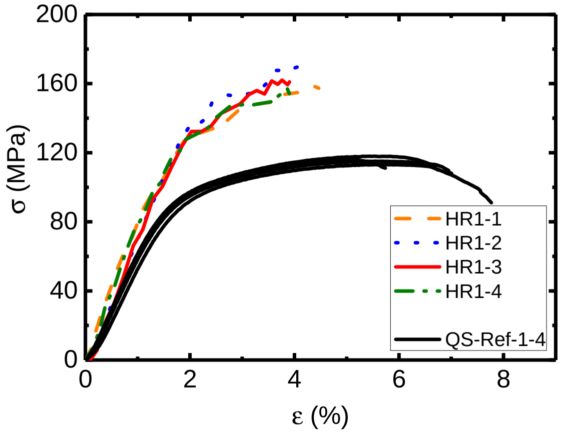

Fig. 5-11 Dynamic (HR1) transverse compressive stress-strain response of all tested specimens.

Tab. 5-6 Dynamic (HR1) transverse compression test results.

Test	**Strain Rate**		**Modulus**	**Strength**	**Failure Strain**
	elastic* (s^{-1})	failure** (s^{-1})	E (GPa)	Y_C^{hr} (MPa)	ϵ_C^u (%)
HR1-1	168.39	199.55	8.42	159.16	4.32
HR1-2	133.68	147.33	6.86	169.82	4.07
HR1-3	162.22	187.00	7.46	162.04	3.76
HR1-4	139.05	166.40	7.86	157.11	3.87
Mean	150.84	175.07	7.65	162.03	4.01
STDV	17.04	22.99	0.66	5.57	0.25
CV (%)	11.30	13.13	8.60	3.44	6.13

* averaged between 0.4 % and 0.6 % strain
** averaged between 0.6 % and failure strain

The dynamic response of the HR2 specimens under loading in transverse fiber direction is shown in Figure 5-12. The curves describe the specimen stress-strain behavior until failure of the composite material. The measured material parameter Y_C^{hr}, ϵ_C^u, and the Young's modulus are listed in Table 5-7. At this strain rate a transverse compressive strength of (183.38 ± 6.85) MPa with a coefficient of variance of 3.73 % was determined. The Young's modulus (5.61 ± 0.90) GPa was computed between 0.4 % and 0.6 % strain. The value of the elastic modulus must be treated with care, because it is influenced by inertia-effects as it can be seen at the beginning of the experiment where the curve has a non-linear behavior.

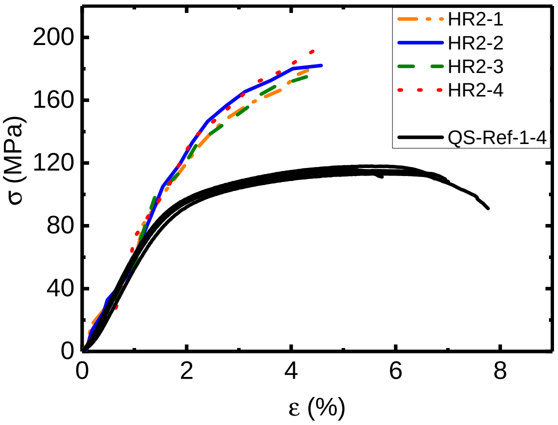

Fig. 5-12 Dynamic (HR2) transverse compressive stress-strain response of all tested specimens.

Tab. 5-7 Dynamic (HR2) transverse compression test results.

Test	**Strain Rate**		**Modulus***	**Strength**	**Failure Strain**
	elastic** (s^{-1})	failure*** (s^{-1})	E (GPa)	$Y_{\mathrm{C}}^{\mathrm{hr}}$ (MPa)	$\epsilon_{\mathrm{C}}^{\mathrm{u}}$ (%)
HR2-1	664.14	893.26	5.00	179.07	4.32
HR2-2	239.80	1080.48	5.40	182.06	4.57
HR2-3	445.22	928.19	5.11	193.42	4.55
HR2-4	202.38	843.61	6.93	178.98	4.49
Mean	387.89	936.38	5.61	183.38	4.48
STDV	212.87	102.14	0.90	6.85	0.12
CV (%)	54.88	10.91	15.98	3.73	2.57

* Influence of inertia-effects on Young's Modulus might be present.
** averaged between 0.4 % and 0.6 % strain
*** averaged between 0.6 % and failure strain

Comparable to the stress-strain behavior of the HR1 specimens the HR2 specimens also exhibit a lower ultimate failure strain than the quasi-static experiments. Due to a shorter specimen length a bending is less likely to occur. After reaching the maximum stress the material fails and does not bend. In Figure 5-13 the stress-strain response of the three tested specimens at HR3 ($2252.71\mathrm{s}^{-1}$) are compared with the quasi-static results under transverse compression loading. The end of the curves indicate the failure of the specimen. The computed material parameters are shown in Table 5-8.

A further increase of the transverse compressive strength to (197.56 ± 11.37) MPa with a coefficient of variance of 5.76 % was found. The Young's modulus was not calculated because the stress-strain curve in the beginning of the experiment is

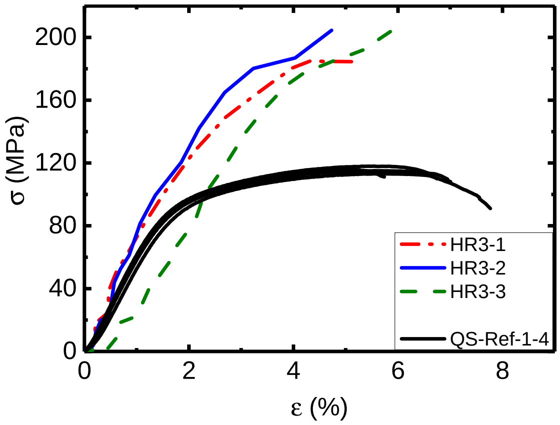

Fig. 5-13 Dynamic (HR3) transverse compressive stress-strain response of all tested specimens.

Tab. 5-8 Dynamic (HR3) transverse compression test results.

Test	**Strength** $Y_{\mathrm{C}}^{\mathrm{hr}}$ (MPa)	**Failure Strain** $\epsilon_{\mathrm{C}}^{\mathrm{u}}$ (%)	**Strain Rate** (s^{-1})
HR3-1	184.43	5.28	2259.86
HR3-2	204.48	4.73	2354.96
HR3-3	203.75	5.85	2143.30
Mean	197.56	5.29	2252.71
STDV	11.37	0.56	106.01
CV (%)	5.76	10.63	4.71

strongly influenced by inertia-effects. The HR3 specimens show a lower elongation at break compared to the quasi-static specimens. For the curve of specimen number 3, no difference in the experimental setup and during the measurement was found, compared to the other HR3 specimens.

In Figure 5-14 sequences of the deformation behavior of the specimen with superimposed axial strain fields for representative HR3, HR2, HR1, and quasi-static transverse compression tests are shown. The position of the respective strain state is marked in the corresponding stress-strain curve in the left diagram.

The first series of high-speed camera images in Figure 5-14 a)-d) show the strain field distribution at HR3. The used camera type only allows to adjust the setup parameters of the frame rate and the image resolution dependently. Thus a suitable configuration and compromise had to be found for each specimen geometry and dynamic strain rate experiment. Thus, only a coarse facet field can be calculated for the HR3 specimens. Therefore the strain field distribution is not sufficient large to be analyzed. A homogeneous deformation behavior until failure can be observed

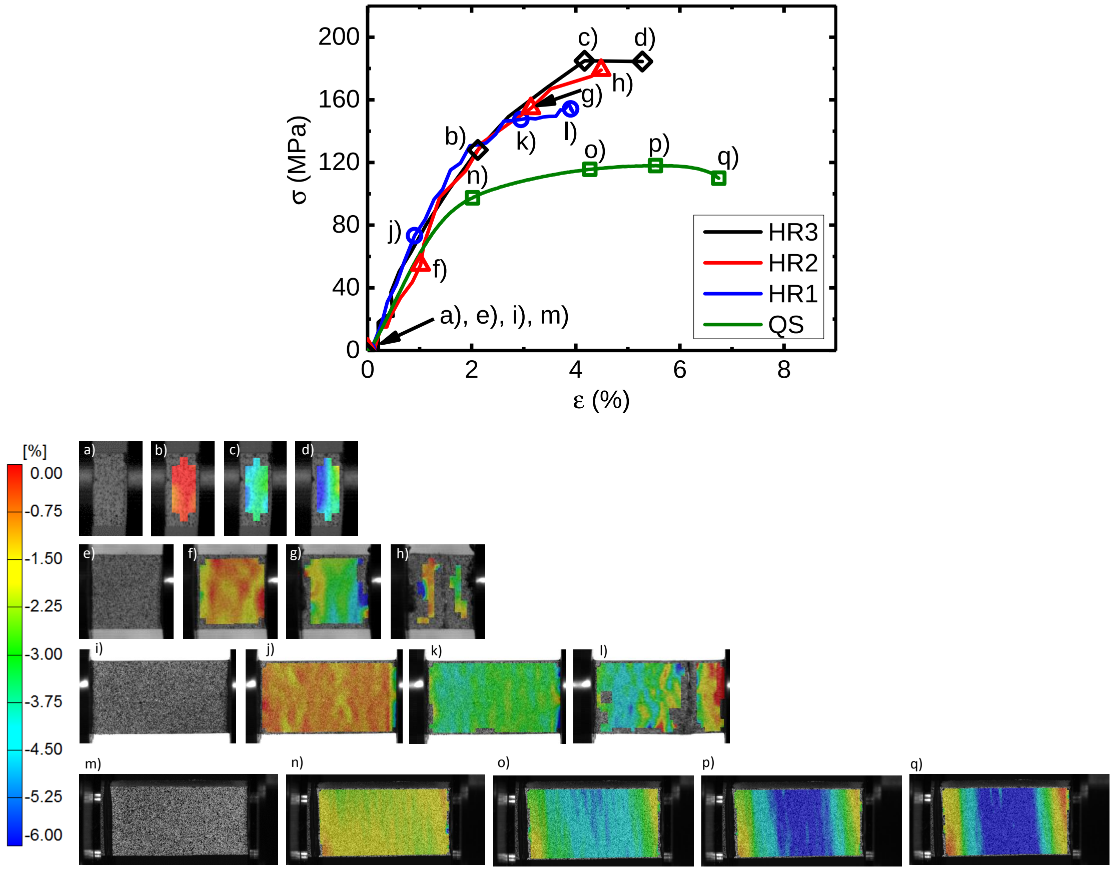

Fig. 5-14 In-plane strain fields in loading direction of transverse compression specimens at HR3 a)-d), HR2 e)-h), HR1 i)-l), and quasi-static loading m)-q).

for the representative HR2 transverse compression specimen in Figure 5-14 e)-h). Here it has to be mentioned that the inhomogeneous strain field near the loading surfaces on the left and right hand side of the specimen does not represent the material behavior. At this load level the molybdenum disulfide lubricant splashed out between the specimen and the bar end-surface. Thus the black-on-white speckle pattern is covered and the DIC computes an incorrect strain distribution in this region. Nevertheless the strain field in the middle of the specimen surface can be analyzed correctly. The Figure 5-14 h) shows the failure mode of the transverse compression specimen with an angle of approximately 50 ° ± 2 in thickness direction in the middle of the surface. The same failure behavior was observed for the HR1 specimens. The strain field in 5-14 i)-l) shows a homogeneous distribution until ultimate failure of the composite material. All dynamically measured specimens failed in the middle of the gauge section and did not show any failure at the loading surfaces. The sequence in Figure 5-14 m)-q) shows the images of the left camera of the used ARAMIS system in 3D configuration. From the beginning of the experiment a homogeneous strain field distribution was found. Right before the stress plateau is reached a slight localization of the strain field, indicated in dark blue, in the middle of the specimen is visible via DIC (Figure 5-14 o)). No failure can be seen on the specimen surface at the maximum stress state (Figure 5-14 p)). After reaching the stress plateau a further increase of the area with higher strain occurs and finally causes the ultimate failure of the material with an angle of 57° to the action plane of the transverse compressive stress. The quasi-static experiment is therefore valid until the maximum stress.

The comparison of the transverse compressive stress-strain curves of the carbon-fiber-reinforced polyamide-6 composite, loaded at quasi-static, intermediate, and three high strain rates (Figure 5-15), indicates a significant increase of the transverse compressive strength.

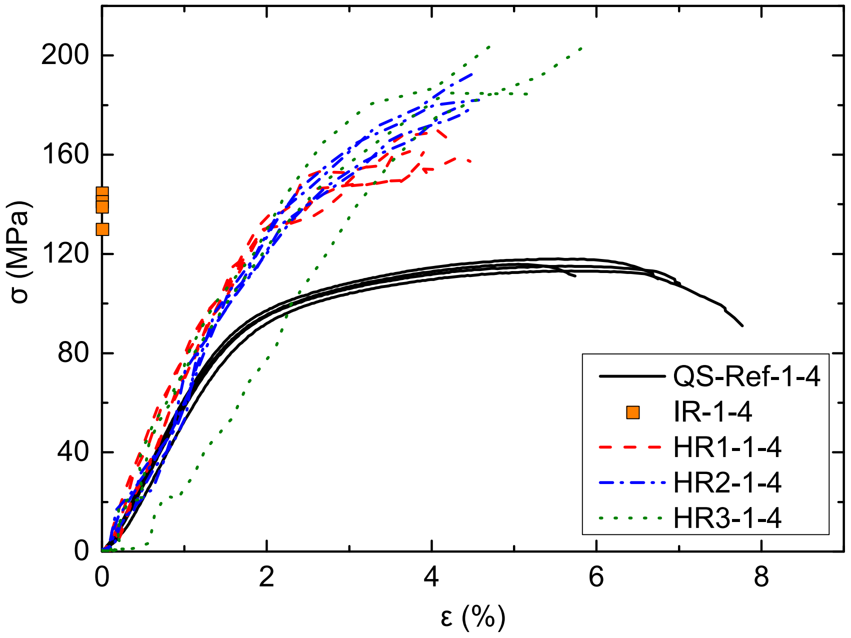

Fig. 5-15 Comparison of the quasi-static transverse compression stress-strain curves from reference and dynamic tests.

The strength value increases of 20 % (IR), 40 % (HR1), 59 % (HR2), and 71 % (HR3) from quasi-static to approximately $0.6\,s^{-1}$ (IR), $175.07\,s^{-1}$ (HR1), $936.38\,s^{-1}$ (HR2), and $2252.71\,s^{-1}$ (HR3), respectively. A comparison of the Young's modulus should be handled with care because the influence of inertia effects at the beginning of the high-rate tests is very crucial for the interpretation of the data. In this high strain rate regime the experimental setup reaches it's limits. Therefore a substantive conclusion concerning the Young's modulus can not be drawn.

5.2 Transverse Tension

5.2.1 Material and Test Specimens

The specimens were manufactured of the same material (Celstran® CFR-TP PA6 CF60-01) used for the transverse compression specimens (section 5.1.1). As already mentioned this unidirectional carbon-fiber-reinforced polyamide-6 tape has a fiber volume content of 48 % according to the material data sheet [115]. The laminates of this material used in the present study for measuring the transverse tensile properties had a fiber volume content of 49 % determined by the test standard ASTM D3171, Method II, Procedure B (digestion of the matrix by a mixture of sulfuric acid and hydrogen peroxide) [116].

To verify, if there is an influence of the size effect on the quasi-static reference test, a recognized test standard is used to determine the material property. Thus a unidirectional laminate with 14-plies was produced for the specimens which were tested according to the standard DIN EN ISO 527-5 and a unidirectional laminate with 16-plies was manufactured for the quasi-static and the dynamic specimens. Comparable to the plates for the transverse compression specimens the laminates were made of single tape stripes and welded at few points at the edges for a better handling of the stack. The stack of tape plies was pressed in a RUCKS hot press and a compression mold at 260 °C with 0.5 MPa pressure for 15 minutes.

For the investigation of the tensile material response a rectangular tension specimen geometry was used. The nominal dimensions for both quasi-static and dynamic specimens was 60 x 8 x 2 mm^3 (length x width x thickness) (Figure 5-16). The fiber direction is perpendicular to the longitudinal edge of the specimen. All specimens were cut on a water-cooled diamond saw to the final dimensions. In order to test the specimen with the split-Hopkinson tension bar method a fixture for attaching the specimen to the bars has to be used. Thus slotted steel adapters with an M 12 x 1.25 outside thread developed by Koerber et al. [120] were manufactured (Figure 5-16). The specimens were bonded with the adapters by using the structural adhesive Scotch-Weld™ DP 490 from 3M (Figure 5-16). To ensure an accurate alignment of the assembled configuration of the specimen and the adapters, a bonding jig with notches was used. The free specimen length was defined to be 20 mm comparable to the transverse tensile specimen tested by Koerber et al. [120]. For both test configurations (quasi-static and dynamic) the same specimen type was used. Koerber et al. [120] showed in their study, that no size or clamping effects affect the quasi-static nor the dynamic test results.

In order to verify if the quasi-static tests with small specimens in this study provide correct material properties, additional tensile tests according to the standard DIN

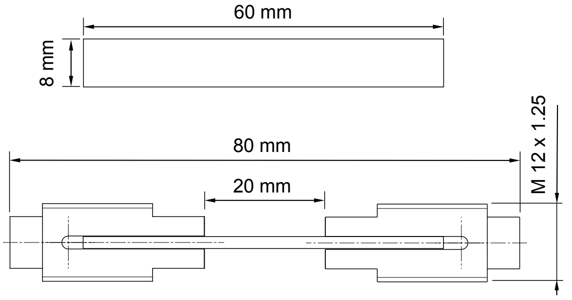

Fig. 5-16 Specimen geometry (nominal thickness 2 mm) for quasi-static and dynamic tests with threaded endcaps.

EN ISO 527-5 were carried out. The nominal dimensions of the specimen geometry for the standard tests were 250 x 25 x 2 mm^3 (length x width x thickness) and a free gauge section of 150 mm. Thus the fiber direction is perpendicular to the longitudinal edge of the specimen. Additionally, glass-epoxy composite tabs were glued to each side on the specimen with the adhesive Scotch-Weld™ DP 490 (3M).

Digital image correlation was used for measuring the strain of all tested specimens. Thus a black-on-white speckle pattern was applied on the surface of each specimen using aerosol spray painting. The random speckles were adjusted in their size for the different image resolutions of the respective cameras (static ARAMIS system and high-speed camera).

Comparable to the compression specimens of polyamide-6 and the transverse compression specimens of fiber-reinforced poylamide-6 all tensile specimens were dried in a drying oven under vacuum at a temperature of 80 °C for 72 hours. This specimen treatment ensures a common ground for the mechanical material characterization, because possible moisture effects, resulting from the hygroscopic behavior of the PA 6 polymer matrix are minimized. Likewise aluminum multi-layer film bags were used to store the dry specimens until start of the experiment. Thus the material is protected from moisture of the environment.

5.2.2 Quasi-Static Experimental Setup

Test Setup for Reference Tests

Quasi-static reference tests were performed using the aforementioned electro-mechanical testing machine (Hegewald & Peschke Inspekt Table 100) with a 100 kN load cell. From eight tested specimens three specimens showed a valid failure mode in the middle of the free gauge section. In general, transverse tensile tests are known to be challenging due to invalid failure directly at the end of the tab towards the free gauge section. This failure is caused by stress concentrations in this regions and is thus a common preliminary failure mode for this test. A constant displacement rate of 0.5 mm/min was defined for testing the tensile specimens with a free gauge length of 20 mm, which corresponds to a quasi-static strain rate of approximately $4 \cdot 10^{-4}\,\mathrm{s}^{-1}$. In Figure 5-17 the quasi-static tensile setup is shown.

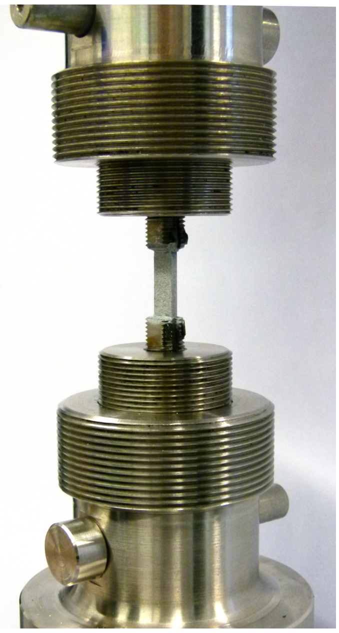

Fig. 5-17 Quasi-static tensile test setup.

The assembled specimen with the bonded adapters was screwed into inserts. The inserts were then attached to the testing machine by a bolt connection. Similar to the previous quasi-static compression tests, the GOM ARAMIS-4M DIC system, with a resolution of 2352 pixels x 1728 pixels and two lenses of the type Titanar 50 mm, were used to measure the quasi-static strain field of the specimen front surface. The stereo camera system and two LED lamps for a uniform illumination were positioned at a distance 225 mm away from the specimen surface. A shutter speed of 80 ms and an acquisition rate of 3 fps was chosen for picture recording. Afterwards the images were post processed with the ARAMIS software and a setting of 17 pixels x 17 pixels as facet size and of 15 pixels x 15 pixels as facet step. Just as for the compression tests, the computation size for deriving the strain field was set to 3 x 3 facets^2. The transverse tensile strain was determined by using the mean value of a 15 x 6 mm^2 strain field at the center of the specimen surface. Furthermore, the transverse tensile strength is calculated as the ratio of the failure load and the specimen cross-sectional area.

Test Setup According to DIN EN ISO 527-5

Quasi-static tests according to the standard DIN EN ISO 527-5 were carried out to verify if the used specimen geometry (60 x 8 x 2 mm^3) with the steel adapter yields correct values for the transverse strength at low strain rate. The standard tests were performed on the same electro-mechanical testing machine with a 100 kN load cell at a constant displacement rate of 1 mm/min. To introduce the load, wedge grips were used to fix the specimen in the testing machine. The specimen strain was obtained by DIC. Due to the larger specimen size the GOM ARAMIS-4M DIC system (resolution and lens type unchanged) and the LED lamps were positioned in a distance 360 mm away from the specimen surface. The shutter speed was set to 36 ms and the acquisition rate to 4 fps. The settings (facet size, facet step, computation size) of the ARAMIS software for post-processing of the images were the same used for the quasi-static tensile reference tests. For calculating the specimen strain the mean value of a 25 x 80 mm^2 strain field at the center of the specimen surface was chosen. The tensile strength was derived by the ratio of the failure load and the specimen cross-section.

5.2.3 Dynamic Experimental Setup

Four dynamic tests at a strain rate of 52 s^{-1} were performed by using a split-Hopkinson tension bar setup (Figure 3-10) consisting of a titanium U-shaped striker-bar and titanium loading-, incident-, and transmission-bars with lengths of 2.5 m, 3 m, and 1.8 m, respectively. The bar diameter was chosen to be 20 mm for the loading-bar and 16 mm for the incident- and transmission-bar. A striker-bar length of 0.5 m is useful for generating a sufficient long pulse for loading the specimen. The tensile specimen was screwed into the incident- and transmission-bar end as shown in Figure 5-18. In addition, a 2 mm thick silicon rubber ring was wrapped around the impact flange at the end of the loading bar. The silicon rubber is used as pulse shaper for the incident pulse. For the detection of the elastic wave, strain gauges are mounted on the incident-bar at 1.6 m and on the transmission-bar at 0.2 m away from the bar ends into which the tensile specimen is screwed. The strain gauges operate with a supply voltage of 7 V. Comparable to the dynamic compression test with the SHPB setup, a high-speed transducer amplifier (FYLDE FE-H379-TA) with a gain setting of 100 and a frequency of 300 kHz was used. The impact velocity of the striker-bar of 4.29 m/s and the amplified signals of the elastic waves were each recorded with a TEKTRONIX TDS2004C oscilloscope. As a result of the nominal specimen length of 20 mm and the striker-bar velocity a strain rate of about 52 s^{-1} was reached.

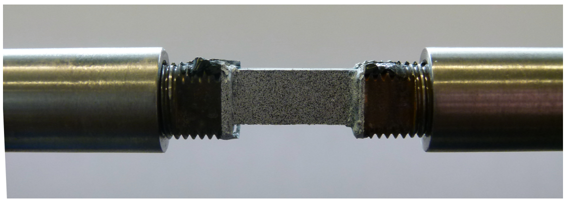

Fig. 5-18 Dynamic transverse tension specimen in an SHTB setup.

The configuration of the SHTB setup was verified by a bars together test. The incident-bar and the transmission-bar were directly connected via a threaded steel cylinder. The striker hits the pulse shaper on the flange with a velocity of 4.96 m/s. In Figure 5-19 the incident-bar strain signal and the transmission-bar strain signal are plotted. It was found, that the elastic wave travels from the incident-bar into the transmission-bar without changing the amplitude, duration, and shape. The difference of about 2.2 % in the strain amplitude is very low and thus negligible. Because of the similarity of the two waves a correct specimen stress-time response can be expected.

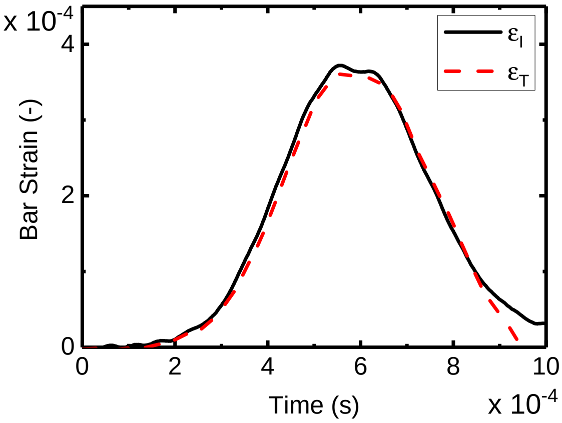

Fig. 5-19 Incident- and transmission-bar strain signals of the bars-together test with the used SHPB configuration.

Comparable to the dynamic compression tests a high-speed camera (Photron SA5) with a ZEISS lens (Makro-Planar T* 2/100 mm ZF) was used. An acquisition rate of 124000 fps was chosen which results in a resolution of 320 pixels x 152 pixels. The lens aperture was set between f/2.8 and f/4. To provide a uniform illumination of the specimen surface two spotlights (DEDOLIGHT 400D) were positioned in front of the specimen. The recorded images of the high-speed camera undergo a post process with the already mentioned digital image correlation software GOM ARAMIS-4M. A facet size of 10 pixels x 10 pixels and a facet step of 8 pixels x 8 pixels was chosen for the computation. The computation size for deriving the strain field was set to

3 x 3 facets^2. Finally the mean value of a strain field (12 x 6 mm^2) at the center of the specimen surface was calculated.

5.2.4 Results of Quasi-Static Experimental Tests

Results of Reference Tests

In Figure 5-20 the transverse tensile stress-strain response of the quasi-static reference specimens is shown. Only for three out of eight specimens valid failure in the free length of the specimen was found (Figure 5-21). In general transverse tensile tests are prone to premature failure directly at the transition region of the bonded tabs to the free specimen length. The curves in Figure 5-20 correspond to the valid specimen results. The end point of the curves indicate the failure load of the specimen. The quasi-static transverse strength $Y_{\mathrm{T}}^{\mathrm{qs}}$ is determined at this point and in addition the ultimate failure strain $\epsilon_{\mathrm{T}}^{\mathrm{u}}$ (Table 5-9). From the beginning of the measurement a homogeneous strain field distribution was identified.

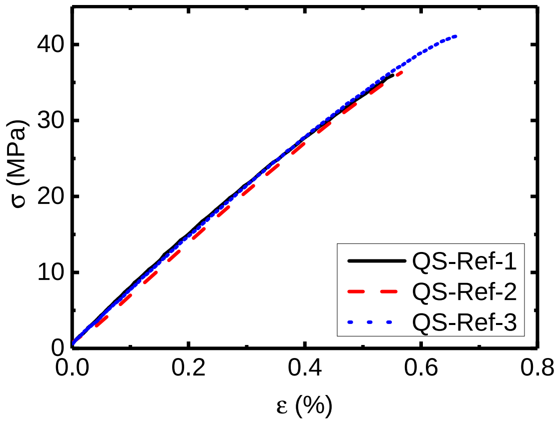

Fig. 5-20 Quasi-static transverse tension stress-strain curves from reference tests.

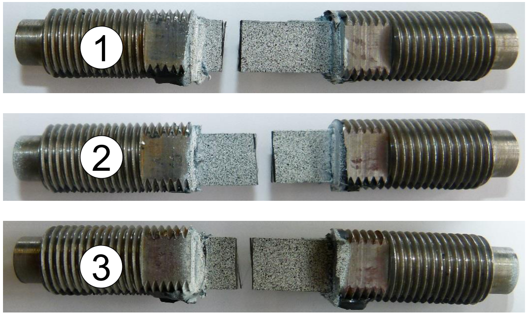

Fig. 5-21 Quasi-static specimen failure mode of reference tests.

In Table 5-9 the results of the reference tests are listed. A mean value of (37.85 ± 2.97) MPa for the transverse tensile strength was measured with a relative high coefficient of variance with 7.84 %. Due to the few valid experiments the statistics is were low for this material parameter. The Young's modulus in the strain region between 0.05 % and 0.25 % was computed to be (7.00 ± 0.04) GPa.

Tab. 5-9 Quasi-static transverse tension reference test results.

Test	**Strength** Y_T^{qs} (MPa)	**Failure Strain** ϵ_T^u (%)	**Modulus** E (GPa)
QS-Ref-1	35.95	0.55	7.05
QS-Ref-2	36.33	0.57	6.97
QS-Ref-3	41.27	0.67	6.98
Mean	37.85	0.60	7.00
STDV	2.97	0.06	0.04
CV (%)	7.84	10.87	0.62

Results of DIN-Tests

Four specimen were tested under quasi-static strain rate according to the test standard DIN EN ISO 527-5. These experiments are compared with the quasi-static reference tests to verify if the specimen geometry influences the measured material properties. Figure 5-22 shows the stress-strain response of all tested carbon-fiber-reinforced polyamide-6 specimen in transverse fiber direction.

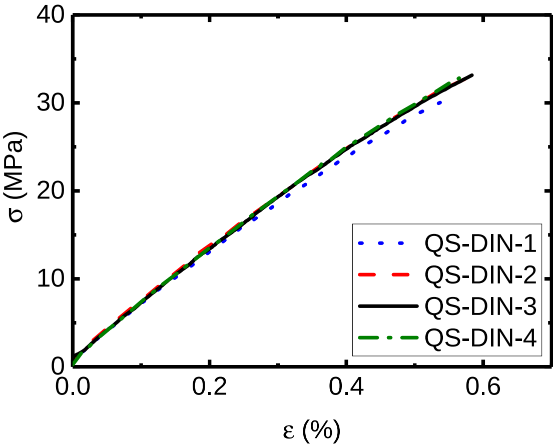

Fig. 5-22 Quasi-static transverse tension stress-strain curves from static DIN tests.

The failure load defines the quasi-static transverse tensile strength Y_T^{qs} and the ultimate failure strain ϵ_T^u. These material properties and the calculated Young's modulus are listed in Table 5-10. The measured transverse tensile strength of (32.55 ± 1.49) MPa is lower than the transverse strength measured at the reference specimens. On the other hand the coefficient of variance for the strength property is lower with 4.58 %. Besides a smaller Young's modulus was found for the DIN-specimens with (6.08 ± 0.09) GPa. The DIN-specimens show a fracture plane in the free gauge length (Figure 5-23).

Tab. 5-10 Quasi-static transverse tension DIN-test results.

Test	**Strength** Y_T^{qs} (MPa)	**Failure Strain** ϵ_T^u (%)	**Modulus** E (GPa)	**Poisson's Ratio** (-)
QS-DIN-1	30.33	0.54	5.94	0.018
QS-DIN-2	33.49	0.59	6.14	0.022
QS-DIN-3	33.31	0.58	6.09	0.018
QS-DIN-4	33.07	0.57	6.14	0.018
Mean	32.55	0.57	6.08	0.019
STDV	1.49	0.02	0.09	0.002
CV (%)	4.58	4.27	1.50	9.40

In conclusion, it can be stated that an obvious difference in the strength and elastic modulus between the two tests was found (Figure 5-24). A difference of approximately 16.3 % was measured between the transverse tensile strength values. It has to be noted, that the small specimens and the large standard specimens were taken from different laminates. The size effect might also play a role in this case, because larger specimen dimension lead to lower strength values compared to small specimen sizes.

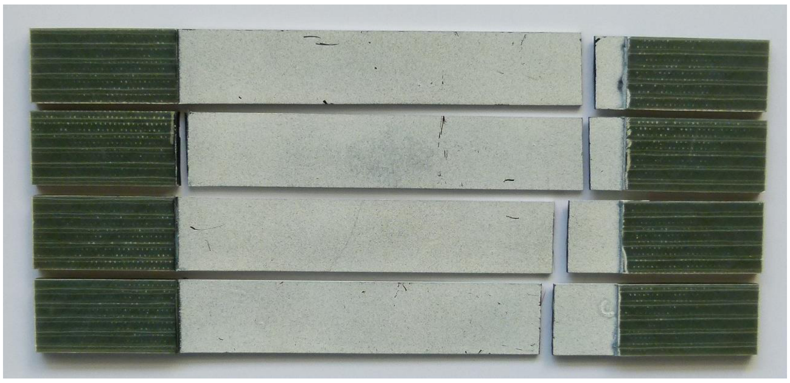

Fig. 5-23 Quasi-static specimen failure mode of DIN tests.

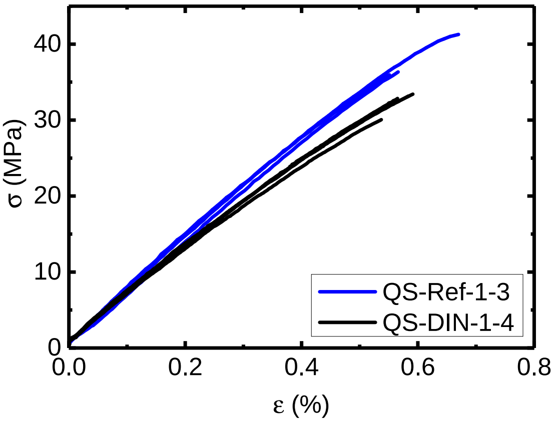

Fig. 5-24 Comparison of the quasi-static longitudinal tension stress-strain curves from reference and DIN tests.

5.2.5 Results of Dynamic Experimental Tests

By using the SHPB Analysis (3.1.4) the dynamic stress response of the carbon-fiber-reinforced polyamide-6 composite material is derived. The results shown in the following were computed via the "1-wave-analysis" (Equation 3-44). The strain rate $\dot{\epsilon}$ was calculated as the time derivative of the strain-time curve measured optically via DIC, comparable to the compression tests. Figure 5-25 shows the filtered incident- and transmission-bar signals of a representative specimen at high strain rate. By means of a Savitzky-Golay filter the digitalization noise caused by the oscilloscope was reduced to a minimum. The overall shape of the bar signals was not influenced by the filtering. The silicon rubber pulse shaper induced a triangular elastic wave as it was expected. The incident-bar signal does not go back to zero strain as it can be seen in the diagram (Figure 5-25). A superposition of the incident- and reflected wave thus occurs and the reflected signal does not start at 0 % strain.

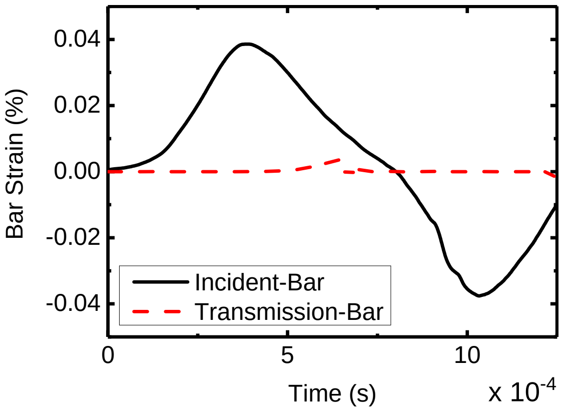

Fig. 5-25 Bar strain wave groups from dynamic tests with triangular shaped incident waves for a representative specimen.

Due to the offset of the incident-bar strain signal discussed before, it is not possible to show the equilibrium condition in the specimen with the 1-wave and 2-wave stress-time signals (Equation 3-44 and 3-45). The 2-wave signal is calculated via the summation of the incident- and reflected-signal which in turn underlays dispersion effects. Figure 5-26 shows the plotted diagram of the high strain rate test with the disturbed stress curves. The strain rate-time signal from the SHPB Analysis and via DIC are included in the diagram. A constant strain rate is hardly found at the end of the measurement. To improve this the pulse shaper must be modified in such a way that the elastic wave is shaped comparable to the transmission signal.

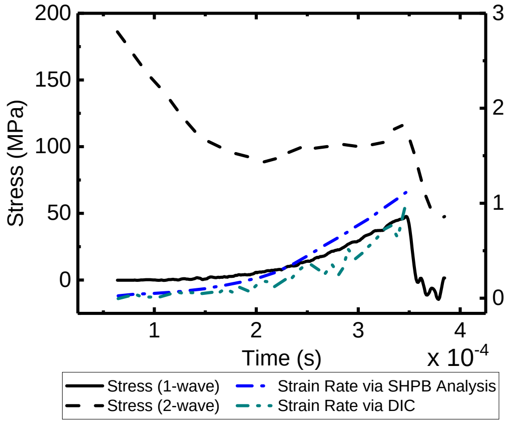

Fig. 5-26 Dynamic stress equilibrium check and corresponding strain rate for a representative specimen.

The in-plane axial strain field of the specimen determined via DIC is taken to demonstrate the existence of the dynamic equilibrium during the measurement. In Figure 5-27 the time dependent evolution of the centrally measured axial strain along the specimen length is shown in a so called multi-stage section diagram. The curve at 0 µs indicates the strain distribution of the unloaded specimen. The noise of the strain along the specimen at the beginning is in the range of ±0.04 %. A slight increase of the strain noise with time can be found. After 282 µs a crack in fiber direction occurs and leads to ultimate failure of the material. The position of failure can be directly indicated by the increase of the strain curve at the position of 14 mm along the specimen (Figure 5-27). Apart from the noise, the strain level increases constantly with time. This is an indicator that the specimen is subjected to a homogeneous stress state over the total specimen length and is thus in dynamic equilibrium.

In Figure 5-28 the transverse tensile stress-strain behavior of the thermoplastic composite material at elevated strain rate is shown. Four out of nine tested specimens showed a valid failure in the free gauge section between the steel adapters (Figure 5-29). The transverse tensile strength $Y_{\mathrm{T}}^{\mathrm{hr}}$, the ultimate failure strain $\epsilon_{\mathrm{T}}^{\mathrm{u}}$, and the

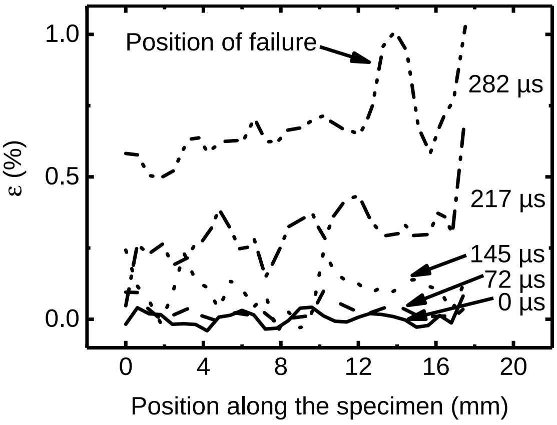

Fig. 5-27 Uniform development of specimen strain along axial direction for a representative specimen.

Young's modulus E were calculated. An overview of the results is listed in Table 5-11. A mean transverse tensile strength of (47.08 ± 5.57) MPa with a coefficient of variance of 11.82 % was found. Similar to the quasi-static result a high variance of the maximum stress is measured at high strain rate. The variance of the Young's modulus of (8.02 ± 0.52) GPa with 6.49 %, however, is lower. The elongation at break of the material seems to increase with high strain rate.

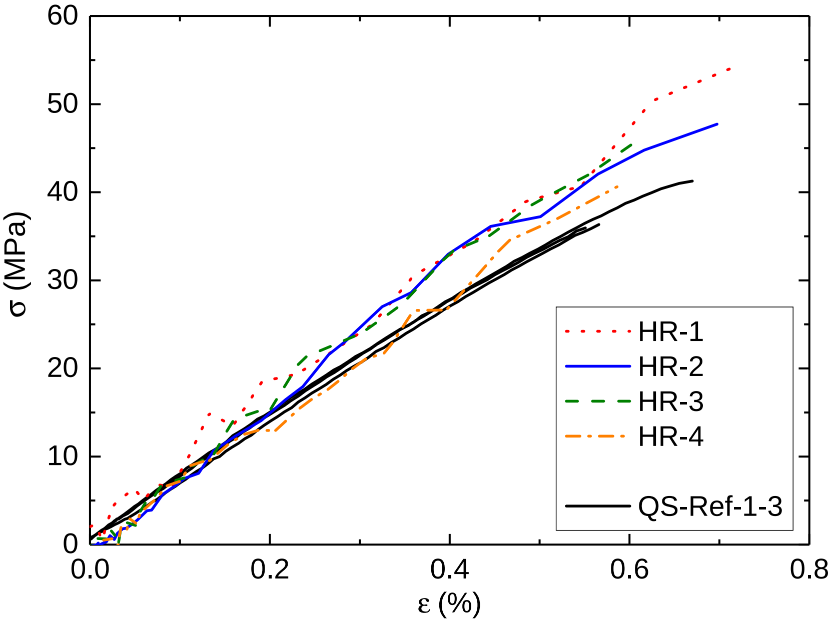

Fig. 5-28 Dynamic transverse tension stress-strain response of all tested specimens.

Figure 5-30 show the deformation sequences of the quasi-static and high strain rate specimen with superimposed axial strain field. The images can be linked to the different positions of the respective strain state in the stress-strain curve in the

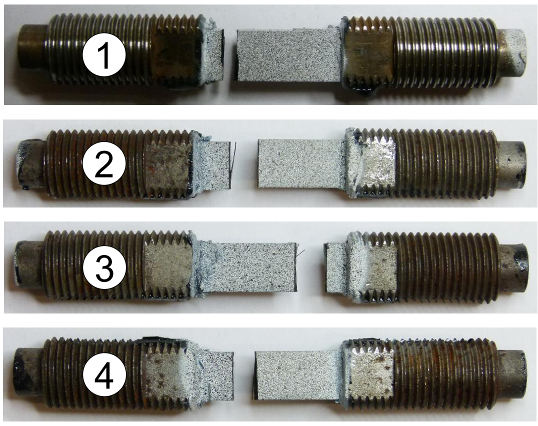

Fig. 5-29 Dynamic specimen failure mode.

Tab. 5-11 Dynamic transverse tension test results.

Test	**Strain Rate**		**Modulus**	**Strength**	**Failure Strain**
	elastic* (s^{-1})	failure** (s^{-1})	E (GPa)	$Y_{\mathrm{C}}^{\mathrm{hr}}$ (MPa)	$\epsilon_{\mathrm{C}}^{\mathrm{u}}$ (%)
HR2-1	27.87	65.59	7.86	54.12	0.71
HR2-2	19.96	49.64	8.48	47.73	0.70
HR2-3	20.46	48.90	8.38	45.84	0.61
HR2-4	19.96	43.38	7.36	40.64	0.59
Mean	22.06	51.88	8.02	47.08	0.65
STDV	3.88	9.56	0.52	5.57	0.06
CV (%)	17.59	18.42	6.49	11.82	9.77

* averaged between 0.05 % and 0.25 % strain
** averaged between 0.16 % and failure strain

beside diagram. The image series in Figure 5-30 a)-c) are recorded with a high-speed camera and the image of the quasi-static experiment Figure 5-30 (d)-f)) are taken from the left camera of the ARAMIS system in stereo configuration. In contrast to the homogeneous strain field distribution of the quasi-static specimen from the beginning of the experiment until failure, the strain field of the dynamic specimen is not that regular. The number of facets of the dynamic specimen are significant smaller compared to the number of facets used for the DIC of the quasi-static specimen. The overall specimen surface has thus a smaller number of measuring point for the total strain field. The strain field of the dynamic specimen is thus more smeared over the total surface than the quasi-static strain field. The failure of the unidirectional carbon-fiber-reinforced composite material occurs in the middle of the free gauge section for the quasi-static and the dynamic specimen, respectively.

Considering the quasi-static and dynamic stress-strain curves, an increase of the transverse tensile strength of 24 % at a strain rate of approximately $52\,\mathrm{s}^{-1}$ was obtained. For the elastic modulus also a strain-rate-dependent behavior was found. An increases of 15 % from low to high strain rate for the modulus was observed.

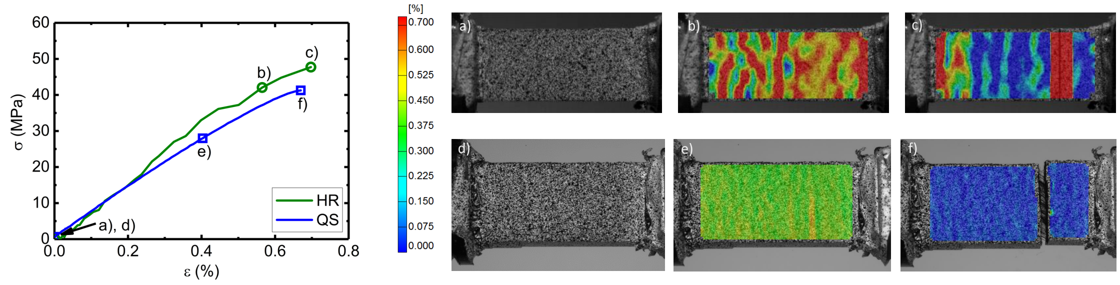

Fig. 5-30 In-plane strain fields in loading direction of transverse tension specimens at HR a)-c) and quasi-static loading d)-f).

6 In-plane Shear Response by Tensile Test of ±45 ° Laminate

The investigation of the shear properties of the carbon-fiber-reinforced polyamide-6 composite material from low to high strain rates is shown in this part of the thesis. Besides the knowledge of the compression and tension properties of a composite material, knowing the shear response is necessary as well to have a full data set, which can be used for basic computational models. Comparable to the transverse tension tests, the in-plane shear response is measured by tensile tests of a ±45 ° rectangular shaped laminate at quasi-static and dynamic loading conditions. The high strain rate experiments were conducted by means of the same split-Hopkinson tension bar system used for the transverse tension tests of the thermoplastic composite material. The results of this investigation, about the in-plane shear behavior, are later used for describing the longitudinal compressive strain rate behavior of a unidirectional thermoplastic composite material in the region of a kink-band (see chapter 7.3).

6.1 Material and Experimental Procedure

6.1.1 Material and Test Specimens

The characterization of the in-plane shear response was performed on the carbon-fiber-reinforced polyamide-6 composite tape material (Celstran® CFR-TP PA6 CF60-01, [115]). This composite material, which is analyzed in the framework of this study also under compression and tension, has a fiber volume content of 48 % according to the material data sheet as already mentioned in the previous sections [115]. The laminate used for the in-plane shear characterization also had a fiber volume content of 48 % determined by the test standard ASTM D3171 (Method II, Procedure B) [116]. The layup of the laminate was $[0\,°/90\,°]_{S,16}$. Similar to the plates for the transverse compression and tension specimens the laminate was made of single tape stripes and welded at a few points at the edges for a better handling of the stack. Then the tape stack was consolidated by using a compression mold placed in a hot press (RUCKS) at 260 °C with 0.5 MPa pressure for 15 minutes.

For both quasi-static and dynamic tensile tests to determine the in-plane shear properties of the ±45 ° laminate, the same rectangular tension specimen geometry as used for the transverse tensile tests with nominal dimensions of 60 x 8 x 2 mm^3 (length x width x thickness) was used (Figure 5-16). By using a water-cooled diamond saw the specimens were cut out at an angle of 45 ° to the fiber direction.

In order to fix the specimen in the split-Hopkinson tension bar system the same adapters used for the transverse tensile tests were used (Figure 5-16). The specimen were glued in the steel adapters with the adhesive BETAMATE™ 1822 from Dow Automotive. The accurate alignment of the specimen with the adapters was ensured by a bonding jig. As for the transverse tensile specimens, a free gauge length of 20 mm was defined.

The results of the quasi-static reference tests are compared with the static material data determined via recognized ASTM standard, to verify if an influence on the material properties due to the size effect can be measured. For the quasi-static tests according to the test standard DIN EN ISO 14129 the nominal dimensions of 250 x 25 x 2 mm^3 (length x width x thickness) and a free gauge section of 150 mm were used. The fiber direction of the specimen was oriented in 45 ° to the loading direction. Instead of glass-epoxy tabs on each side of the specimen abrasive cloth (grain size 320) was wrapped around to enhance the gripping of the clamping device.

Similar to the previous transverse tensile tests digital image correlation was used for measuring the strain field of the specimen. Thus a black-on-white speckle pattern was required. The random speckles were applied with an aerosol spray painting. The size of the dots was adjusted for the different image resolutions of the respective cameras (ARAMIS system and high-speed camera).

As already mentioned for all other experimental tests, the specimens were dried in a drying oven under vacuum (80 °C, 72 hours) to guarantee a common basis for the material characterization and were subsequently stored in multi-layer polymer-aluminum-film bags. Thus, possible moisture effects, resulting from the hygroscopic behavior of the matrix material PA 6 polymer could be minimized.

6.1.2 Quasi-Static Experimental Setup

Test Setup for Reference Tests

In order to test the material under tensile loading the same electro-mechanical testing machine (Hegewald & Peschke Inspekt Table 100) with a 100 kN load cell used for all other quasi-static tests was applied. The quasi-static strain rate of approximately $4 \cdot 10^{-4}\,\mathrm{s}^{-1}$ is defined by the constant displacement rate of 0.5 mm/min and the free gauge length of the specimen with 20 mm. The same quasi-static setup, which is shown in Figure 5-17, as for the transverse tensile tests was used. The assembly of specimen and adapters was screwed into inserts which in turn were mounted in the testing machine and fixed with bolts. The same setup for the DIC (GOM ARAMIS-4M) as for the other quasi-static tests was positioned (distance 225 mm) in front of the specimen to measure the 3D quasi-static strain field of the material under loading. The shutter speed was set to 60 ms and an acquisition rate of 1 fps was chosen for picture recording. The final post-processing of the camera data was performed with the ARAMIS software and a setting of 17 pixels x 17 pixels as facet size and a facet step of 15 pixels x 15 pixels. Just as for the transverse tensile tests, the computation size for deriving the strain field was set to 3 x 3 facets^2. The shear strain value, γ_{12}, of the specimen was determined within a strain field of 12 x 6 mm^2 at the center of the specimen surface from the mean values of the axial strain, ϵ_x, and the transverse strain, ϵ_y, by the following equation:

$$\gamma_{12} = \epsilon_\mathrm{x} - \epsilon_\mathrm{y}. \tag{6-1}$$

Following the test standard DIN EN ISO 14129, the shear strength was calculated as:

$$\tau_{12} = \frac{F}{2wh}. \tag{6-2}$$

where F is the load and w and h are the width and thickness of the specimen, respectively.

Test Setup According to DIN EN ISO 14129

Quasi-static tests according to the standard DIN EN ISO 14129 were performed to verify if the used specimen geometry (60 x 8 x 2 mm^3) and the usage of steel adapters yields correct values for the in-plane shear strength. The same electro-mechanical testing machine used before with a 100 kN load cell was used to introduce the load into the specimen with wedge grips. A constant displacement rate of 4 mm/min was chosen. The strain field of the specimen was obtained by DIC. Comparable to the tensile tests described in section 5.2.2 the GOM ARAMIS-4M DIC system (resolution and lens type see section 5.2.2) and two LED lamps were positioned in a distance 360 mm away from the specimen surface. The camera settings were set to a shutter speed of 36 ms and the acquisition rate to 1 fps. For post-processing of the images the same facet size, facet step, and computation size used for the quasi-static reference shear tests were defined. The shear strain was calculated with Equation 6-1. A strain field of 25 x 80 mm^2 was defined for computing ϵ_x and ϵ_y at the center of the specimen surface. The shear stress was derived by Equation 6-2.

6.1.3 Dynamic Experimental Setup

Four dynamic tests were carried out by using a split-Hopkinson tension bar system (Figure 3-10) at a strain rate of approximately 520 s^{-1}. The setup consists of a titanium U-shaped striker-bar with a length of 1 m to generate a sufficient long pulse for loading the specimen. The same setting as for the transverse tensile tests were used with a loading-bar (length 2.5 m, diameter 20 mm) and an incident- and transmission-bar (lengths of 2.5 m and 3 m, diameter 16 mm). The specimen was screwed with the adapters into the incident- and transmission-bar end as already shown in Figure 5-18. A 1 mm thick copper wire was used as pulse shaper which was wrapped around the impact flange at the end of the loading bar. Due to an expected pronounced plastic behavior of the material under shear loading an elastic wave with a trapezoidal shape was necessary which can be generated by a copper wire as previous experiments showed. The impact velocity of the striker-bar was set to about 5.2 m/s. The strain rate reached with the chosen striker-bar velocity and the nominal specimen length of 20 mm were the above mentioned 520 s^{-1}.

The SHTB setup with the respective settings and configurations was verified by a bars together test where the incident-bar and the transmission-bar were connected with each other by using a threaded steel cylinder. The velocity of the striker-bar impacting on the flange was 5.25 m/s. In Figure 6-1 the incident-bar and transmission-bar strain signal are shown. At this point it must be mentioned that for the BT test a silicon rubber pulse shaper was positioned at the flange and no cooper wire. Nevertheless, a less shaped signal is expected for the elastic wave induced with a striker hitting a wire. In general it could be shown, that the pulse travels from the incident-bar into the transmission-bar without changing the shape. The difference in the amplitude of 2.5 % is very low and therefore negligible.

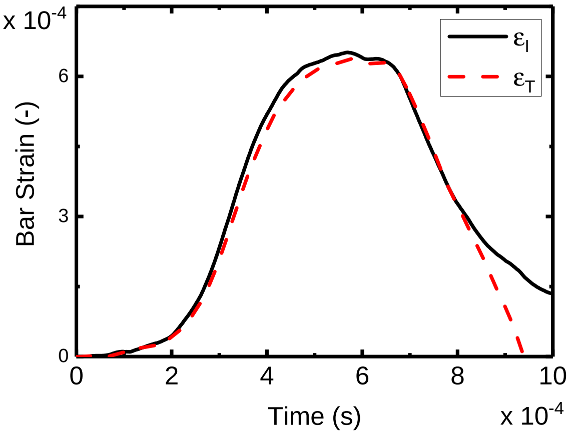

Fig. 6-1 Incident- and transmission-bar strain signals of the bars-together tests with the used SHPB configuration.

The deformation of the specimen was recorded with the previously mentioned high-speed camera (Photron SA5) using a ZEISS lens (Makro-Planar T* 2/100 mm ZF) and an acquisition rate of 124000 fps. The resolution of the images was 320 pixels x 152 pixels. The lens aperture was set between f/2.8 and f/4. Similar to all other dynamic tests of this study two spotlights (DEDOLIGHT 400D) were used to illuminate the specimen surface. The post-processing of the high-speed camera images was performed with the DIC software GOM ARAMIS-4M using a facet size of 10 pixels x 10 pixels and a facet step of 8 pixels x 8 pixels. The computation size (3 x 3 facets^2) remained unchanged. For the calculation of the shear strain, a field of 12 x 6 mm^2 at the center of the specimen surface was defined.

6.2 Results and Discussion

6.2.1 Quasi-Static Experimental Results

Results of Reference Tests

The shear stress - shear strain response of the carbon-fiber-reinforced polyamide-6 composite material under quasi-static loading is shown from 0 % to 5 % shear strain in Figure 6-2. The quasi-static shear strength, τ_{12M}^{qs}, is determined at 5 % shear strain, because at higher shear strains the fiber orientation aligns more and more in loading direction and the curve beyond 5 % shear strain does not represent the actual shear stress - shear strain response of the material anymore.

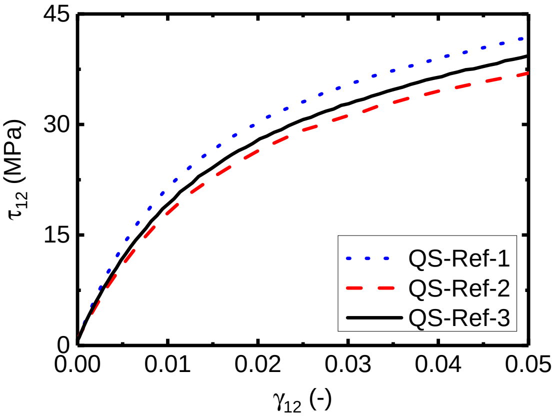

Fig. 6-2 Quasi-static in-plane shear stress-strain curves from reference tests.

The shear modulus, G_{12}^{qs}, was calculated between 0.1 % and 0.5 % shear strain. The specimens with number QS-Ref-1 and Q-Ref-3 were pulled out of the bottom adapter during the experiment at approximately 100 MPa shear stress. The reason for this was a cohesive failure of the adhesive in the adapter. Specimen QS-Ref-2 was loaded until failure of the composite material in the free gauge section. Even two specimens showed an invalid failure, the shear strength of the material could be measured correctly at 5 % shear strain because the adhesive failure occurred at a load level where the fibers have already rotated in loading direction. From the beginning of the measurement a homogeneous strain field distribution was identified. The measured material properties for each specimen are listed in Table 6-1. A mean value of (39.37 ± 2.47) MPa for the shear strength with a coefficient of variance with 6.26 % was found. The shear modulus of (2.18 ± 0.27) GPa exhibits a high coefficient of variance with 12.38 %.

Tab. 6-1 Quasi-static in-plane shear reference test results.

Test	**Shear Strength**	**Shear Modulus**
	τ_{12M}^{qs} (MPa)	G_{12}^{qs} (GPa)
QS-Ref-1	41.85	2.47
QS-Ref-2	36.92	2.12
QS-Ref-3	39.34	1.94
Mean	39.37	2.18
STDV	2.47	0.27
CV (%)	6.26	12.38

Results of DIN-Tests

Four standard tests were carried out according to DIN EN ISO 14129 at quasi-static strain rate. The results of these experiments are compared with the quasi-static reference shear tests to verify if the specimen geometry of the bonded adapters influence the measured material properties. In Figure 6-3 the quasi-static in-plane shear stress-strain curves up to 5 % shear strain (left) and the corresponding load-displacement curves of the full test (right) are plotted.

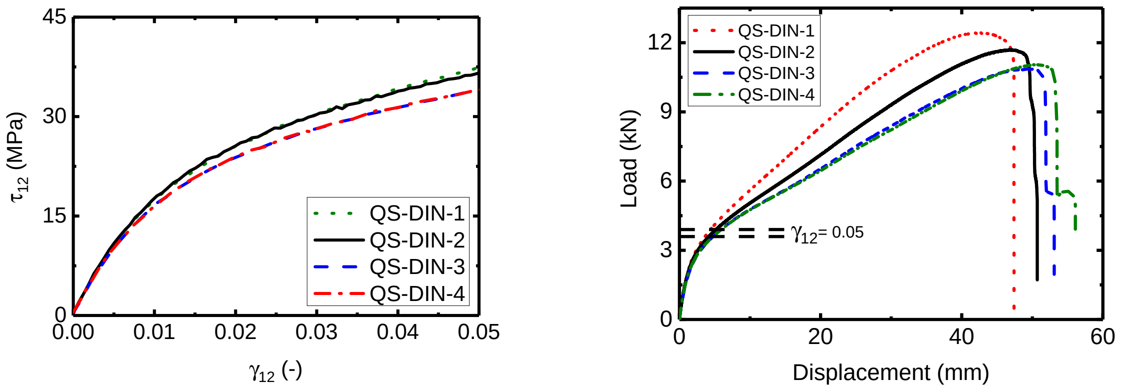

Fig. 6-3 Quasi-static in-plane shear stress-strain curves from static DIN tests (left) and Load-displacement curves from static DIN tests (right).

The dashed lines in the right diagram of Figure 6-3 indicate the load level at which the specimens have reached 5 % shear strain. It is known that thermoplastic composite material exhibit a large plastic deformation before failure occurs. This behavior differs from common thermoset systems.

The quasi-static shear strength, $\tau_{12\mathrm{M}}^{\mathrm{qs}}$, and the shear modulus, G_{12}^{qs}, were measured and are listed in Table 6-2. A mean strength of (35.43 ± 1.73) MPa with a coefficient of 4.89 % and a shear modulus of (1.96 ± 0.06) GPa with a coefficient of 2.85 % were determined.

Tab. 6-2 Quasi-static in-plane shear DIN test results.

Test	**Shear Strength** $\tau_{12\mathrm{M}}^{\mathrm{qs}}$ (MPa)	**Shear Modulus** G_{12}^{qs} (GPa)
QS-DIN-1	37.36	2.00
QS-DIN-2	36.44	2.02
QS-DIN-3	34.00	1.91
QS-DIN-4	33.94	1.92
Mean	35.43	1.96
STDV	1.73	0.06
CV (%)	4.89	2.85

The failure mode of the DIN tests are shown in Figure 6-4. It can be seen that the matrix strongly deforms and orientates the fibers in the loading direction. The comparison of the reference and standard tests lead to the result that the small specimens show a 11 % higher shear strength and 11 % higher shear modulus (Figure 6-5). This means that the specimen geometry influences the material property, which is known as the size effect. Nevertheless the strain-rate dependency can still be analyzed, because the specimen dimensions remain unchanged for the high-strain-rate tests. Thus the percentage of increase of the material strength can still be measured.

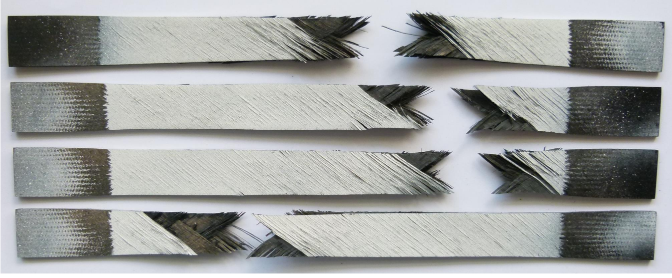

Fig. 6-4 Quasi-static specimen failure mode of DIN tests.

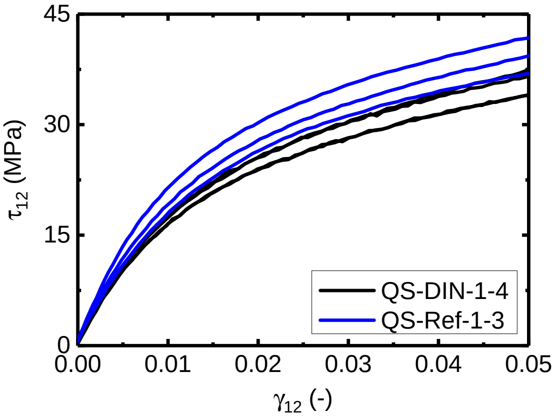

Fig. 6-5 Comparison of the quasi-static in-plane shear stress-strain curves from reference and DIN tests.

6.2.2 Dynamic Experimental Results

The dynamic stress response of the investigated fiber-reinforced composite material was derived by the SHPB Analysis (section 3.1.4). Thereby the "1-wave-analysis" (Equation 3-44) was applied to calculate the specimen stress. Similar to all other dynamic tests in this study, the strain rate, $\dot{\epsilon}$, was calculated as the time derivative of the strain-time curve measured via DIC. In Figure 6-6 the incident-bar and transmission-bar signals, which were filtered with a Savitzky-Golay filter, are plotted. The filter was chosen in such a way that the overall shape of the signals were not affected. Due to the copper pulse shaper a trapezoidal elastic wave could be produced in the incident-bar (Figure 6-6). Similar to the dynamic transverse tensile tests the incident-bar signal does not reach the zero strain level again. It is assumed that a superposition of the incident- and reflected-bar signal occur and thus the reflected signal starts with an offset.

The offset of the reflected bar strain signal makes it impossible to show the equilibrium condition in the specimen with the comparison of the 1-wave and 2-wave stress-time signals (Equation 3-44 and 3-45). Figure 6-7 shows the strain rate-time curves from the SHPB Analysis and via DIC. A constant strain rate could be reached right after the start of the loading. The specimens could be loaded above 5 % strain but not until final failure. The reason is that no longer incident wave could be generated with the used SHTB setup. Due to this fact, the strain rate decreases at the end of the measurement.

The determined in-plane axial shear strain field of the specimen was taken to demonstrate the occurrence of the dynamic equilibrium during the experiment. In Figure 6-8 a multi-stage section diagram of a representative specimen is shown.

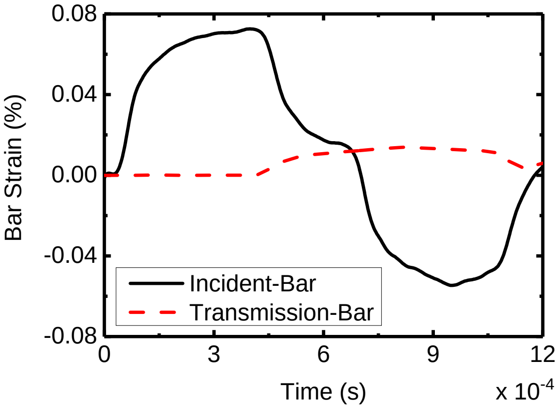

Fig. 6-6 Bar strain wave groups from dynamic tests with trapezoidal shaped incident waves for a representative specimen.

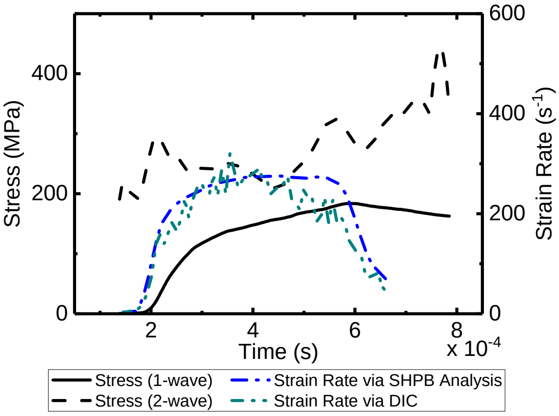

Fig. 6-7 Dynamic stress equilibrium check and corresponding strain rate for a representative specimen tested at high strain rate.

The stages begin at 0 µs with a low noise of the strain distribution (0.05 %) of the unloaded specimen. After 64µs the strain development in axial direction is shown in the diagram. Along the specimen the strain varies locally and thus a zig-zag curve is formed. With increasing measurement time the strain level increases constantly. It is thus assumed that dynamic equilibrium condition during testing holds.

In conclusion, the results of the dynamic in-plane shear tests of the ±45 ° laminate are shown in Figure 6-9. Four specimens were measured at high strain rate. It was not possible with the SHTB setup to load the specimens until failure, because the incident wave duration was not long enough. For the thermoplastic material investigated in this work, the strain-rate dependency of the in-plane shear response can still be investigated, considering the stress-strain response up to 5 % shear strain.

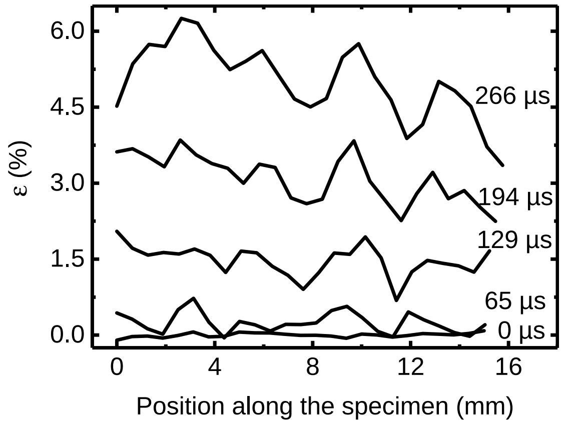

Fig. 6-8 Uniform development of specimen strain along axial direction for a representative specimen tested at high strain rate.

The dynamic shear strength at 5 % shear strain, $\tau_{12\mathrm{M}}^{\mathrm{hr}}$, and the dynamic shear modulus, G_{12}^{hr}, are listed in Table 6-3 for each tested specimen. The shear strength of (57.80 ± 4.93) MPa shows a coefficient of variance of 8.52 %. The measured shear modulus (2.35 ± 0.22) GPa likewise shows a variance of 9.17 %. Comparing the quasi-static and dynamic stress-strain curves at approximately 517 s^{-1}, an increase of the in-plane shear strength of 47 % was obtained. The elastic shear modulus shows only a slightly strain-rate sensitivity of 8 % from quasi-static to high strain rate.

Tab. 6-3 Dynamic in-plane shear test results.

Test	**Strain Rate**		**Shear Modulus**	**Shear Strength**
	elastic* (s^{-1})	at 5% strain (s^{-1})	G_{12}^{hr} (GPa)	$\tau_{12\mathrm{M}}^{\mathrm{hr}}$ (MPa)
HR-1	55.37	446.93	2.06	52.65
HR-2	150.11	548.29	2.39	55.04
HR-3	144.11	521.41	2.58	59.82
HR-4	160.69	551.28	2.38	63.68
Mean	127.55	516.98	2.35	57.80
STDV	48.65	48.59	0.22	4.93
CV (%)	38.14	9.40	9.17	8.52

* averaged between 0.1 % and 0.5 % strain

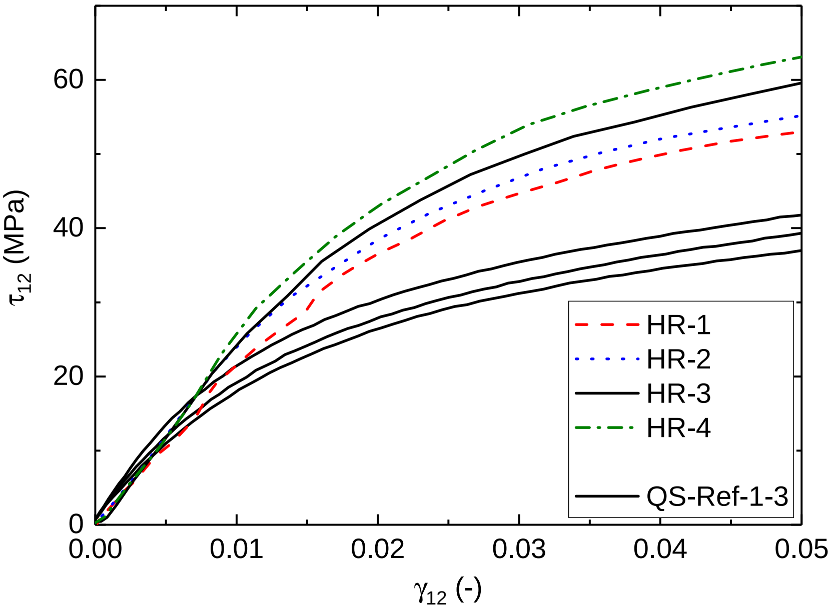

Fig. 6-9 Dynamic in-plane shear stress-strain response of all tested specimens.

7 Longitudinal Compression Properties of UD Laminate

The purpose of the work, presented in this chapter, is to develop a simple dynamic experimental testing method to characterize the longitudinal compression behavior of unidirectional carbon composite materials by means of the split-Hopkinson pressure bar method and optical image recording of the failure behavior. The first part of the chapter shows an experimental procedure for composites of low fiber volume content. The developed specimen geometry and the experimental results were previously publised in [121]. In the second part of this chapter a further development of the experimental procedure is described, to measure the longitudinal compression behavior of UD composites with high fiber volume content. Particular attention is given to prevent bending of the specimen and failure at the loading surfaces, generally resulting in an underprediction of the longitudinal compressive strength. The results were published in the journal Composites Structures [122].

7.1 Experimental Procedure for UD Composites of Low Fiber Volume Content[1]

An experimental investigation has been performed to characterize the strain rate dependency of unidirectional carbon-fiber-reinforced polyamide-6 composite for longitudinal compression loading. An end-loaded compression specimen geometry, suitable for contactless optical strain measurement via digital image correlation and dynamic loading in a split-Hopkinson pressure bar, was developed. For the dynamic experiments at a constant strain rate of $100\,\mathrm{s}^{-1}$ a modified version of the Dynamic Compression Fixture, developed by Koerber and Camanho [15] was used. The results were compared with quasi-static test results at a strain rate of $3 \cdot 10^{-4}\,\mathrm{s}^{-1}$ using the same specimen geometry. It was found that the longitudinal compressive strength increased by 61% compared to the strength value obtained from the quasi-static tests.

---

[1] Published in: M. Ploeckl, P. Kuhn, H. Koerber, EPJ Web of Conferences, vol. 94, 2015, pp. 01 041 1-6.

7.1.1 Material and Specimen

The specimens were prepared from Celstran® CFR-TP PA6 CF60-01, a 60 % carbon fiber by weight polyamide-6 unidirectional reinforced thermoplastic composite tape. According to the material data sheet [115] a fiber volume content of 48 % is then obtained. In the present study the fiber volume content was determined to be 49 %, using the test standard ASTM D3171, Method II, Procedure B (digestion of the matrix by a mixture of sulfuric acid and hydrogen peroxide) [116]. This material system is used in industrial, automotive, and sporting goods applications and is commonly processed with automated fiber placement technologies. To manufacture 16-ply unidirectional plates, stripes of the tape were laid parallel and brick-like above each other such that the abutting edges of the stripes are at different locations in the individual layers. For a better handling of the stack the frame was welded at few points with an ultra-sonic welding apparatus (ProteUS, EM-Systeme GmbH) with a sonotrode frequency of 30 kHz. Using a RUCKS hot press and a compression mold the composite plates were consolidated at 260 °C with 0.5 MPa pressure for 15 minutes.

In the presented work, an end-loaded compression specimen geometry suitable for contactless optical strain measurement via digital image correlation and dynamic loading in a split-Hopkinson pressure bar was developed (Figure 7-1). The specimen consists of a flat rectangular UD base-laminate with dimensions of 30 x 10 x 2 mm^3 (length x width x thickness). To improve the stability of the specimen and to prevent premature failure at the loading ends, the cross-sectional area at the loading ends was increased by bonding two layers of glass-epoxy composite tabs to both sides, using the adhesive Scotch-Weld™ DP 490 from 3M (for the quasi-static test specimens) and BETAMATE™ 1822 from Dow Automotive (for the dynamic test specimens). This leaves a free gauge section with a length of 10 mm at the middle of the specimen. Although two different adhesives were used, they exhibit similar material properties. Therefore it is assumed that the adhesive does not influence the presented experimental results. The specimens were cut on a water-cooled diamond saw. The loading surfaces were treated with a grinding machine to generate plane and parallel end-faces of good quality. The surface parallelism of the loading surfaces was found to be within 0.02 mm. A black-on-white speckle pattern for the digital image correlation method was applied on the surface of each specimen using aerosol spray painting. Based on the different image resolutions of the respective cameras the random speckles of the quasi-static specimens were smaller than the speckles of the dynamic specimens.

To verify if the developed end-loaded compression specimen geometry (Figure 7-1) yields correct values for the static longitudinal compressive strength, quasi-static

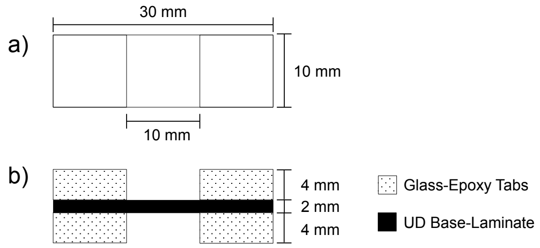

Fig. 7-1 Top view a) and side view b) of end-loaded compression specimen geometry for quasi-static and high strain rate measurements.

tests according to the standard ASTM D6641 [118] were carried out using the above mentioned electro-mechanical testing machine at a constant displacement rate. For the quasi-static tests according to ASTM D6641 the default specimen geometry with nominal dimensions of 140 x 12 x 2 mm^3 (length x width x thickness) and a free gauge section of 12.5mm was used. For these specimens glass-epoxy composite tabs were bonded to each side using the adhesive Scotch-Weld™ DP 490 from 3M. All specimens were cut on a water-cooled diamond saw. The specimens were equipped with two linear strain gauges of the type TML FLA-3-11-1L in a back-to-back configuration at the free gauge section to measure the strain and possible bending of the specimen. To establish a common ground for the mechanical material characterization, all specimens were dried in a drying oven under vacuum at a temperature of 80 °C for 72 hours to minimize possible moisture effects, resulting from the hygroscopic behavior of the PA 6 polymer. The dry specimens were stored in an aluminum multi-layer film bag until start of the experiment to avoid moisture absorption after drying.

7.1.2 Quasi-Static and Dynamic Experimental Setup

Five quasi-static reference tests were performed using an electro-mechanical testing machine of the type Hegewald & Peschke Inspekt Table 100 with a 100 kN load cell. The tests were carried out with a constant displacement rate of 0.5 mm/min, which corresponds to a quasi-static axial strain rate of approximately $3 \cdot 10^{-4}\,\mathrm{s}^{-1}$, when considering a nominal specimen length of 30 mm. The load was introduced by means of a self-aligning end-loaded compression setup with embedded polished tungsten-carbide inserts at the loading surfaces (Figure 7-2). The latter prevent damage on the loading surfaces of the compression fixture due to the high compressive strength of the specimen in fiber direction. To minimize friction effects at the loading surfaces, a thin layer of molybdenum disulfide lubricant was applied to the end-surface of the specimen. The GOM ARAMIS-4M DIC system, consisting of two CCD cameras with a resolution of 2352 pixels x 1728 pixels and two lenses of the type Titanar

50 mm, were used to obtain the three-dimensional quasi-static strain field of the specimen front surface. The DIC system was positioned at a distance of 225 mm away from the specimen surface. To ensure a uniform illumination of the specimen surface two LED lamps were used. The acquisition rate of the cameras was set to 5 frames per second (fps) with a shutter speed of 75 ms. For post processing of the recorded images with the ARAMIS software a facet size of 17 pixels x 17 pixels and a facet step of 15 pixels x 15 pixels was used. The computation size for deriving the strain field was set to 3 x 3 facets^2. For the determination of the longitudinal compressive specimen strain, used in the later shown stress-strain curves, the mean value of a 6 x 6 mm^2 strain field at the center of the specimen surface was calculated. The quasi-static longitudinal compressive strength is defined as the ratio of the failure load and the specimen cross-section.

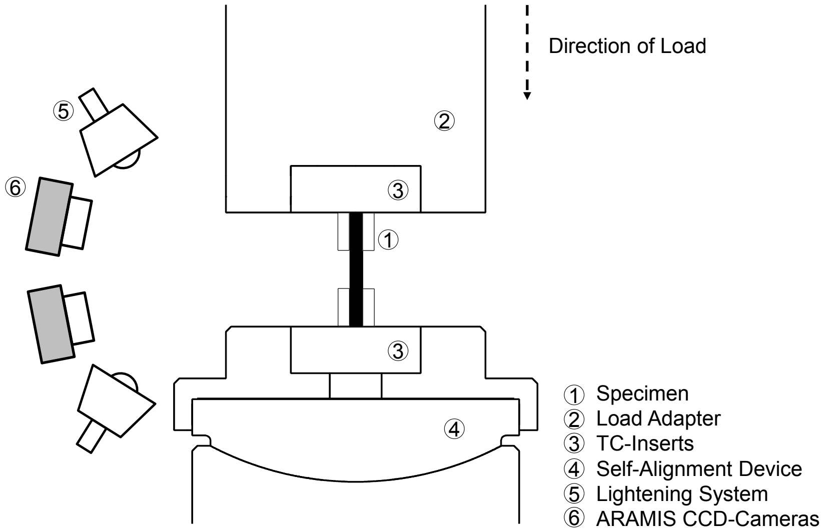

Fig. 7-2 Quasi-static compression test setup with tungsten-carbide inserts.

Five quasi-static tests according to the standard ASTM D6641 [118] were carried out on the same electro-mechanical testing machine at a constant displacement rate of 1.3 mm/min. For these tests the combined-loading-compression (CLC) test fixture defined in [118] was used. The strain gauges were connected to an HBM MX840A amplifier, used for the data acquisition. As defined in the standard, the specimen strain was obtained by calculating the average value from the two strain gauge signals and the quasi-static longitudinal compressive strength was calculated as the ratio of the failure load and the specimen cross-section.

High-strain-rate tests were performed for five end-loaded compression specimens. A split-Hopkinson pressure bar setup (Figure 7-3) was used consisting of diameter 18 mm steel striker-, incident-, and transmission-bars with lengths of 0.6 m, 2.6 m, and 1.6 m, respectively. The strain gauges for the detection of the elastic wave are located on the incident-bar at 1.3 m and on the transmission-bar at 0.3 m away from the bar-specimen interfaces and operate with a supply voltage of 7 V. The bar-gauge signals were amplified by using a high-speed transducer amplifier of the type FYLDE FE-H379-TA with a gain setting of 100 and a frequency setting of 300 kHz. The amplified signals and the impact velocity of the striker-bar were each recorded with a TEKTRONIX TDS2004C oscilloscope. To generate an elastic wave with a triangular shape in the incident-bar, a copper pulse shaper with a diameter of 4 mm and a thickness of 1 mm was used. The pulse shaper provides a triangular shape which is best suited for specimens exhibiting a linear stress-strain behavior up to failure [15]. For the high-strain-rate tests a striker-bar impact velocity of approximately 7 m/s was used. As a result of the nominal specimen geometry and the striker-bar velocity a strain rate of approximately 100 s^{-1} was reached.

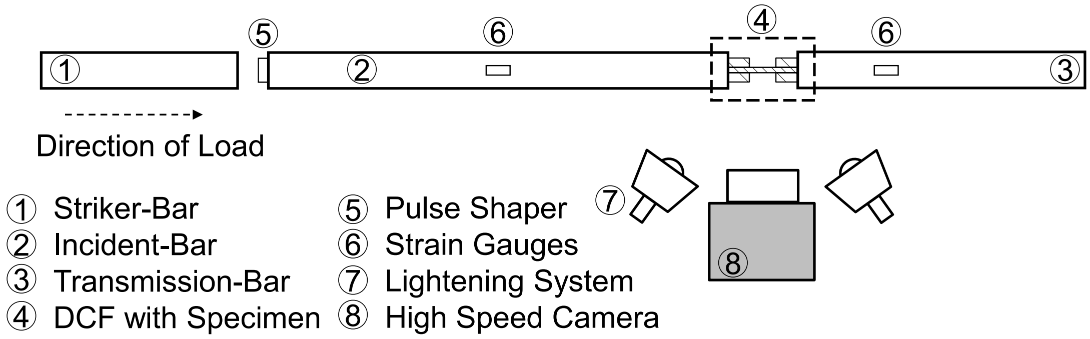

Fig. 7-3 Split-Hopkinson pressure bar test setup with modified Dynamic Compression Fixture (DCF).

To verify the configuration for the dynamic tests, a bars together (BT) test, with incident- and transmission-bar directly in contact, was carried out. The striker-bar was impacting with a velocity of 6.8 m/s on the copper pulse shaper at the incident-bar. Figure 7-4 shows the inverted incident-bar strain signal and the transmission-bar strain signal. The measured bar strain signals indicate, that the elastic wave travels from the incident-bar into the transmission-bar without changing the amplitude, duration, and shape. The difference of about 2 % in the strain amplitudes is negligible. Due to the similarity of the two signals a correct specimen stress-time response can be expected.

In the presented work, a modified version of the Dynamic Compression Fixture (DCF), developed by Koerber and Camanho [15] was used. The modified DCF (Figure 7-5) consists of two tungsten-carbide (TC) inserts, surrounded by support-rings and placed between the bars and the specimen loading surfaces. Thus, indentation of the bar-ends and stress concentrations at the specimen end-surfaces could be avoided. To prevent an influence of the TC-inserts on the bar strain waves, the mechanical impedance between TC-inserts and the Hopkinson bars was matched

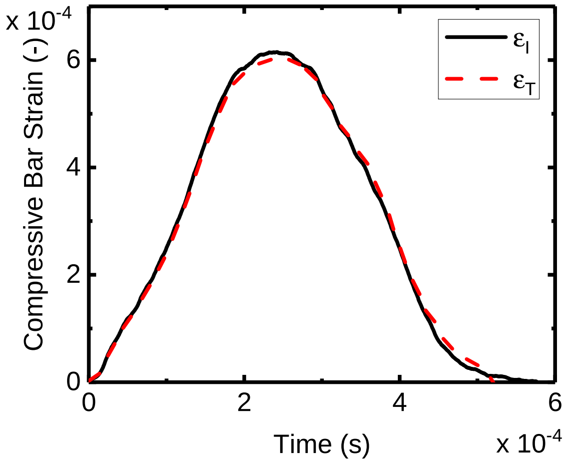

Fig. 7-4 Incident- and transmission-bar strain signals of the bars-together test with the used SHPB configuration.

by choosing an appropriate diameter ratio. The TC-inserts/support-rings are then aligned and held in place by a freely sliding tube, containing a cut-out window to monitor the specimen deformation and failure mode using a high-speed camera. The specimen was clamped between the two inserts without any additional fixation.

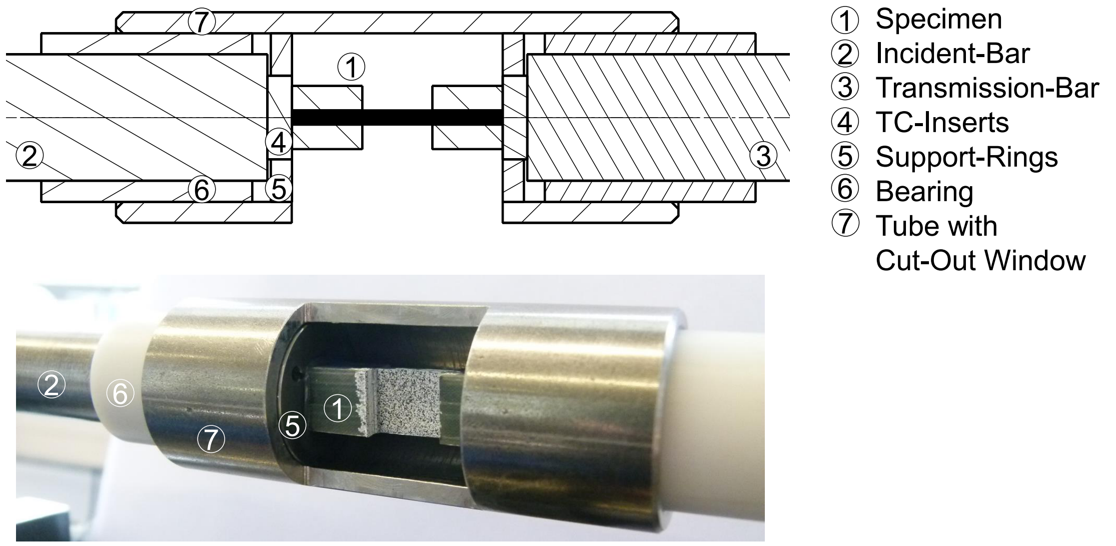

Fig. 7-5 Modified Dynamic Compression Fixture used in the SHPB setup.

A Photron SA5 high-speed camera with a ZEISS Makro-Planar T* 2/100 mm ZF lens was positioned 950 mm away from the specimen surface to capture images with a frame rate of 372000 fps at a resolution of 128 pixels x 80 pixels during the experiment. The lens aperture was set to f/2.8. Two spotlights of type DEDOLIGHT 400D were used to provide a well illuminated specimen surface. For post processing of the recorded images the digital image correlation software of the GOM ARAMIS-4M system with a facet size of 10 pixels x 10 pixels and a facet step of 8 pixels x 8 pixels was used. The computation size was set to 5 x 5 facets^2. For the determination of the axial specimen strain, the mean value of a 6 x 6 mm^2 strain field at the center of the specimen surface was calculated.

7.1.3 Results and Discussion

Quasi-Static Experimental Results

Five quasi-static reference specimens were loaded until failure at constant displacement rate. The longitudinal compressive stress-strain response for all tested specimens is shown in Figure 7-6. The end point of each curve indicates the failure load and correlates with the quasi-static longitudinal compressive strength, X_C^{qs}, and the ultimate failure strain, ϵ_C^u. The results of the reference tests are summarized in Table 7-1. The mean static compressive strength of 604.86 ± 98.61 MPa shows a relative high coefficient of variance with 16.30 %, yet no correlation to varying failure modes could be observed. The Young's modulus, evaluated in the strain interval between 0.1 % to 0.3 % was found to be 84.15 ± 6.46 GPa. For all quasi-static reference tests, valid failure occurred in the form of fiber kinking away from the loading surfaces (Figure 7-7). The kink-bands for every specimen are marked with yellow arrows respectively (Figure 7-7).

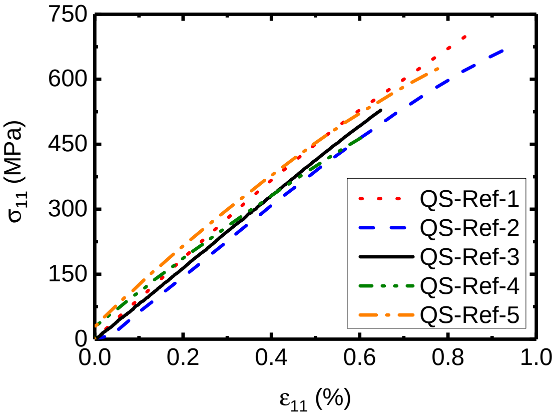

Fig. 7-6 Quasi-static longitudinal compressive stress-strain curves from reference tests.

Five quasi-static tests according to the test standard ASTM D6641 with corresponding specimen geometry and test fixture were carried out to verify the developed specimen geometry. Figure 7-8 shows the longitudinal compressive stress-strain response for all tested specimens. The end point of each curve corresponds to the failure load and indicates the quasi-static longitudinal compressive strength, X_C^{qs}, and the ultimate failure strain, ϵ_C^u. The results of the ASTM tests are listed in the Table 7-2. The mean compressive strength of 520.24 ± 57.40 MPa is less than the

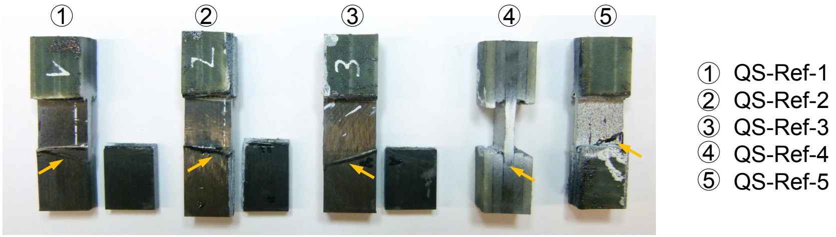

Fig. 7-7 Tested quasi-static reference specimens. Arrow indicates position of compressive failure mode (kink band).

Tab. 7-1 Quasi-static reference test results.

Test	**Strength**	**Failure Strain**	**Modulus**
	$X_{\mathrm{C}}^{\mathrm{qs}}$ (MPa)	$\epsilon_{\mathrm{C}}^{\mathrm{u}}$ (%)	E (GPa)
QS-Ref-1	708.66	0.85	93.20
QS-Ref-2	678.49	0.95	81.87
QS-Ref-3	528.53	0.65	83.70
QS-Ref-4	477.63	0.62	75.52
QS-Ref-5	630.99	0.79	86.46
Mean	604.86	0.77	84.15
STDV	98.61	0.14	6.46
CV (%)	16.30	17.90	7.68

compressive strength observed for the developed end-loaded specimen geometry; exhibits a lower coefficient of variance however. A slightly higher Young's modulus of 93.65 ± 3.41 GPa was measured for the static ASTM tests. Again, all specimen fail due to fiber kinking in the gauge section (Figure 7-9). In summary it can be stated that both static tests, the end-loaded specimen geometry developed for the subsequent dynamic tests and the tests performed according to a well-established ASTM test method, yield similar results (Figure 7-10), therefore verifying the applicability of the end-loaded specimen geometry.

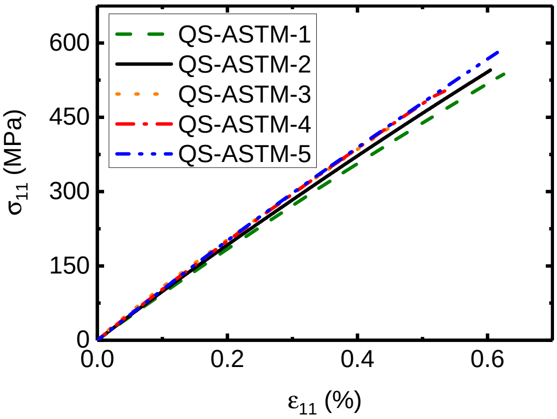

Fig. 7-8 Quasi-static longitudinal compressive stress-strain curves from static ASTM tests.

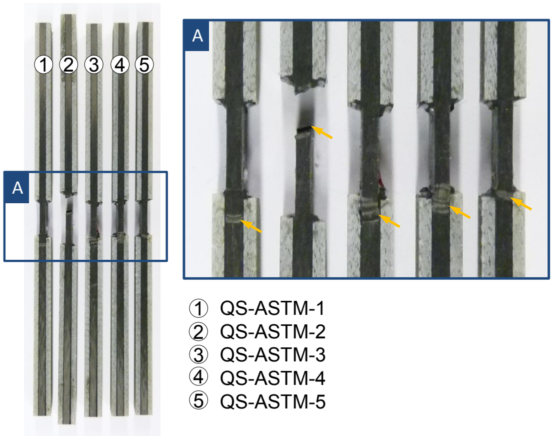

Fig. 7-9 Quasi-static specimen failure mode of ASTM tests.

Dynamic Experimental Results

The dynamic test results were calculated by using the classic SHPB Analysis which is based on the one-dimensional wave propagation theory [61] and already described in chapter 3.1.4. It is noted that in the present work Equation 3-38 and 3-39 (s. chapter 3.1.4) are only used for comparison because the specimen strain and the specimen strain rate were directly obtained by contactless optical strain measurement via digital image correlation.

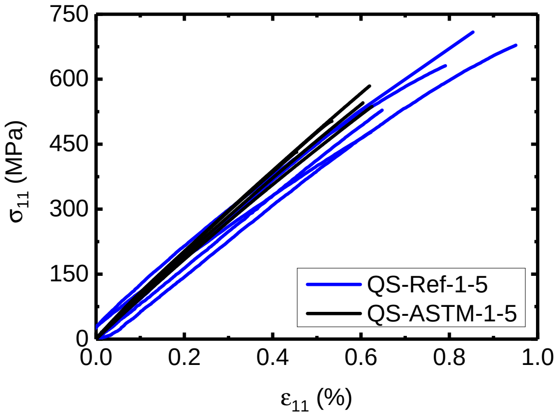

Fig. 7-10 Comparison of the quasi-static longitudinal compressive stress-strain curves from reference and ASTM tests.

Tab. 7-2 Quasi-static longitudinal compression ASTM test results.

Test	**Strength** X_C^{qs} (MPa)	**Failure Strain** ϵ_C^u (%)	**Modulus** E (GPa)
QS-ASTM-1	536.98	0.63	88.80
QS-ASTM-2	545.42	0.60	92.24
QS-ASTM-3	431.60	0.45	93.58
QS-ASTM-4	502.85	0.53	96.21
QS-ASTM-5	584.34	0.62	97.44
Mean	520.24	0.57	93.65
STDV	57.40	0.07	3.41
CV (%)	11.03	12.85	3.64

Figure 7-11 shows the post-processing results of the bar strain waves for a representative specimen (specimen HR-1). The graphs serve as illustration of the SHPB Analysis. The unfiltered incident- and transmission-bar signals are shown in Figure 7-11 a). As a first step the bar strain waves detected at the two strain gauges on the incident- and transmission-bar are filtered with a Savitzky-Golay filter, eliminating the digitalization noise from the oscilloscope without changing the overall signal shape. The waves are then shifted to the time at which they occurred at the specimen (Figure 7-11 b)). The loads, F_1 and F_2, were calculated with Equation 3-40 and 3-41 (s. chapter 3.1.4) and plotted over time (Figure 7-11 c)). The reason for the initial offset of the forces is the nonzero bar strain at the beginning of the reflected signal. Taking this into account, the load-time responses on both sides of the specimen are similar and thus dynamic equilibrium during the experiment could be presumed. A comparison of the specimen strain calculated with Equation 3-39 (s. chapter 3.1.4) and the specimen strain measured optically by using the ARAMIS system is shown in Figure 7-11 d). In this case, both specimen strain signals correlate well which is not necessarily the case as demonstrated by Koerber and Camanho for a similar test configuration [15]. The strain rate-time response obtained from Equation 3-38 (s. chapter 3.1.4) and from the time derivative of the ARAMIS strain signal is compared in Figure 7-11 e). Due to the small noise of the ARAMIS strain signal (Figure 7-11 d)), the optically measured strain rate signal exhibits a higher scatter compared to the SHPB strain signal obtained with Equation 3-38. The ARAMIS strain signal was therefore filtered to evaluate the strain rate evolution directly measured at the specimen. An approximately constant strain rate could be achieved after half of the experiment. Figure 7-11 f) shows the dynamic longitudinal compressive stress-strain response for this representative dynamic specimen, using both the specimen strain obtained with Equation 3-39 and the optically measured specimen strain.

The compressive stress-strain response of all dynamically tested specimens is shown in Figure 7-12, using only the optical measured strain. The end point of each curve corresponds to the longitudinal compressive strength, $X_{\mathrm{C}}^{\mathrm{qs}}$, and the ultimate failure strain, $\epsilon_{\mathrm{C}}^{\mathrm{u}}$. For specimen HR-3 only the failure load was recorded because of a non-functioning high-speed camera record.

In Table 7-3 all dynamic experimental results are listed. A mean compressive strength of $974.93 \pm 63.10\,\mathrm{MPa}$ with a coefficient of variance of $6.47\,\%$ was measured for the unidirectional carbon-fiber-reinforced polyamide-6 composite. To evaluate the Young's modulus, a further data treatment described by Koerber and Camanho [15] was applied to the dynamic stress-strain response. The curves were fitted by quadratic trend lines and a shift of the stress-axis towards zero was performed. The obtained mean value of the Young's modulus, evaluated in the strain region between

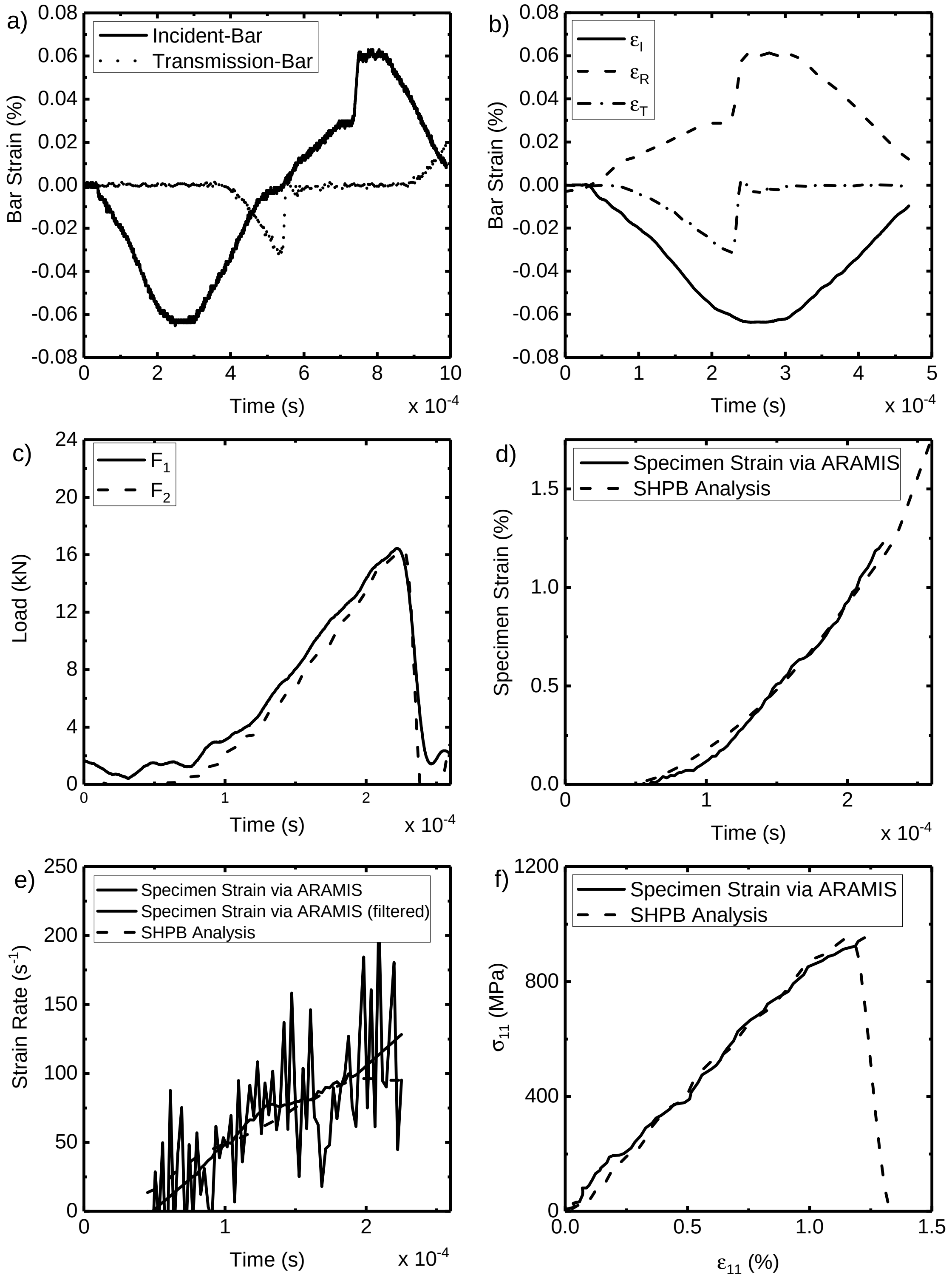

Fig. 7-11 Incident- and transmission-bar signals of the specimen HR-1 a) and SHPB Analysis results of the specimen HR-1 for the shifted bar strain waves b), the loads acting on the specimen c), the specimen strain behavior d), the specimen strain rate e) over time, and the stress-strain response f).

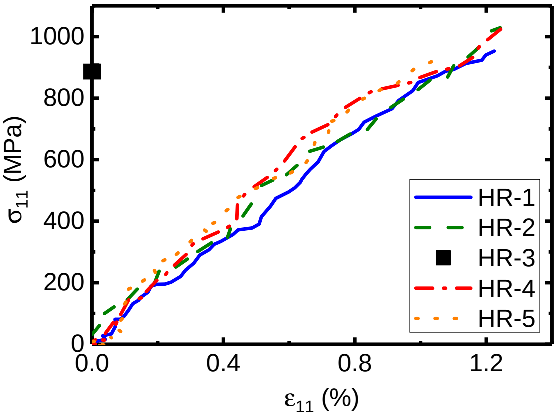

Fig. 7-12 Dynamic longitudinal compressive stress-strain response of all tested specimens.

0.1 % and 0.3 %, is 97.13 ± 14.08 GPa. All specimen fail similar to the quasi-static specimens away from the loading surface (Figure 7-13) with the formation of a kink-band, followed by through thickness fiber failure.

Tab. 7-3 Dynamic longitudinal compression test results.

Test	**Strength** X_C^{hr} (MPa)	**Failure Strain** ϵ_C^u (%)	**Modulus** E (GPa)	**Strain Rate** $\dot{\epsilon}$ (s^{-1})
HR-1	952.88	1.22	87.09	96.05
HR-2	1034.52	1.22	83.08	85.93
HR-3	888.05	-	-	-
HR-4	1039.13	1.26	107.29	110.72
HR-5	960.05	1.06	111.04	92.56
Mean	974.93	1.19	97.13	96.32
STDV	63.10	0.09	14.08	10.48
CV (%)	6.47	7.45	14.50	10.88

Figure 7-14 shows the failure mode observed for a representative dynamic test (specimen HR-1) by means of the stress-time diagram and four high-speed camera images taken at different time steps. The images are oriented such that the incident-bar is on the left side of the specimen. Figure 7-14 a) shows the specimen at time t_0. Figure 7-14 b) indicates the initiation of a kink-band in the upper left corner at a stress of 942.03 MPa and a time of 183 μs. After 188 μs (Figure 7-14 c)) the kink-band is fully developed. The initial fiber kinking failure mode is then followed by longitudinal splitting as observed in Figure 7-14 d). By means of Figure 7-14 it is shown that the dynamic longitudinal compressive test yields a valid failure mode. Therefore the strain rate's effect on the longitudinal compressive strength can be derived.

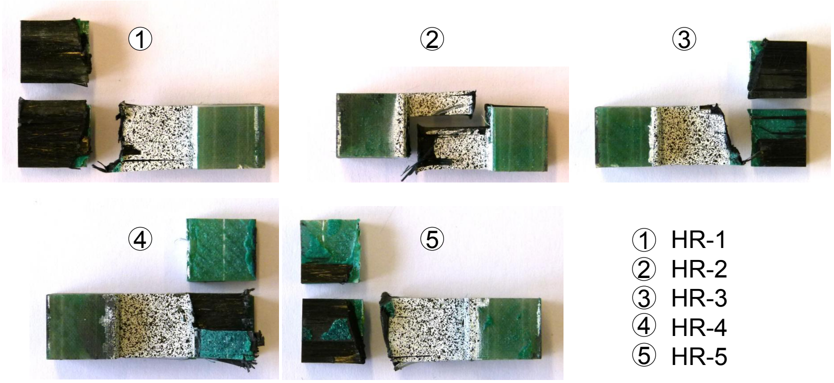
①
②
③
④
⑤
① HR-1
② HR-2
③ HR-3
④ HR-4
⑤ HR-5

Fig. 7-13 Dynamic specimen failure mode.

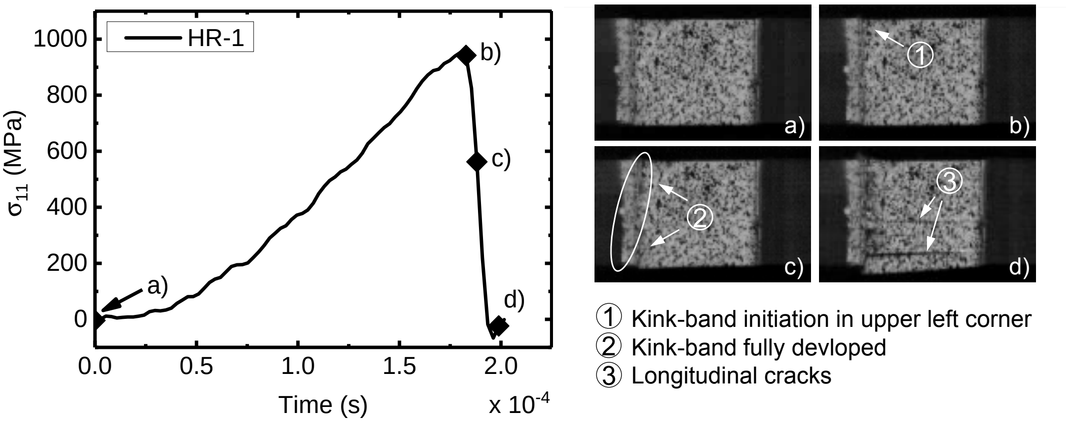

Fig. 7-14 High-speed camera images and stress-time response of the dynamic compression specimen HR-1 at t_0 a), $t_0 + 183\,\mu\text{s}$ b), $t_0 + 188\,\mu\text{s}$ c), and $t_0 + 199\,\mu\text{s}$ d).

A comparison of the longitudinal compressive stress-strain response of the unidirectional carbon-fiber-reinforced polyamide-6 composite, loaded at quasi-static and dynamic (approx. $100\,\mathrm{s}^{-1}$) strain rates (Figure 7-15), indicates a slight increase of the longitudinal compressive modulus (15 %) and a significant increase of the longitudinal compressive strength (61 %).

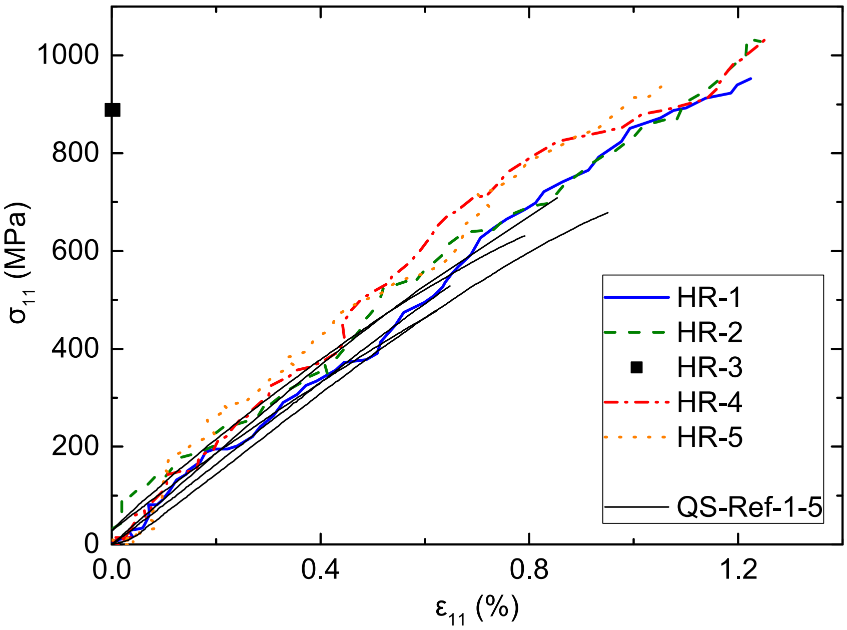

Fig. 7-15 Comparison of the quasi-static longitudinal compressive stress-strain curves from reference and dynamic tests.

7.2 Development of a Dynamic Test Methodology for UD Composites of High Fiber Volume Content[2]

The above shown experimental procedure is useful for fiber-reinforced composite materials with relatively low longitudinal compressive strength. In case of composite materials with high fiber volume content this procedure does not lead to valid results. Then the longitudinal compressive strength is very high and the specimen is likely to fail at the end-loaded surfaces. Thus a dynamic test methodology was developed to measure high fiber volume content composite materials which contain high performance fibers that exhibit high compressive strength.

In the past research groups used different methods to measure the strength of composite materials with relatively high fiber volume content. Hsiao and Daniel [44] used a falling-weight impact tower and thick composite specimens with bonded-steel end caps to investigate longitudinal compressive strength at high strain rates. The thick composite laminates were end loaded for the high-strain-rate tests. An increase in the longitudinal compressive strength with increasing strain rate was measured. No rate-effect was observed for the longitudinal compressive Young's modulus. Premature crushing failure at the specimens' ends caused dynamically measured longitudinal compressive strength values to be underestimated. Bing and Sun [123] used a split-Hopkinson pressure bar (SHPB) to investigate the off-axis compression behavior of UD composite specimens at different strain rates. Linear extrapolation was applied to the measured off-axis strength data to compute the composite's longitudinal compressive strengths at high strain rates. Wiegand [124] used an SHPB to characterize the quasi-static and dynamic compression behavior of a cross-ply epoxy composite. The laminate was inserted into slotted end caps and fastened with additional clamps. The specimens exhibited failure near the grip-termination region. A linear increase in compressive strength with increasing strain rate was found; however, compressive strength in the fiber direction on the ply level was not further investigated. Koerber and Camanho [15] used an SHPB system for dynamic tests to measure the effects of strain rate on the longitudinal compressive strength and longitudinal compressive Young's modulus of UD IM7/8552. Although analysis of the strain rate's effect on the longitudinal compressive modulus was conclusive, all of the specimens, measured at quasi-static and dynamic strain rates exhibited preliminary failure mode at the loading surfaces. A qualitative evaluation of the strain rate's effect on longitudinal compressive strength was possible because the failure mode was the same at all strain rates. The measured static and dynamic strengths values were thought to be significantly lower than the actual values, due to the observed preliminary failure mode. Characterization of the strain rate's effect on the longitudinal compressive stress-strain behavior of UD carbon composites is still challenging and subject to debate.

---

[2] Ploeckl et al., *Composite Structures*, vol. 180, pp. 429-438, 2017.

This study aims to develop an SHPB compression-test methodology for investigating the strain rate's effect on the longitudinal compression response of UD carbon composites. Particular emphasis is placed on generating a valid failure mode during quasi-static and high-strain-rate loading, which was not achieved in earlier studies such as [15, 44]. The main advantage of SHPB systems over drop towers or servohydraulic testing machines is that the measured stress-strain response is much less influenced by inertia effects in the load chain, thereby enabling high-quality dynamic stress-strain response to be measured. UD and quasi-isotropic (QI) IM7/8552 carbon-epoxy composite and UD carbon-fiber-reinforced polyamide-6 (PA 6) composite laminates were tested to demonstrate that the developed testing method is suitable for different laminate layups and different types of matrices.

Greater static and dynamic strengths were achieved for high-strength UD IM7/8552 carbon-epoxy composite laminate than during an earlier study [15]. The static compressive strength closely resembled the longitudinal compressive strength reported in an earlier study [125] for this composite-material system. However, the observed damage location suggested that the measured strength stemmed from premature failure. Valid failure in the middle of the specimen caused significantly higher strengths to be determined via back-calculation of a UD ply's longitudinal compressive strength using experimental data from the QI laminate. A quantitatively higher strain-rate sensitivity than that for epoxy-based composite was found for the thermoplastic composite also investigated in this study. It bears noting that a complete data set for the dynamic in-plane mechanical response of an IM7/8552 UD carbon-epoxy laminate at strain rates in the $100\,\mathrm{s}^{-1}$ to $300\,\mathrm{s}^{-1}$ range now exists given the results of this study and earlier research published by the authors in [14, 15] and [126].

7.2.1 Material and Specimen

Two types of carbon-fiber-reinforced composite material systems were investigated: the HexPly® IM7/8552 thermoset prepreg material system [127], which is used mainly for primary structure components in the aerospace industry operating in environments up to 121 °C, and Celstran® CFR-TP PA6 CF60-01, a 60 % carbon-fiber-by-weight polyamide-6 unidirectional fiber-reinforced thermoplastic composite tape [115]. The latter material system is used in industrial, automotive, and sporting goods applications and is commonly processed using automated fiber-placement technologies.

For IM7/8552, two laminates—a 14-ply, unidirectional laminate and a 16-ply, quasi-isotropic $[(90°/0°/+45°/-45°)_2]_{2S}$ laminate—were manufactured on a 75t Cannon hot press by applying the curing cycle recommended in the material's data sheet [127]. A unidirectional plate with 14 plies was manufactured for the carbon-fiber-reinforced polyamide-6 composite. The thermoplastic laminate was made of single tape stripes laid parallel and brick-like above each other. To better handle the stack, the frame was welded at a few points using an ultrasonic welding apparatus (ProteUS, EM-Systeme GmbH) with a 30 kHz sonotrode frequency. Using a RUCKS hot press and a compression mold, the thermoplastic composite plates were consolidated for 15 minutes at 260 °C and 0.5 MPa pressure.

Unidirectional carbon-fiber-reinforced composite materials to be tested dynamically in the fiber direction manifest great failure strength. Various difficulties impede the testing of such high-performance composite materials. The main problems are preventing premature failure at the loading ends and material failure due to specimen bending. Denting the incident- and transmission-bar ends when loading the compression specimen should also be avoided. A compression device made of steel and suitable for high-strain-rate loading in a split-Hopkinson pressure bar as well as for quasi-static tests in a universal testing machine was developed based on these requirements (Figure 7-16).

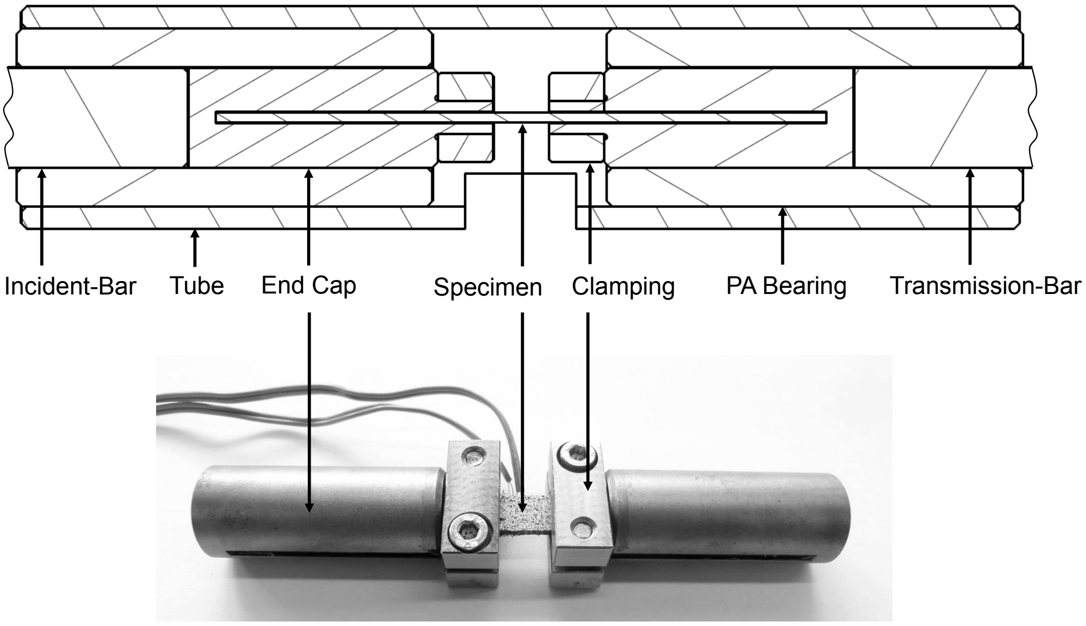

Fig. 7-16 Compression device for quasi-static and dynamic measurements.

The device's design was motivated by the well-established combined-loading-compression (CLC) device used in the ASTM D6641/D6641M [118] standard. This loading principle of introducing the compressive force into the specimen via combined end and shear loading has been found to be most suitable for testing unidirectional composite laminates. It was thus adopted for development of the high-strain-rate compression-test device presented. A simple compression device with less mass is needed for the Hopkinson-bar setup in contrast to the CLC-test fixture with its massive loading blocks, alignment rods, and fixture bolts. This is why screwed or bolted joints are infeasible for introducing force into the specimen. An adhesive joint between the specimen and the end caps was therefore chosen. With this joining technique, a region of shear is created that transmits force from the specimen's flanks to the free gauge length. The laminate is also loaded at the end surfaces, which requires exact tolerances of the composite laminate and the slotted steel end cap. The external clamps, adjacent to the free gauge section, are needed to apply additional pressure to the specimen's end caps thus enhancing internal friction between specimen's surface, the adhesive, and the end cap. All three loading mechanisms mutually contribute to introducing load into the specimen. The end cap's 18 mm diameter equals that of the bars used.

The flat, rectangular 110 mm x 8 mm x 2 mm (length x width x thickness) specimens were cut using a water-cooled diamond saw and glued into the slotted end caps using Scotch-Weld™ DP 490 adhesive from 3M for the thermoset IM7/8552 specimens and BETAMATE™ 1822 from Dow Automotive for the thermoplastic polyamide-6 specimens. While the adhesive cures, the specimens lie in a V-shaped notch of a plate rail and are fastened to ensure the specimen's and the end caps' axial alignment and parallel end surfaces. This leaves a 10 mm long free gauge section in the middle of the specimen. The tube, which can slide freely on PA bearings, surrounds the specimen and serves to guide and stabilize it while loading. Finally, the specimens were equipped with two TML FLA-3-11-1L linear strain gauges in a back-to-back configuration on the free gauge section to measure strain and possible specimen bending.

To establish a common basis for mechanical material characterization, all carbon-fiber-reinforced polyamide-6 specimens were dried in a drying oven under vacuum at 80 °C for 72 hours to minimize possible moisture effects arising from the PA 6 polymer's hygroscopic behavior. The dry specimens were stored in a multi-layer polymer-aluminum-film bag until start of the experiment to prevent moisture absorption after drying. The carbon-epoxy specimens needed no drying due to the thermoset polymer's weak hygroscopicity.

7.2.2 Quasi-static Test Setup

For each laminate (UD carbon-epoxy, QI carbon-epoxy, and UD carbon-PA 6) five quasi-static tests were performed using a Hegewald & Peschke Inspekt Table 100 electromechanical testing machine with a 100 kN load cell (Figure 7-17 left). The tests were conducted at a constant displacement rate of 0.5 mm/min, which corresponds to a quasi-static axial strain rate of approximately $8.3 \cdot 10^{-4}\,\mathrm{s}^{-1}$ when considering a 10 mm free gauge length. The load was introduced using shortened steel rods comparable in diameter to the incident- and transmission-bar (Figure 7-17 left). The strain gauges were connected to an HBM MX840A amplifier, used for data acquisition. Specimen strain was obtained by averaging the two strain gauges' signals. Quasi-static longitudinal compressive stress was calculated as the ratio of load to specimen cross section.

7.2.3 Dynamic Test Setup

Five compression specimens were tested under high-strain-rate conditions for each laminate. A split-Hopkinson pressure bar setup (Figure 7-17 right), consisting of 18 mm diameter steel striker-, incident-, and transmission-bar with respective

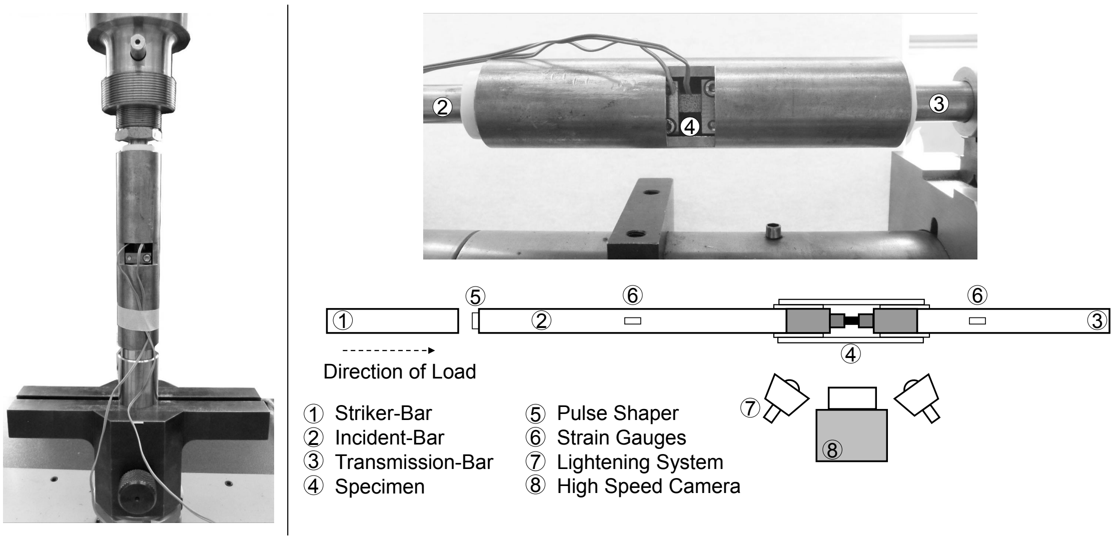

Fig. 7-17 Compression device developed in a universal testing machine for quasi-static tests (left) and in a split-Hopkinson pressure bar for dynamic tests (right).

lengths of 0.6 m, 2.6 m, and 1.6 m, was used. The strain gauges for detecting of the elastic wave were located on the incident-bar at 1.3 m and on the transmission-bar at 0.3 m away from the bar-specimen interfaces and operated with a 7 V supply voltage. The bar-gauge signals were amplified using an FE-H379-TA high-speed transducer amplifier from FYLDE Modular Instrumentation with a gain setting of 100 and a 300 kHz frequency setting. The amplified signals of the bar strain gauges and the impact velocity of the striker-bar were each recorded with a TDS2004C oscilloscope from Tektronix. A 1 mm thick copper pulse shaper with a 4 mm diameter was used. The pulse shaper provided a triangular shape, which is best suited for specimens exhibiting linear stress-strain behavior up to failure [15]. A striker-bar impact velocity of approximately 8 m/s was used for the high-strain-rate tests. As a result of the nominal specimen geometry and the striker-bar velocity, a strain rate of approximately $100\,\mathrm{s}^{-1}$ was achieved.

A bars-together (BT) test, with incident- and transmission-bar in direct contact, was conducted to verify the bar-strain-wave measurements' accuracy. The striker-bar impacted at $V_0 = 8.5\,\mathrm{m/s}$ on the copper pulse shaper at the incident-bar. Figure 7-18 shows the inverted incident-bar and transmission-bar strain signal. The measured bar strain signals indicate that the elastic wave travels from the incident-bar into the transmission-bar without changing amplitude, duration, or shape. The theoretical amplitude of $\epsilon_{\mathrm{I}}^{\max} = V_0/2c_{\mathrm{B}}$ with $c_{\mathrm{B}} = 5123\,\mathrm{m/s}$ was reached. The 1.2 % difference between the incident- and transmission-bar strain amplitudes is negligible. A correct determination of dynamic specimen stress could therefore be expected with the SHPB apparatus used.

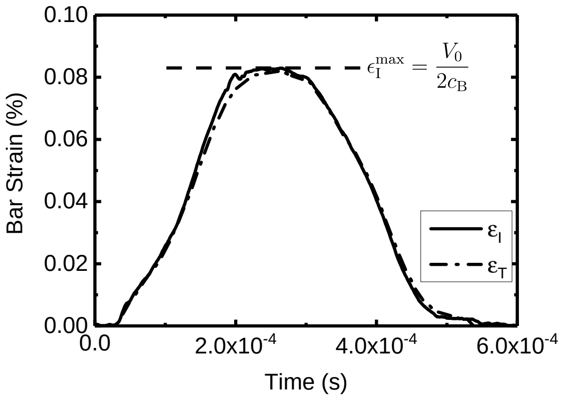

Fig. 7-18 Incident- and transmission-bar strain signals of the bars-together test with the SHPB configuration used.

The specimen with the slotted end caps was placed between the bar end surfaces. A thin layer of molybdenum disulfide lubricant was applied to the end caps' end surfaces and the incident- and transmission-bar. The specimen was thus clamped between the two bars without any additional fastening. A steel tube sliding freely on PA bearings surrounded the specimen to support the latter's alignment. The tube contained a cut-out window to monitor the specimen's deformation and failure mode via a high-speed camera. A Photron Fastcam SA-Z high-speed camera was positioned 610 mm away from the specimen's surface during the experiment to capture images of the deforming specimen and its ultimate material failure with a frame rate of 400000 fps and a resolution of 128 pixels x 96 pixels. The lens's aperture was set to f/5.6. Two LED lamps provided a well-illuminated specimen surface.

Figure 7-19 shows a representative example of the bar strain waves detected at the strain gauge on the incident-bar and at the strain gauge on the transmission-bar. These signals were filtered with a Savitzky-Golay filter to eliminate the digitalization noise from the oscilloscope without changing the overall signal shape. The dynamic test results were calculated by applying the classical SHPB analysis, which is based on one-dimensional wave-propagation theory [61], to the recorded bar-strain signals.

The forces acting on the incident-bar, F_1, and the transmission-bar, F_2, sides of the specimen are defined in section 3.1.4 by Equation 3-40 and Equation 3-41, respectively. For the dynamic stress-strain curves presented, the specimen stress, σ_S, was calculated as the ratio of F_2 to the initial specimen cross section A_S. The specimen strain and the strain rate were obtained directly from strain gauges in back-to-back configuration on the specimen's surface.

Representative examples of force-time curves are plotted in Figure 7-20. These diagrams can be used to determine whether or not specimen loading occurred under dynamic equilibrium. An equilibrium stress state within the specimen was

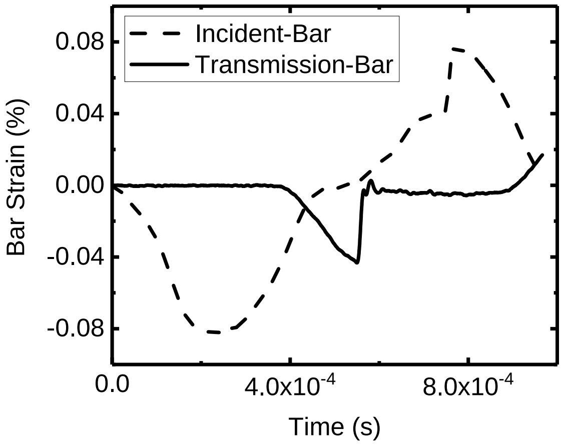

Fig. 7-19 Representative incident- and transmission-bar strain signals of a UD IM7/8552 specimen.

established if the forces acting on the specimen's incident- and the transmission-bar sides were the same from the early transient loading process until ultimate failure. It can be stated that dynamic equilibrium predominated for all test specimens.

7.2.4 Experimental Results

The quasi-static specimens were loaded at constant displacement rate until failure. The longitudinal compressive stress-strain response for all tested specimens, displayed as solid black curves, is shown together with the dynamic experimental results in Figure 7-21. The end of each curve marks the point of ultimate failure. Table 7-4 summarizes the quasi-static and dynamic measurements' results.

For quasi-static loading, a near-linear stress-strain response tending toward nonlinear behavior under higher loads was found for all three of the laminates tested. The mean quasi-static compressive strength of UD IM7/8552, QI IM7/8552, and UD carbon-PA 6 show a relatively small coefficient of variance. Using the developed experimental methodology, it was possible to measure larger static strengths for UD IM7/8552 than those obtained with a dynamic compression fixture developed earlier [15]. At the same time, the static compressive strength value closely resembled that of the longitudinal compressive strength reported for this composite material system in an earlier study [125]. Still, greater static longitudinal compressive strength can be expected for this high-performance carbon-epoxy composite. For all quasi-static unidirectional specimens of IM7/8552 and carbon-PA 6, except for one carbon-PA 6 specimen, which failed in the middle of the free gauge section, failure occurred in the form of fiber kinking in the gauge section near the grip-termination region. The measured strength can therefore be considered to stem from premature failure. In contrast, all of the quasi-isotropic IM7/8552 specimens exhibit ultimate failure

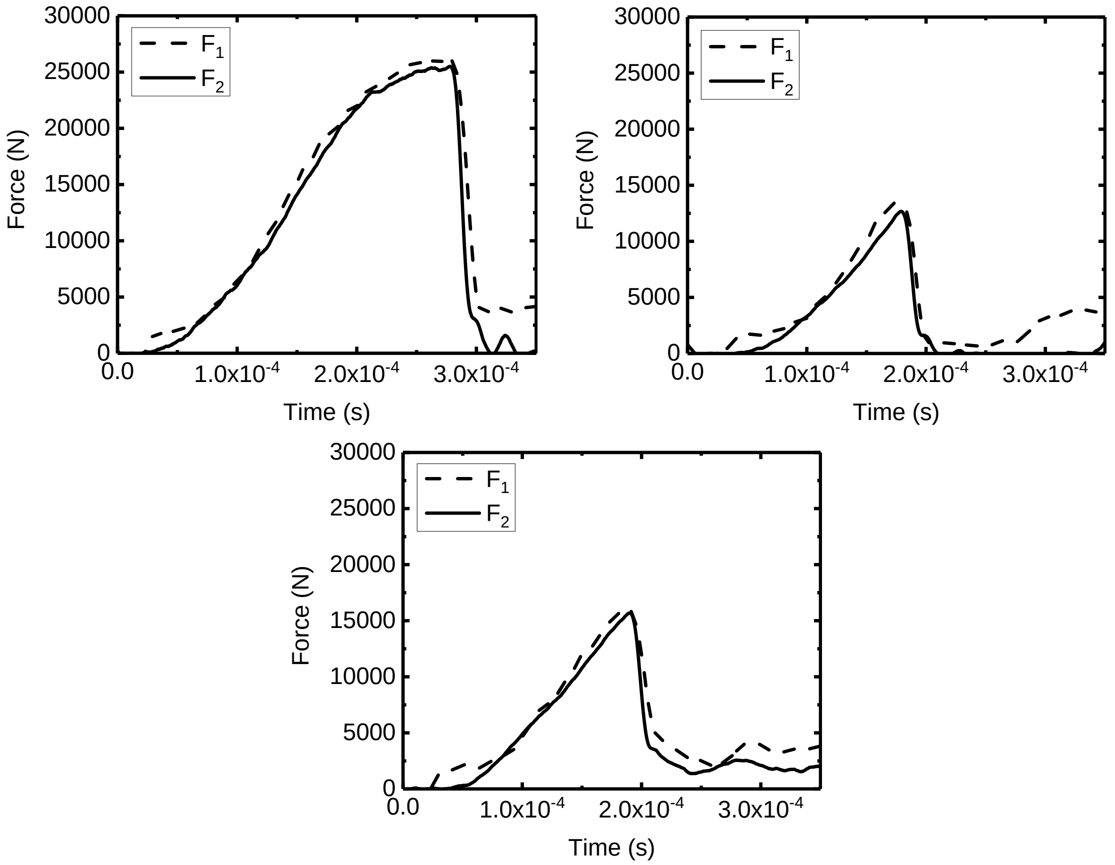

Fig. 7-20 Equilibrium check of forces acting on opposite sides of a representative specimen of UD IM7/8552 (top left), QI IM7/8552 (top right), and UD carbon-fiber-reinforced polyamide-6 (bottom).

in the middle of the free gauge section. Small variation was also observed for the dynamic-test results regardless of material and laminate type. A more pronounced tendency toward nonlinear stress-strain response was observed for each composite laminate in contrast to the quasi-static stress-strain curves. Comparing the static and dynamic stress-strain curves, the strain rate's effect on the elastic modulus appears to be insignificant. A strength increase of 41 % for UD IM7/8552, 44 % for QI IM7/8552, and 60 % for UD carbon-PA 6 with increasing strain rate was found. The dynamically tested UD specimens for IM7/8552 and carbon-PA 6 exhibited a failure mode resembling that observed during static loading. Initial failure occurred in the form of fiber kinking in the gauge section near the grip-termination region, as can be seen from the areas framed with the dashed lines in Figure 7-22 a) and c). This was followed by the laminate splitting along the fiber direction. The recorded high-speed camera images revealed that all of the QI IM7/8552 specimens ultimately failed in the middle of the free gauge section (Figure 7-22 b), dashed line).

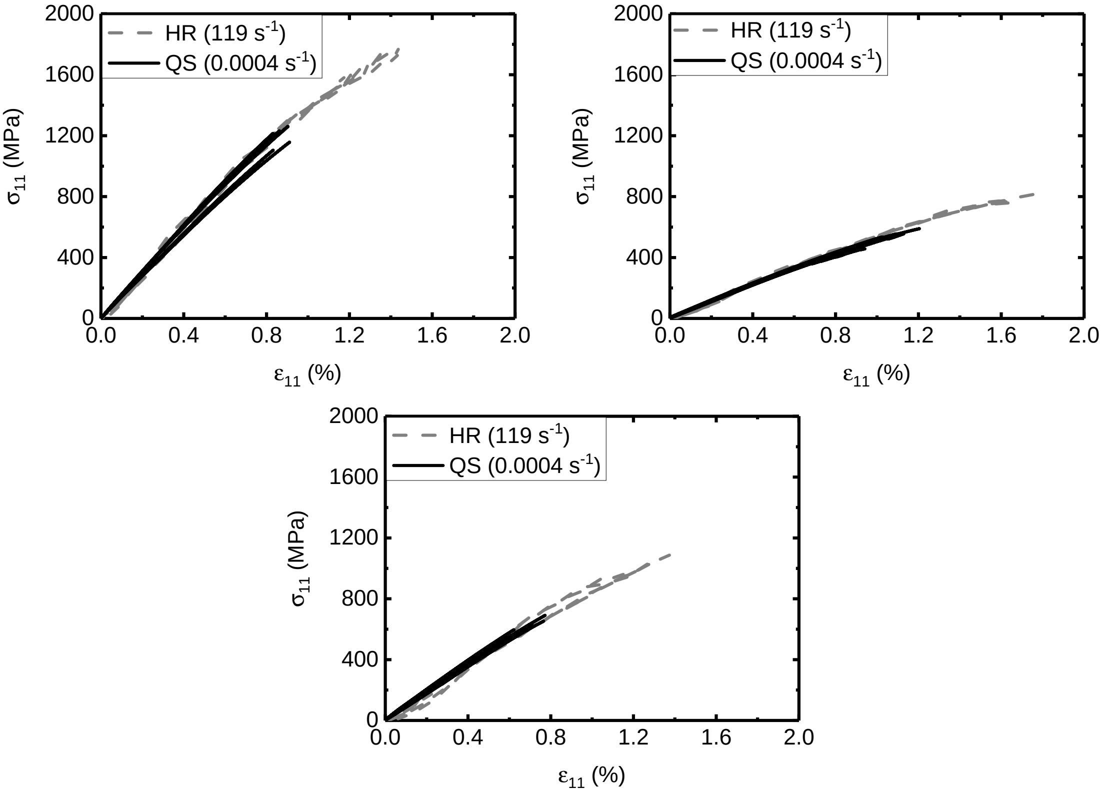

Fig. 7-21 Quasi-static and dynamic longitudinal compressive stress-strain curves for UD IM7/8552 (top left), QI IM7/8552 (top right), and UD carbon-fiber-reinforced polyamide-6 (bottom).

Tab. 7-4 Quasi-static and dynamic longitudinal compression test results.

Material	**Tests**		**Strain Rate** (s^{-1})	**Strength** (MPa)	**Failure Strain** (%)
UD IM7/8552	5	**Mean**	$8.3 \cdot 10^{-4}$	1194	0.87
		STDV	-	63	0.04
		CV (%)	-	5.2	4.4
	5	**Mean**	63	1681	1.32
		STDV	7	86	0.12
		CV (%)	11	5.1	9.4
QI IM7/8552	5	**Mean**	$8.3 \cdot 10^{-4}$	539	1.08
		STDV	-	50	0.10
		CV (%)	-	9.2	9.1
	5	**Mean**	119	774	1.65
		STDV	3	24	0.08
		CV (%)	2.6	3.1	4.8
UD Carbon-PA 6	5	**Mean**	$8.3 \cdot 10^{-4}$	626	0.70
		STDV	-	52	0.07
		CV (%)	-	8.3	10.7
	5	**Mean**	82	999	1.23
		STDV	2	61	0.11
		CV (%)	2.9	6.1	8.8

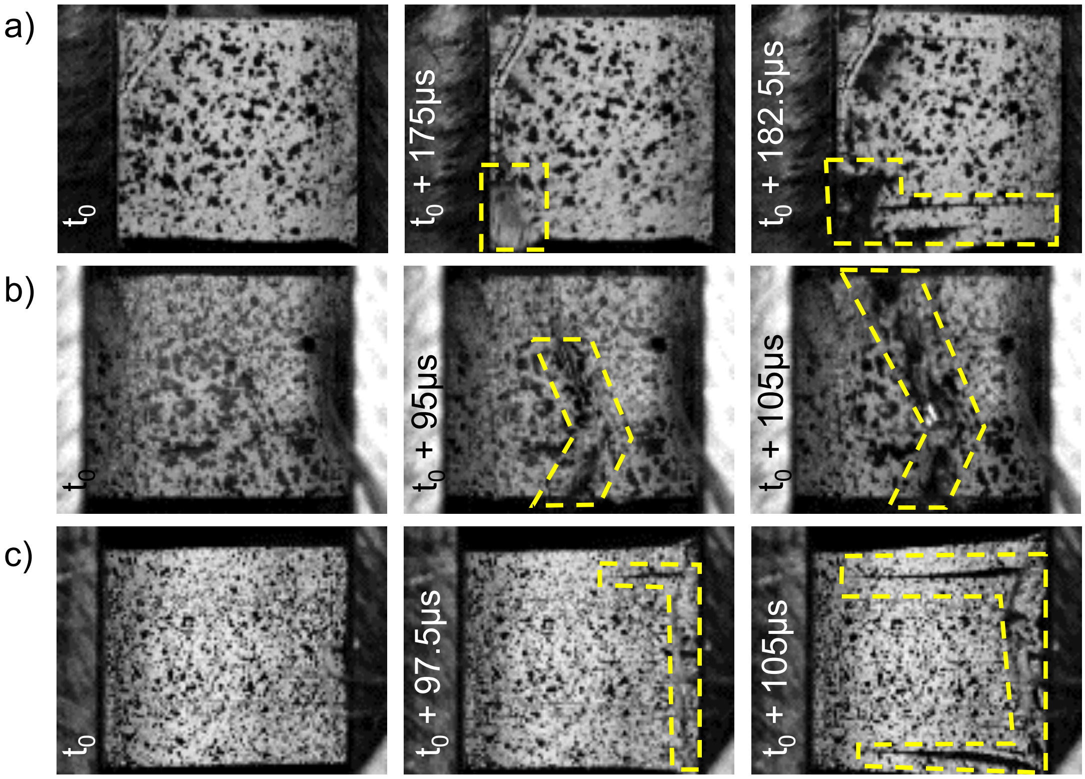
a)
b)
c)
t_0
t_0 + 175µs
t_0 + 182.5µs
t_0
t_0 + 95µs
t_0 + 105µs
t_0
t_0 + 97.5µs
t_0 + 105µs

Fig. 7-22 Failure initiation and propagation during a dynamic experiment on a UD IM7/8552 specimen (a), QI IM7/8552 specimen (b), and UD carbon-fiber-reinforced polyamide-6 specimen (c).

Following the ASTM D6641/D6641M compression-test standard [118], specimen bending during testing was evaluated using back-to-back linear strain gauges and the following equation:

$$B_y = \text{percent bending} = \frac{\epsilon_1 - \epsilon_2}{\epsilon_1 + \epsilon_2} \cdot 100. \tag{7-1}$$

In this case, ϵ_1 denotes the strain of strain gauge number 1 and ϵ_2 that of strain gauge number 2. Percent bending was calculated for each specimen and plotted as a function of longitudinal strain to verify the tests' validity. Figure 7-23 shows the results of the quasi-static longitudinal compression tests. At failure, most specimen show a bending response less than or approaching the ±10 % criterion from ASTM D6641/D6641M [118]. The standard states that as much as 30 % to 40 % bending may not significantly affect the compressive strength value obtained. No significant difference was observed between the measured elastic modulus or strength of specimens outside of the ±10 % range and that of the specimens satisfying the ±10 % criteria. All of the static specimens were therefore considered to be valid. Figure 7-24 shows the same diagram for all of the specimens tested at high strain rate and it is apparent that the bending behavior lies within the ±10 % criterion defined in the ASTM standard [118].

Maintaining a constant strain rate during the experiment is another essential requirement for validly determining dynamic material properties. The strain signal's time derivative was thus calculated for each test to obtain the strain rate. Figure 7-25 shows a representative example with a strain rate and stress curve as functions of time. The dashed vertical lines mark the start and end of specimen loading. The strain rate's mean value (Table 7-4) is calculated for this time interval.

7.2.5 Discussion of Experimentally and Analytically Derived Material Properties

Further analysis was performed to determine whether the measured strain-rate sensitivity of the IM7/8552 represents the material's actual behavior. It is known that stress concentrations near the grip-termination region induce failure, as observed for the UD IM7/8552 laminate. The material can thus be assumed to have failed prematurely, yielding a lower ultimate failure strength in the tested material. Since a valid failure mode with failure in the middle of the gauge section and percent bending values within the suggested interval was observed for the quasi-isotropic IM7/8552 laminate, the longitudinal compressive strength, σ_x^0, of a UD ply is determined from the QI laminate's static and dynamic experimental data using a methodology that Welsh and Adams proposed [128, 129]. The multi-directional

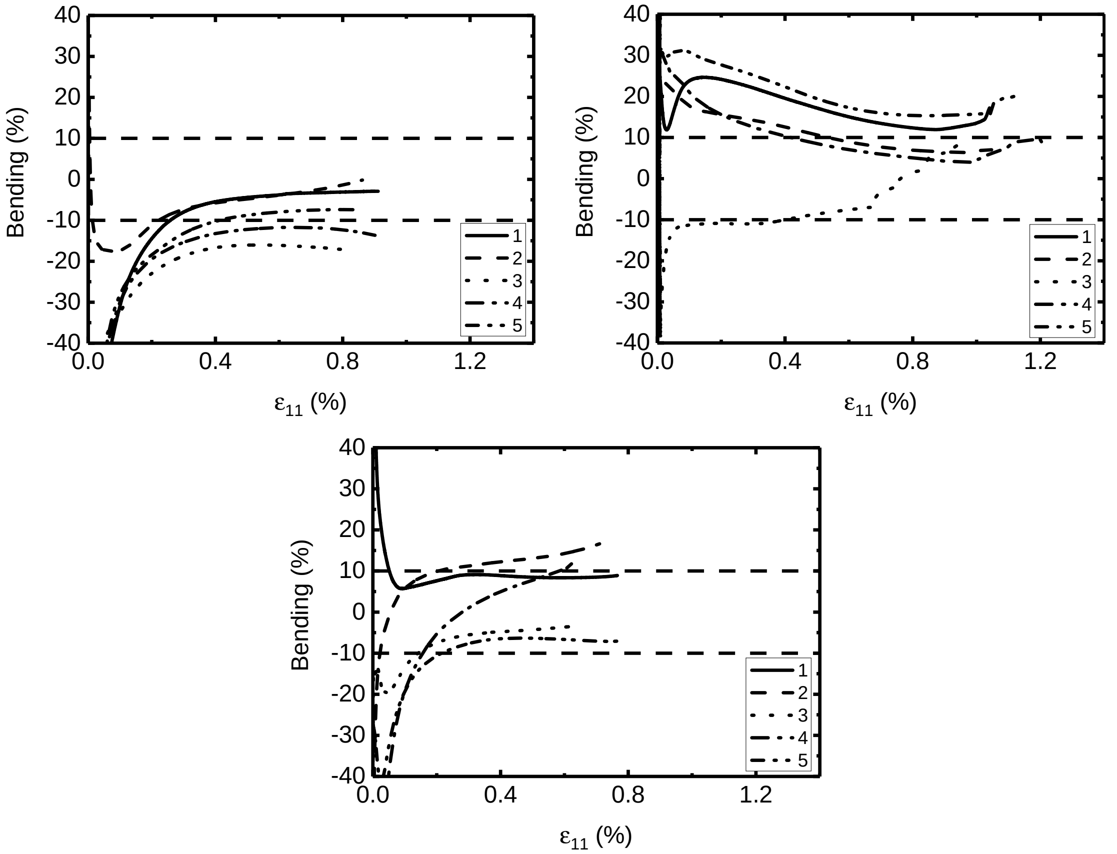

Fig. 7-23 Bending behavior as a function of longitudinal strain for all quasi-static UD IM7/8552 (top left), QI IM7/8552 (top right), and UD carbon-fiber-reinforced polyamide-6 (bottom) specimens.

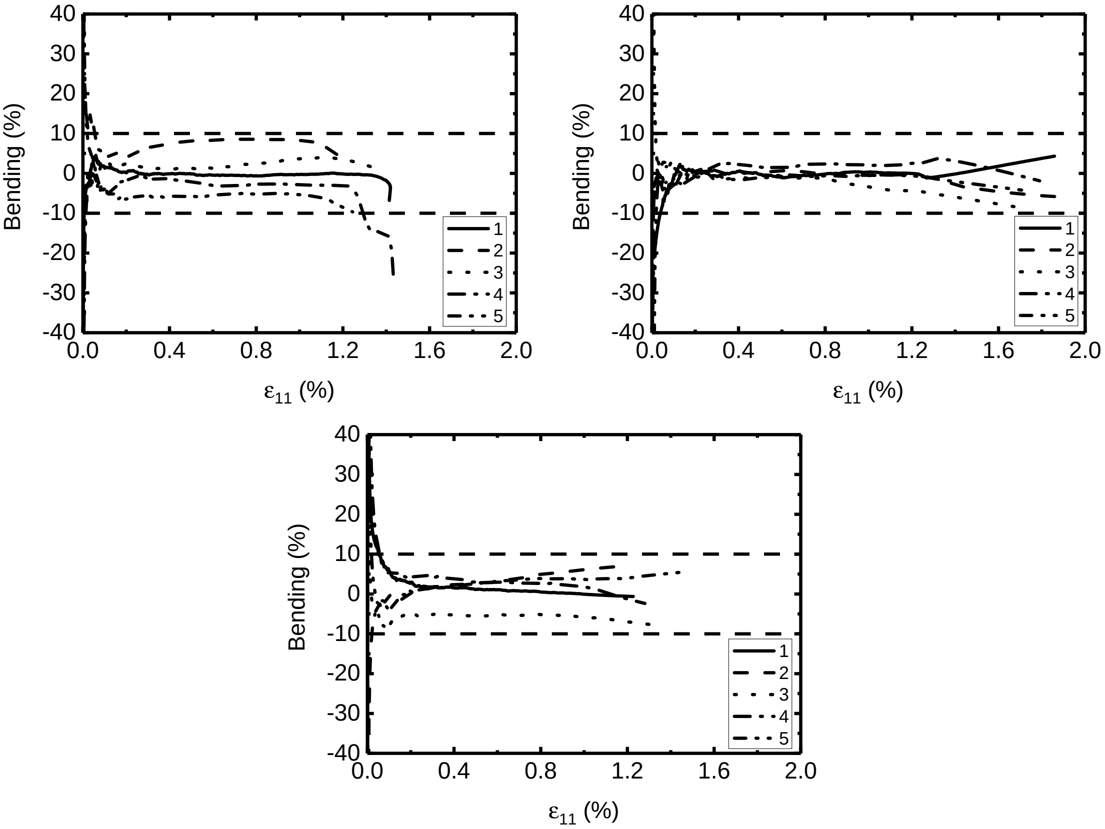

Fig. 7-24 Bending behavior as a function of longitudinal strain for all dynamic UD IM7/8552 (top left), QI IM7/8552 (top right), and UD carbon-fiber-reinforced polyamide-6 (bottom) specimens.

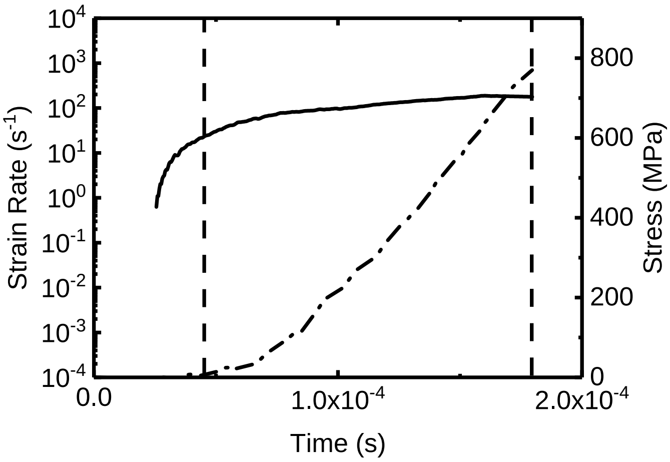

Fig. 7-25 Strain rate and stress as a function of time of a representative QI IM7/8552 specimen. Dashed vertical lines indicate time interval in which the mean strain rate is calculated.

laminate's measured compressive strength, $\sigma_{\mathrm{multi-directional}}$, is thereby multiplied by a back-out factor (BF):

$$\sigma_x^0 = \mathrm{BF} \cdot \sigma_{\mathrm{multi-directional}}. \tag{7-2}$$

The back-out factor is given by the following equation, which is based on classical laminate theory:

$$\mathrm{BF} = (Q_{11}a_{11} + Q_{12}a_{12})t. \tag{7-3}$$

The laminate's thickness is determined by t. Q_{ij} defines the ijth element in the plane-stress reduced-stiffness matrix for unidirectional lamina. It is obtained from the basic in-plane elastic properties: Young's modulus in the longitudinal direction, E_1, the major Poisson's ratio, ν_{12}, and the minor Poisson's ratio, ν_{21}:

$$Q_{11} = \frac{E_1}{1 - \nu_{12}\nu_{21}} \tag{7-4}$$

and

$$Q_{12} = \frac{\nu_{21}E_1}{1 - \nu_{12}\nu_{21}}. \tag{7-5}$$

The variables a_{11} and a_{12} are defined as follows:

$$a_{11} = \frac{A_{22}A_{66}}{d} \tag{7-6}$$

and

$$a_{12} = \frac{-A_{12}A_{66}}{d} \tag{7-7}$$

with

$$d = A_{11}A_{22}A_{66} - A_{12}^2A_{66}. \tag{7-8}$$

A_{ij} represents the ijth element in the ABD matrix from classical laminate theory:

$$A_{11} = Q_{11}\cos^4\Theta + 2(Q_{12} + 2Q_{66})\sin^2\Theta\cos^2\Theta + Q_{22}\sin^4\Theta + 0.5\cdot Q_{11} + 0.5\cdot Q_{22} \tag{7-9}$$

$$A_{22} = A_{11} \tag{7-10}$$

$$A_{12} = Q_{12}(\sin^4\Theta + \cos^4\Theta) + (Q_{11} + Q_{22} - 4Q_{66})\sin^2\Theta\cos^2\Theta + Q_{12} \tag{7-11}$$

$$A_{66} = (Q_{11} + Q_{22} - 2Q_{12} - 2Q_{66})\sin^2\Theta\cos^2\Theta + Q_{66}(\sin^4\Theta + \cos^4\Theta) + Q_{66} \tag{7-12}$$

$$\Theta = \pi/4. \tag{7-13}$$

Table 7-5 summarizes the IM7/8552 composite material's in-plane elastic material properties, which were used in this study to calculate the static and dynamic back-out factor.

Tab. 7-5 IM7/8552 material properties used to compute the static and dynamic back-out factor, BF.

Variable	**Value for**		**Reference**
	static BF	**dynamic BF**	
E_1	150000 MPa		Property not strain-rate dependent Experiment (this study) Koerber and Camanho [15] IM7/8552 Data Sheet [127]
E_2	8930 MPa	10019 MPa	Koerber et al. [14]
G_{12}	5068 MPa	6345 MPa	Koerber et al. [14]
ν_{12}	0.32		Camanho and Lambert [125]
ν_{21}	0.019		Equation: $\nu_{21} = \nu_{12} E_2 / E_1$

Each strength value determined for the quasi-isotropic IM7/8552 laminate at quasi-static and high strain rate was multiplied by the respective static and dynamic back-out factors while taking the individual laminate thickness for each specimen into consideration. The analytically derived longitudinal compressive strength at quasi-static and high strain rate thus yields respectively 1454 MPa and 2008 MPa. The experimentally and analytically obtained longitudinal compressive strength, X_c, of IM7/8552 is compared in Figure 7-26. As expected from the observed failure mode, the longitudinal compressive strength values derived from the quasi-isotropic laminate were greater than those measured for the unidirectional laminate. For both static and dynamic loading, a difference of about 17 % was observed when comparing the longitudinal compressive strength measured for the UD laminate with that derived from the QI laminate using the analysis described above. The strength increase with increasing strain rate for the predicted longitudinal compressive strength obtained from measurement of a QI laminate is 38.09 %. A very similar increase of 40.78 % was measured for the UD laminate tested in this study, despite the observed premature failure mode. Both results again closely resemble the 39.33 % strength increase that Koerber and Camanho report [15], where premature failure and relatively low longitudinal compressive strengths were also achieved for the tested UD laminate. Regardless of the differences between the experimental setup used in the present study and that used in [15], and regardless of whether a valid or premature failure mode was achieved, the increase in longitudinal compressive strength, X_c, of the UD carbon-epoxy IM7/8552 from static to high strain-rate loading at 100 s^{-1} manifests itself as about 40 %. Using the new dynamic test setup presented in this study with the approach of testing a multi-directional laminate, which yields a valid compressive failure in the specimen's free gauge section, then calculating the longitudinal compressive strength of the embedded 0°-UD ply via the procedure outlined above, the strain rate's effect on the longitudinal compressive strength of UD carbon-epoxy IM7/8552 was not only quantified, but realistic dynamic strengths were achieved for the first time.

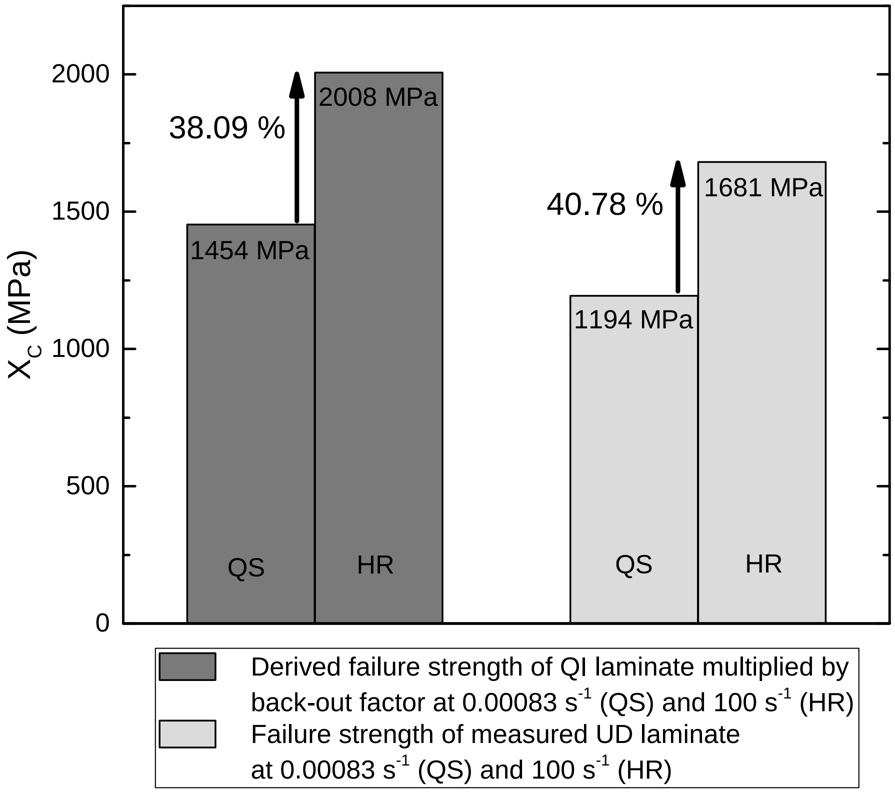

Fig. 7-26 Comparison of the predicted IM7/8552 longitudinal compressive strength by measurement of a quasi-isotropic laminate and the longitudinal compressive strength by measurement of a unidirectional laminate for two different strain rates.

The carbon-fiber-reinforced polyamide-6 composite material's longitudinal compression results agree with published data from Ploeckl et al. [121], where in contrast to this study, an end-loaded compression specimen geometry with additional tabs was used for the quasi-static and dynamic tests. As observed in the present work, failure occurred near the tab termination region. In [121], a quasi-static compressive strength of (605 ± 99) MPa was measured compared to the (626 ± 52) MPa strength determined in this study. During the high-strain-rate tests $(100\,\mathrm{s}^{-1})$ in [121], performed with an SHPB, a longitudinal compressive strength of about (975 ± 63) MPa was measured. This closely resembles the (999 ± 61) MPa value determined in the present work. The same static and dynamic longitudinal compressive strength was measured for the carbon-fiber-reinforced polyamide-6 composite despite the very different specimen geometries used in each study.

7.3 Strain Rate in Kink-Bands

Motivation

In Figure 7-27 the normalized strength of the transversal and longitudinal compression loading results of the carbon-fiber-reinforced polyamide-6 composite material as a function of strain rate are shown. The transverse compressive strength at about $175\,\mathrm{s}^{-1}$ increases 41 %. In comparison the longitudinal compressive strength at approximately $100\,\mathrm{s}^{-1}$ increases 61 %, i.e. a discrepancy of 20 % in strength is measured at this strain rate. This result is remarkable, because the strain rate sensitivity is not caused by the carbon fibers (see introduction of chapter 4, [54, 96, 97]).

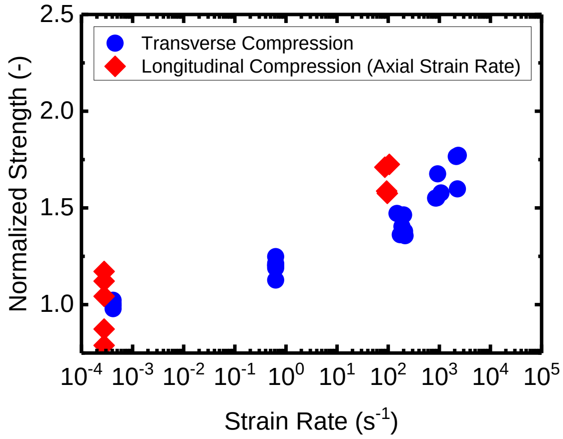

Fig. 7-27 Normalized strength as a function of the axial strain rate for transversal and longitudinal compression.

The strain rates of the longitudinal compressive results are determined by calculating the time derivative of the strain in axial loading direction. Thus the question arises if the axial strain rate represents the real strain rate in the instant of specimen failure. Therefore a closer look at the mechanics of the failure mode involving fiber compression is necessary. In fiber-reinforced composites kinking of the material occurs. Thereby a localized shear deformation along a band across the specimen evolves, in which the fibers have rotated by a large amount and finally break at the band edges or in the band interior. The initial misalignment of the fibers causes shear stress between the fibers. As a consequence the shear stresses cause a rotation of the fibers which in turn increases the shear stresses. In chapter 6 concerning the in plane shear response by the tensile test of a ±45 ° laminate, the strain was not calculated in axial but in the shear direction of ±45 °. The same consideration regarding the fiber angle in comparison to the axial load direction can now be transferred to the kink-band failure mode. The objective of the following discussion is now to calculate the strain and hence the strain rate in the kink-band. It is assumed that the strain rate in the kink-band is significantly higher than in the axial loading direction. The consequence of this considerations would be, that the normalized strength values (Figure 7-27) would be shifted to higher strain rates and the discrepancy to the transverse strength values decreases. This would underpin that the dominating factor of the strain rate sensitivity is the viscoelastic behavior of the matrix and thus it is assumed that the strain-rate effect in transverse and longitudinal compression is the same.

2D Kink-Band Model

In the following section the 2D kinking model proposed by Pinho et al. [130] is introduced. This model is based on the approach of Argon [131] and the later developments of Dávila et al. [132–134]. A schematic drawing of a kink-band and the misalignment frame at failure is shown in Figure 7-28. For the differentiation of the used coordinate systems, subscripts for the stresses are used. The subscript m is applied to the misalignment frame at failure and the subscript mc stands for the misalignment frame at failure but for pure axial compression. Assuming a generic plane stress loading, the stresses in the misalignment frame are given by [130]:

$$\sigma_{\mathrm{a^m}} = \frac{\sigma_{\mathrm{a}} + \sigma_{\mathrm{b}}}{2} + \frac{\sigma_{\mathrm{a}} - \sigma_{\mathrm{b}}}{2} \cos(2\theta_{\mathrm{c}}) + \tau_{\mathrm{ab}} \sin(2\theta_{\mathrm{c}}), \tag{7-14}$$

$$\sigma_{\mathrm{b^m}} = \frac{\sigma_{\mathrm{a}} + \sigma_{\mathrm{b}}}{2} - \frac{\sigma_{\mathrm{a}} - \sigma_{\mathrm{b}}}{2} \cos(2\theta_{\mathrm{c}}) - \tau_{\mathrm{ab}} \sin(2\theta_{\mathrm{c}}), \tag{7-15}$$

$$\tau_{\mathrm{a^m b^m}} = -\frac{\sigma_{\mathrm{a}} - \sigma_{\mathrm{b}}}{2} \sin(2\theta_{\mathrm{c}}) + \tau_{\mathrm{ab}} \cos(2\theta_{\mathrm{c}}). \tag{7-16}$$

The misalignment angle at failure, θ_{c}, is defined as the sum of the initial misalignment angle, θ_{i}, and the rotation due to loading:

$$\theta_{\mathrm{c}} = \theta_{\mathrm{i}} + \gamma_{\mathrm{m}}. \tag{7-17}$$

The stresses in the misalignment frame for pure compression ($\sigma_{\mathrm{a}} = -X_{\mathrm{c}}$, $\sigma_{\mathrm{b}} \equiv \tau_{\mathrm{ab}} \equiv 0$) are:

$$\sigma_{\mathrm{a^m}} = -\frac{X_{\mathrm{c}}}{2} + (1 + \cos(2(\theta_{\mathrm{i}} + \gamma_{\mathrm{m}}))), \tag{7-18}$$

$$\sigma_{\mathrm{b^m}} = -\frac{X_{\mathrm{c}}}{2} + (1 - \cos(2(\theta_{\mathrm{i}} + \gamma_{\mathrm{m}}))), \tag{7-19}$$

$$\tau_{\mathrm{a^m b^m}} = \tau_{\mathrm{m}} = \frac{X_{\mathrm{c}}}{2} \sin(2(\theta_{\mathrm{i}} + \gamma_{\mathrm{m}})). \tag{7-20}$$

Applying the small angle approximation to the shear stress, τ_{m}, yields:

$$\tau_{\mathrm{m}} \approx X_{\mathrm{c}}(\theta_{\mathrm{i}} + \gamma_{\mathrm{m}}). \tag{7-21}$$

It has to be noted that the initial misalignment angle, θ_i, has a strong influence on the strain rate calculation. Therefore a determination and verification of the initial misalignment angle is performed prior to the strain rate calculation.

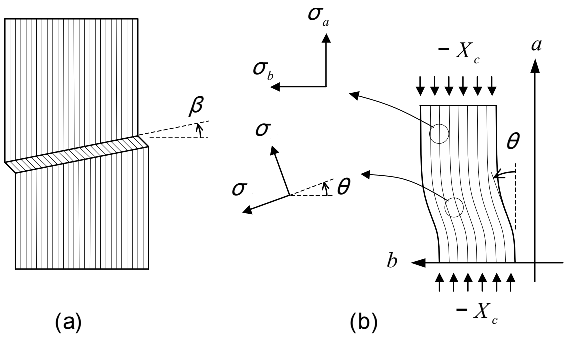

(a) (b)

Fig. 7-28 (a) Kinking band; (b) fiber misalignment frame [130].

Determination and Verification of the Initial Misalignment Angle θ_i

For the determination of the initial misalignment angle Equation 7-17 is used. Besides θ_i the misalignment angle at failure θ_c is also unknown. The rotation of the fibers or rather the shear non-linearity of the thermoplastic composite material can be approximated by using the Ramberg-Osgood Fit [135]. Equation 7-17 is thus given by:

$$\theta_\mathrm{c} \overset{!}{=} \theta_\mathrm{i} + \frac{\sigma_\mathrm{a}\sin(2\theta_\mathrm{c})}{2G_{12}} + \left(\frac{\sigma_\mathrm{a}\sin(2\theta_\mathrm{c})}{2A}\right)^n . \tag{7-22}$$

In chapter 6 the shear stress-strain behavior of the carbon-fiber-reinforced polyamide-6 composite material was investigated. The three quasi-static stress-strain curves of this ±45 ° tensile tests where taken and a mean value curve was calculated. In Figure 7-29 this mean value curve of the experimental in-plane shear data is denoted as black solid line.

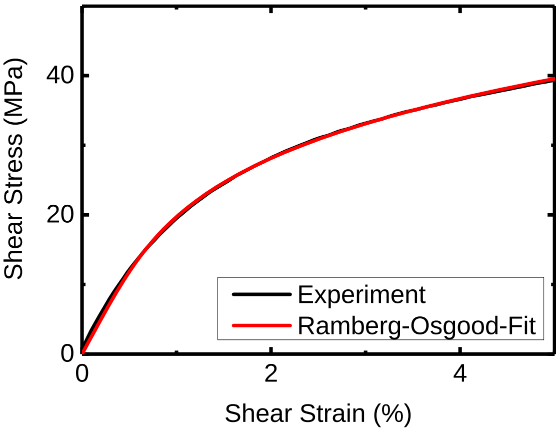

Fig. 7-29 In-plane shear curve from dynamic experiment and Ramberg-Osgood fit curve.

The mean value curve was taken and approximated with the Ramberg-Osgood Fit (red sold line in Figure 7-29). The fitting parameters are: $G_{12} = 2500$, $A = 92$, and $n = 4$.

To solve Equation 7-22 with two unknown variables, θ_i and θ_c, and the substituted fitting parameters, an iterative process is performed (Figure 7-30). The quasi-static stress state (σ_a) is determined via Table 7-1 in which the quasi-static longitudinal reference test results are listed. The highest measured strength value of the composite material with $\sigma_\mathrm{a} = -708.66\,\mathrm{MPa}$ is used because this represents the maximum loading condition under pure compression which the material can withstand. Substituting σ_a and the fitting parameters into Equation 7-22 yields:

$$\theta_\mathrm{c} \overset{!}{=} \theta_\mathrm{i} + \frac{708.66\sin(2\theta_\mathrm{c})}{2\cdot 2500} + \left(\frac{708.66\sin(2\theta_\mathrm{c})}{2\cdot 92}\right)^4 . \tag{7-23}$$

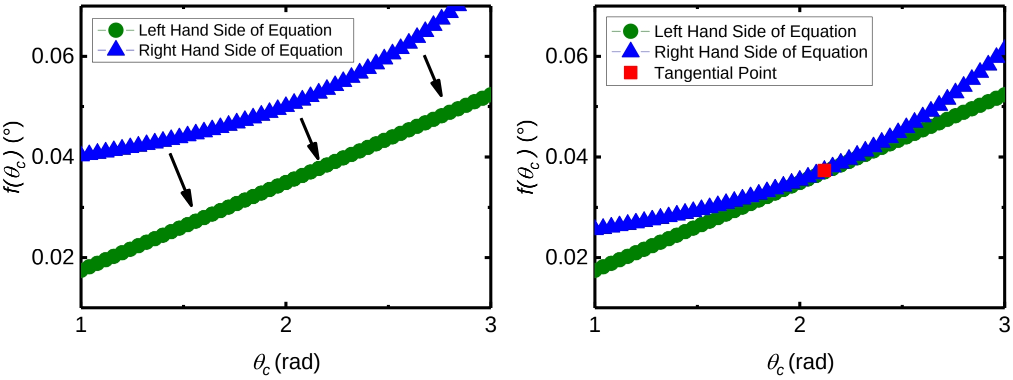

Fig. 7-30 Iterative process to find tangential point for example $\theta_\mathrm{i} = 2°$ (left) and $\theta_\mathrm{i} = 1.16°$ (right) (Equation 7-23).

In the here chosen iterative process, a solution is found by varying the angle θ_i such that the right hand side of the Equation 7-23 is equal to the left hand side of the Equation 7-23. In Figure 7-30 the left diagram shows the left and right hand side of the Equation 7-23 for an arbitrary chosen angle of $\theta_\mathrm{i} = 2°$. There, no tangential point is found for the curves. By choosing smaller angles the blue curve is shifted towards the green curve (black arrows in Figure 7-30). A tangential point is found at an angle of $\theta_\mathrm{i} = 1.16°$ (Figure 7-30 right diagram). Pinho et al. [130] proposes that the initial misalignment angle is a material property. It can be regarded as an equivalent angle that involves different defects. For instance micostructural defects, microcracks in the resin or oscillations in the fiber volume fraction or in the bonding to the resin. In this consideration about the calculation of the strain rate in a kink-band, the now calculated material parameter, θ_i, can be verified, because it should be the same for the quasi-static and dynamic specimens. A sketch in Figure 7-31 shows as a first part the determination by an iterative process to yield, θ_i, and as a second part the verification process. In the following the verification loop with the three steps "Iterative calculation of σ_a at dynamic stress state", "Comparison of σ_a with experimental value", and " Verification of θ_i" is described.

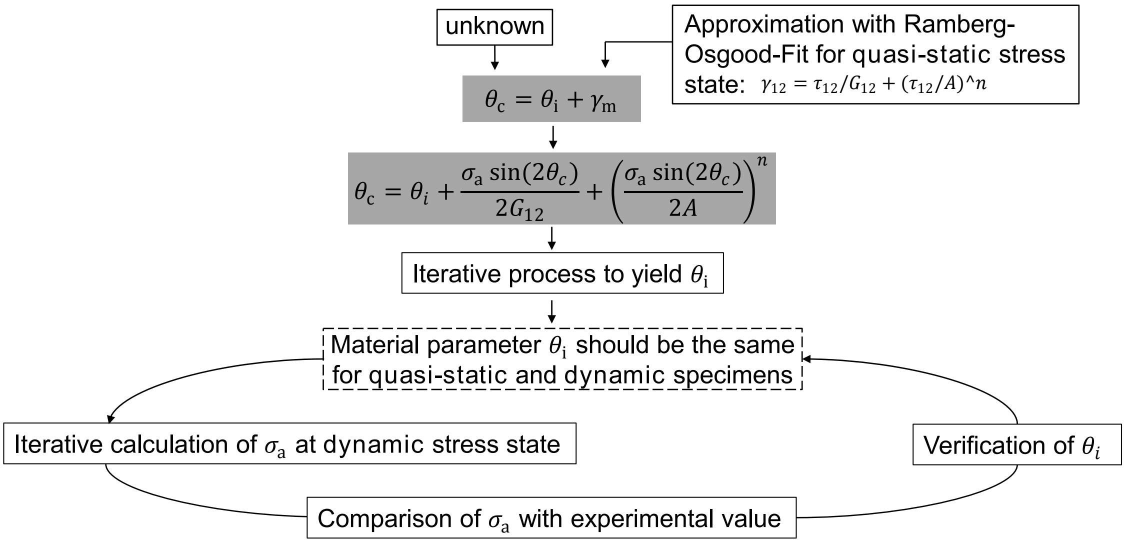
unknown
Approximation with Ramberg-Osgood-Fit for quasi-static stress state: $\gamma_{12} = \tau_{12}/G_{12} + (\tau_{12}/A)^\wedge n$
$\theta_c = \theta_i + \gamma_m$
$\theta_c = \theta_i + \frac{\sigma_a \sin(2\theta_c)}{2G_{12}} + \left(\frac{\sigma_a \sin(2\theta_c)}{2A}\right)^n$
Iterative process to yield θ_i
Material parameter θ_i should be the same for quasi-static and dynamic specimens
Iterative calculation of σ_a at dynamic stress state
Verification of θ_i
Comparison of σ_a with experimental value

Fig. 7-31 Scheme for the determination and verification of the initial misalignment angle, θ_i.

As a first step of the verification loop an iterative computation is performed to find σ_a in the dynamic stress state. Therefore the Equation 7-22 is solved iterativley by using the previous computed angle of 1.16° for θ_i. The fitting parameters ($G_{12} = 2300$, $A = 107$, and $n = 6$) were determined from the mean value curve of the dynamic in-plane shear stress-strain curves (Figure 7-32). It has to be noted that the in-plane shear curves were measured at a strain rate of approximately $520\,\mathrm{s}^{-1}$ and not at a strain rate of about $100\,\mathrm{s}^{-1}$ which is considered in this case for the calculation. It can be seen later in the strain rate diagram 8-1 which summarizes all results from the compression, tension, and shear tests of the studied fiber-reinforced thermoplastic composite, that the shear strengths within the strain rate regime from $100\,\mathrm{s}^{-1}$ to $500\,\mathrm{s}^{-1}$ might change in a maximum of 10 %.

Substituting the appropriate fitting parameters of the dynamic stress state into Equation 7-22 yields:

$$\theta_c \overset{!}{=} \theta_i + \frac{\sigma_a \sin(2\theta_c)}{2 \cdot 2300} + \left(\frac{\sigma_a \sin(2\theta_c)}{2 \cdot 107}\right)^6 . \tag{7-24}$$

A solution for the above equation is found by varying σ_a. The tangential point is reached at 998 MPa (Figure 7-33). At this computed stress state it is predicted that under dynamic compressive loading kinking in the specimen occurs and leads to final failure of the unidirectional fiber-reinforced polymer. This value can now be compared with the measured longitudinal compressive strength of 975 MPa at high strain rate which is listed in the Table 7-3. The difference between the measured and predicted dynamic longitudinal compressive strength is only 2.4 %. Thus it is concluded that the initial misalignment angle of $\theta_\mathrm{i} = 1.16°$, determined from the quasi-static load case, is also valid for dynamic loading and therefore represents a material parameter. The following considerations and calculations of the strain rate in a kink-band are hence based on this angle.

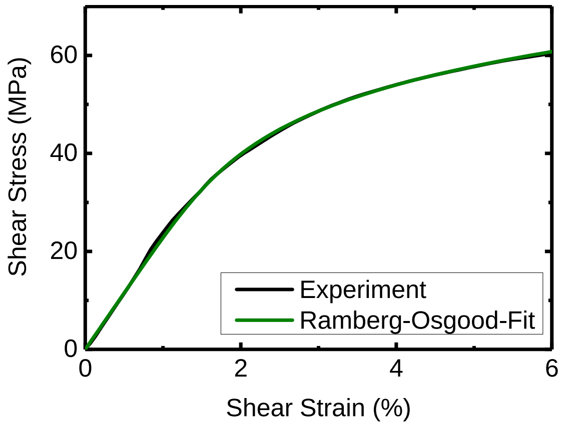

Fig. 7-32 In-plane shear curve from dynamic experiment and Ramberg-Osgood fit curve.

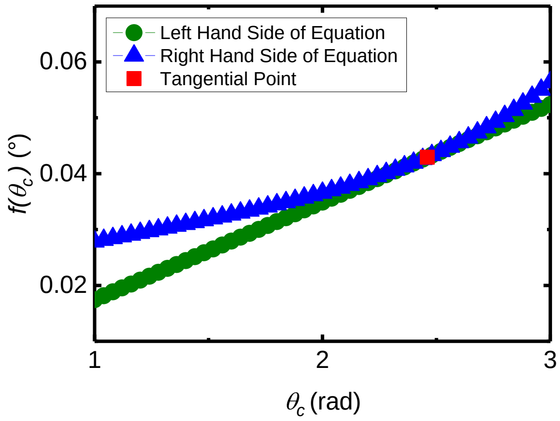

Fig. 7-33 Iterative process to find tangential point for 1.16° (dynamic fitting parameters).

Shear Strain in a Kink-Band

For the strain rate calculation in a kink-band the shear strain in the kink-band region has to be determined. From the constitutive law it is known that the shear stress at failure is a function of the shear strain:

$$\tau_\mathrm{m} = f_\mathrm{CL}(\gamma_\mathrm{m}). \tag{7-25}$$

For a material with linear shear behavior the constitutive law is defined as:

$$\tau_{\mathrm{m}} = G_{\mathrm{ab}}\gamma_{\mathrm{m}}. \tag{7-26}$$

This equation is commonly known as Hooke's Law. For a material with non-linear shear behavior, $f_{\mathrm{CL}}(\gamma_{\mathrm{m}})$, is derived from experimental shear stress-strain curves [130]. Furthermore the shear stress, τ_{m}, in the misalignment frame for pure compression is known (Equation 7-21). This yields [130]:

$$f_{\mathrm{CL}}(\gamma_{\mathrm{m}}) \approx X_{\mathrm{c}}\gamma_{\mathrm{m}} + X_{\mathrm{c}}\theta_{\mathrm{i}}. \tag{7-27}$$

The left hand side (LHS) of Equation 7-27 represents the shear stress-strain material law. The right hand side (RHS) of Equation 7-27 is defined by the shear stress in a rotated coordinate system which results from the compressive longitudinal loading of the unidirectional fiber-reinforced composite material. In Figure 7-34 the LHS and RHS are schematically visualized for different cases of failure onset.

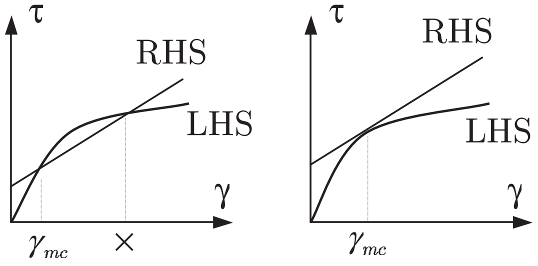

Fig. 7-34 Left and right hand side of Equation 7-27 for a material with a nonlinear shear behavior and failure by matrix cracking (left), and failure by instability (right) [136].

With increasing compressive loading the RHS curve, representing a general stress level, shifts up. At the point where the LHS curve intersects with the RHS curve the strain in the misalignment frame, γ_{m}, is defined, because then it is equal for the left and right hand side of Equation7-27. When the failure of the materials occurs the compressive stress equals X_{c} and the strain in the misalignment frame is then denoted as γ_{mc}. For materials with nonlinear shear behavior more than one intersection point might emerge. There the first intersection of the two curves defines the strain in the misalignment frame γ_{mc} because there the energy state is lower than at the second intersection (Figure 7-34). In this case the compressive strength measured for pure longitudinal compression is due to matrix failure [130]. A matrix failure criterion, such as the LaRC02/03 matrix failure criterion from Dávila et al. [132, 133] can be applied to predict failure. If the LHS and RHS curves are tangential to each other, failure might result due to an elastic instability of the matrix and not only by matrix cracking (Figure 7-34). Any further increase of the compressive stress will never lead to a situation of intersection of the curves and thus no equilibrium position is reached. Pinho et al. [130] physical interpretation of this case is that due to an unstable rotation of the fibers, denoted as instability, a catastrophic failure of the material is the result of the applied compressive stress, rather than matrix cracking.

Calculation of the Strain Rate in a Kink-Band

In the work of Pinho et al. [130], where the fiber-kinking model is described, no further considerations have been made to calculate the strain rate in a kink-band. To the knowledge of the author no other publications are present that describe the strain rate during fiber kinking. Therefore a subsequent approach needed to be found in this study.

The strain rate itself is based on the time-dependent behavior of the strain. So far no variable is considered to change with time in the above Equation 7-27. A closer look at the equation shows that the pure compressive state not only can be described with the ultimate failure strength, X_c, but also with a time-dependent stress variable, $\sigma_\mathrm{c}(t)$. Hence not only the shear strain at failure can be computed but also shear strains at lower loading levels and instants of time respectively. Thus the shear law is defined as:

$$f_\mathrm{CL}(\gamma_\mathrm{m}) \approx \sigma_\mathrm{c}(t)\gamma_\mathrm{m} + \sigma_\mathrm{c}(t)\theta_\mathrm{i}. \tag{7-28}$$

This equation can now iteratively be solved to yield γ_m. The following listing gives an overview of the known variables:

- $f_\mathrm{CL}(t)$ is given by the experimental shear stress-strain curve at high strain rate (Figure 7-32, Experiment).
- $\sigma_\mathrm{c}(t)$ are given stress values (Table 7-6) from experiment at different instants of time ($\sigma_\mathrm{c1}(t_1)$, $\sigma_\mathrm{c2}(t_2)$, $\sigma_\mathrm{c3}(t_3)$ etc.).
- θ_i is given by 1.16°.

Figure 7-35 shows an example for Equation 7-28. The LHS represents the experimental shear stress-strain curve and the straight lines are the RHS for different $\sigma_\mathrm{c1}(t_1)$, $\sigma_\mathrm{c2}(t_2)$, $\sigma_\mathrm{c3}(t_3)$ etc. listed in Table 7-6. The intersection and tangential points determine the shear strain in the misalignment frame at these stress levels (Table 7-6). In the example of Figure 7-35 the failure initiation starts with matrix cracking at 983 MPa and then an unstable rotation of the fibers occur. The derivative of the shear strain at 983 MPa determines then the strain rate, $\dot{\gamma}$, in the misalignment frame - kink-band - at the initial failure of the specimen. Thus the slope of the

Tab. 7-6 Stress and corresponding time values of a typical dynamic longitudinal compression test and shear strain calculated with Equation 7-28 (intersection and tangential points in Figure 7-35).

t (s)	σ_c (MPa)	γ_m (-)
$8.33 \cdot 10^{-5}$	465	$4.9 \cdot 10^{-3}$
$1.10 \cdot 10^{-4}$	643	$7.6 \cdot 10^{-3}$
$1.32 \cdot 10^{-4}$	838	$11.2 \cdot 10^{-3}$
$1.48 \cdot 10^{-4}$	961	$16.8 \cdot 10^{-3}$
$1.53 \cdot 10^{-4}$	983	$23.2 \cdot 10^{-3}$
$1.61 \cdot 10^{-4}$	$X_c = 1028$	-

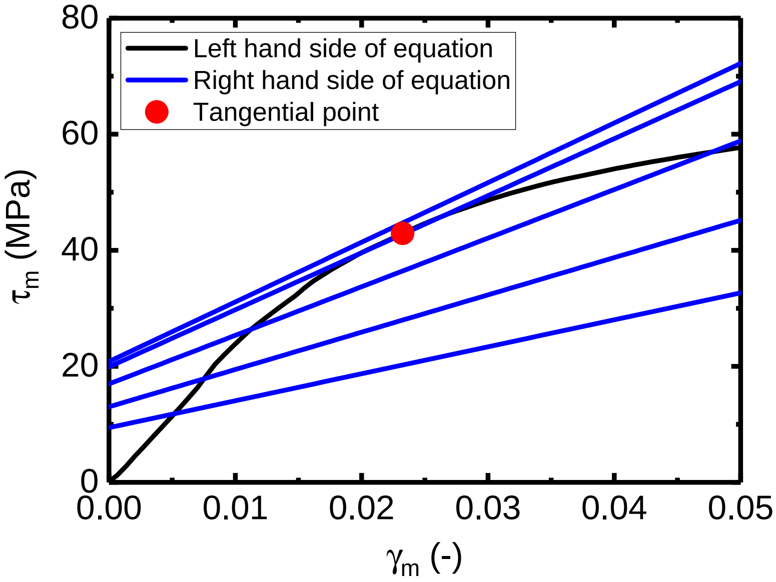

Fig. 7-35 Example for solving the Equation 7-28. The stress values for different instants of time are listed in Table 7-6.

time-shear strain function with the pair of variables listed in Table 7-6 is calculated by the commonly used equation:

$$\dot{\gamma} = \frac{1}{2}\left(\frac{\gamma_{\mathrm{m,i+1}} - \gamma_{\mathrm{m,i}}}{t_{\mathrm{i+1}} - t_{\mathrm{i}}} + \frac{\gamma_{\mathrm{m,i}} - \gamma_{\mathrm{m,i-1}}}{t_{\mathrm{i}} - t_{\mathrm{i-1}}}\right). \tag{7-29}$$

In Table 7-7 the calculated strain rates in the failure plane of the kink-band for four dynamic specimen are shown. A significant increase of the strain rate is observed from $96.32\,\mathrm{s}^{-1}$ calculated in axial loading direction to $809.37\,\mathrm{s}^{-1}$ in the kink-band region. Additionally the same approach is performed on the quasi-static experimental results of the longitudinal compression reference tests (Table 7-7). Compared to the axial strain rate of $2.8 \cdot 10^{-4}\,\mathrm{s}^{-1}$ the strain rate in the failure plane raise up to $6.8 \cdot 10^{-4}\,\mathrm{s}^{-1}$. It is observed that, if the failure strength lies under the predicted strength value, matrix cracking occurs. Thus a low strain rate in the kink-band is determined. In the opposite case if the failure strength lies above the predicted strength value the proposed instability of the fibers appear. In this case a high strain rate is observed.

Tab. 7-7 Strain rate in axial direction and in the failure plane of the kink-band for the quasi-static and dynamic tests.

Quasi-static Tests			**Dynamic Tests**		
Test	**Strain Rate**		**Test**	**Strain Rate**	
	Axial $\dot{\gamma}$ (s^{-1})	Kink-band $\dot{\gamma}$ (s^{-1})		Axial $\dot{\gamma}$ (s^{-1})	Kink-band $\dot{\gamma}$ (s^{-1})
QS-Ref-1	$2.8 \cdot 10^{-4}$	$1.9 \cdot 10^{-3}$	HR-1	96.05	225.41
QS-Ref-2	$2.8 \cdot 10^{-4}$	$5.9 \cdot 10^{-4}$	HR-2	85.93	1190.40
QS-Ref-3	$2.8 \cdot 10^{-4}$	$3.1 \cdot 10^{-4}$	HR-3	-	-
QS-Ref-4	$2.8 \cdot 10^{-4}$	$1.6 \cdot 10^{-4}$	HR-4	110.72	1538.36
QS-Ref-4	$2.8 \cdot 10^{-4}$	$4.7 \cdot 10^{-4}$	HR-5	92.56	283.32
Mean	$2.8 \cdot 10^{-4}$	$6.8 \cdot 10^{-4}$		96.32	809.37
STDV	-	$7.0 \cdot 10^{-4}$		10.48	656.85
CV (%)	-	102.13		10.88	81.16

To summarize these results both strain rates for the quasi-static and dynamic test specimens are plotted in Figure 7-36. The red diamond and the red solid diamond symbol indicate the individual results for the axial strain rate and for the actual strain shear strain rate acting in the kink-band, respectively. It could be shown that particularly the matrix material influences the strain rate dependency of the carbon fiber-reinforced thermoplastic composite. This reinforces the postulated link between the viscoelastic material behavior of the polymer with the strain rate dependency. The strain-rate effect of the transverse compressive strength and the longitudinal compressive strength behaves equally from low to high strain rates due to the mechanical response of the matrix.

Finally the strain rate calculation in a kink band leads to the consideration that an estimation of the longitudinal compressive failure strength at a selected axial high strain rate can be made without performing dynamic longitudinal compression tests. The initial misalignment angle, θ_i, can be calculated by using a quasi-static experimental shear stress-strain curve of the investigated composite material. Therefore only simple in-plane shear tension tests at quasi-static strain rate have to be carried out. Then σ_a as a longitudinal compressive failure strength can be computed. For this calculation the stress-strain curve obtained by dynamic in-plane shear tension tests at the selected high strain rate are used. The predicted stress is a lower boundary for the longitudinal compressive failure strength caused by matrix cracking. Also due to higher failure strength an elastic instability of the material can occur. But to underpin, that this approach might be applicable to other carbon-fiber-reinforced thermoplastic composite materials to characterize the longitudinal compressive strength without carrying out challenging dynamic compression tests in fiber direction, further studies have to be carried out with different materials.

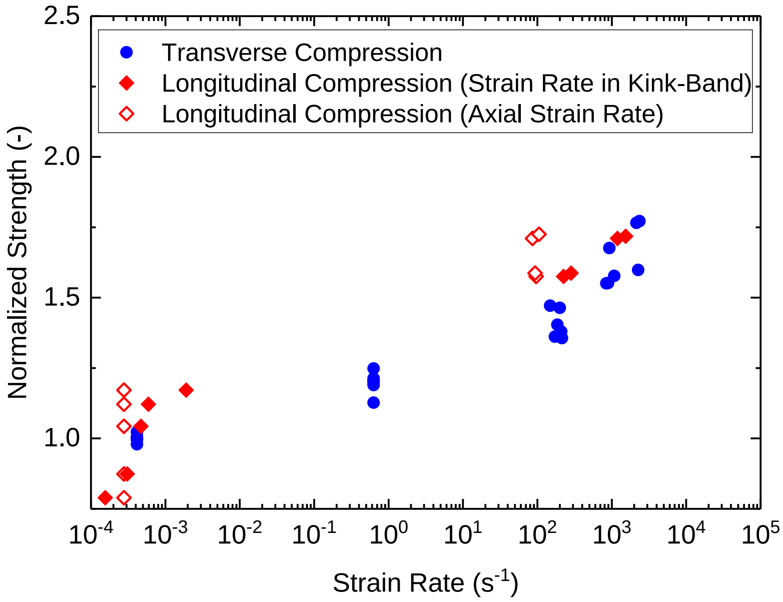

Fig. 7-36 Normalized strength as a function of the strain rate for transversal and longitudinal compression. The strain rate is shown in axial loading direction and in the failure plane of the kink-band.

8 Conclusions

In the aerospace and automotive industry, lightweight constructions made of composite materials are increasingly attractive due to their potential of weight reduction and the resulting improvement on the overall energy efficiency. These fiber-reinforced thermoset or thermoplastic matrix composite materials have extraordinary strength to weight and stiffness to weight ratio. The potential, lying in the optimization of the mechanical performance of composite structures, is however not yet fully exhausted and improvements about the understanding of the mechanical material behavior is still needed. A material behavior of fiber-reinforced composites in the focus is strain rate dependency, since many primary structural applications are exposed to impact and crash load cases.

The mechanical behavior of materials depends on the nuclear structure of the atoms which in turn is strongly influenced by many environmental factors. Compared to metals and ceramic, polymers exhibit a strong time-temperature dependency due to their viscoelastic nature. A decreasing of the temperature has an equivalent influence on the mechanical behavior as an increasing of the strain rate. As it is described in detail in Chapter 2 the root cause of this strain rate dependency of polymers is attributed to the shift of the secondary and primary transition temperatures to higher temperatures with higher strain rates. These transition temperatures are provoked by different relaxation processes of the polymer chains which refer to distinct degrees of freedom for the molecular motion of polymer chains. At higher strain rates molecular motions of the polymer chains are blocked and thus the overall material behavior shows a rigid and brittle response.

In this study the semi-crystalline thermoplastic polymer polyamide-6 was chosen due to its upcoming relevance for structural lightweight applications in the automotive and aerospace industry. Beside the very low commodity price, the thermoplastic polymer offers several other advantages such as a very good chemical resistance, thermoformability, weldability, nearly infinite shelf life, high fracture toughness, recyclability, and a fast processing. Polyamide-6 is one of the most commonly used polymers and currently receives much attention as a matrix material for future carbon-fiber-reinforced composite structures. Common material properties of polyamide-6 are well documented [30–32]. While for the neat polyamide-6 polymer some few studies exist that characterize the strain rate sensitivity of the compression and tensile response only minor attempts were performed to measure stress-strain behavior of carbon-fiber-reinforced polyamide-6 composite at quasi-static and high strain rates. Thus a meaningful description of the strain-rate-dependent mechanical behavior of the composite material cannot be given because of minor reliable and secure results from international studies. This can be attributed to the fact that there are no established testing standards and very few specialized laboratories, research institutes, and universities which are appointed with the necessary testing equipment.

Based on the comprehensive literature review the question arose: How does the loading velocity affect the mechanical properties of unidirectional fiber-reinforced thermoplastic composites when the material is subjected to tensile, compression, and shear loads? This thesis discussed this question in a scientific manner and dealt with further topics that emerged in this context. For example an experimental methodology had to be found that is suitable to measure the effect of strain-rate on the longitudinal compression behavior and is there a way to predict the strain-rate sensitivity on basis of few relatively simple measurements. The following sections give a conclusion of the study and its outcome.

8.1 Simplified Approach for Prediction of Strain Rate's Effect on Mechanical Response of Polymers

The strain rate sensitivity of the unidirectional carbon-fiber-reinforced polyamide-6 under various loading conditions was investigated in this thesis. It is known from literature that carbon fibers are not strain rate sensitive [54, 96, 97]. In contrast to carbon fibers in the composite material the mechanical behavior of the matrix material around the fibers strongly depends on the loading velocity. Regardless of whether thermoset polymers [51, 55, 98–103], elastomeric polymers [104–106] or thermoplastic polymers [19, 20, 28, 29, 33, 35, 51, 107–112], all polymers show strain rate effects. One of the often-cited studies are the works of Walley and Field [19] and Pouriayevali et al. [33] who characterized the compressive stress-strain response of polyamide-6 over a broad strain rate regime, while Shan et al. [35] studied the tensile properties. The measurement of the mechanical response at high strain rates were carried out by using advanced measurement equipment and time consuming post-processing of data. Thus the objective of this study was to find a simple approach to predict the strain rate's effect on the mechanical response of a polymer without complex test setups. Therefore a dynamic mechanical analysis was performed at different frequencies to study the strain rate dependency of neat polyamide-6. A time-temperature shift approach established by Mulliken and Boyce [28] for amorphous polymers was successfully applied to the results of the dynamic mechanical analysis of the semi-crystalline polymer polyamide-6. By means of this method it is possible to predict the rate-dependent elastic storage modulus at high strain rates around $1000\,\mathrm{s}^{-1}$, corresponding to frequencies, which cannot be realized with a DMA test instrument. In this method, the different rate dependencies of the α- and β-transitions temperatures are analyzed and used to shift the storage modulus curve to higher temperatures (Figure 4-4). This allows the analysis of the strain rate sensitivity of the thermoplastic polymer especially at various temperatures and the corresponding storage modulus as a function of strain rate can be drawn. The result shows a bilinear behavior of this correlation. The storage modulus increases with increasing strain rate and at a strain rate of approximately $200\,\mathrm{s}^{-1}$ a significant further increase of the modulus was found.

This result was then compared with the results from dynamic compression tests of PA 6 from low to high strain rates also carried out in this study. For the dynamic test a split-Hopkinson pressure bar system was used. The objective of the comparison was to find out, whether the observed distinctive strain rate regime around $200\,\mathrm{s}^{-1}$, where a significant change of the rate-dependent storage modulus occurs, is comparable with the behavior of the rate-dependent yield strength of polyamide-6 measured with a split-Hopkinson pressure bar system in this strain rate regime. It was shown at this characteristic strain rate around $200\,\mathrm{s}^{-1}$, that in a qualitative manner the same behavior of increasing yield strength with increasing strain rate occurs. It can be concluded that a simple dynamic mechanical analysis measurement at different frequencies and a subsequent data analysis by means of the time-temperature shift method can be used to investigate the strain rate regime, where the material parameters significantly increase.

8.2 Developed Experimental Methodology for Dynamic Longitudinal Compression Tests

Longitudinal compressive stress-strain behavior is investigated in this study at different strain rates for a carbon-fiber-reinforced epoxy and a carbon-fiber-reinforced thermoplastic composite material. Strain-rate-dependent material data about the longitudinal compressive strength of composite materials is generally rare yet important. The longitudinal compressive strength of unidirectional (UD) composites is significantly less than the longitudinal tensile strength and can therefore be a driver for composite-structure design. Whereas it is well accepted that the longitudinal tensile strength of UD carbon composites is not strain-rate sensitive [54, 96, 97], significant rate sensitivity was observed for longitudinal compressive strength in earlier studies. A comprehensive literature review, described in detail in chapter 7.2 showed that the measurement of the longitudinal compression properties is still challenging and subject of debate. The main problem during testing is the premature failure of the specimen. Thus a significantly lower strength value is measured for the investigated material compared to the actual value which would be measured in a compression test with valid failure mode.

A comprehensive study was conducted investigating the effect of strain rate on the longitudinal compressive properties of unidirectional carbon-fiber-reinforced composites. An experimental methodology for SHPB systems was developed to generate a valid failure mode in the free gauge section under static and high-strain-rate loading. Evidence of the dynamic equilibrium condition and minimal bending of the specimen underline the reliability of the developed test setup.

For the investigated UD and quasi-isotropic IM7/8552 laminates, compressive strength was found to increase by 40 %, with strain rates increasing from quasi-static to $100\,\mathrm{s}^{-1}$. At the same strain-rate levels, a 60 % increase in the longitudinal compressive strength was observed for the UD carbon-PA 6 thermoplastic composite also investigated. Compared to the strain rate's effect on strength, its effect on the elastic modulus was found to be insignificant for the laminates and strain rates investigated in this study. The typical non-linear stress-strain behavior of a UD composite material subjected to a compressive load was observed at both strain-rate levels.

The high-quality static and dynamic stress-strain curves may therefore be used to derive the required input for non-linear and strain-rate-dependent composite material models. Using the developed compression test setup, measuring higher values for the static and dynamic longitudinal compressive strength, X_c, of an IM7/8552 UD laminate than in an earlier study [15] proved possible. It was thought that the values measured for the UD laminate still fell short of the actual static and dynamic strength. By testing a multi-directional laminate, which yielded a valid compressive failure in the specimen's free gauge section, then calculating the longitudinal compressive strength of the embedded 0°-UD ply via the procedure outlined in section 7.2.5, larger strength values were indeed derived, whereas the strain rate's effect on longitudinal compressive strength was found to be the same as measured for the UD laminate. Using this approach, realistic dynamic compressive strengths were achieved for this composite material system for the first time.

8.3 Correlation between Strain-Rate-Dependent Mechanical Properties

8.3.1 Neat and Carbon-Fiber-Reinforced Polyamide-6

The effect of strain-rate on the mechanical properties of neat and carbon-fiber-reinforced polyamide-6 was investigated in this study. A comparison has been drawn to show the major correlation between the strain rate sensitive properties of the thermoplastic matrix polymer with and without carbon fibers as reinforcement. A quasi-static and high strain rate characterization of the compressive properties of the neat polymer and of the transverse compression, transverse tension, in-plane shear, and longitudinal compression properties of the composite material were performed.

For the compression tests of the neat polyamide-6 as well as for the transverse compression tests of the carbon-fiber-reinforced polyamide-6 rectangular shaped specimens were used. It could be show that this specimen geometry is useful not only for the composite specimens but also for the neat polymer specimens. A special designed geometry was used for the longitudinal compression specimens. For the tensile tests rectangular shaped specimens were glued into specimen adapters.

The quasi-static and intermediate strain rate experiments were carried out by means of a universal testing machine, while the dynamic measurements were performed with a split-Hopkinson pressure and tension bar system. Special attention was given to the reliability of the high strain rate experiments concerning the possible dispersion effects, pulse shaping, and dynamic stress equilibrium. The dynamic test setup for each experiment was checked by previous bars-together tests to identify whether the wave propagation in the bars underlies dispersion effects or not. Suited incident pulses for the respective specimen stress-strain response were generated by using the pulse shaping technique. For the high-strain-rate tests the specimen strain was measured via digital image correlation by using a high-speed camera with a suitable combination of spatial resolution and frame rate. In addition, the recorded images gave information about the failure mode of the respective specimen type. For the quasi-static and intermediate strain rate tests two CCD cameras in stereo configuration were used to measure the strain field of the specimen surface. A DIC software was used to calculate the in-plane strain field on the entire specimen surface. An exception are the longitudinal compression tests, were strain gauges were used instead of digital image correlation. The reason is that with two strain gauges in back-to-back configuration the percent bending of the loaded specimen can be measured. In addition, a relatively small failure strain is expected for longitudinal compression specimens, which can be measured more accurately with a strain gauge.

For the longitudinal tests the developed experimental method, described in the above section 7.2.5 was used. The final post-processing of the recorded data at the Hopkinson bar system to calculate the stress-time response of the specimen, was carried out by using the classic split-Hopkinson bar analysis method based on the one-dimensional wave propagation theory. It could be shown that all dynamic specimens were loaded under virtually constant strain rate and dynamic equilibrium. Thus a reliable material data set for different load cases from low to high strain rates was obtained. In summary, high deformation rates affect the mechanical properties as follows:

- Compression (PA 6):
  - The Young's modulus increased slightly by 10 % ($340\,\mathrm{s}^{-1}$).
  - The yield strength increased significantly by 91 % ($1260\,\mathrm{s}^{-1}$).
- Transverse Compression (CF/PA 6):
  - The Young's modulus decreased slightly by 15 % ($531\,\mathrm{s}^{-1}$, possible influence of inertia effects).
  - The transverse compression strength increased significantly by 71 % ($2253\,\mathrm{s}^{-1}$).
- Transverse Tension (CF/PA 6):
  - The Young's modulus increased slightly by 15 % ($22\,\mathrm{s}^{-1}$).
  - The transverse tensile strength increased by 24 % ($52\,\mathrm{s}^{-1}$).
- In-Plane Shear (CF/PA 6):
  - The in-plane shear modulus increased slightly by 8 % ($128\,\mathrm{s}^{-1}$).
  - The in-plane shear strength increased by 47 % ($517\,\mathrm{s}^{-1}$).
- Longitudinal Compression (CF/PA 6):
  - The Young's modulus decreased slightly by 15 % ($68\,\mathrm{s}^{-1}$).
  - The longitudinal compressive strength increased by 60 % ($82\,\mathrm{s}^{-1}$).

The strength values for all tested specimen types were normalized to the mean value of the respective quasi-static tests and plotted as a function of strain rate on a logarithmic x-axis (s. Figure 8-1). A linear fitting curve from $3 \cdot 10^{-4}\,\mathrm{s}^{-1}$ to approximately $200\,\mathrm{s}^{-1}$ and another linear fitting curve from approximately $200\,\mathrm{s}^{-1}$ to $2252\,\mathrm{s}^{-1}$ was plotted into the diagram (Figure 8-1). For the second fitting curve at high strain rates the result of the longitudinal compression tests with strain rate in axial direction was not included in the fitting. The result of the longitudinal compression tests, where the strain rate is calculated in a kink-band (see section

7.3), was included in the linear fitting. The curves clearly show a bilinear behavior with a bend at around $200\,s^{-1}$. This correlates with the work from Walley and Field [19], which was presented in section 2.1.2. They showed in their study that polymers can have a bilinear behavior with a sharp increase in gradient at a certain strain rate.

The diagram highlights the correlation between the two material types. When the linear fitting curves are inserted, as shown in Figure 8-1, it is even better to see that an equal strain-rate effect occurred for both material types the neat polymer and the carbon-fiber-reinforced thermoplastic polymer.

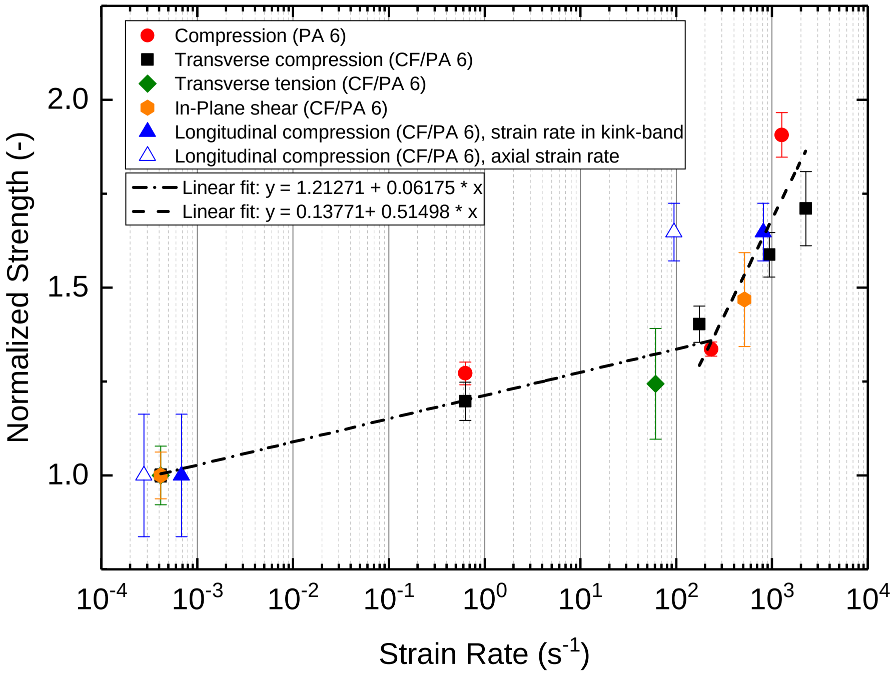

Fig. 8-1 Normalized strength values from experiment as a function of strain rate for different load cases and trend line.

Also for different loading conditions the same influence of the deformation rate on the strength values was found. In short, this shows the dominant influence of the strain-rate-dependent polymer structure on the macroscopic behavior of the material under loading at different strain rates. Even for the compression strength in fiber direction this influence is visible, due to the strain-rate-dependent shear behavior of the polymer matrix in a kink-band.

On the on hand the same behavior of the nominal strength with increasing strain rate was found for the different loading types. On the other hand the experiments in this study demonstrate that the stress-strain curves show very strong differences between transverse tension, transverse compression, in-plane shear and longitudinal compression loading. If this and especially the failure strain are relevant for FE-model purposes, a simple compression test of the neat polymer is not sufficient to characterize the material behavior.

8.3.2 Carbon-Epoxy Prepreg IM7/8552

The reason for carrying out experiments with IM7/8552 was the development of a dynamic test methodology that is useful to measure the longitudinal compressive strength of carbon composites with high performance fibers and high fiber volume content. For this development, comparative values are required which are already available in great abundance for IM7/8552.

The effect of strain-rate on the longitudinal compressive property of the carbon-epoxy prepreg IM7/8552 was investigated by performing compression tests with a universal testing machine and a split-Hopkinson pressure bar system. The same attention to the reliability of the experimental procedure concerning possible dispersion effects, pulse shaping, and dynamic stress equilibrium, as already described in the above section, was given for these longitudinal compression tests. In this case, due to the expected low failure strains, strain gauges were used for recording the specimen strain accurately during loading. The tests were carried out by following the developed experimental method described in the above section 7.2.5. All dynamic specimens were loaded under virtually constant strain rate and dynamic equilibrium, which can be seen by means of the results of the classic split-Hopkinson pressure bar analysis. With this study a reliable data set for the longitudinal compression property at different strain rates was obtained. The strain rate's effect on this mechanical property (s. also Figure 8-2) is as follows:

- The Young's modulus decreased by 1 % at around $100\,\mathrm{s}^{-1}$ which is negligible. Thus one can state that an effect of the strain rate on the Young's modulus was not observed.
- The longitudinal compressive strength increased by 40 % at around $100\,\mathrm{s}^{-1}$.

Figure 8-2 displays a comparison between the effect of strain-rate on 0° compression strength for the IM7/8552 UD and QI laminates tested in this study with tension and compression results published earlier for the same composite material [14, 15, 126, 137]. The graph shows normalized strength values as a function of strain rate plotted on a logarithmic scale. The 0° compressive strength for the UD laminate and the analytically derived 0° compressive strength of the QI laminate determined in this study agree well with the earlier published data. With the results presented in this study and earlier research published by the authors [14, 15] and [126], a complete data set for the dynamic in-plane mechanical response of an IM7/8552

UD carbon-epoxy laminate at strain rates in the range of $100\,\mathrm{s}^{-1}$ to $300\,\mathrm{s}^{-1}$ now exists.

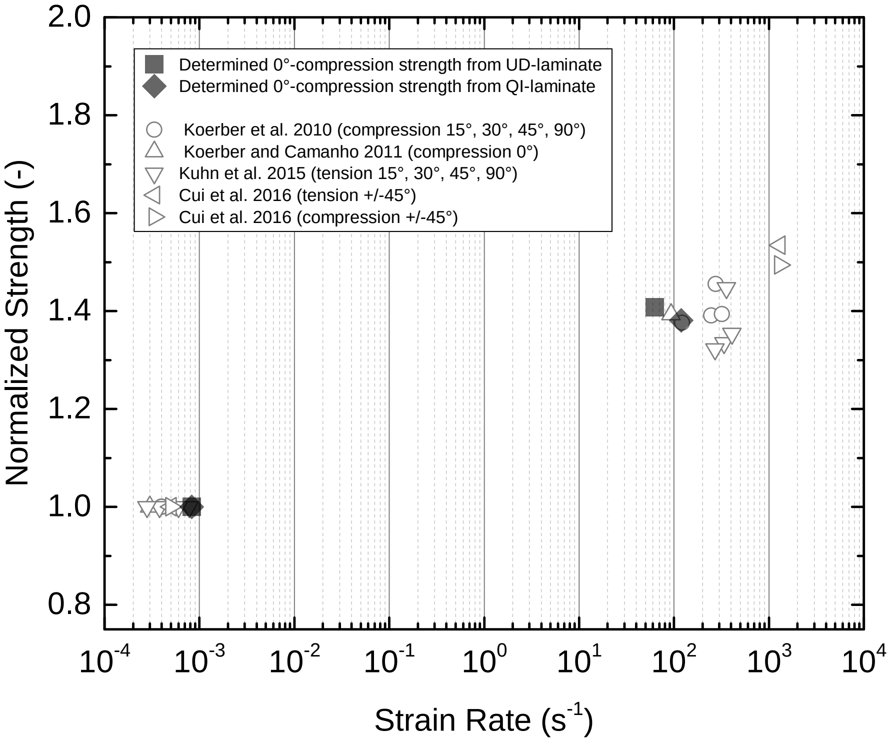

Fig. 8-2 Normalized 0° compression strength determined from IM7/8552 UD and QI laminate compared with normalized tension and compression strength results of published data from Koerber et al. [14], Koerber and Camanho [15], Kuhn et al. [126], and Cui et al. [137].

9 Outlook

In this study a material characterization was presented to investigate the effect of strain-rate on the mechanical properties of carbon-fiber-reinforced thermoplastic composite material. Tensile, compressive, and shear measurements were carried out at different strain rates, for example transverse compression tests were performed at quasi-static strain rate of around $3 \cdot 10^{-4}\,\mathrm{s}^{-1}$ to high strain rates of approximately $2253\,\mathrm{s}^{-1}$. Experiments at intermediate strain rate at around $1\,\mathrm{s}^{-1}$ were only performed for compression tests of the neat polymer and for transverse compression tests of the carbon-fiber-reinforced polymer (s. Figure 8-1). In order to obtain a better understanding of the material behavior at this intermediate strain rate further experiments at different load cases should be carried out to receive a well-grounded data set of results.

Beyond the investigation of the basic mechanical properties such as elastic modulus and strength, which were presented in this study, an investigation of the strain rate sensitivity of the fracture toughness could be a future research task. Thermoplastic composite materials have generally better fracture toughness properties than thermoset composites. This is one reason why these materials are especially used for crash carrying structures. A further knowledge about the strain-rate-dependent fracture toughness would help designers to develop an optimized structural part for such load cases in future. In general the mechanical properties of fiber-reinforced composite materials strongly depend on the connection between the fibers and the surrounding matrix. A week interface between fibers and matrix reduce the mechanical performance drastically. A major role in this case plays the sizing of the fibers which should be adapted to the used matrix polymer. Amongst other characterization methods, the characterization of the fracture toughness can provide information about the connection between fibers and matrix. Thus future investigations should also consider the effect of strain rate on the interface.

Thermoplastic polymers can either have an amorphous microscopic structure or a semi-crystalline structure. In this study a semi-crystalline thermoplastic polymer was analyzed. The crystallinity strongly depends on the cooling rate of the material during processing. There are different ways to manufacture thermoplastic composite parts such as thermoforming in a hot press or double band press and Automated Fiber Placement Technologies. In these manufacturing process the material cools down differently and thus a different degree of crystallinity can be found in the composite material. Thus it would be of interest for future work to analyze the influence of the cooling rate and thus the degree of crystallinity in the thermoplastic composite material on the strain-rate-dependent mechanical material response.

The characterization of composite materials, especially from the perspective of an engineer, is restricted to a selection of mechanical or thermo-analytical methods described in this study. But thinking outside the box draws attention to another field of characterization methods, namely the analysis via spectroscopy. By using neutron or synchrotron radiation, which can be found at major research institutions, the diffraction pattern of a material can be analyzed. Thus it is possible to measure not only the position of the atoms in the atomic structure but also the inner stresses. An investigation of the inner stresses of both fiber and matrix is only possible if the diffraction pattern of fiber and matrix can be well separated. Therefore the best combination might be crystal-like fibers like carbon fibers in an amorphous polymer matrix. Finally a highly time-resolved diffraction could be performed to characterize rapid structural deformations within the matrix, interfacial region, and fiber.

Bibliography

[1] H. Schürmann, *Konstruieren mit Faser-Kunststoff-Verbunden.* Springer Verlag Berlin Heidelberg, 2007, vol. 2.

[2] G. Menges, E. Haberstroh, W. Michaeli, and E. Schmachtenberg, *Menges Werkstoffkunde Kunsstoffe.* Carl Hanser Verlag, 2011, vol. 6.

[3] J. Hopkinson, "On the rupture of iron wire by a blow," *Artikel 39, Original Papers by the late John Hopkinson, Scientific Papers, Cambridge Univ. Press*, vol. 2, pp. 316–324, 1901.

[4] J. Hopkinson, "Further experiments on the rupture of iron wire," *Artikel 39, Original Papers by the late John Hopkinson, Scientific Papers, Cambridge Univ. Press*, vol. 2, pp. 316–320, 1901.

[5] B. Hopkinson, "The effects of momentary stresses in metals," *Proc. R. Soc. London, Serie A*, vol. 74, pp. 498–506, 1905.

[6] B. Hopkinson, "A method of measuring the pressure produced in the detonation of high explosives or by the impact of bullets," *Philos. Trans. R. Soc. London, Serie A*, vol. 213, pp. 437–456, 1914.

[7] R. W. Armstrong and S. M. Walley, "High strain rate properties of metals and alloys," *International Materials Reviews*, vol. 53, no. 3, pp. 105–128, 2008.

[8] H. M. Hsiao, I. M. Daniel, and R. D. Cordes, "Strain rate effects on the transverse compressive and shear behavior of unidirectional composites," *Journal of Composite Materials*, vol. 33, no. 17, pp. 1620–1642, 1999.

[9] M. V. Hosur, J. Alexander, U. K. Vaidya, and S. Jeelani, "High strain rate compression response of carbon/epoxy laminate composites," *Composite Structures*, vol. 52, pp. 405–418, 2001.

[10] J. L. Tsai and C. T. Sun, "Strain rate effect on in-plane shear strength of unidirectional polymeric composites," *Composite Science and Technology*, vol. 65, pp. 1941–1947, 2005.

[11] M. Kawai and S. Saito, "Off-axis strength differential effects in unidirectional carbon/epoxy laminates at different strain rates and predictions of associated failure envelopes," *Composites Part A*, vol. 40, pp. 1632–1649, 2009.

[12] D. Lee, H. Tippur, and P. Bogert, "Quasi-static and dynamic fracture of graphite/epoxy composites: an optical study of loading-rate effects," *Composites Part B*, vol. 41, pp. 462–474, 2010.

[13] A. Gilat, T. E. Schmidt, and A. L. Walker, “Full field strain measurement in compression and tensile split-hopkinson bar experiments,” *Experimental Mechanics*, vol. 49, pp. 291–302, 2009.

[14] H. Koerber, J. Xavier, and P. P. Camanho, “High strain rate characterisation of unidirectional carbon-epoxy IM7-8552 in transverse compression and in-plane shear using digital image correlation,” *Mechanics of Materials*, vol. 42, pp. 1004–1019, 2010.

[15] H. Koerber and P. P. Camanho, “High strain rate characterisation of unidirectional carbon-epoxy IM7-8552 in longitudinal compression,” *Composites Part A*, vol. 42, pp. 462–470, 2011.

[16] H. Koerber, J. Xavier, P. P. Camanho, Y. E. Essa, and F. Martin de la Escalera, “High strain rate behaviour of 5-harness-satin weave fabric carbon-epoxy composite under compression and combined compression-shear loading,” *International Journal of Solids and Structures*, vol. 54, pp. 172–182, 2015.

[17] R. O. Ebewele, *Polymer Science and Technology.* CRC Press, 1996.

[18] S. Koltzenburg, M. Maskos, and O. Nuyken, Eds., *Polymer: Synthese, Eigenschaften und Anwendungen.* Springer Verlag Berlin Heidelberg, 2014.

[19] S. M. Walley and J. E. Field, “Strain rate sensitivity of polymers in compression from low to high rates,” *DYMAT Journal*, vol. 1, no. 3, pp. 211–227, 1994.

[20] C. R. Siviour, S. M. Walley, W. G. Proud, and J. E. Field, “The high strain rate compressive behaviour of polycarbonate and polyvinylidene difluoride,” *Polymer*, vol. 46, pp. 12 546–12 555, 2005.

[21] J. C. Bauwens, “Relation between the compression yield stress and the mechanical loss peak of bisphenol-a-polycarbonate in the beta transition range,” *Journal of Materials Science*, vol. 7, pp. 577–584, 1972.

[22] C. Bauwens-Crowet, “The compression yield behaviour of polymethyl methacrylate over a wide range of temperature and strain-rates,” *Journal of Materials Science*, vol. 8, pp. 968–979, 1973.

[23] F. Rietsch and B. Bouette, “The compression yield behaviour of polycarbonate over a wide range of strain rates and temperatures,” *European Polymer Journal*, vol. 26, no. 10, pp. 1071–1075, 1990.

[24] B. Brulé, J. L. Halary, and L. Monnerie, “Molecular analysis of the plastic deformation of amorphous semi-aromatic polyamides,” *Polymer*, vol. 42, pp. 9073–9083, 2001.

[25] D. Rana, V. Sauvant, and J. L. Halary, “Molecular analysis of yielding in pure and antiplasticized epoxy-amine thermosets,” *Journal of Materials Science*, vol. 37, pp. 5267–5274, 2002.

[26] G. M. Swallowe and S. F. Lee, “A study of the mechanical properties of PMMA and PS at strain rates of 10^{-4} to 10^{3} over the temperature range 293-363 K,” *Journal de Physique IV France*, vol. 110, pp. 33–38, 2003.

[27] J. Richeton, S. Ahazi, L. Daridon, and Y. Rémond, “A formulation of the cooperative model for the yield stress of amorphous polymers for a wide range of strain rates and temperatures,” *Polymer*, vol. 46, pp. 6035–6043, 2005.

[28] A. D. Mulliken and M. C. Boyce, “Mechanics of the rate-dependent elastic-plastic deformation of glassy polymers from low to high strain rates,” *International Journal of Solids and Structures*, vol. 43, no. 5, pp. 1331–1356, 2006.

[29] J. Richeton, S. Ahzi, K. S. Vecchio, F. C. Jiang, and R. R. Adharapurapu, “Influence of temperature and strain rate on the mechanical behavior of three amorphous polymers: Chracterization and modeling of compressive yield stress,” *International Journal of Solids and Structures*, vol. 43, pp. 2318–2335, 2006.

[30] M. Biron, *Thermoplastics and thermoplastic composites*, 1st ed. Oxford: Butterworth-Heinemann, 2007.

[31] E. Baur, S. Brinkmann, T. A. Osswald, and E. Schmachtenberg, *Saechtling Kunststoff Taschenbuch*, 30th ed. Hanser, 2007.

[32] L. Bottenbruch, R. Binsack, G. W. Becker, and D. Braun, *Polyamide. Kunststoffhandbuch 3/4*. Hanser, 1998.

[33] H. Pouriayevali, S. Arabnejad, Y. B. Guo, and V. P. W. Shim, “A constitutive description of the rate-sensitive response of semi-crystalline polymers,” *International Journal of Impact Engineering*, vol. 62, pp. 35–47, 2013.

[34] A. Vashchenko, I. Spiridonova, and E. Sukhovaya, “Deformation and fracture of structural materials under high-rate strain,” *Metalurgija*, vol. 39, no. 2, pp. 89–92, 2000.

[35] G.-F. Shan, W. Yang, M. Yang, B. Xie, J. Feng, and Q. Fu, “Effect of temperature and strain rate on the tensile deformation of polyamide 6,” *Polymer*, vol. 48, pp. 2958–2968, 2007.

[36] M. Hokka, V.-T. Kuokkala, and S. Ihme, “Dynamic tensile testing of polyamide sheets using the HSB technique,” in *Proceedings of the SEM Annual Conference*, Albuquerque New Mexico USA, 2009.

[37] S. Nemat-Nasser, *Introduction to high strain rate testing, ASM handbook mechanical testing and evaluation.* ASM International Ohio USA, 2000, vol. 8.

[38] Z. Wang, Y. Zhou, and P. K. Mallick, "Effects of temperature and strain rate on the tensile behavior of short fiber reinforced polyamide-6," *Polymer Composites*, vol. 23, no. 5, pp. 858–871, 2002.

[39] B. Mouhmid, A. Imad, N. Benseddiq, S. Benmedakhène, and A. Maazouz, "A study of the mechanical behaviour of a glass fibre reinforced polyamide 6,6: Experimental investigation," *Polymer Testing*, vol. 25, pp. 544–552, 2006.

[40] S. J. H. Kuhlman and S. I. Hill, "High strain rate mechanical properties of long glass fiber filled polypropylene and nylon," *SAE Technical Paper 2014-01-1056*, 2014.

[41] M. Todo, K. Takahashi, P. Béguelin, and H. H. Kausch, "Strain-rate dependence of the tensile fracture behaviour of woven-cloth reinforced polyamide composites," *Composites Science and Technology*, vol. 60, pp. 763–771, 2000.

[42] Z. Jendli, J.-C. Walrick, M. Bocquet, and J. Fitoussi, "Strain rate effects on the mechanical behavior of carbon-thermoplastic matrix woven composites," in *Proceedings ECCM16 - 16th European Conference on Composite Materials*, Seville, Spain, 2014, pp. 1–8.

[43] R. Bardenheier, *Dynamic Impact Testing - VHS High Rate Testing Systems.* High Wycombe, UK: Instron Ltd., 2005.

[44] H. M. Hsiao and I. M. Daniel, "Strain rate behavior of composite materials," *Composites Part B*, vol. 29, no. 5, pp. 521–533, 1998.

[45] R. M. Davies, "A critical study of the hopkinson pressure bar," *Philos. Trans. R. Soc. London, Serie A*, vol. 240, no. 821, pp. 375–457, 1948.

[46] H. Kolsky, "An investigation of the mechanical properties of materials at very high rates of loading," *Proc. Phys. Soc.*, vol. 62, no. II-B, pp. 676–700, 1949.

[47] J. Harding, E. O. Wood, and J. D. Campbell, "Tensile testing of materials at impact rates of strain," *Journal of Mechanical Engineering Science*, vol. 2, pp. 88–96, 1960.

[48] U. Lindholm and L. Yeakley, "High strain rate testing: Tension and compression," *Experimental Mechanics*, vol. 8, pp. 1–9, 1968.

[49] J. P. Noble and J. Harding, "Temperature-measurement in the tensile hopkinson bar test," *Measurement Science and Technology*, vol. 5, no. 9, pp. 1163–1171, 1994.

[50] H. Huh, W. J. Kang, and S. S. Han, "A tension split hopkinson bar for investigating the dynamic behavior of sheet metals," *Experimental Mechanics*, vol. 42, no. 1, pp. 8–17, 2002.

[51] W. Chen, F. Lu, and M. Cheng, "Tension and compression tests of two polymers under quasi-static and dynamic loading," *Polymer Testing*, vol. 21, pp. 113–121, 2002.

[52] T. Yokoyama, "Impact tensile stress-strain characteristic of wrought magnesium alloys," *Strain*, vol. 39, no. 4, pp. 167–175, 2003.

[53] R. Smerd, S. Winkler, C. Salisbury, M. Worswick, D. Lloyd, and M. Finn, "High strain rate tensile testing of automotive aluminum alloy sheet," *International Journal of Impact Engineering*, vol. 32, no. 1-4, pp. 541–560, 2005.

[54] N. Taniguchi, T. Nishiwaki, and H. Kawada, "Tensile strength of unidirectional CFRP laminate under high strain rate," *Advanced Composite Materials*, vol. 16, no. 2, pp. 167–180, 2007.

[55] R. Gerlach, C. R. Siviour, N. Petrinic, and J. Wiegand, "Experimental characterisation and constitutive modelling of RTM-6 resin under impact loading," *Polymer*, vol. 49, pp. 2728–2737, 2008.

[56] X. Nie, B. Song, Y. Ge, W. W. Chen, and E. Weerasooriya, "Dynamic tensile testing of soft materials," *Experimental Mechanics*, vol. 49, no. 4, pp. 451–458, 2009.

[57] M. R. Arthington, C. R. Siviour, and N. Petrinic, "Improved materials characterisation through the application of geometry reconstruction to quasi-static and high-strain-rate tension tests," *International Journal of Impact Engineering*, vol. 46, pp. 86–96, 2012.

[58] R. Gerlach, C. R. Siviour, J. Wiegand, and N. Petrinic, "In-plane and through-thickness properties, failure modes, damage and delamination in 3 D woven carbon fiber composites subjected to impact loading," *Composites Science and Technology*, vol. 72, no. 3, pp. 397–411, 2012.

[59] R. Gerlach, C. Kettenbeil, and N. Petrinic, "A new split hopkinson tensile bar design," *International Journal of Impact Engineering*, vol. 50, pp. 63–67, 2012.

[60] K. T. Ramesh, *Springer Handbook of experimental solid mechanics*, 1st ed. Springer US, 2008, ch. High strain rate and impact experiments, pp. 1–30.

[61] G. T. Gray III., *Classic split-Hopkinson pressure bar testing. ASM handbook mechanical testing and evaluation.* ASM International Ohio USA, 2000, vol. 8.

[62] B. A. Gama, S. L. Lopatnikov, and J. W. G. Jr., “Hopkinson bar experimental technique: A critical review,” *Applied Mechanics Reviews*, vol. 57, no. 4, pp. 223–250, Juli 2004.

[63] H. Koerber, “Mechanical response of advanced composites under high strain rates,” Ph.D. dissertation, Faculdade de Engenharia da Universidade do Porto, Departamento de Engenharia Mecânica, 2010.

[64] M. A. Meyers, *Dynamic behavior of materials.* New York: John Wiley & Sons, Inc., 1994.

[65] C. Kittel, *Introduction to solid state physics*, 8th ed. John Wiley & Sons, Inc., 2004.

[66] P. K. Misra, *Physics of condensed matter.* Academic Press, Elsevier, 2011.

[67] H. Ibach and H. Lüth, *Festkörperphysik: Einführung in die Grundlagen*, 7th ed. Springer-Verlag Berlin Heidelberg, 2009.

[68] N. W. Ashcroft and D. N. Mermin, *Festkörperphysik.* Oldenbourg-Verlag, 2013.

[69] G. Subhash, *Split-Hopkinson pressure bar testing of ceramics. ASM handbook mechanical testing and evaluation.* ASM International Ohio USA, 2000, vol. 8.

[70] C. E. Frantz, P. S. Follansbee, and W. J. Wright, “New experimental techniques with the split hopkinson pressure bar,” in *Proceedings of the 8th international conference on high energy rate fabrication, pressure vessel and piping division, ASME*, I. Berman and J. Schroeder, Eds., San Antonio, TX, 1984.

[71] P. S. Follansbee, *The hopkinson bar, mechnical testing, metals handbook*, 9th ed. Metals Park, Ohio: American Society for Metals, 1985, vol. 8.

[72] D. J. Frew, M. J. Forrestal, and W. Chen, “Pulse shaping techniques for testing brittle materials with a split hopkinson pressure bar,” *Experimental Mechanics*, vol. 42, no. 1, pp. 93–106, 2002.

[73] S. Ellwood, L. J. Griffiths, and D. J. Parry, “Material testing at high constant strain rates,” *Journal of Physics E: Scientific Instruments*, vol. 15, pp. 280–282, 1982.

[74] S. Nemat-Nasser, J. B. Isaacs, and J. E. Starrett, “Hopkinson techniques for dynamic recovery experiments,” in *Proceedings of the Royal Society of London Series A*, vol. 435, 1991, pp. 371–391.

[75] T. Kreis, *Handbook of Holographic Interferometry: Optical and Digital Methods.* Wiley-VCH Verlag GmbH & Co. KGaA, Weinheim, 2005.

[76] P. Jacquot, “Speckle interferometry: A review of the principal methods in use for experimental mechanics applications,” *Strain*, vol. 44, no. 1, pp. 57–69, 2008.

[77] D. Post and B. Han, *Moiré Interferometry.* Boston, MA: Springer US, 2008, pp. 627–654.

[78] J. S. Sirkis and T. J. Lim, “Displacement and strain-measurement with automated grid methods,” *Experimental Mechanics*, vol. 31, pp. 382–388, 1991.

[79] H. T. Goldrein, S. J. P. Palmer, and J. M. Huntley, “Automated fine grid technique for measurement of large-strain deformation maps,” *Optics and Lasers in Engineering*, vol. 23, pp. 305–318, 1995.

[80] B. Pan, K. Qian, H. Xie, and A. Asundi, “Two-dimensional digital image correlation for in-plane displacement and strain measurement: a review,” vol. 20, no. 6, p. 062001 (17pp), 2009.

[81] W. H. Peters and W. F. Ranson, “Digital imaging technique in experimental stress analysis,” *Optical Engineering*, vol. 21, no. 3, pp. 427–431, 1982.

[82] T. C. Chu, W. F. Ranson, M. A. Sutton, and W. H. Peters, “Applications of digital-image-correlation technique to experimental mechanics,” *Experimental Mechanics*, vol. 25, pp. 232–244, 1985.

[83] M. A. Sutton, C. Mingqi, W. H. Peters, Y. J. Chao, and S. R. McNeill, “Application of an optimized digital correlation method to planar deformation analysis,” *Image and Vision Computing*, vol. 4, pp. 143–150, 1986.

[84] W. H. Peters, W. F. Ranson, M. A. Sutton, T. C. Chu, and J. Anderson, “Application of digital correlation methods to rigid body mechanics,” *Optical Engineering*, vol. 22, pp. 738–742, 1983.

[85] M. A. Sutton, S. R. McNeill, J. D. Helm, and Y. J. Chao, *Advances in Two-dimensional and three-dimensional computer vision, Topics in applied physics*, P. Rastogi, Ed. Berlin: Springer, 2000, vol. 77.

[86] H. W. Schreier, “Investigation of two and three-dimensional image correlation technique with applicatioins in experimental mechanics,” Ph.D. dissertation, University of South Carolina, 2003.

[87] A. Giachetti, “Matching technique to compute image motion,” *Image and Vision Computing*, vol. 18, pp. 247–260, 2000.

[88] W. Tong, “An evaluation of digital image correlation criteria for strain mapping applications,” *Strain*, vol. 41, pp. 167–175, 2005.

[89] H. W. Schreier and M. A. Sutton, “Systemtic errors in digital image correlation due to undermaunder subset shape functions,” *Experimental Mechanics*, vol. 42, pp. 303–310, 2002.

[90] H. Lu and P. D. Cary, “Deformation measurement by digital image correlation: implementation of a second-order displacement gradient,” *Experimental Mechanics*, vol. 40, pp. 393–400, 2000.

[91] M. A. Sutton, J. J. Orteu, and H. Schreier, *Image Correlation for Shape, Motion and Deformation Measurements: Basic Concepts, Theory and Applications.* Springer Berlin, 2009.

[92] I. Ward and D. Hadley, *An introduction to the mechanical properties of solid polymers*, 3rd ed. New York: John Wiley and Sons, 1993.

[93] T. Kawaguchi, “The dynamic mechanical properties of nylons,” *Journal of Applied Polymer Science*, vol. 2, no. 4, pp. 56–61, 1959.

[94] N. G. McCrum, B. E. Read, and G. Williams, *Anelastic and dielectric effects in polymer solids.* New York: Wiley, 1967.

[95] T. R. Crompton, *Polymer Reference Book.* UK: Rapra Technology Limited, 2006.

[96] Y. Zhou, D. Jiang, and Y. Xia, “Tensile mechanical behavior of T300 and M40J fiber bundles at different strain rate,” *Journal of Materials Science*, vol. 36, pp. 919–922, 2001.

[97] J. Harding and L. M. Welsh, “A tensile testing technique for fiber-reinforced composites at impact rates of strain,” *Journal of Materials Science*, vol. 18, no. 6, pp. 1810–1826, 1983.

[98] A. E. Mayr, W. D. Cook, and G. H. Edward, “Yielding behaviour in model epoxy thermosets - I. effect of strain rate and composition,” *Polymer*, vol. 39, no. 16, pp. 3719–3724, 1998.

[99] J. P. Hou, C. Ruiz, and A. Trojanowski, “Torsion tests of thermosetting resins at impact strain rate and under quasi-static loading,” *Materials Science and Engineering A*, vol. 283, pp. 181–188, 2000.

[100] C. P. Buckley, J. Harding, J. P. Hou, C. Ruiz, and A. Trojanowski, “Deformation of thermosetting resins at impact rates of strain. Part I: Experimental study,” *Journal of the Mechanics and Physics of Solids*, vol. 49, no. 7, pp. 1517–1538, 2001.

[101] A. Gilat, R. K. Goldberg, and G. D. Roberts, “Experimental study of strain-rate-dependent behavior of carbon/epoxy composite,” *Composites Science and Technology*, vol. 62, no. 10-11, pp. 1469–1476, 2002.

[102] A. Gilat, R. K. Goldberg, and G. D. Roberts, “Strain rate sensitivity of epoxy resin in tensile and shear loading,” NASA/TM-2005-213595, NASA, Technical Report, 2005.

[103] N. K. Naik, P. J. Shankar, V. R. Kavala, G. Ravikumar, J. R. Pothnis, and H. Arya, “High strain rate mechanical behavior of epoxy under compression loading: Experimental and modeling studies,” *Materials Science and Engineering A*, vol. 528, pp. 846–854, 2011.

[104] J. Yi, M. C. Boyce, G. F. Lee, and E. Balizer, “Large deformation rate-dependent stress-strain behavior of polyurea and polyurethanes,” *Polymer*, vol. 47, no. 1, pp. 319 – 329, 2006.

[105] C. M. Roland, J. N. Twigg, Y. Vu, and P. H. Mott, “High strain rate mechanical behavior of polyurea,” *Polymer*, vol. 48, pp. 574–578, 2007.

[106] S. S. Sarva, S. Deschanel, M. C. Boyce, and W. Chen, “Stress-strain behavior of a polyurea and a polyurethane from low to high strain rates,” *Polymer*, vol. 48, pp. 2208–2213, 2007.

[107] G. M. Swallowe, J. O. Fernandez, and S. Hamdan, “Crystallinity increases in semi crystalline polymers during high rate testing,” *J. Phys. IV France*, vol. 07, pp. C3–453–C3–458, 1997.

[108] H. Zhao, “A study of specimen thickness effects in the impact tests on polymers by numeric simulations,” *Polymer*, vol. 39, no. 5, pp. 1103–1106, 1998.

[109] A. Dasari and R. D. K. Misra, “On the strain rate sensitivity of high density polyethylene and polypropylenes,” *Materials Science and Engineering A*, vol. 358, pp. 356–371, 2003.

[110] P. J. Rae, E. N. Brown, and E. B. Orler, “The mechanical properties of poly(ether-ether-ketone) (PEEK) with emphasis on the large compressive strain response,” *Polymer*, vol. 48, no. 2, pp. 598–615, 2007.

[111] J. Ingram, Y. Zhou, S. Jeelani, T. Lacy, and M. F. Horstemeyer, “Effect of strain rate on tensile behavior of polypropylene and carbon nanofiber filled polypropylene,” *Materials Science and Engineering A*, vol. 489, pp. 99–106, 2008.

[112] T. Yokoyama and K. Nakai, “Determination of high strain-rate compressive stress-strain loops of selected polymers,” *Applied Mechanics and Materials*, vol. 24-25, pp. 349–355, 2010.

[113] “Material data sheet: Ultramid (PA) product range (Europe),” (2015/04/16). [Online]. Available: http://www.plasticsportal.net/wa/plasticsEU~en_GB/function/conversions:/publish/common/upload/engineering_plastics/Ultramid_range_chart.pdf

[114] S. C. Chou, K. D. Robertson, and J. H. Rainey, “The effect of strain rate and heat developed during deformation on the stress-strain curve of plastics,” *Experimental Mechanics*, vol. 13, pp. 422–432, 1973.

[115] “Internal communication: Material data sheet - Standard product values Celstran CFR-TP PA6 CF60-01, (2014/07/29).”

[116] *ASTM D3171-99, Standard Test Methods for Constituent Content of Composite Materials, ASTM International, West Conshohocken, PA*, Std., 1999.

[117] E. Woldesenbet and J. R. Vinson, “Specimen geometry effects on high-strain-rate testing of graphite/epoxy composites,” *AIAA Journal*, vol. 37, no. 9, pp. 1102–1106, 1999.

[118] *ASTM D6641 / D6641M-09, Standard Test Method for Compressive Properties of Polymer Matrix Composite Materials Using a Combined Loading Compression (CLC) Test Fixture, ASTM International, West Conshohocken, PA*, Std., 2009.

[119] M. Knops, *Analysis of failure in fiber polymer laminates.* Springer-Verlag Berlin Heidelberg New York, 2008.

[120] H. Koerber, M. Vogler, P. Kuhn, and P. P. Camanho, “Experimental characterisation and modelling of non-linear stress-strain behaviour and strain rate effects for undirectional carbon-epoxy,” in *Proceedings ECCM16 - 16th European Conference on Composite Materials*, Seville, Spain, 2014, pp. 1–8.

[121] M. Ploeckl, P. Kuhn, and H. Koerber, “Characterization of unidirectional carbon fiber reinforced polyamide-6 thermoplastic composite under longitudinal compression loading at high strain rate,” in *EPJ Web of Conferences*, vol. 94, 2015, pp. 01 041 1–6.

[122] M. Ploeckl, P. Kuhn, J. Grosser, M. Wolfahrt, and H. Koerber, “A dynamic test methodology for analyzing the strain-rate effect on the longitudinal compressive behavior of fiber-reinforced composites,” *Composite Structures*, vol. 180, pp. 429–438, 2017.

[123] Q. Bing and C. T. Sun, “Modelling and testing strain rate-dependent compressive strength of carbon/epoxy composites,” *Composite Science and Technology*, vol. 65, pp. 2481–2491, 2005.

[124] J. Wiegand, "Constitutive modelling of composite materials under impact loading," Ph.D. dissertation, University of Oxford, 2008.

[125] P. P. Camanho and M. Lambert, "A design methodology for mechanically fastened joints in laminated composite materials," *Composites Science and Technology*, vol. 66, no. 15, pp. 3004–3020, 2006.

[126] P. Kuhn, M. Ploeckl, and H. Koerber, "Experimental investigation of the failure envelope of unidirectional carbon-epoxy composite under high strain rate transverse and off-axis tensile loading," in *EPJ Web of Conferences*, vol. 94, 2015, pp. 01 040 1–6.

[127] "Hexcel product data: Hexply 8552 epoxy matrix," (2016/10/12). [Online]. Available: http://www.hexcel.com/Resources/DataSheets/Prepreg-Data-Sheets/8552_us.pdf

[128] J. S. Welsh and D. F. Adams, "Unidirectional composite compression strengths obtained by testing mini-sandwich, angle- and cross-ply laminates," Composite Materials Research Group, University of Wyoming, Laramie, WY, Tech. Rep. No. UW-CMRG-R-95-106, April 1995.

[129] J. S. Welsh and D. F. Adams, "Testing of angle-ply laminates to obtain unidirectional composite compression strengths," *Composites Part A*, vol. 28A, pp. 387–396, 1997.

[130] S. T. Pinho, L. Iannucci, and P. Robinson, "Physically-based failure models and criteria for laminated fibre-reinforced composites with emphasis on fibre kinking: Part I: development," *Composites Part A*, vol. 37, pp. 63–73, 2006.

[131] A. S. Argon, *Fracture of composites, In: Treatise on materials science and technology.* New York: Academic Press, 1972.

[132] C. G. Dávila, N. Jaunky, and S. Goswami, "Failure criteria for FRP laminates in plane stress," in *44th AIAA/ ASME/ ASCE/ AHS/ ASC Structures, Structural Dynamics, and Materials Conference*, AIAA Paper 2003-1991, Ed., 2003.

[133] C. G. Dávila and P. P. Camanho, "Failure criteria for FRP laminates in plane stress," Tech. Rep. NASA/TM-2003-212663, National Aeronautics and Space Administration, USA, Tech. Rep., 2003.

[134] C. G. Dávila, P. P. Camanho, and C. A. Rose, "Failure criteria for FRP laminates," *Journal of Composite Materials*, vol. 39, no. 4, 2005.

[135] W. Ramberg and W. R. Osgood, "Description of stress–strain curves by three parameters," Technical Note No. 902, National Advisory Committee For Aeronautics, Washington DC, Tech. Rep., 1943.

[136] S. T. Pinho, “Modelling failure of laminated composites using physically-based failure models,” Ph.D. dissertation, Department of Aeronautics, Imperial College London, South Kensintong Campus, London SW7 2AZ U.K., 2005.

[137] H. Cui, D. Thomson, A. Pellegrino, J. Wiegand, and N. Petrinic, “Effect of strain rate and fibre rotation on the in-plane shear response of ±45° laminates in tension and compression tests,” *Composites Science and Technology*, vol. 135, pp. 106–115, 2016.